International Journal of Modern Physics E
© World Scientific Publishing Company

arXiv:2208.13440v1 [nucl-th] 29 Aug 2022

Dynamics of Hot QCD Matter – Current status and developments

Santosh K. Das[1*], Prabhakar Palni[2†], Jhuma Sannigrahi[1], Jan-e Alam[3], Cho Win Aung[4], Yoshini Bailung[5], Debjani Banerjee[6], Gergely Gábor Barnaföldi[7], Subash Chandra Behera[8], Partha Pratim Bhaduri[3], Samapan Bhadury[9], Rajesh Biswas[9], Pritam Chakraborty[10], Vinod Chandra[11], Prottoy Das[6], Sadhana Dash[10], Saumen Datta[12], Sudipan De[13], Vaishnavi Desai[2], Suman Deb[5], Debarshi Dey[14], Jayanta Dey[5], Sabyasachi Ghosh[4], Najmul Haque[9], Mujeeb Hasan[14], Amaresh Jaiswal[9], Sunil Jaiswal[12], Chitrasen Jena[15], Gowthama K K[11], Salman Ahamad Khan[14], Lokesh Kumar[16], Sumit Kumar Kundu[5], Manu Kurian[11], Neelkamal Mallick[5], Aditya Nath Mishra[7], Sukanya Mitra[12], Lakshmi J. Naik[17], Sonali Padhan[10] Ankit Kumar Panda[9], Pushpa Panday[14], Suvarna Patil[1], Binoy Krishna Patra[14], Pooja[1], Raghunath Pradhan[8], Girija Sankar Pradhan[5], Jai Prakash[1], Suraj Prasad[5], Prabhat R. Pujahari[8], Shubhalaxmi Rath[10], Sudhir Pandurang Rode[18], Ankhi Roy[5], Victor Roy[9], Marco Ruggieri[19], Rohan V S[20], Raghunath Sahoo[5], Nihar Ranjan Sahoo[21], Dushmanta Sahu[5], Nachiketa Sarkar[9], Sreemoyee Sarkar[22], Sarthak Satapathy[13], Captain R. Singh[5], V. Sreekanth[17], K. Sreelakshmi[17], Sumit[14], Dhananjaya Thakur[23], Sushanta Tripathy[24], Thandar Zaw Win[4], (authors)[‡]

[1] *School of Physical Sciences, Indian Institute of Technology Goa, Ponda-403401, Goa, India*
[2] *School of Physical and Applied Sciences, Goa University, Goa, India*
[3] *Variable Energy Cyclotron Centre, HBNI, 1/AF Bidhan Nagar, Kolkata 700064, India*
[4] *Indian Institute of Technology Bhilai, GEC Campus, Sejbahar, Raipur 492015, Chhattisgarh, India*
[5] *Department of Physics, Indian Institute of Technology Indore, Simrol, Indore 453552, India*
[6] *Department of Physics, Bose Institute, Kolkata - 700091, WB, India*
[7] *Wigner Research Center for Physics, 29-33 Konkoly-Thege Miklós Str., H-1121 Budapest, Hungary*
[8] *Indian Institute Of Technology, Madras, Chennai, Tamilnadu 600036, India*
[9] *School of Physical Sciences, National Institute of Science Education and Research, An OCC of Homi Bhabha National Institute, Jatni-752050, India*
[10] *Department of Physics, Indian Institute of Technology Bombay, Mumbai, Maharashtra, Pin-400076, India*
[11] *Indian Institute of Technology Gandhinagar, Gandhinagar-382355, Gujarat, India*
[12] *Tata Institute of Fundamental Research, Homi Bhabha Road, Mumbai 400005, India*
[13] *Department of Physics, Dinabandhu Mahavidyalaya, Bongaon, West Bengal State University, P.O. - Bongaon, North 24 Parganas, West Bengal, PIN - 743235, India*
[14] *Department of Physics, Indian Institute of Technology Roorkee, Roorkee, Uttarakhand-247667, India*
[15] *Indian Institute of Science Education and Research, Tirupati, Rami Reddy Nagar, Mangalam, Tirupati, Andhra Pradesh, PIN - 517507, India*
[16] *Department of Physics, Panjab University, Chandigarh 160014, India*
[17] *Department of Sciences, Amrita School of Physical Sciences, Coimbatore Amrita Vishwa Vidyapeetham, India*
[18] *Veksler and Baldin Laboratory of High Energy Physics, Joint Institute for Nuclear Research, Dubna 141980, Moscow region, Russian Federation*
[19] *School of Nuclear Science and Technology, Lanzhou University 222 South Tianshui Road, Lanzhou 730000, China*
[20] *Amrita School of Physical Sciences, Amrita Vishwa Vidyapeetham, Amritapuri Kollam, Kerala 690525, India*

[21] *Institute of Frontier and Interdisciplinary Science, Shandong University, Qingdao, Shandong, 266237, China and Key Laboratory of Particle Physics and Particle Irradiation, Shandong University, Qingdao, Shandong, 266237, China*
[22] *Mukesh Patel School of Technology Management and Engineering, NMIMS University, Mumbai-56, India*
[23] *Institute of Modern Physics, Chinese Academy of Sciences, Lanzhou, Gansu, 730000, China*
[24] *INFN - sezione di Bologna, via Irnerio 46, 40126 Bologna BO, Italy*

The discovery and characterization of hot and dense QCD matter, known as Quark-Gluon Plasma (QGP), remains the most international collaborative effort and synergy between theorists and experimentalists in modern nuclear physics to date. The experimentalists around the world not only collect an unprecedented amount of data in heavy-ion collisions, at Relativistic Heavy Ion Collider (RHIC), at Brookhaven National Laboratory (BNL) in New York, USA, and the Large Hadron Collider (LHC), at CERN in Geneva, Switzerland but also analyze these data to unravel the mystery of this new phase of matter that filled a few microseconds old universe, just after the Big Bang. In the meantime, advancements in theoretical works and computing capability extend our wisdom about the hot-dense QCD matter and its dynamics through mathematical equations. The exchange of ideas between experimentalists and theoreticians is crucial for the progress of our knowledge. The motivation of this first conference named "HOT QCD Matter 2022" is to bring the community together to have a discourse on this topic. In this article, there are 36 sections discussing various topics in the field of relativistic heavy-ion collisions and related phenomena that cover a snapshot of the current experimental observations and theoretical progress. This article begins with the theoretical overview of relativistic spin-hydrodynamics in the presence of the external magnetic field, followed by the Lattice QCD results on heavy quarks in QGP, and finally, it ends with an overview of experiment results.

Keywords: Heavy-ion Collisions, Quark-gluon plasma, Heavy quark, Strangeness, Jets

PACS numbers:12.38.-t, 12.38.Aw

Contents

1. Relativistic Dissipative Spin-hydrodynamics and spin-magnetohydrodynamics 4
2. Heavy Quarks in QGP: Results From Lattice QCD 9
3. Relativistic Hydrodynamics with momentum-dependent relaxation time approximation 14
4. Recent results in small systems from CMS 18
5. Heavy Quark Diffusion in QCD Matter: Glasma vs Plasma 23
6. The Impact of Memory on Heavy Quarks Dynamics in Hot QCD Medium 27
7. Modification of intra-jet properties in high multiplicity pp collisions at $\sqrt{s} = 13$ TeV with ALICE 30

*santosh@iitgoa.ac.in
†prabhakar.palni@unigoa.ac.in
‡The contributors on this author list have contributed only to those sections of the report, which they cosign with their name. Only those have collaborated together, whose names appear together in the header of a given section.

8. Heavy Quarkonia in a hot and dense strongly magnetized QCD medium . 33
9. Measurement of charged-particle jet properties in p-Pb collisions at $\sqrt{s_{\rm NN}} = 5.02$ TeV with ALICE 37
10. Strange particles femtoscopic correlation in PbPb collisions at $\sqrt{s_{\rm NN}}$= 5.02 TeV 40
11. Measurement of exclusive vector meson photoproduction in pPb and PbPb collisions with the CMS experiment 44
12. Investigation of jet quenching effects due to different energy loss mechanisms in heavy-ion collisions using JETSCAPE framework 47
13. Recent Results from STAR and ALICE Experiments 51
14. Impact of Time Varying Electromagnetic Field on Electrical Conductivity of Hot QCD Matter 55
15. Study of Electromagnetic Effect by Charged-dependent Directed Flow in Isobar Collisions at $\sqrt{s_{NN}} = 200$ GeV using STAR at RHIC 58
16. Suppressed Charmonium production in *pp* Collisions at the LHC Energies 62
17. Spatial Diffusion of Heavy Quarks in Magnetic Field 66
18. Weak Interaction driven bulk viscosity of hot and dense plasma 70
19. Study of jet fragmentation functions at RHIC and LHC energies using the JETSCAPE framework 74
20. First-order stable and causal hydrodynamics from kinetic theory 78
21. Hydrodynamical Attractor and Signals from Quark-Gluon Plasma . . . 81
22. Dependence of anisotropic flow and particle production on particlization models and nuclear equation of state 84
23. Conductivity of massless quark matter for its lowest possible relaxation time 87
24. Exploring the numerical bands of electrical conductivity of quark gluon plasma and decay profile of magnetic field 91
25. Causal hydrodynamics based on effective kinetic theory and particle yield from QGP 94
26. Relativistic Dissipative Magnetohydrodynamic from Kinetic Theory . . . 98
27. Parameters estimation of the Viscous Blast-Wave model using Machine learning techniques 103
28. Charge and heat transport properties of a weakly magnetized hot QCD matter at finite density 107
29. Multiplicity dependent study of $\Lambda(1520)$ production in pp collisions at $\sqrt{s} = 5$ and 13 TeV 112
30. Non-identical particle femtoscopy in Pb–Pb collisions at $\sqrt{s_{\rm NN}} = 5.02$ TeV with ALICE 115
31. Estimation of hadronic phase lifetime and locating the QGP phase boundary 119
32. First deep learning based estimator for elliptic flow in heavy-ion collisions122
33. Thermoelectric response in a thermal QCD medium with chiral quasiparticle masses 125

34. Charge and heat transport in hot quark matter with chiral dependent quark masses 128
35. NLO quark self-energy and dispersion relation using the hard thermal loop resummation 131
36. Overview of experimental results 135

1. Relativistic Dissipative Spin-hydrodynamics and spin-magnetohydrodynamics

Samapan Bhadury and Amaresh Jaiswal

We write semi-classical kinetic equations for a relativistic fluid of spin-1/2 particles within the relaxation time approximation, with and without magnetic field. Building on these, we then go on to formulate the theory of relativistic hydrodynamics in both cases. Consequently, we obtain the theories of relativistic dissipative spin-hydrodynamics and spin-magnetohydrodynamics. While in the former case, we find, for the first time, the dissipation mechanism of spin degrees of freedom, in the latter case, we note effects analogous to Einstein-de Haas and Barnett effects at the dissipation level.

1.1. *Introduction*

In the ultra-relativistic non-central heavy-ion collisions at the collider facilities such as Relativistic Heavy-Ion Collider (RHIC) and Large Hadron Collider (LHC), a large angular momentum[1] as well as a large magnetic field[2] are generated at the early stages of the evolution, which can couple with the intrinsic spin of the constituent particle via the processes similar to Einstein-de Haas and Barnett effects. It was predicted that such couplings lead to the spin polarization of the medium,[3,4] which can be observed in particles emitted during freeze-out. This was latter confirmed experimentally[6–11] giving a significant boost to the study of spin-polarization.

The hydrodynamic models assuming equilibrated spin degrees of freedom successfully explained these observations of global spin-polarization but failed to show similar success in the case of longitudinal spin-polarization.[11,12] This indicated different possible origins of spin-polarization, which then led to the belief that the spin degrees of freedom in the transverse plane may not achieve equilibration at the time of freeze-out,[13] and consequently, we may require dissipative theories of hydrodynamics.

Hence, we formulated a theory of relativistic dissipative spin-hydrodynamics first without the influence of an external field and then in the presence of a magnetic field from the relativistic kinetic theory that is consistent with macroscopic conservation laws. In the latter case, we found it may be possible to observe effects similar to Einstein-de Haas and Barnett effects if the fluid is magnetizable in addition to being spin-polarizable.

1.2. *Relativistic Spin-hydrodynamics*

The theory of hydrodynamics is built on the basis of conservation laws of the fluid under consideration. Such conservation laws lead to the equations of motion that govern the evolution dynamics of that specific fluid. Noting that the origin of spin-polarization is traced back to the rotation of the fluid, the relevant conservation laws for a spin-polarizable fluid are - (i) Particle/Baryon/Charge four-current, (ii) Stress-energy tensor, (iii) Angular momentum tensor. In this section, we will first provide the equations of motion of relativistic spin-polarized fluid of a single species, without a magnetic field and then with a magnetic field.

1.3. *Without magnetic field*

The particle four-current of a dissipative relativistic fluid is given by,

$$N^{\mu} = n_0\, u^{\mu} + n^{\mu}, \tag{1}$$

where n_0 is the equilibrium particle number density, n^{μ} is particle diffusion current and u^{μ} is the fluid four-velocity. In writing Eq. (1) we have assumed the out-of-equilibrium number density is, $n = n_0$. This is one of the Landau matching conditions. Then the conservation law is,

$$\partial_{\mu} N^{\mu} = 0. \tag{2}$$

The next conservation law is for the stress-energy tensor of the fluid, which is given by,

$$T_{\rm f}^{\mu\nu} = \epsilon_0 u^{\mu} u^{\nu} - (P + \Pi)\, \Delta^{\mu\nu} + \pi^{\mu\nu}, \tag{3}$$

where ϵ_0 is the equilibrium energy density, P is the equilibrium pressure, Π is the bulk viscous pressure, and $\pi^{\mu\nu}$ is the shear viscous pressure. As before, we have assumed in writing Eq. (3) that the out-of equilibrium energy density is $\epsilon = \epsilon_0$, i.e., the other matching condition. Additionally, we also assumed the Landau frame definition for the fluid four-velocity, which satisfied the relation, $T^{\mu\nu} u_{\nu} = \epsilon u^{\mu}$. The associated conservation law is given by,

$$\partial_{\mu} T_{\rm f}^{\mu\nu} = 0. \tag{4}$$

The final relevant conservation law is the one for angular momentum tensor. This becomes important for rotating fluids and is given by,

$$\partial_{\lambda} J_{\rm f}^{\lambda,\mu\nu} = 0, \tag{5}$$

where $J_{\rm f}^{\lambda,\mu\nu}$ is the total angular momentum tensor of the fluid that consists of two parts, an orbital part ($L_{\rm f}^{\lambda,\mu\nu}$) and a spin part ($S^{\lambda,\mu\nu}$) i.e. $J_{\rm f}^{\lambda,\mu\nu} = L_{\rm f}^{\lambda,\mu\nu} + S^{\lambda,\mu\nu}$. As the orbital part is defined as the moment of the stress-energy tensor (i.e. $L_{\rm f}^{\lambda,\mu\nu} = x^{\mu} T_{\rm f}^{\lambda\nu} - x^{\nu} T_{\rm f}^{\lambda\mu}$), it does not carry any new information that was not already present

in the stress-energy tensor. Therefore, the good conservation law to describe system is the one for spin tensor and for a symmetric tress-energy tensor, we have,

$$\partial_\lambda S^{\lambda,\mu\nu} = 0. \tag{6}$$

Thus, Eqs. (2), (4) and (6) are the conservation laws satisfied by a relativistic spin-polarizable fluid in absence of any external field.

1.4. *With magnetic field*

The next step is to consider the effect of the magnetic field. The conservation law for the particle four-current remains the same, and since we consider only a single species, the charge four-current of the fluid is simply $J^\alpha_{\rm f} = \mathfrak{q}N^\mu$ ($\mathfrak{q}$ being the particle's electric charge). Since it is the charge currents that generate the magnetic field, it is important to note that other charge currents may exist (say, $J^\mu_{\rm ext}$). In fact, in the case of heavy-ion collisions, the charged current that produces the majority of the magnetic field is that of the spectator particles. The field strength tensor due to the total current, J^μ ($= J^\mu_{\rm f} + J^\mu_{\rm ext}$) is $F^{\mu\nu}$. While the conservation law for the particle four-current still holds true, the laws for energy and momentum (both linear and angular) for the fluid are no longer satisfied due to interaction with the produced field. Consequently, the fluid stress-energy tensor ($T^{\mu\nu}_{\rm f}$) and angular momentum tensor ($J^{\lambda,\mu\nu}_{\rm f}$) do not remain conserved. One should note that the conservation laws for the whole system are still satisfied.[15] Hence for a spin-polarizable magnetizable fluid, we have,

$$\partial_\nu T^{\mu\nu}_{\rm f} = F^\mu{}_\alpha J^\alpha_{\rm f} + \frac{1}{2}\left(\partial^\mu F^{\alpha\beta}\right) M_{\alpha\beta}, \tag{7}$$

$$\partial_\lambda J^{\lambda,\mu\nu}_{\rm f} = -\tau^{\mu\nu}, \tag{8}$$

where $M^{\alpha\beta}$ is the magnetization tensor and $\tau^{\mu\nu}$ is the torque generated by the force term appearing on the R.H.S. of Eq. (7). Owing to the definition of the orbital angular momentum, we can show the spin tensor is still conserved, and we get back Eq. (6). Hence, the only relevant modification in conservation laws for the formulation of spin-magnetohydrodynamics as compared to field-free case is in Eq. (7). Therefore, the equations of motion of relativistic spin-magnetohydrodynamics are give by Eqs. (2), (6) and (7). Next, we describe the kinetic theory formulation of spin hydrodynamics, with and without magnetic field.

1.5. *Relativistic Kinetic Theory*

Spin, being a purely quantum mechanical effect, must be introduced in the kinetic theory via quantum field theory. Hence, our starting point is the Wigner function for spin-1/2 particles and its Clifford-algebra decomposition,[16–21]

$$\mathcal{W}(x,k) = \frac{1}{4}\left[\mathcal{F}(x,k) + i\gamma_5\mathcal{P}(x,k) + \gamma^\mu\mathcal{V}_\mu(x,k) + \gamma_5\gamma^\mu\mathcal{A}_\mu(x,k) + \Sigma^{\mu\nu}\mathcal{S}_{\mu\nu}(x,k)\right], \tag{9}$$

where x is the space-time coordinate, $k^\mu = (k^0, \mathbf{k})$ denotes the particle momentum and, γ^μ are the Dirac gamma matrices with $\gamma^5 = i\gamma^0\gamma^1\gamma^2\gamma^3$. It is possible to show that not all the coefficients of the right-hand side of Eq. (9) are totally independent. For the formulation of spin-hydrodynamics, it suffices to work with only two of the components, which in our case are, the scalar component ($\mathcal{F}$) and the axial component ($\mathcal{A}$). Their kinetic equations can be obtained from the Dirac equation to be given by,

$$k^\mu \partial_\mu \mathcal{F}(x,k) = C_\mathcal{F}, \qquad k^\mu \partial_\mu \mathcal{A}^\nu(x,k) = C^\nu_\mathcal{A}, \qquad k_\nu \mathcal{A}^\nu(x,k) = k_\nu C^\nu_\mathcal{A} = 0, \quad (10)$$

where $\mathcal{C}_\mathcal{F}$ and $\mathcal{C}^\mu_\mathcal{A}$ are the collision kernels. In the absence of an external field, following the approach as described in Ref.,[14] we can obtain a Boltzmann-like equation of scalar phase-space distribution functions, $f^\pm(x,p,s)$ with an extended phase-space for particles and anti-particles under the relaxation time approximation as,

$$p^\mu \partial_\mu f^\pm(x,\mathbf{p},s) = (u\cdot p)\,\frac{f^\pm_{\rm eq}(x,\mathbf{p},s) - f^\pm(x,\mathbf{p},s)}{\tau_{\rm eq}}, \quad (11)$$

where $\tau_{\rm eq}$ is the relaxation time. We can use this distribution function, $f(x,\mathbf{p},s)$ to express the scalar and axial components of the Wigner function. The zeroth and first moment of Eq. (11) will result in the conservation laws of Eqs. (2) and (4) and the spin moment will lead to Eq. (6) provided we use appropriate frame and matching conditions. One can easily check this by noting the definitions of the conserved currents from kinetic theory i.e.,

$$N^\mu = \int dP dS p^\mu \left(f^+ - f^-\right), \quad (12)$$

$$T^{\mu\nu}_{\rm f} = \int dP dS p^\mu p^\nu \left(f^+ + f^-\right), \quad (13)$$

$$S^{\lambda,\mu\nu} = \int dP dS s^{\mu\nu} \left(f^+ + f^-\right), \quad (14)$$

where $dP \equiv d^3p/[p^0(2\pi)^3]$ and $dS \equiv m/(\pi\mathfrak{s})\, d^4s\, \delta(s\cdot s + \mathfrak{s}^2)\, \delta(p\cdot s)$ are the momentum and spin integral measures respectively with p^0 being the zeroth component of the momentum four-vector and $\mathfrak{s}$ being the eigenvalue of the Casimir operator. In the presence of a magnetic field, however, we obtain a modified Boltzmann equation under RTA as,

$$\left(p^\alpha \frac{\partial}{\partial x^\alpha} + m\,\mathcal{F}^\alpha \frac{\partial}{\partial p^\alpha}\right) f^\pm = -\,(u\cdot p)\,\frac{\left(f^\pm - f^\pm_{\rm eq}\right)}{\tau_{\rm eq}}, \quad (15)$$

where the force term is given by,

$$\mathcal{F}^\alpha = \frac{dp^\alpha}{d\tau} = \frac{\mathfrak{q}}{m} F^{\alpha\beta} p_\beta + \frac{1}{2}\left(\partial^\alpha F^{\beta\gamma}\right) m_{\beta\gamma}, \quad (16)$$

with $m^{\alpha\beta}$ being the magnetic dipole moment that is related to the internal angular momentum, $s^{\alpha\beta}$ as, $m^{\alpha\beta} = \chi s^{\alpha\beta}$. The quantity, χ is analogous to the gyromagnetic

ratio. We can define the magnetization tensor, $M^{\alpha\beta}$ using this $m^{\alpha\beta}$ as,

$$M^{\alpha\beta} = m \int dP dS m^{\alpha\beta} \left(f^{+} + f^{-}\right), \tag{17}$$

where m is the mass of the particle. It should be noted that in Eq. (15) we have left out one term that we call the 'pure torque' term (associated to $d\mathcal{S}^{\alpha\beta}/d\tau$). A derivation of spin-magnetohydrodynamics with this term will be provided in some other publications. It is straightforward to recover Eq. (11) from Eq. (15) by setting $F^{\alpha\beta} \to 0$. We can arrive at the macroscopic conservation laws for spin-magnetohydrodynamics by starting from Eq. (15) and taking the zeroth, first and spin moments i.e. Eqs. (2), (7) and (6).

1.6. *Transport Coefficients*

We can now solve the Eqs. (11) and (15) to obtain the non-equilibrium correction to the phase-space distribution functions and use them to get the dissipative currents. For this purpose, we consider a Chapman-Enskog like iterative expansion, where the out-of-equilibrium phase-space distribution function can be expressed as a sum of the equilibrium part ($f^{\pm}_{\rm eq}$) and the non-equilibrium correction part ($\delta f^{\pm}_{\rm eq}$) i.e.,

$$f^{\pm}(x, \mathbf{p}, s) = f^{\pm}_{\rm eq}(x, \mathbf{p}, s) + \delta f^{\pm}(x, \mathbf{p}, s). \tag{18}$$

We can use Eq. (18) in Eqs. (11) and (15) to obtain the expressions of $\delta f^{\pm}(x, \mathbf{p}, s)$ in both cases of with and without magnetic field.

In the field-free case, we find the dissipative corrections to the currents, N^{μ} and $T^{\mu\nu}$ remain unaffected by the spin-polarization. However, we obtained the dissipation mechanism of the spin degrees of freedom for the first time to be given by,[14]

$$\delta S^{\lambda,\mu\nu} = \tau_{\rm eq}\Big[B^{\lambda,\mu\nu}_{\Pi}\,\theta + B^{\kappa\lambda,\mu\nu}_{n}\left(\nabla_{\kappa}\xi\right) + B^{\alpha\kappa\lambda,\mu\nu}_{\pi}\,\sigma_{\alpha\kappa} + B^{\kappa\lambda\alpha\beta,\mu\nu}_{\Sigma}\left(\nabla_{\kappa}\omega_{\beta\alpha}\right)\Big]. \tag{19}$$

where, $\theta = \partial \cdot u$ is the scalar expansion, $\sigma^{\mu\nu} = \Delta^{\mu\nu}_{\alpha\beta}\partial^{\alpha}u^{\beta}$ is the shear stress tensor and, $\nabla^{\alpha}\xi$ and $\nabla^{\alpha}\omega^{\mu\nu}$ are the particle and spin diffusion respectively. Here we have defined the spacelike derivative as, $\nabla^{\mu} \equiv \Delta^{\mu}_{\alpha}\partial^{\alpha}$, with $\Delta^{\mu\nu} = g^{\mu\nu} - u^{\mu}u^{\nu}$ being the projection operator orthogonal to the fluid four-velocity. We have defined another projection operator is defined as, $\Delta^{\mu\nu}_{\alpha\beta} = \left(\Delta^{\mu}_{\alpha}\Delta^{\nu}_{\beta} + \Delta^{\mu}_{\beta}\Delta^{\nu}_{\alpha}\right)/2 - \Delta^{\mu\nu}\Delta_{\alpha\beta}/3$ that is symmetric and traceless in the indices μ, ν and α, β.

In the presence of magnetic field, the dissipative currents for the spin-polarizable

and magnetizable relativistic fluid are given by,[15]

$$n^{\mu} = \tau_{\rm eq}\Big[\beta_{n\Pi}^{\langle\mu\rangle}\,\theta + \beta_{na}^{\langle\mu\rangle\alpha}\dot{u}_{\alpha} + \beta_{nn}^{\langle\mu\rangle\alpha}\,(\nabla_{\alpha}\xi) + \beta_{nF}^{\langle\mu\rangle\alpha\beta}\,(\nabla_{\alpha}B_{\beta}) + \beta_{n\pi}^{\langle\mu\rangle\alpha\beta}\sigma_{\alpha\beta} + \beta_{n\Omega}^{\langle\mu\rangle\alpha\beta}\Omega_{\alpha\beta} + \beta_{n\Sigma}^{\langle\mu\rangle\alpha\beta\gamma}\,(\nabla_{\alpha}\omega_{\beta\gamma})\Big], \tag{20}$$

$$\Pi = \tau_{\rm eq}\Big[\beta_{\Pi\Pi}\,\theta + \beta_{\Pi a}^{\alpha}\dot{u}_{\alpha} + \beta_{\Pi n}^{\alpha}\,(\nabla_{\alpha}\xi) + \beta_{\Pi F}^{\alpha\beta}\,(\nabla_{\alpha}B_{\beta}) + \beta_{\Pi\pi}^{\alpha\beta}\sigma_{\alpha\beta} + \beta_{\Pi\Omega}^{\alpha\beta}\Omega_{\alpha\beta} + \beta_{\Pi\Sigma}^{\alpha\beta\gamma}\,(\nabla_{\alpha}\omega_{\beta\gamma})\Big], \tag{21}$$

$$\pi^{\mu\nu} = \tau_{\rm eq}\Big[\beta_{\pi\Pi}^{\langle\mu\nu\rangle}\theta + \beta_{\pi a}^{\langle\mu\nu\rangle\alpha}\dot{u}_{\alpha} + \beta_{\pi n}^{\langle\mu\nu\rangle\alpha}(\nabla_{\alpha}\xi) + \beta_{\pi F}^{\langle\mu\nu\rangle\alpha\beta}(\nabla_{\alpha}B_{\beta}) + \beta_{\pi\pi}^{\langle\mu\nu\rangle\alpha\beta}\sigma_{\alpha\beta} + \beta_{\pi\Omega}^{\langle\mu\nu\rangle\alpha\beta}\Omega_{\alpha\beta} + \beta_{\pi\Sigma}^{\langle\mu\nu\rangle\alpha\beta\gamma}(\nabla_{\alpha}\omega_{\beta\gamma})\Big], \tag{22}$$

$$\delta S^{\lambda,\mu\nu} = \tau_{\rm eq}\Big[B_{\Pi}^{\lambda,[\mu\nu]}\,\theta + B_{a}^{\lambda,[\mu\nu]\alpha}\dot{u}_{\alpha} + B_{n}^{\lambda,[\mu\nu]\alpha}(\nabla_{\alpha}\xi) + B_{F}^{\lambda,[\mu\nu]\alpha\beta}(\nabla_{\alpha}B_{\beta}) + B_{\pi}^{\lambda,[\mu\nu]\alpha\beta}\sigma_{\alpha\beta} + B_{\Omega}^{\lambda,[\mu\nu]\alpha\beta}\Omega_{\alpha\beta} + B_{\Sigma}^{\lambda,[\mu\nu]\alpha\beta\gamma}(\nabla_{\alpha}\omega_{\beta\gamma})\Big], \tag{23}$$

where, $\dot{u}^{\mu} \equiv (u\cdot\partial)\,u^{\mu}$ is the acceleration four-vector, $\Omega_{\alpha\beta} = (\nabla_{\alpha}u_{\beta} - \nabla_{\beta}u_{\alpha})/2$ is the vorticity tensor and, B^{α} is the magnetic four-vector that is related to the field strength tensor as, $F^{\mu\nu} = \epsilon^{\mu\nu\alpha\beta}u_{\alpha}B_{\beta}$. In Eqs. (19)-(23) the transport coefficients are denoted by β_i's and B_i's.

1.7. *Summary and Conclusion*

In this work, we demonstrated how to formulate the relativistic dissipative hydrodynamics for spin-polarizable particles with and without magnetic field starting from the kinetic theory. First, we obtained the dissipation mechanism of the spin degrees of freedom of a relativistic fluid in absence of any magnetic field for the first time and found it to depend on multiple hydrodynamic gradients. Next, we extended the framework to study the effect of magnetic field on a spin-polarizable relativistic fluid at the dissipation level. We found that it is necessary to consider the system to be magnetizable if we want to observe the coupling between spin and magnetic field. In this case, we found that all the dissipative currents depend on multiple hydrodynamic gradients, showing resemblance to the Einstein-de Haas and Barnett effects for the first time.

2. Heavy Quarks in QGP: Results From Lattice QCD

Saumen Datta

The energy loss of low and intermediate momentum charm and bottom quarks in quark-gluon plasma can be understood in a Langevin framework. Lattice QCD can play a crucial role in this understanding, by calculating the relevant transport coefficients. Here I summarize the current status of the results obtained from lattice QCD.

Heavy quarks are among the most interesting probes of the medium created

in ultrarelativistic heavy ion collisions (URHIC). If $m_Q \gg T$, the heavy quarks are expected to be created only by hard gluons within $\tau \sim \frac{1}{2m_Q}$ of the collision. [a] Therefore a heavy quark probe is expected to carry information about the whole history of the fireball. Besides, the heavy mass $m_Q \gg \Lambda_{\overline{\rm MS}}$ gives an additional small parameter which allows use of various theoretical tools.

The energy loss of heavy quark in the plasma has been of great interest in recent times. The energy loss mechanisms of heavy quarks are different from that of light quarks: gluon radiation is suppressed[22] in a cone of angle $\frac{m_Q}{E}$. For quarks of moderate energy, collision with thermal particles is the leading energy loss mechanism.[23] Since even for a near-thermalized heavy quark, its momentum $p_Q \sim \sqrt{m_Q T} \gg T$, individual collisions with light thermal particles with momentum $\sim T$ do not change the momentum of a heavy quark significantly. Therefore, a Langevin description of the heavy quark energy loss for low-intermediate energy heavy quarks was proposed:[23–25]

$$\frac{dp_i}{dt} \;=\; -\eta\, p_i \;+\; \xi_i(t), \qquad \langle \xi_i(t)\, \xi_j(t') \rangle \;=\; \kappa\, \delta_{ij}\, \delta(t-t') \tag{24}$$

where the second term denotes a white noise. Since η is related to κ by Einsten's relation, the motion can be described by only one parameter κ. This formalism has been very successful in explaining the R_{AA} and v_2 of D mesons.[26] It is, however, difficult to calculate κ from thermal QCD: the leading order (LO) result[23,24] is far too small for phenomenology. Perturbation theory for this object is also quite ill-behaved: for temperatrues of interest, the next to leading order (NLO) result is an order of magnitude larger than LO.[27] A nonperturbative estimation of the diffusion coefficient is therefore called for.

In phenomenological studies, one often tweaks the LO calculation to get a value suitable for explaining the experimental data: for example, by altering the gluon propagator from its perturbative form, by changing the running of the coupling, or by calculating the scattering cross-sections through a tuned potential.[28,29] A direct extraction of κ from data using a Bayesian analysis has also been attempted.[30] But of course, for a satisfactory understanding of the formalism, one would like to calculate κ from QCD. This is where lattice calculations have made a significant progress. I will describe the status of such calculations in this report. Except for a comment near the end, all the results I will describe are for a gluonic plasma only, i.e., the plasma has no thermal quarks. The results are still very useful, as they give us an idea about the size of the nonperturbative effects.

Standard relations connect the drag coefficient η in eq. (24) and the spatial diffusion coefficient D_s to κ:

$$\eta \approx \frac{\kappa}{2\,M\,T}, \qquad D_s \approx \frac{2T^2}{\kappa}\,. \tag{25}$$

A fluctuation-dissipation theorem relates D_s to the vector current correlator $\langle J_i(\vec{p}=$

[a] This condition may not hold for the charm in LHC.

$0, t+\tau)\ J_i(\vec{p}=0,t)\rangle$.[31] This correlator can be easily calculated on the lattice. From this, an extraction of D_s has been attempted.[32] This extraction though is quite difficult: D_s is related to the width of the transport peak of the spectral function of the correlator. The spectral function is connected to the correlator by an integral transform similar to a Laplace transform. It is very difficult to invert the transform accurately enough to extract the width of its transport peak. The transport peak is in the infrared and it further gets affected by the infrared cutoffs put in the calculation, like size of the system.

A far more promising approach has been to calculate κ directly from its defining relation: the force-force correlator.[33,34] In the leading order in $\frac{1}{m_Q}$, the force term ξ in eq. (24) is gE_i, the color electric field. So one can extract κ from the spectral function of the color electric field correlator: $\langle (gE_i)(\vec{p}=0,t+\tau)\ (gE_i)(\vec{p}=0,t)\rangle$. The advantage is that there is no transport peak in this spectral function $\rho_T(\omega)$ (see Fig. 1). In the infrared $\rho_T(\omega) \sim \omega$, and the coefficient of this linear term, $\kappa_{_E}$, is the estimate for κ for static quarks.[34] The $\frac{1}{m_Q}$ correction to this term has also been estimated: under certain assumptions,[35]

$$\kappa \;=\; \kappa_{_E} \;+\; \frac{2}{3}\,\langle v^2\rangle\,\kappa_{_B} \;+\; \ldots \qquad \langle v^2\rangle \;=\; \frac{3T}{m_{\rm kin}}\,\left(1 \,-\, \frac{5T}{2m_{\rm kin}}\right) \tag{26}$$

where $\kappa_{_B}$ is obtained from the color magnetic field correlator in an analogous way to $\kappa_{_E}$. Note that treating the expansion as a series in $\langle v^2\rangle$, the average velocity squared of the heavy quark, leads to better stability.[35]

There have been several[36–41] lattice calculations for $\kappa_{_E}$ in a gluonic plasma, estimated from the EE correlator. All these works use a model of $\rho_T(\omega)$ to extract $\kappa_{_E}$ from the EE correlator. We know the form of $\rho_T(\omega)$ at very high and low energies: it approaches the perturbative spectral function at very high ω and a dispersive form $\sim \kappa_{_E}\omega$ in the infrared. For intermediate values of ω, different calculations use different models. The calculations also differ in how they renormalize the lattice correlators. The left panel of Fig. 1 shows the results for $\rho_T(\omega)$ obtained at 1.5 T_c in a recent calculation[41] when using different models (stylistically I have followed here a similar plot of an earlier calculation[37]). The right panel of Fig. 1 shows a compilation of the results obtained in these calculations, in the 1-4 T_c range. To reduce clutter, where the same group has published two calculations, I have only kept the new one. There seems to be a good agreement between the different calculations, within the large error bars (which are dominated by systematics: the effect of using different models of $\rho_T(\omega)$).

Figure 1 also shows the NLO result for κ.[33] For the scale of the coupling, I have taken $\mu_{\rm opt} \sim 6.7\,T$,[42] which is the scale obtained using the principle of minimum sensitivity, and used the range $[0.5, 2]\,\mu_{\rm opt}$ to get the band shown in the figure. The lattice data seems to agree quite well with the perturbative result. Note, however, that perturbation theory is inherently unstable here. The LO result (with the same scale) is very different: it even turns negative at moderately high temperatures.

What are the missing ingredients for comparing these results with phenomenol-

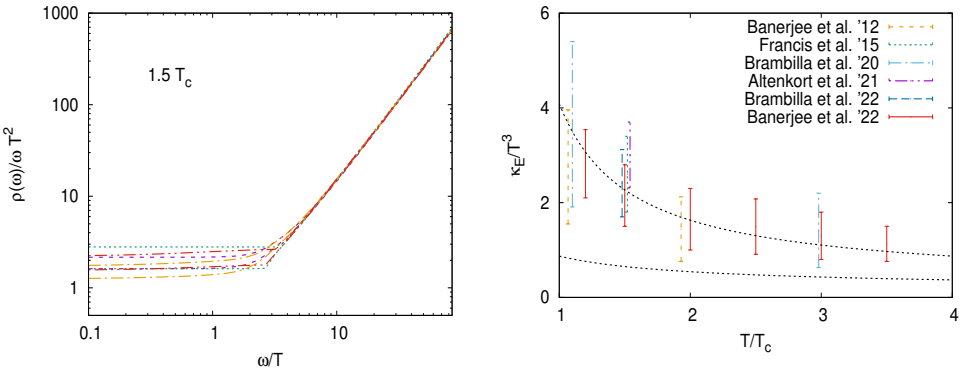


Fig. 1: (Left) Structure of the spectral function at 1.5 T_c.[41] Different line styles show the results of using different models of $\rho_T(\omega)$. $\rho_T(\omega)$ has no transport peak: it goes $\sim \kappa_E\,\omega$ at low ω. (Right) A collation of the available lattice results for κ_E in a gluon plasma. The results shown are from Banerjee et al.,[36,41] Francis et al.,[37] Brambilla et al.[38,40] and Altenkort et al.[39]

ogy? Within the gluonic plasma approximation, one needs an estimate of the size of the $\frac{1}{m_Q}$ correction. And the major next step is the inclusion of the dynamical quarks.

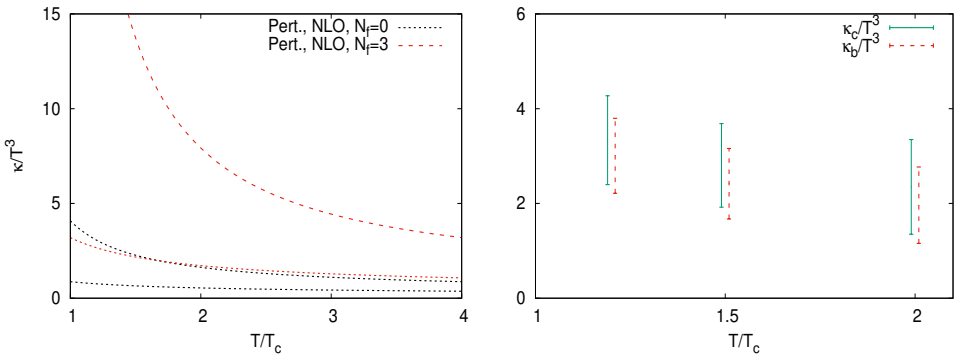


Fig. 2: (Left) A comparison of the NLO results[27] for κ_E/T^3 for the gluon plasma and for QGP with 3 light flavors. (Right) κ_b and κ_c for the gluon plasma[43] .

The $\frac{1}{m_Q}$ correction coefficient in eq. (26) has been calculated recently: κ_B has been computed in the temperature range 1.2-2 T_c.[43] A second calculation at 1.5

T_c[40] agrees very well within errorbars. Using eq. (26) and an estimate of $\langle v^2 \rangle$ from ratio of susceptibilities, κ_b and κ_c have been estimated.[43] These results are shown in the right panel of Fig. 2, where I have updated the figure (as well as Fig. 3 below) with a recent estimate[41] of κ_E.

Perturbation theory would suggest a large effect of the dynamical quarks: the left panel of Fig. 2 compares the NLO results of the theory with three light quark flavors with that of the gluon plasma. There are no published lattice results with dynamical quarks, but preliminary results from a dynamical study was presented in Quark Matter.[44] The unquenching effect, from the first results, is expected to be large.

In what follows, we will stick to the gluon plasma results. Other quantities of interest can be calculated from the results for κ using eq. (25). Fig. 3 shows the results[43] for η and $2\pi\, T\, D_s$.

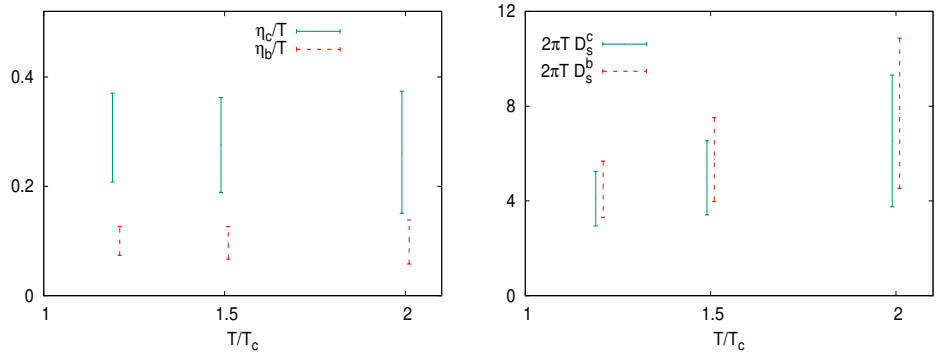


Fig. 3: (Left)Estimate[43] for $\eta_{c,b}$ and (right) $2\pi\, T\, D_s$ for charm and bottom in a gluon plasma.

The relaxation time is given by the inverse of η. From the figure one sees $\tau_b \sim 10fm > \tau_c \sim 3fm$. So b quark may only be partially thermalized. The spatial diffusion coefficient $2\pi\, T\, D_s$ does not play any direct role in the Langevin calculation. However, the results of the diffusion calculations are often expressed in terms of $2\pi\, T\, D_s$ rather than κ.[28] An analysis of experimental data prefers $2\pi\, T\, D_s \sim 1.5 - 4.5$ in the LHC, which is consistent with Fig. 3.

To summarize, lattice QCD calculations have provided important ingredients for an understanding of the energy loss pattern of heavy quarks in terms of a Langevin description. The static result has been available for a while; the first correction terms $\mathcal{O}(v^2 \sim \frac{T}{M})$ have also been calculated recently. These results are for quenched lattices; the first unquenched studies are ongoing.

3. Relativistic Hydrodynamics with momentum-dependent relaxation time approximation

Sukanya Mitra

A relativistic hydrodynamic theory up to second order in gradient expansion, has been derived using momentum dependent relaxation time approximation (MDRTA) in the relativistic transport equation. A correspondence has been established between the out of equilibrium system dissipation and the thermodynamic field redefinition of the macroscopic variables through MDRTA. It is found that the result from the numerical solution of the Boltzmann equation lies somewhere in between the two popular extreme limits: linear and quadratic ansatz, indicating a fractional power of momentum dependence in relaxation time to be appropriate. Finally, the causality and stability of the first-order relativistic theory with hydrodynamic field redefinition via MDRTA have been analyzed.

3.1. *Introduction*

Relativistic dissipative hydrodynamic theory has been proved to be reasonably successful in describing the out of equilibrium dynamics of a system in the long wavelength limit. The evolution of the relevant macroscopic quantities such as temperature and charge chemical potential is given by a set of coupled differential equations where the dissipative effects are included by the transport coefficients such as viscosity and conductivities. However, the macroscopic thermodynamic quantities such as energy density and particle number density in these equations are usually set to their equilibrium values even in the dissipative medium by imposing certain matching or fitting conditions. In this work, these dissipative corrections have been included in the out of equilibrium thermodynamic fields from gradient expansion technique of solving the relativistic transport equation using momentum dependent relaxation time approximation (MDRTA).[45–50]

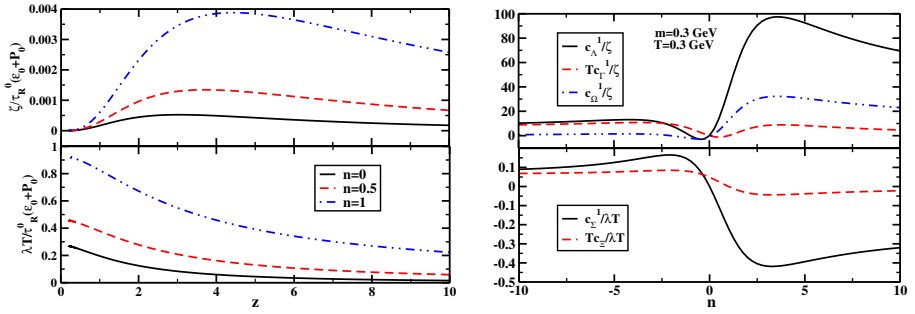
The manuscript is organised as follows. Section II contains the formal framework for hydrodynamic field redefinition obtained from relativistic transport equation using MDRTA upto second order of gradient correction. Section III provides a quantitative estimation of the effect of momentum dependent relaxation time on the pressure anisotropy of the system. In section IV the causality and stability of a first order theory with fields redefined under MDRTA have been analyzed. Finally, in section V the work has been summarized with prior conclusions and useful remarks.

3.2. *Field redefinition with MDRTA*

In relaxation time approximation, the relativistic transport equation for the single particle distribution function $f(x,p)$ with particle four-momenta p^μ and space-time variable x^μ is given by,

$$p^\mu \partial_\mu f = -\frac{(p\cdot u)}{\tau_R} f^{(0)}(1 \pm f^{(0)})\phi \ , \quad \tau_R(x,p) = \tau_R^0(x)\left(\frac{p\cdot u}{T}\right)^n \ , \tag{27}$$

with $f^{(0)}$ as the equilibrium distribution, ϕ as the out of equilibrium distribution deviation, τ_R^0 as the momentum independent part and n as a number specifying



(a) Scaled ζ and λ as a function of z. (b) Correction coefficients as function of n.

Fig. 4: MDRTA modified field corrections and transport coefficients

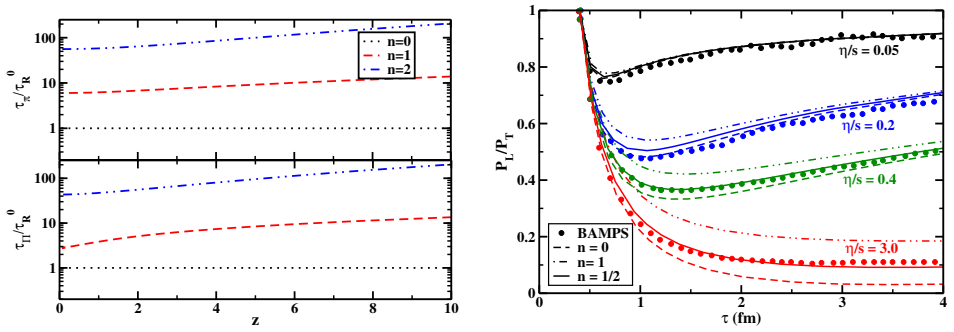
the power of the scaled energy. In order to solve Eq.(27), here the well known iterative technique of gradient expansion, the Chapman-Enskog (CE) method has been adopted.[51] With this, the first order corrections in energy density, particle number density, pressure, particle flux and energy flow are respectively given by,

$$\delta\epsilon^{(1)} = c^1_\Lambda(\partial\cdot u)\ ,\quad \delta\rho^{(1)} = c^1_\Gamma(\partial\cdot u)\ ,\quad \delta P^{(1)} = c^1_\Omega(\partial\cdot u)\ ,$$
$$W^{(1)\alpha} = -c_\Sigma\hat{h}(\nabla^\alpha T/T - Du^\alpha)\ ,\quad V^{(1)\alpha} = c_\Xi(\nabla^\alpha\tilde{\mu}). \tag{28}$$

Including field corrections, the expressions for particle four-flow and energy-momentum tensor read,

$$N^\mu = (\rho_0+\delta\rho)u^\mu + V^\mu\ , \tag{29}$$
$$T^{\mu\nu} = (\epsilon_0+\delta\epsilon)u^\mu u^\nu - (P_0+\delta P)\Delta^{\mu\nu} + (W^\mu u^\nu + W^\nu u^\mu) + \pi^{\mu\nu}\ . \tag{30}$$

Here, $\pi^{\mu\nu} = \Delta^{\mu\nu}_{\alpha\beta}\delta T^{\alpha\beta} = 2\eta\sigma^{\mu\nu}$ is the shear stress tensor. The expressions of first order field correction coefficients and the physical transport coefficients bulk viscosity (ζ), thermal conductivity (λ) and shear viscosity (η) in MDRTA are given in.[49] It has been checked that $\zeta/\tau^0_R, \lambda/\tau^0_R, \eta/\tau^0_R > 0$ for all values of n for various combinations of $z(=m/T), T$ and μ. They have been plotted in Fig.(4) (left panel) as a function of the scaled mass z for several n values. Next, we observe that for any n value, $c^1_\Omega - c^1_\Lambda\big(\frac{\partial P_0}{\partial\epsilon_0}\big)_{\rho_0} - c^1_\Gamma\big(\frac{\partial P_0}{\partial\rho_0}\big)_{\epsilon_0} = -\zeta$, $c^1_\Sigma - \frac{(\epsilon_0+P_0)}{\rho_0}c^1_\Xi = -\frac{\lambda T}{\hat{h}}$, such that, $\delta P^{(1)} - (\frac{\partial P_0}{\partial\epsilon_0})_{\rho_0}\delta\epsilon^{(1)} - (\frac{\partial P_0}{\partial\rho_0})_{\epsilon_0}\delta\rho^{(1)} = \Pi^{(1)}$, $W^{(1)\mu} - \hat{h}TV^{(1)\mu} = q^{(1)\mu}$, with $\Pi^{(1)}$ and $q^{(1)\alpha}$ as first order bulk viscous and diffusion flow. This shows that the individual correction coefficients combine to give the physical transport coefficients as predicted by.[52] The coefficients of first order dissipative correction (scaled by physical transport coefficients) have been plotted for $m = 0.3$ GeV and $T = 0.3$ GeV as a function of n in right panel of Fig.(4). For momentum independent case $n = 0$, $c^1_\Lambda = c^1_\Gamma = c^1_\Sigma = 0$. c^1_Ξ vanishes for $n = 1$ with $c^1_\Lambda = 3c^1_\Omega$. Fig.(4) shows that the individual field corrections take how much fractional part of the dissipative flux, is decided by the value of n. The second order hydrodynamic evolution equations



(a) τ_π/τ_R^0 and τ_Π/τ_R^0 as a function of z. (b) Time evolution of pressure anisotropy.

Fig. 5: Effect of MDRTA on macroscopic quantities.

for bulk and shear viscous pressure with MDRTA is respectively given by.

$$\Pi = -\zeta\partial\cdot u - \tau_\Pi D\Pi + c_\Pi^\sigma \pi^{\mu\nu}\sigma_{\mu\nu} + c_\Pi^\theta \Pi(\partial\cdot u)\ , \tag{31}$$

$$\pi^{\mu\nu} = 2\eta\sigma^{\mu\nu} - \tau_\pi D\pi^{\langle\mu\nu\rangle} + c_\pi^\omega \pi_\rho^{\langle\mu}\omega^{\nu\rangle\rho} + c_\pi^\sigma \pi_\rho^{\langle\mu}\sigma^{\nu\rangle\rho} + c_\pi^\theta \pi^{\mu\nu}(\partial\cdot u) + c_\pi^\zeta \Pi\sigma^{\mu\nu} \tag{32}$$

The explicit expression of the associated coefficients can be found in.[49] It can be observed that $\tau_\pi = \tau_\Pi = \tau_R^0$ holds only for $n = 0$. For all other n, the three time scales are evidently separate (Fig (5) left panel).

3.3. *Phenomenological application*

To have a quantitative idea about how MDRTA affects the physical observables, the second order hydro equations have been solved for a conformal, boost invariant Bjorken system with ultrarelativistic equation of state ($\epsilon = 3P$) as the following,[48]

$$\frac{d\epsilon}{d\tau} = -\frac{\epsilon + P}{\tau} + \frac{\pi}{\tau}\ , \qquad \frac{d\pi}{d\tau} = -\frac{\pi}{\tau_\pi} + \beta_\pi \frac{4}{3\tau} - \frac{(4+\lambda)}{3}\frac{\pi}{\tau}\ , \tag{33}$$

with initial time, temperature and viscous pressure at $\tau_i = 0.4$ fm, $T_i = 0.5$ GeV and $\pi_i = 0$. Fig.(5) (right panel) shows the proper time (τ) evolution of pressure anisotropy $P_L/P_T = (P-\pi)/(P+\pi/2)$ for the three values of n and four sets of η/s ratio. The $n = 0$ case as shown in[53] under predicts the BAMPS data[54] which becomes prominent for large values of viscosity. $n = 1$ case clearly over predicts the data a good deal showing even larger deviation from BAMPS for high η/s. However, the $n = 1/2$ situation remarkably agrees with BAMPS results even with large viscosity like $\eta/s = 3.0$ throughout the evolution range. In[55] the $n = 1/2$ momentum dependence has been related to the dynamics of a two-flavoured quark-gluon gas where the BAMPS data has been extracted for the same by a parton cascade model.[56] This reasonable agreement of numerical data with fractional power of momentum dependence is very illuminating in the context of Ref[55] which argued

that most of the interaction theories relevant for QGP lie between the two extreme limits of linear ($n = 0$) and quadratic ($n = 1$) ansatz.

3.4. *Stability and causality of a first order theory*

Recently, studies have been carried out that propose a causal and stable first order hydrodynamic theory.[52,57–60] Motivated from these studies, in this work, the stability and causality of the first order theory derived in previous section has been tested. At local rest frame for small wave number (k) we have the frequency modes, $\omega^{\parallel}_{1,2} = \frac{i}{2}\left[\frac{4\eta/3+\zeta}{(\epsilon_0+P_0)}\right]k^2 \pm kc_s$, $\omega^{\parallel}_3 = i\left[\frac{\lambda T}{(\epsilon_0+P_0)}\right]k^2$, which are always stable because of the positive imaginary parts of all the modes. At large k, the modes and the associated group velocity v_g become,

$$\omega^{\parallel}_{1,2} = \frac{i}{2}\left\{\frac{B}{A} - \frac{E}{D}\right\} \pm k\sqrt{\frac{D}{A}} \ , \quad \omega^{\parallel}_3 = i\frac{E}{D} \ , \quad v_g = \lim_{k\to\infty}\left|\frac{\partial\ \mathrm{Re}(\omega)}{\partial k}\right| = \sqrt{\frac{D}{A}} \ . \tag{34}$$

(detailed expressions are given in[50]). v_g turns out to be subluminal with small mass and non-zero values of the exponent n of MDRTA (Eq.(27)), giving rise to a causal propagating mode previously absent in Navier-Stokes (NS) theory. However, with a boosted background with arbitrary velocity $\mathbf{v}$, at shear channel with small k we have, $\omega^{\perp}_1 = \mathbf{v}k + \mathcal{O}(k^2)$, $\omega^{\perp}_2 = -\frac{i}{\gamma\Gamma\mathbf{v}^2} + \frac{(2-\mathbf{v}^2)}{\mathbf{v}}k + \mathcal{O}(k^2)$, with $\Gamma = \eta/(\epsilon_0+P_0)$ and $\gamma = 1/\sqrt{1-\mathbf{v}^2}$. At large k the shear modes becomes, $\omega^{\perp}_{1,2} = \frac{1}{\mathbf{v}}k$. For a background velocity $0 < \mathbf{v} < 1$, these modes are both acausal and unstable. In small k limit, the sound modes become,

$$\begin{aligned}
&\omega^{\parallel}_1 = \mathbf{v}k + \mathcal{O}(k^2) \ , \quad \omega^{\parallel}_{2,3} = \frac{1}{2}\left[M \pm \sqrt{M^2 - 4N}\right]k + \mathcal{O}(k^2) \ , \\
&\omega^{\parallel}_{4,5} = \frac{i}{2}\left[Q \pm \sqrt{Q^2 + 4R}\right] + \mathcal{O}(k) \ .
\end{aligned} \tag{35}$$

The additional modes $\omega^{||}_{4,5}$ are unstable for any combination of the field correction coefficients. In the limit of large wave numbers, the roots of $v^{\parallel}_g$ are obtained as,

$$v^{\parallel}_{g,1} = \mathbf{v} \ , \quad v^{\parallel}_{g,2,3} = \frac{\left[\mathbf{v}(A-D) \pm \sqrt{AD - 2AD\mathbf{v}^2 + AD\mathbf{v}^4}\right]}{A - D\mathbf{v}^2} \ , \quad v^{\parallel}_{g,4,5} = \pm\frac{1}{\mathbf{v}} \ . \tag{36}$$

where the two new roots $v^{\parallel}_{g,4,5}$ are always acausal for $0 < \mathbf{v} < 1$. So although at local rest frame the asymptotic causality condition and stability criteria are maintained, the new modes of shear and sound channels due to the boosted background are conclusively showing that the theory is acausal and unstable.

3.5. *Summary and discussions*

In this work, momentum dependent relaxation time approximation has been used to redefine the thermodynamic fields in order to include the out of equilibrium dissipative effects up to second order in gradient correction. The key finding is that, these corrections are not independent but constrained to give the dissipative

flux of same tensorial rank where the associated coefficients are sensitive to the interaction. The derived equations have been applied for hydrodynamic simulation for a conformal system which demonstrates that the pressure anisotropy for the fractional power of MDRTA shows an impressive agreement with the numerical solution of Boltzmann equation. Finally, motivated from a series of recent studies, the causality and stability of the first order theory have been analyzed. In local rest frame, the equations of motion give a causal propagating mode which was previously absent in the usual NS theory but with a boosted background new modes appear which are both acausal and unstable. Hence, in order to establish a first order relativistic, stable-causal theory, an alternate microscopic approach of field redefinition is required which has been recently explored in.[61]

4. Recent results in small systems from CMS

Prabhat R. Pujahari (for the CMS collaboration)

The observation of a wide variety of physical phenomena in the context of the formation of a strongly interacting QCD matter in heavy-ion nuclear collisions at the LHC has drawn significant attention to the high energy heavy-ion physics community. The appearance of a varieties of similar phenomena as in heavy-ion in the high multiplicity proton-proton and proton-nucleus collisions at the LHC energies has triggered further investigation to understand the dynamics of particle production mechanism in a highly dense and small QCD medium. The CMS collaboration uses many different probes in these studies ranging from the particle production cross section to multi-particle correlations. In this proceeding, I report a few selected recent CMS results from the small systems with the main focus on the measurement of collective phenomena in high multiplicity pp and pPb collisions.

4.1. *Introduction*

In the context of high energy heavy-ion physics, the collisions between protons or a proton with a nucleus is commonly referred to as small system and they can provide baseline measurements for heavy-ion collisions. Traditionally, it is thought that such small systems do not show characteristics of QGP formation a priori. However, in the recent few years, this simplistic view of a small system has been challenged at the LHC – thanks to the new frontier in energies and state-of-the-art instrumentations. The individual events in a high multiplicity pp and pPb collisions can have very high charged particle multiplicity and energy density which is comparable to that of AA collisions.[62]

With the advent of the LHC, high multiplicity pp and pPb collisions show unexpected phenomena which have never been observed before in such small systems. The observation of a long range rapidity ridge in the measurement of two-particle angular correlation in heavy-ion collisions is no surprise to us and this can be well explained by hydrodynamical collective flow of a strongly interacting and expanding medium.[64] However, the appearance of similar structures in a high multiplicity pp and pPb collisions has drawn a lot of attention and prompted studies to understand

the cause of such behaviour in small systems. In particular, the discovery of the ridge by CMS collaboration[63] in high multiplicity pp collisions is one of such intriguing results observed in small systems.[65] Long-range, near-side angular correlations in particle production emerged in pp and subsequently in pPb collisions paved the way for a systematic investigation of the existence of the collective phenomena. Much information can also be gained by focusing on collective properties of each event, such as multi-particle correlations, or event-by-event fluctuations of such quantities. We observe signatures traditionally attributed to a collective behaviour not only in PbPb collisions but also in small systems. Since then, a wealth of new, unexpected phenomena has been observed with striking similarities to heavy-ion observations.

4.2. *Transverse energy density*

The total transverse energy, E_T, is a measure of the energy liberated by the "stopping" of the colliding nucleons in a heavy-ion or proton-nucleus collision. From Figure 72 it can be seen that $dE_T/d\eta\ |_{\eta=0} \approx 22$ GeV. This is 1/40 of the value observed for the 2.5% most central PbPb collisions. However, since the cross sectional area of pPb collisions is much smaller than that of central PbPb collisions, this result implies that the maximum energy density in pPb collisions is comparable to that achieved in PbPb collisions.[62] Several modern generators are compared to these results but none is able to capture all aspects of the η and centrality dependence of the data.[62]

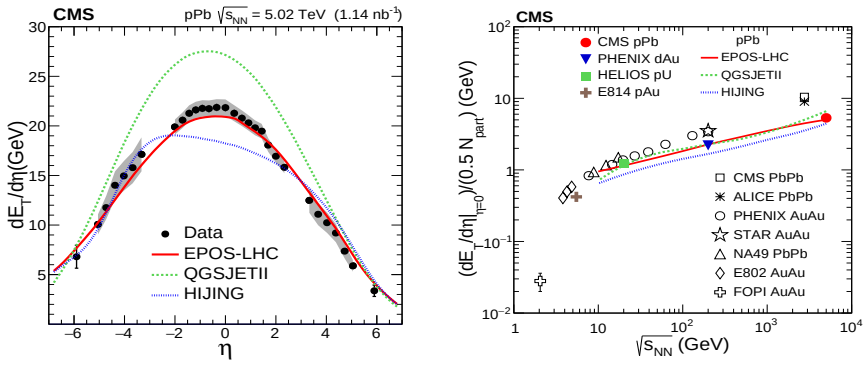


Fig. 6: (left) Transverse energy density versus η from minimum bias pPb collisions at $\sqrt{s_{NN}}$ =5.02 TeV. (right) Transverse energy density per participating nucleon-nucleon pair evaluated at various $\sqrt{s_{NN}}$ for minimum bias pAu, pU, dAu, and pPb collisions.[62]

4.3. *Collectivity in small systems at the LHC*

The p_{T} distributions of identified hadrons are one of the important tools to probe the collective behaviour of particle production. The p_{T} distributions in pp and pPb collisions show a clear evolution, becoming harder as the multiplicity increases.[66] As it is shown in Figure 73, models including hydrodynamics describes the data better for the p_{T} spectra. Data-to-model agreement is good at higher charged particle multiplicity, N_{ch}. In addition, the evolution of the p_{T} spectra with multiplicity can be compared more directly by measuring the average transverse kinetic energy, $\langle KE_T \rangle$.[66] If collective radial flow develops, this would result in a characteristic dependence of the shape of the transverse momentum distribution on the particle mass.

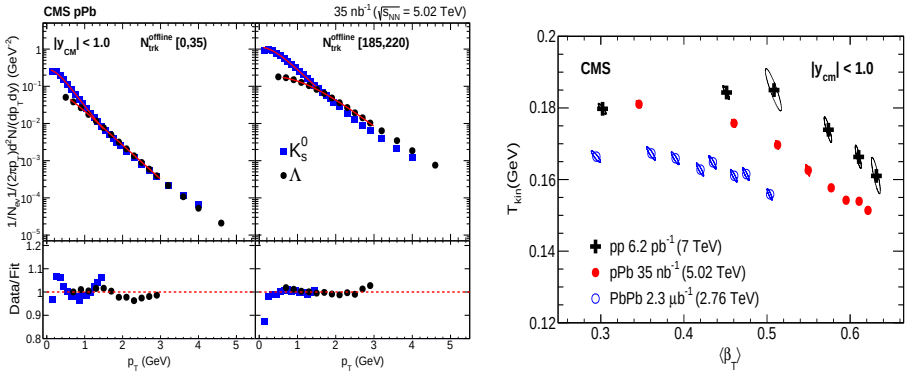


Fig. 7: (left) Simultaneous blast-wave fits of the p_{T} spectra of ${K_s}^0$ and Λ in low- and high-multiplicity pPb events. (right) The extracted kinetic freeze-out temperature, T_{kin}, versus the average radial-flow velocity, $\langle \beta_T \rangle$, from a simultaneous blast-wave fit to the ${K_S}^0$ and Λ p_{T} spectra at $|y_{cm}| < 1$ for different multiplicity intervals in pp , pPb , and PbPb collisions.

The $\langle KE_T \rangle$ for ${K_s}^0$, Λ and Ξ particles as a function of multiplicity are shown in Figure 31. For all particle species, $\langle KE_T \rangle$ increases with increasing multiplicity. A theoritical Blast-wave model[67] fits have also been performed to the p_{T} spectra of strange particles in several multiplicity bins as shown in Figure 73. The interpretation of the parameters of these fits, such as kinetic freeze-out temperature, T_{kin} and transverse radial flow velocity, β_T, are model dependent. In the context of the Blast-Wave model, when comparing the parameters of different systems at similar $dN_{ch}/d\eta$, it was found that β_T is larger for small systems i.e., $\beta_T(\mathrm{pp}) > \beta_T(\mathrm{pPb}) > \beta_T(\mathrm{PbPb})$. This could be an indication of a larger radial flow in small systems as a consequence of stronger pressure gradients due to a more explosive system. However, a similar decreasing trend is observed for T_{kin} and β_T as a func-

tion of multiplicity in all three collision systems. One of the key questions about

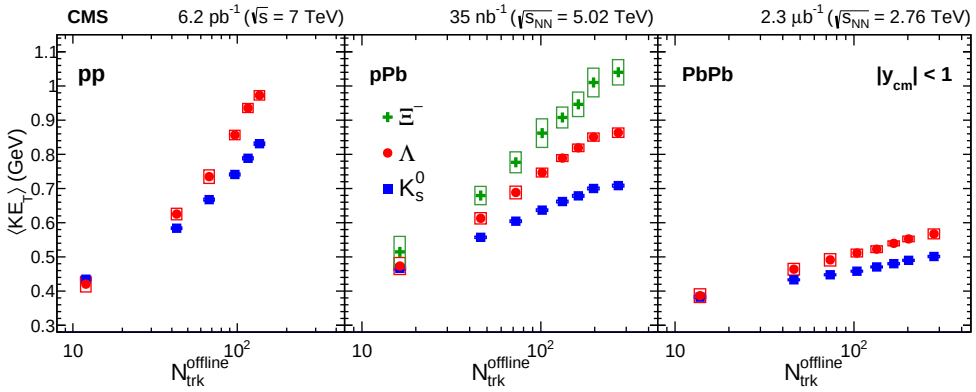


Fig. 8: The average transverse kinetic energy for ${K_s}^0$, Λ and Ξ particles as a function of multiplicity in pp, pPb, and PbPb collisions.[66]

the nature of the ridge and its collectivity is whether the two-particle azimuthal correlation structures observed at large relative pseudorapidity in pp and pPb collisions result from correlations exclusively between particle pairs, or if it is a multi-particle genuine collective effect, needs to be further understood. A strong hint for multi-particle correlations in high multiplicity pp and pPb collisions was reported by the CMS collaboration.[68,76] Figure 9 shows the second-order azimuthal anisotropy Fourier harmonics (v_2) measured in pp, pPb and PbPb collisions over a wide pseudorapidity range based on correlations calculated up to eight particles. The v_2 values stay high and show similar trends in all three systems. The v_2 computed from two-particle correlations is found to be larger than that obtained with four-, six- and eight-particle correlations, as well as the Lee-Yang zeroes method. However, the v_2 obtained from multi-particle correlations, all yield to similar v_2 values i.e., $v_2\{4\} \approx v_2\{6\} \approx v_2\{8\} \approx v_2\{\mathrm{LYZ}\}$.[68] These observations support the interpretation of a collective origin for the observed long-range correlations in high-multiplicity pp and pPb collisions. Another useful observable in the study of collectivity is the event-by-event correlation between Fourier harmonics of different order flow coefficients. The CMS Collaboration has measured these normalized symmetric cumulants, SC(m, n), where m and n are different order flow coefficients, in pp, pPb and PbPb collisions, as a function of track multiplicity.[69] Similar observations are made in all three systems. In the case of $\mathrm{SC}(2,3)$, which gauges the correlation between v_2 and v_3, an anti-correlation is found at high track multiplicity, as shown in Figure 10. On the contrary, $\mathrm{SC}(2,4) > 0$: the v_2 and v_4 values are positively correlated event-by-event. Similar trends are observed in pPb and PbPb collisions, and high multiplicity pp collisions, regarding the trend of these observables as a function

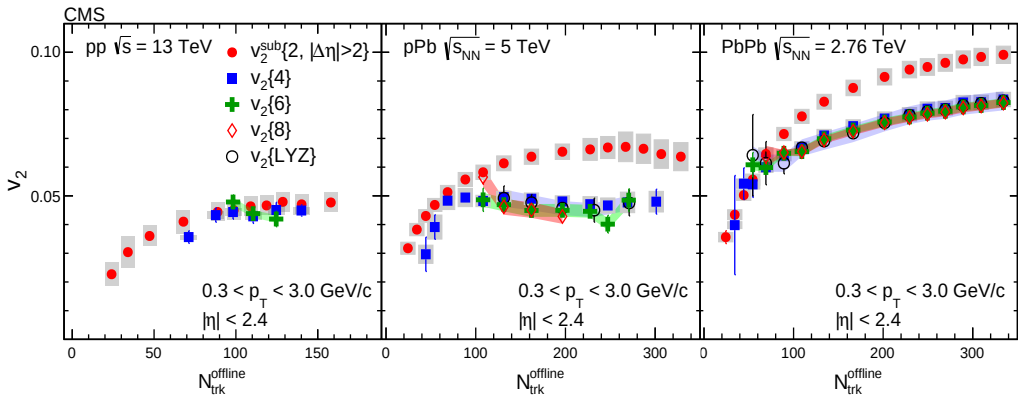


Fig. 9: Second-order azimuthal anisotropy Fourier harmonics, v_2 measured by CMS in pp, pPb and PbPb collisions based on multi-particle correlations.[68]

of track multiplicity. A long-range near-side two-particle correlation involving an identified particle is also observed.[68,70] Results for both pPb and pp collisions are shown in Figure 11. Moving to high-multiplicity events for both systems, a particle species dependence of v_2 is observed. The mass ordering of v_2 was first seen in AA collisions at RHIC and LHC energies,[71,72] which can be understood as the effect of radial flow pushing heavier particles towards higher p_T. This behavior is found to be qualitatively consistent with both hydrodynamic models[73] and an alternative initial state interpretation.[74] A measurement of the elliptic flow of prompt J/Ψ me-

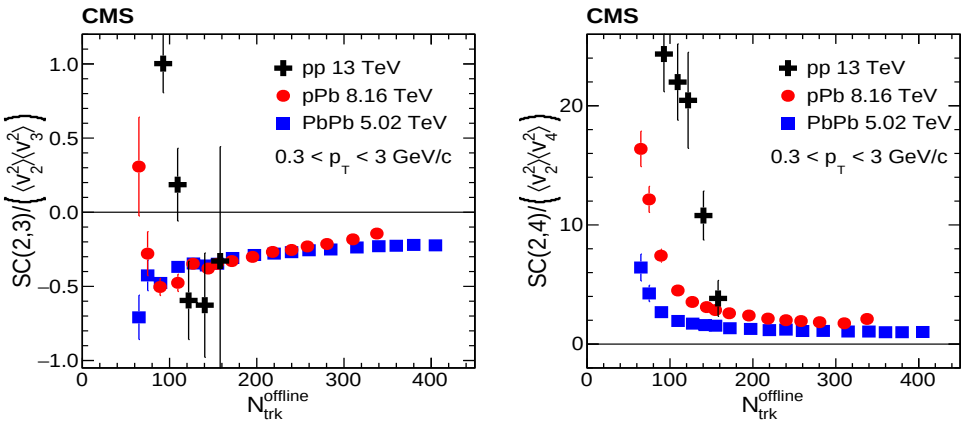


Fig. 10: The normalized symmetric cumulant for the second and third coefficients (left) and the second and fourth coefficients (right) are shown for pp (black cross), pPb (red circle), and PbPb (blue square). Tracks with transverse momentum between 0.3 and 3.0 GeV are used.[69]

son in high-multiplicity pPb collisions is reported by the CMS experiment.[75] The prompt J/Ψ results are compared with the v_2 values for open charm mesons (D^0) and strange hadrons. As shown in Figure 11, positive v_2 values are observed for the prompt J/Ψ meson, as extracted from long-range two-particle correlations with charged hadrons, for $2 < p_T < 8$ GeV. The prompt J/Ψ meson results, together

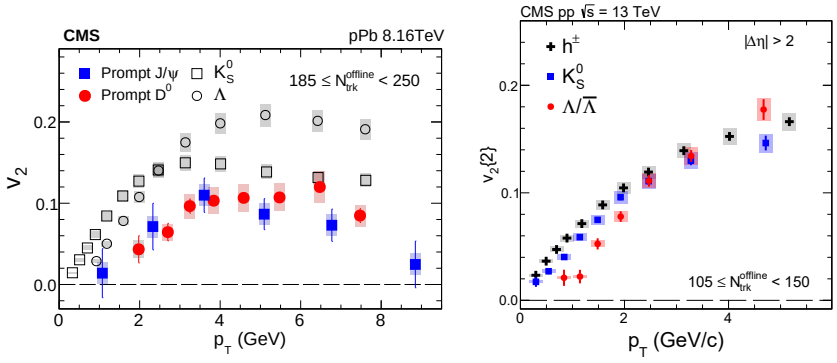


Fig. 11: The v_2 results for ${K_s}^0$, and Λ, prompt D^0 and prompt J/Ψ in high-multiplicity pPb (left) events. (right) The v_2 results for inclusive charged particles, ${K_s}^0$, and Λ as a function of p_T in pp collisions at $\sqrt{s} = 13$ TeV.

with results for light-flavor and open heavy-flavor hadrons, provide novel insights into the dynamics of the heavy quarks produced in small systems that lead to high final-state multiplicities.

4.4. *Conclusions*

Several effects, such as mass-dependent hardening of $p_{\rm T}$ distributions, near-side long-range correlations, multi-particle azimuthal correlations, etc, which in nuclear collisions are typically attributed to the formation of a strongly-interacting collectively-expanding quark-gluon medium, have been observed in high-multiplicity pp and pPb collisions at the LHC. The study of small collision systems at high multiplicity is undoubtedly of considerable interest. While a lot of progress has been made towards understanding the long-range correlation phenomena in small colliding systems, there are still many open questions to be addressed by the experiemental and theoritical communities.

5. Heavy Quark Diffusion in QCD Matter: Glasma vs Plasma

Pooja, Marco Ruggieri, and Santosh Kumar Das

Heavy quarks (HQs) are considered potential probes of the quantum chromodynamics (QCD) matter produced in high-energy nuclear collisions. In the pre-equilibrium stage of

relativistic heavy-ion collisions, strong quasi-classical gluon fields called Glasma emerge at about $\tau_0 = 0.08$ fm/c that evolves according to the classical Yang-Mills (CYM) equations. The diffusion of HQs, namely, charm and bottom quarks in the evolving Glasma fields is compared with that of the Markovian-Brownian motion in a thermalized medium. The diffusion of HQs in the evolving Glasma (EvGlasma) is investigated within the framework of Wong equations while we use famous Langevin equations for the Brownian motion with diffusion coefficients evaluated within the pQCD framework. We observe that for a smaller value of saturation scale, Q_s, the average transverse momentum broadening is approximately the same for the two cases, but for larger Q_s, Langevin dynamics underestimates the σ_p. This difference is related to the fact that HQs in the Glasma fields experience diffusion in strong, coherent gluon fields that lead to a faster momentum broadening due to memory, or equivalently to a strong correlation in the transverse plane.

5.1. *Introduction*

The initial condition produced in the relativistic high-energy collisions and its evolution to quark-gluon plasma (QGP) is of prime importance to study the QCD matter in the extremum conditions. According to the color-glass condensate (CGC) effective theory, the collision of two nuclei at ultra-relativistic velocities results in strong longitudinal color electric and magnetic fields called Glasma[77] which evolves according to classical Yang-Mills[81] (CYM) equations. The typical lifetime of this pre-equilibrium Glasma phase is 0.2 -1 fm/c. Heavy quarks,[78–82] namely, charm and beauty quarks, work as an excellent probe to study the early stages of high-energy collisions.

This research aims to do a systematic comparison of the diffusion of the HQs in the EvGlasma and a hot thermalized medium by fixing the saturation scale, Q_s, and the QCD coupling,[83] g in our calculations. For this, we compute the transverse momentum broadening defined as

$$\sigma_p = \frac{1}{2}\langle (p_x(t) - p_{0x})^2 + (p_y(t) - p_{0y})^2 \rangle. \tag{37}$$

5.2. *Formalism*

The diffusion of HQs in the EvGlasma is investigated by the means of Wong equations:[81,83–87]

$$\frac{dx^i}{dt} = \frac{p^i}{E}, \tag{38}$$

$$\frac{dp^i}{dt} = gQ_a F_a^{i\nu} p_\nu, \tag{39}$$

$$\frac{dQ_a}{dt} = \frac{g}{E} f_{abc} A_b^\nu p_\nu Q_c. \tag{40}$$

The motion of HQs in the gluonic Plasma is studied using Langevin equations.[86] We assume that this is a Markovian process with no drag included.

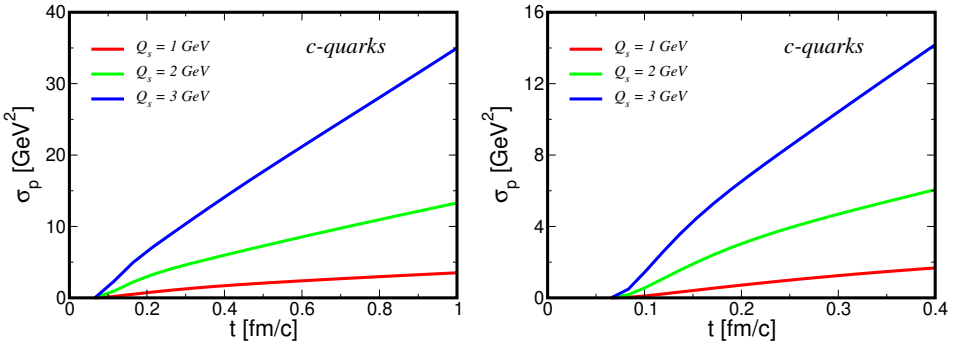


Fig. 12: σ_p versus proper time for charm quarks, for the initial $p_T = 0.5$ GeV. The calculations correspond to evolving Glasma fields in a static box.

5.3. *Results*

5.4. *Momentum broadening in the static box*

In Fig. 12, we plot σ_p for charm quarks versus proper time, for several values of Q_s, up to $\tau = 0.4$ fm/c and $\tau = 1.0$ fm/c. During the very early time, σ_p doesn't increase linearly due to the correlations of the Lorentz force acting on the charm quarks at different times, namely to the memory of the gluon fields. The memory time, τ_{mem}, has been calculated in Ref. 86: $\tau_{mem} \approx \frac{1}{Q_s}$. After the initial transient, σ_p rises linearly, similar to the standard Brownian motion without a drag.

5.5. *Comparison with the Langevin dynamics*

In Fig. 13, we plot the time-averaged transverse momentum broadening, Avσ_p versus Q_s for charm and beauty quarks. We find that for smaller Q_s, Avσ_p is comparable for EvGlasma and collisional Langevin dynamics. It is because, for smaller Q_s, EvGlasma behaves like a system of dilute gluons resulting in momentum diffusion which is similar to the collisional dynamics. On the other hand, for larger Q_s, the HQs in the EvGlasma feel strong coherent gluonic fields, while the dynamics remain the same as collisional for pQCD Langevin. Hence, the difference between the two systems is quite substantial.

5.6. *Spin polarisation of heavy quarks in the evolving Glasma*

In Fig. 14, we show a preliminary result for the evolution of averaged J_x^2, J_y^2 and J_z^2 of HQs in the evolving Glasma in a static box geometry. Starting with a non-polarised system of HQs, the Glasma dynamics result in the polarization of HQs, i.e., HQs have more spin in the longitudinal z-direction as compared to the spin in the transverse x and y directions.

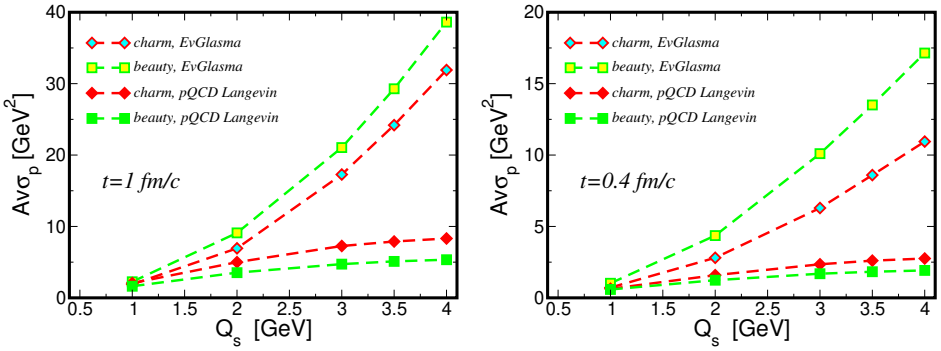


Fig. 13: Time-averaged σ_p versus Q_s for charm and beauty quarks, for EvGlasma and pQCD Langevin dynamics. Calculations correspond to the static box geometry.

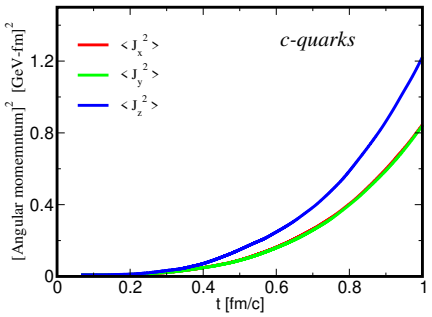


Fig. 14: Average of square of angular momentum components versus proper time for charm quarks, for $Q_s = 2$ GeV .

5.7. *Conclusions and Outlook*

Glasma, the pre-equilibrium stage of high-energy nuclear collisions, affects the HQs dynamics significantly. We observe that the diffusion of HQs in the early stage of high energy collisions is affected by the strong coherent gluon fields and memory effects become substantial. The time-averaged momentum broadening of HQs in the EvGlasma is in agreement with the standard pQCD-Langevin for small values of Q_s, while differs significantly for larger Q_s.

Spin polarization of HQs is another interesting aspect to be explored. The first results in this direction tell that HQs spin is polarized in the longitudinal direction.

6. The Impact of Memory on Heavy Quarks Dynamics in Hot QCD Medium

Jai Prakash, Marco Ruggieri, Pooja, Suvarna Patil, Santosh Kumar Das

We study the effect of memory on the heavy quarks (HQs) dynamics in the Quark-Gluon Plasma (QGP) within the scope of integro-differential Langevin where the memory enters through the thermal noise, η, and the dissipative force. We assume that the time correlations of the η decay exponentially over a time scale called the memory time, τ. We have observed the significant impact of memory on transverse momentum broadening, σ_p, and the nuclear modification factor, R_{AA} of the HQs dynamics in QGP. We notice that the HQs dynamics are very sensitive to memory.

6.1. *Introduction*

In an ultra-relativistic heavy-ion collision, the existence of hot and dense nuclear matter, QGP, has been realized at Relativistic Heavy-Ion Collider (RHIC) and the Large Hadron Collider (LHC). The HQs are one of the novel probes[28,78,89] to study the evolution of QGP. The estimated thermalization time of the HQs is greater than the QGP lifetime, which makes HQs a witness to the entire evolution of QGP. The dynamics of the HQs in QGP are usually studied within the framework of the standard Langevin equation, where the time correlation of noise is the delta function. We have studied the dynamics of HQs in the bath of time-correlated thermal noise within the framework of the Langevin equation, where the time correlation of thermal noise is an exponentially decaying function over a particular time span, τ. The drag coefficient is related to the thermal noise through the fluctuation-dissipation theorem. We have observed that the presence of memory slows down the momentum evolution of the HQs in the thermal bath resulting into slowing down of the formation of R_{AA} and evolution of transverse momentum broadening.

6.2. *Formalism*

We can study the momentum evolution of the HQs in the QGP within the ambit of Langevin equation as follow,

$$\frac{dp_i}{dt} = -\int_0^t \gamma(t-s)p(s)ds + \eta(t), \tag{41}$$

where p is the momentum of the particles, the integral term in "Eq. (177)" is a dissipative force and $\eta(t)$ is stochastic term that governs the noise, the correlation of thermal noise does not vanish at different time, which is written as follow,

$$\langle \eta(t)\eta(t')\rangle = 2\mathcal{D}f(|t-t'|). \tag{42}$$

The drag coefficient, $\gamma(t,t')$ is related to the thermal noise through the fluctuation-dissipation theorem in the relativistic limit as follow,

$$\gamma(t,t') = \frac{1}{ET}\langle \eta(t)\eta(t')\rangle. \tag{43}$$

In this model, we have assumed the correlator to be a decaying exponential function of time,

$$f(|t-t'|) = \frac{1}{2\tau} e^{-|t-t'|/\tau}, \tag{44}$$

where τ is memory time. We have fixed t', and analyzed the momentum evolution of HQs in QGP for $t \geq t'$.

6.3. *Ancillary process*

We introduce an ancillary process to generate the time-correlated thermal noise in the hot QCD medium for the Langevin equation as follow,[90]

$$\frac{dh}{dt} = -\alpha h + \alpha \xi, \tag{45}$$

where h stands for the ancillary process, ξ is the uncorrelated noise and dimensionless parameter having the properties, $\langle \xi \rangle = 0$, $\langle \xi(t)\xi(t') \rangle = \frac{1}{\alpha}\delta(t-t')$, where α is the inverse of memory time, $\alpha \equiv \frac{1}{\tau}$, which balances the dimension of time. The other study on memory has been made in Ref. 91. The approximate solution of "Eq. (45)", can be written as,

$$\langle h(t)h(t') \rangle \approx \frac{e^{-\alpha|t-t'|}}{2}. \tag{46}$$

With the properties $\langle h(t) \rangle = 0$, $h(t)$ is a memory process, which we use in the Langevin equation to study the momentum evolution of the HQs.

6.4. *Results*

6.5. *Transverse momentum broadening*

The transverse momentum broadening, σ_p, is calculated in the presence of memory in the system, which is written as follows,

$$\sigma_p = \langle (p_T - \langle p_T \rangle)^2 \rangle. \tag{47}$$

We have plotted the σ_p for three different temperatures at $\tau = 1\ fm$ and $0.2\ fm$, at a constant diffusion coefficient, $\mathcal{D}$=0.2 GeV^2/fm for illustrative purposes only, as depicted in fig. (15).[90] The evolution of σ_p slows down in the presence of memory.

6.6. *Nuclear modification factor*

We have studied the impact of memory on the nuclear modification factor, R_{AA}, of HQs within perturbative QCD (pQCD) at temperature 1 GeV and quasiparticle model (QPM) at temperature 0.25 GeV. The impact has been calculated for the evolution time, $t = 1\ fm$ and $3\ fm$ with two values of τ as depicted in the fig.(16).[90]

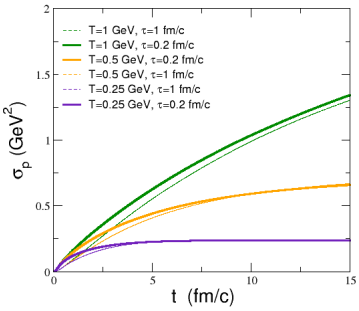


Fig. 15: σ_p versus versus time (t), for three values of the temperature (T= 0.25 GeV, 0.5 GeV, 1 GeV) and for $\tau = 1\ fm$ and 0.2 fm.

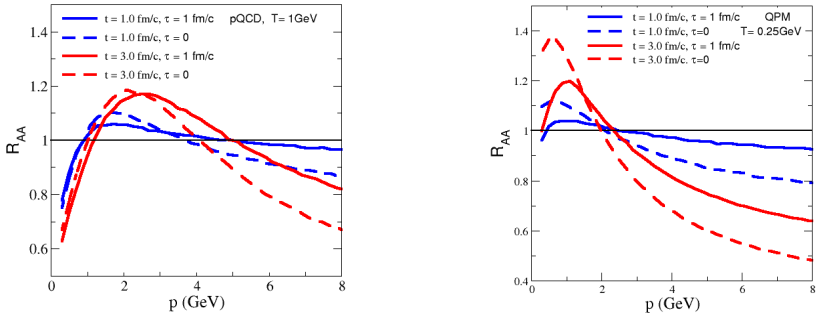


Fig. 16: R_{AA} versus transverse momentum (p) at temperature 1 GeV for pQCD (left panel) and for temperature 0.25 GeV for QPM (right panel), time (t) = 3 fm and 1 fm.

The effect of memory on R_{AA} is quite significant. The formation of R_{AA} delays when τ increases in the system, which means the HQ energy loss will be less than that without memory in the system.

6.7. *Summary and Outlook*

We have studied the effect of time-correlated thermal noise on the momentum evolution of HQs in thermalized QGP. The dissipative force and thermal noise play a role in implementing the memory in the dynamics of HQs in QGP within the integro-differential Langevin equation. In the system, as $\tau \to 0$, the memory disappears and tends to idealize the system.[79,92] We have observed the significant impact of memory on the momentum evolution of HQs in the hot QCD matter and calculated the R_{AA} and σ_p of the HQs, namely, charm quark under the framework of the stochastic Langevin equation. In the presence of memory, the formation of R_{AA} and the evolution of σ_p are slowed down, delaying the energy loss and thus

increasing the thermalization time of HQs in the medium.

7. Modification of intra-jet properties in high multiplicity pp collisions at $\sqrt{s} = 13$ TeV with ALICE

Debjani Banerjee for the ALICE Collaboration

We present measurements of mean charged-particle multiplicity and jet fragmentation function for leading jets in minimum bias and high multiplicity proton-proton (pp) collisions at $\sqrt{s} = 13$ TeV with ALICE. Jets are reconstructed at midrapidity from charged particles using the sequential recombination anti-k_{T} jet finding algorithm for $R = 0.4$. The results are compared to predictions from PYTHIA8 Monash2013 and EPOS LHC.

7.1. *Introduction*

The partons produced with large transverse momentum in high energy nuclear or hadronic collisions fragment into a collimated spray of final state particles, known as jets. Jets are the key ingredient to test the perturbative quantum chromodynamics (pQCD) predictions. In addition, jet measurement in small collision system such as high-multiplicity pp is important in order to look for the onset of QGP-like effects as a function of particle multiplicity. In this work, we present the measurements of intra-jet properties, the mean charged particle multiplicity and fragmentation functions and their multiplicity dependence for leading jets in pp collisions at $\sqrt{s} = 13$ TeV with ALICE.

7.2. *Analysis details and Jet observables*

The data presented here were recorded by the ALICE detector in 2016, 2017 and 2018 by colliding protons at center-of-mass energy ($\sqrt{s}$) = 13 TeV. Events are rejected if the vertex z-position, $|z_{\mathrm{vtx}}| > 10$ cm from the nominal interaction point (IP). Minimum Bias (MB) events are selected using ALICE MB trigger condition which requires the coincidence in the V0A and V0C forward scintillator arrays[93] whereas high multiplicity (HM) events are selected using HM trigger condition which requires the sum of V0A and V0C amplitudes to be more than 5 times the mean MB signal. The used data samples consist of ~ 1802 M for MB and ~ 183 M for HM event classes. Charged particles detected by both the Time Projection Chamber (TPC)[94] and the Inner Tracking System (ITS)[95] with $p_{\mathrm{T}} > 0.15$ GeV/c in the pseudorapidity $|\eta| < 0.9$ and azimuthal angle $0 < \varphi < 2\pi$ are considered for this analysis. Jets are constructed from these selected charged particles with FastJet 3.2.1[96] using the anti-k_{T} algorithm with p_{T} recombination scheme for jet resolution parameter $R = 0.4$. Mean charged-particle multiplicity, $\langle N_{\mathrm{ch}} \rangle$ and jet fragmentation function, $z^{\mathrm{ch}} = p_{\mathrm{T}}^{\mathrm{particle}}/p_{\mathrm{T}}^{\mathrm{jet,ch}}$ are measured for leading jets in the range of jet p_{T} from 5–110 GeV/c.

7.3. *Correction procedure and estimation of systematic uncertainty*

Instrumental effects such as tracking inefficiency, particle-material interactions and track p_{T} resolution are corrected by performing a 2D unfolding in $p_{\mathrm{T}}^{\mathrm{jet,ch}}$ and N_{ch} or z^{ch} using the iterative Bayesian unfolding[97] algorithm implemented in the RooUnfold package.[98] To account for the instrumental effects, PYTHIA8 (version 8.210) Monash2013 and GEANT detector simulation are used to construct a 4D response matrix (R) that describes the response of detector and background in $p_{\mathrm{T}}^{\mathrm{jet,ch}}$ and N_{ch} or z^{ch} contained within R ($p_{\mathrm{T,det}}^{\mathrm{jet,ch}}$, $N_{\mathrm{ch,det}}/z_{\mathrm{det}}^{\mathrm{ch}}$, $p_{\mathrm{T,truth}}^{\mathrm{jet,ch}}$, $N_{\mathrm{ch,truth}}/z_{\mathrm{truth}}^{\mathrm{ch}}$), where $p_{\mathrm{T,det}}^{\mathrm{jet,ch}}$ is detector level jet p_{T} and $p_{\mathrm{T,truth}}^{\mathrm{jet,ch}}$ is truth level jet p_{T} and analogously for N_{ch} and z^{ch}. Underlying events (UE) coming from sources other than jets are estimated using well established perpendicular cone method used by ALICE.[99] UE subtraction is performed on a statistical basis after unfolding both the raw distributions and UE contributions separately.

The sources of systematic uncertainties include tracking efficiency, MC dependence, choice of regularization parameter, number of iterations in Bayesian unfolding and change in prior distribution. The total systematic uncertainty for $\langle N_{\mathrm{ch}} \rangle$ is found to be 2–8% (3–6%) for MB (HM) events whereas for z^{ch} ($p_{\mathrm{T}}^{\mathrm{jet,ch}}$ = 10–20 GeV/c) it is found to be 5–12% (7–15%) for MB (HM) events. However the uncertainty on z^{ch} distributions in minimum bias also depends on the jet p_{T} range, it varies from 5–20% for jet $p_{\mathrm{T}}^{\mathrm{jet,ch}}$ = 20–30 GeV/c whereas it is 12–24% for higher jet p_{T} (= 40–60 GeV/c).

7.4. *Results and discussion*

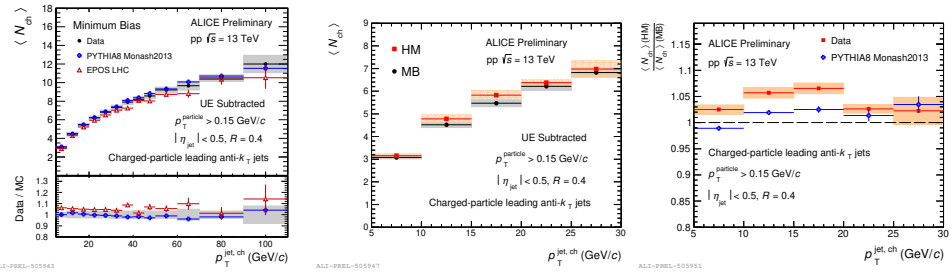


Fig. 17: Fully corrected $\langle N_{\mathrm{ch}} \rangle$ as a function of $p_{\mathrm{T}}^{\mathrm{jet,ch}}$. Left: Blue and red markers show PYTHIA8 Monash2013 and EPOS LHC predictions respectively. Bottom panel shows the ratio between data and MC. Middle: Red and Black markers show HM and MB results respectively. Shaded region represents systematic uncertainties. Right: Ratio of $\langle N_{\mathrm{ch}} \rangle$ in HM to the same in MB as a function of $p_{\mathrm{T}}^{\mathrm{jet,ch}}$.

Figure 17 (left) shows $\langle N_{\mathrm{ch}} \rangle$ as a function of leading $p_{\mathrm{T}}^{\mathrm{jet,ch}}$. The black markers

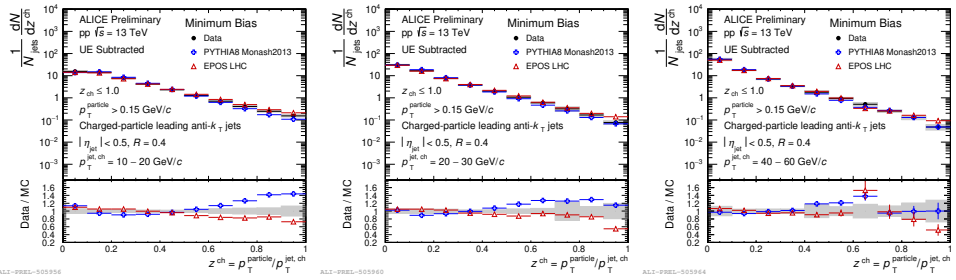


Fig. 18: Fully corrected z^{ch} distributions for leading $p_T^{jet,ch}$ = 10 - 20 GeV/c (left), 20 - 30 GeV/c (middle) and 40 - 60 GeV/c (right). Blue and red markers show PYTHIA8 Monash2013 and EPOS LHC predictions respectively. Bottom panels show the ratio between data and MC. Shaded region represents systematic uncertainties.

represent the data whereas blue and red markers show PYTHIA8 Monash2013 and EPOS LHC (version 3400) predictions respectively. PYTHIA is a parton based MC generator where the hadronization is treated using the Lund string fragmentation model for collider physics with an emphasis on pp interactions. EPOS is based on perturbative QCD, Gribov-Regge multiple scattering, and string fragmentation for pp and AA collisions. In this figure the ratios between data and MC predictions are shown in the bottom panel. In Fig. 17 (middle), red and black markers show $\langle N_{ch} \rangle$ as a function of leading $p_T^{jet,ch}$ for HM and MB respectively. The ratio of $\langle N_{ch} \rangle$ (HM)/$\langle N_{ch} \rangle$ (MB) is shown as a function of leading $p_T^{jet,ch}$ in Fig. 17 (right). It is observed that $\langle N_{ch} \rangle$ increases with leading $p_T^{jet,ch}$ for HM and MB events. EPOS LHC slightly underestimates the data whereas PYTHIA8 Monash2013 describes the data within systematic uncertainty. Figure 17 (right) shows that $\langle N_{ch} \rangle$ is slightly larger for HM events and qualitatively reproduced by PYTHIA8 Monash2013 for $p_T^{jet,ch} < 20$ GeV/c.

Figure 18 shows z^{ch} distributions for leading $p_T^{jet,ch}$ = 10 - 20 GeV/c (left), 20 - 30 GeV/c (middle) and 40 - 60 GeV/c (right). Red and blue markers show EPOS LHC and PYTHIA8 Monash2013 predictions respectively. The ratios between data and MC predictions are presented in bottom panels. It is observed that for low z^{ch} (< 0.5), both models predict the data well within systematic uncertainties whereas for high z^{ch} (> 0.5) and lower jet p_T range, EPOS LHC explains the data better than PYTHIA8 Monash2013. Moreover for high z^{ch} (> 0.5) and higher jet p_T range, both models explain the data within systematic uncertainties.

Figure 19 (left) shows z^{ch} distributions in three jet p_T domains. Scaling of charged-particle jet fragmentation with jet p_T is observed except at highest and lowest z^{ch}. In Figure 19 (middle) red and black markers show z^{ch} distributions for HM and MB events respectively. Figure 19 (right) shows the ratio of z^{ch} distributions obtained in HM and MB events. It is interesting to notice that jet fragmen-

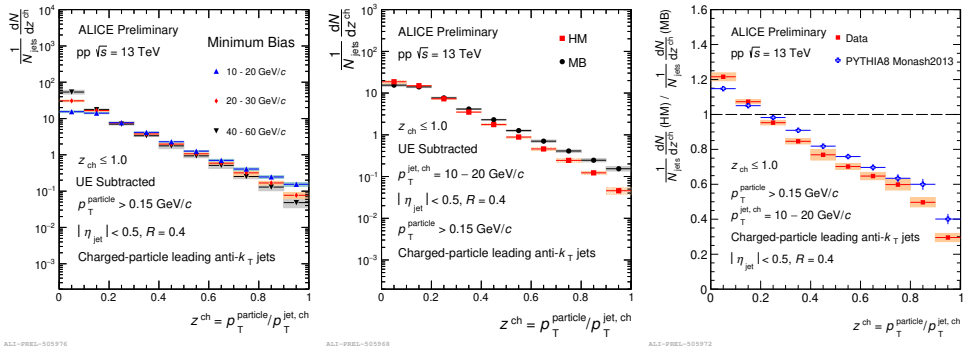


Fig. 19: Left: z^{ch} distributions in MB events for leading $p_{\mathrm{T}}^{\mathrm{jet,ch}}$ = 10 - 20 GeV/c (blue), 20 - 30 GeV/c (red) and 40 - 60 GeV/c (black). Middle: z^{ch} distributions for MB and HM. Right: Ratio of z^{ch} in HM to the same in MB. Model comparison is superimposed in this figure.

tation is softer in HM events explaining more interactions between the jet and the partons.

7.5. *Summary*

We have presented the measurement of intra-jet properties and their multiplicity dependence in pp collisions at 13 TeV in ALICE. Results are compared with PYTHIA8 Monash2013 and EPOS LHC predictions. We have observed significant modification in z^{ch} distributions in HM events compared to MB events. We have also observed that the jet fragmentation is softer in the HM events.

8. Heavy Quarkonia in a hot and dense strongly magnetized QCD medium

Salman Ahamad Khan, Mujeeb Hasan, and Binoy Krishna Patra

We have studied the effects of the finite quark chemical potential (μ) on the $Q\bar{Q}$ potential and have further studied the various properties like binding energy, decay width and dissociation temperatures for the J/ψ and Υ states. We have noticed that the real part of the potential becomes more attractive while magnitude of the imaginary part gets reduced. The dissociation temperature slightly gets enhanced in a medium having finite amount of μ.

8.1. *Introduction*

Heavy quarkonia (bound state of $c\bar{c}$ and $b\bar{b}$) is a very promising signature of the hot and dense quark matter produced at the heavy ion collision experiments at RHIC and LHC. In non-central collisions, a very strong magnetic field (around $m_\pi^2 - 15m_\pi^2$)

is also generated whose life time is elongated by the electrical conductivity of the medium. In addition to this a large quark chemical potential (100-200 MeV) is also present near the deconfinement region .[100,101] The influence of the strong magnetic field on the properties of the heavy quarkonia immersed in hot QCD medium have been studied in recent years by two of us in strong [102,103] as well as in weak magnetic field.[104] In other works the effect of the magnetic field has been investigated for the case of a harmonic interaction and for Cornell potential plus a spin spin interaction term in[105,106] and using the generalized Gauss law in.[107] In present work, we have explored the effects of finite μ on the $Q\bar{Q}$ bound states immersed in strongly magnetized hot QCD medium. In order to incorporate the non-perturbative part we have added a phenomenological term induced by dimension two gluon condensate in gluon propagator in addition to usual HTL resummed propagator.

8.2. *Medium modification to the $Q\bar{Q}$ potential*

The medium modification to the heavy quark potential can be obtained from the inverse Fourier transform of the resummed gluon propagator in the static limit as[108]

$$V(r;T,B,\mu) = C_F\ g^2 \int \frac{d^3p}{(2\pi)^3}(e^{ip.r}-1)\ D^{00}(p_0=0,p), \tag{48}$$

where C_F is the cashimir factor and D^{00} is the static limit of the temporal component of the resummed gluon propagator in the strongly magnetized hot QCD medium which will be calculated in the next subsection.

8.3. *Covariant structure of gluon self energy and resummed propagator in magnetic field*

In order to obtain the resummed gluon propagator, we need the gluon self energy in the above mentioned environment. In the presence of the magnetic field the rotational invariance is broken and a extended tensor basis is required. The covariant tensor structure of the gluon self energy in the presence of the magnetic field is given by [109]

$$\Pi^{\mu\nu}(P) = b(P)B^{\mu\nu}(P) + c(P)R^{\mu\nu}(P) + d(P)M^{\mu\nu}(P) + a(P)N^{\mu\nu}(P), \tag{49}$$

here the various projection tensors are constructed as

$$B^{\mu\nu}(P) = \frac{\bar{u}^\mu\bar{u}^\nu}{\bar{u}^2}, \quad R^{\mu\nu}(P) = g_\perp^{\mu\nu} - \frac{P_\perp^\mu P_\perp^\nu}{P_\perp^2}, \tag{50}$$

$$M^{\mu\nu}(P) = \frac{\bar{n}^\mu\bar{n}^\nu}{\bar{n}^2}, \quad N^{\mu\nu}(P) = \frac{\bar{u}^\mu\bar{n}^\nu + \bar{u}^\nu\bar{n}^\mu}{\sqrt{\bar{u}^2}\sqrt{\bar{n}^2}}, \tag{51}$$

$u^\mu = (1,0,0,0)$ is the four velocity of the heat bath and $n_\mu = (0,0,0,1)$ represents the direction of B.

The form factors defined in (49) can be evaluated by taking the appropriate contractions as

$$b(P) = B^{\mu\nu}(P)\ \Pi_{\mu\nu}(P) \quad c(P) = R^{\mu\nu}(P)\ \Pi_{\mu\nu}(P), \tag{52}$$

$$d(P) = M^{\mu\nu}(P)\ \Pi_{\mu\nu}(P), \quad a(P) = \frac{1}{2}N^{\mu\nu}(P)\ \Pi_{\mu\nu}(P). \tag{53}$$

The resummed gluon propagator in magnetized medium in the Landau gauge is given as[109]

$$D^{\mu\nu}(P) = \frac{(P^2-d)B^{\mu\nu}}{(P^2-b)(P^2-d)-a^2} + \frac{R^{\mu\nu}}{P^2-c} + \frac{(P^2-b)M^{\mu\nu}}{(P^2-b)(P^2-d)-a^2} + \frac{aN^{\mu\nu}}{(P^2-b)(P^2-d)-a^2}. \tag{54}$$

Since we are interested in the static $Q\bar{Q}$ potential, $D^{00}(P)$ in the static limit becomes

$$D^{00}(P) = -\frac{1}{(P^2-b)}, \tag{55}$$

which requires the real and imaginary parts of the form factor b that can be calculated from

$$b(P) = B^{\mu\nu}(P)\Pi_{\mu\nu}(P) = \frac{u^\mu u^\nu}{\bar{u}^2}\Pi_{\mu\nu}(P). \tag{56}$$

We calculate the real and imaginary parts of the form factor b which give the real and imaginary parts of the resummed gluon propagator in the static limit as

$$\text{Re } D^{00}(p_0=0,p) = -\frac{1}{p^2+m_D^2} - \frac{m_G^2}{(p^2+m_D^2)^2}, \tag{57}$$

$$\text{Im } D^{00}(p_0=0,p) = \sum_f \frac{g^2|q_fB|m_f^2}{4\pi}\frac{1}{p_3^2(p^2+m_D^2)^2} + \frac{\pi T m_g^2}{p(p^2+m_D^2)^2} + \frac{2\pi T m_g^2 m_G^2}{p(p^2+m_D^2)^3}. \tag{58}$$

where $m_G^2 = 2\sigma/\alpha$. The last term in the above Eqs. (57) and (58) are due to the dimension two gluon condensate and corresponds to the non-perturbative part of the potential. m_D^2 is the Debye screening mass which reads as

$$m_D^2(T,\mu;B) = \sum_f g^2\frac{|q_fB|}{4\pi^2T}\int_0^\infty dk_3\ \{n^+(E_1)(1-n^+(E_1)) + n^-(E_1)(1-n^-(E_1))\} + \frac{N_C}{3}g^2T^2. \tag{59}$$

8.4. *Real and imaginary part of the $Q\bar{Q}$ potential*

The real part of the $Q\bar{Q}$ potential has been calculated using the real part of the resummed propagator from Eq. (57) in Eq. (48) as

$$\text{Re } V(r;T,B,\mu) = -\frac{4}{3}\alpha_s\left(\frac{e^{-\hat{r}}}{r} + m_D(T,\mu,B)\right) + \frac{4}{3}\frac{\sigma}{m_D(T,\mu,B)}\left(1-e^{-\hat{r}}\right), \quad (60)$$

similarly using (58), we obtain the imaginary part as

$$\text{Im } V(r,T,B,\mu) = \sum_f \alpha_s g^2 m_f \frac{|q_f B|}{3\pi^2}\left[\frac{\pi}{2m_D^3} - \frac{\pi e^{-\hat{r}}}{2m_D^3} - \frac{\pi\hat{r}e^{-\hat{r}}}{2m_D^3} - \frac{2\hat{r}}{m_D}\int_0^\infty \frac{pdp}{(p^2+m_D^2)^2}\right.$$
$$\left.\int_0^{pr}\frac{\sin t}{t}dt\right] - \frac{4}{3}\frac{\alpha_s T m_g^2}{m_D^2}\psi_1(\hat{r}) - \frac{16\sigma T m_g^2}{3m_D^4}\psi_2(\hat{r}) \quad (61)$$

where the functions $\psi_1(\hat{r})$ and $\psi_2(\hat{r})$ are given by

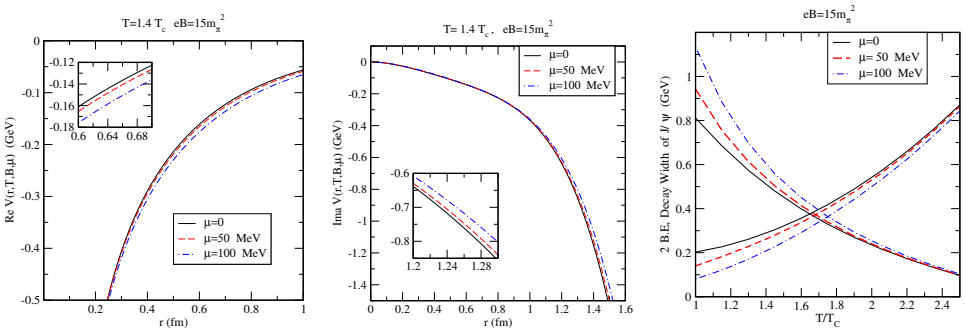
$$\psi_1(\hat{r}) \approx -\frac{1}{9}\hat{r}^2\left(3\ln\hat{r} - 4 + 3\gamma_E\right), \quad \psi_2(\hat{r}) \approx \frac{\hat{r}^2}{12} + \frac{\hat{r}^4}{900}\left(15\ln\hat{r} - 23 + 15\gamma_E\right)$$

8.5. *Results and Discussions*

We have observed that the Debye mass gets reduced at finite chemical potential but the effect is only visible at the low T region. The real part of the $Q\bar{Q}$ potential becomes more attractive due to the less screening in the medium [Fig 20(a)] while the magnitude of the imaginary part gets decreased [Fig 20(b)]. The binding energy of the J/ψ and Υ states is found to be increased at the finite μ whereas the decay width gets reduced. The dissociation temperature of the J/ψ state has been calculated in [Fig 20(c)] by studying the competition between twice the binding energy and decay width and it becomes slightly higher in comparison to medium with $\mu = 0$. The dissociation temperatures for J/ψ are found to be 1.64 T_c ,1.68 T_c,and 1.75 T_c at the $\mu = 0, 50$ and 100 MeV respectively whereas Υ is dissociated at 1.95 T_c, 1.97 T_c and 2.00 T_c for $\mu = 0, 50$ and 100 MeV respectively.

8.6. *Summary*

We have examined the effects of finite baryon density on the properties of the heavy quarkonia immersed in strongly magnetized hot QCD medium. For that purpose we have calculated the inverse Fourier transform of the (complex) resummed gluon propagator in the static limit. We conclude that quark chemical potential (μ) prevents early dissociation of the quarkonia by reducing the screening mass of the medium.



(a) (b) (c)

Fig. 20: **(a)** Variation of real part with inter-quark separation r **(b)** Variation of imaginary part with inter-quark separation r **(c)** Competition between twice the binding energy and decay width of J/ψ

9. Measurement of charged-particle jet properties in p-Pb collisions at $\sqrt{s_{\rm NN}} = 5.02$ TeV with ALICE

Prottoy Das on behalf of ALICE Collaboration

We present the measurement of charged-particle jet properties in minimum bias p–Pb collisions at $\sqrt{s_{\rm NN}} = 5.02$ TeV in ALICE. Jets are reconstructed from charged particles at midrapidity using the anti-$k_{\rm T}$ jet finding algorithm with jet resolution parameter $R = 0.4$. The mean charged particle multiplicity and jet fragmentation function for leading charged-particle jets in the $p_{\rm T}$ interval $10 < p_{\rm T,jet}^{\rm ch} < 100$ GeV/c are measured and compared with theoretical model predictions.

9.1. *Introduction*

Jets are collimated sprays of particles produced from the fragmentation and hadronization of hard-scattered partons in high-energy hadronic and nuclear collisions. Jet properties are sensitive to the details of parton showering process and are expected to be modified in the presence of a dense partonic medium. Measurements of intra-jet properties in p–Pb collisions are useful to investigate cold nuclear matter effects[110] and enrich our current understanding of particle production in such collision systems. In this work, we present the measurement of charged-particle jet properties, such as the mean charged particle multiplicity and fragmentation functions, for leading jets in the $p_{\rm T}$ interval $10 < p_{\rm T,jet}^{\rm ch} < 100$ GeV/c at midrapidity in p–Pb collisions at a center of mass energy per nucleon-nucleon pair $\sqrt{s_{\rm NN}} = 5.02$ TeV with ALICE. Results are compared with theoretical model predictions.

9.2. *Analysis details*

The data presented here were collected with the ALICE apparatus in 2016. Detailed information about the ALICE detector can be found in Ref.[111] Events are selected

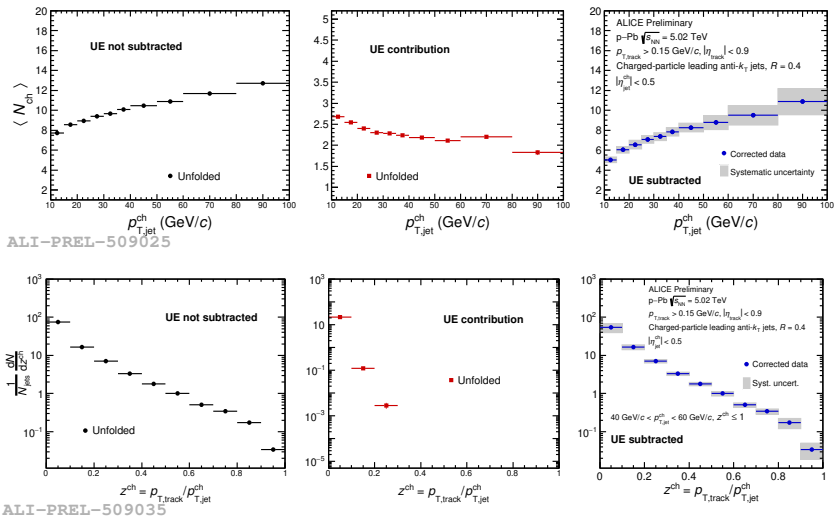


Fig. 21: Correction procedure to subtract UE contributions for $\langle N_{\rm ch} \rangle$ and $z^{\rm ch}$ ($40 < p_{\rm T,jet}^{\rm ch} < 60$ GeV/c): Unfolded distributions without UE subtraction (left), UE contribution (middle) and after UE subtraction (right).

for this analysis using a minimum bias trigger condition which requires the coincidence of signals in the V0A and V0C forward scintillator arrays.[93] Only events with a primary vertex within 10 cm from the nominal interaction point along the beam direction ($|z_{\rm vertex}| = 0$) are considered which results in total $5.15{\times}10^8$ events. Charged particles reconstructed with the Inner Tracking System (ITS)[95] and the Time Projection Chamber (TPC)[94] are used for the reconstruction of the primary vertex and jets. These detectors are placed inside a large solenoidal magnet that provides a homogeneous magnetic field $B = 0.5$ T.

Charged tracks with $p_{\rm T} > 0.15$ GeV/c within a pseudorapidity range $|\eta| < 0.9$ over the full azimuth are accepted. Charged-particle jets are reconstructed from the selected tracks using anti-$k_{\rm T}$ jet finding algorithm[112] with the $p_{\rm T}$-recombination scheme of FastJet package[96] with jet resolution parameter, $R = 0.4$. Only leading jets (jet of highest $p_{\rm T}$ in an event) with $10 < p_{\rm T,jet}^{\rm ch} < 100$ GeV/c are considered for this analysis. The mean charged particle multiplicity in leading jet ($\langle N_{\rm ch} \rangle$) and leading-jet fragmentation function ($z^{\rm ch} = p_{\rm T,track}/p_{\rm T,jet}^{\rm ch}$, where $p_{\rm T,track}$ is the $p_{\rm T}$ of jet constituent inside the leading-jet cone) are studied as a function of jet $p_{\rm T}$.

Contribution from the underlying event (UE; coming from sources other than the hard scattered partons) is estimated using the perpendicular-cone method and subtracted on a statistical basis after unfolding as reported in Fig. 21. In the perpendicular-cone method, circular cones of radius $R = 0.4$ at the same η as the leading jet and perpendicular to the leading jet axis are used for the estimation of the contribution from the UE.

A 2-dimensional Bayesian unfolding technique[97] (implemented in RooUnfold[113] package) is applied to correct for instrumental effects such as track-reconstruction efficiency and momentum resolution. For each of the jet observables, a 4D response matrix is constructed from a Monte Carlo (MC) simulation performed with the DPMJET[114] event generator and the generated particles are transported through the GEANT detector simulation. DPMJET is a multipurpose generator based on the Dual Parton Model (DPM) and is able to simulate a wide variety of collision systems for energies ranging from a few GeV up to the highest cosmic-ray energies. To construct the response matrix, the detector- and particle-level jets are matched geometrically and only the leading detector-level jet and the corresponding matched particle-level jet in an event are considered.

Systematic uncertainties from various sources such as tracking efficiency, modelling of the jet properties and the detector response in the MC simulation, choice of regularization parameter or number of iterations in Bayesian unfolding, change in prior distribution, and underlying event contribution are estimated and added in quadrature to calculate the total systematic uncertainty. The total systematic uncertainty is found to be 5% - 12% in the $\langle N_{\rm ch}\rangle$ analysis whereas in the $z^{\rm ch}$ analysis, it is estimated to be ∼20% for $20 < p_{\rm T,jet}^{\rm ch} < 30$ GeV/c and 25% - 45% for $40 < p_{\rm T,jet}^{\rm ch} < 60$ GeV/c.

9.3. *Results and discussion*

Figure 22 (top left) shows the $\langle N_{\rm ch}\rangle$ distribution as a function of leading jet $p_{\rm T,jet}^{\rm ch}$ in the top panel. The blue markers represent the data and the green curve shows the DPMJET (GRV94[115]) prediction. The ratio between the data and DPMJET is depicted in the bottom panel. It is observed that $\langle N_{\rm ch}\rangle$ increases with $p_{\rm T,jet}^{\rm ch}$ and DPMJET reproduces the data for $p_{\rm T,jet}^{\rm ch} > 30$ GeV/c within uncertainties. Figure 22 (top right and bottom left) show the $z^{\rm ch}$ distributions for leading jets with $20 < p_{\rm T,jet}^{\rm ch} < 30$ GeV/c and $40 < p_{\rm T,jet}^{\rm ch} < 60$ GeV/c respectively in the to panels. Results are compared with the DPMJET (GRV94) predictions. The ratios between the data and DPMJET predictions are shown in the bottom panels. It is found that DPMJET reproduces the $z^{\rm ch}$ distributions in both $p_{\rm T,jet}^{\rm ch}$ ranges within systematic uncertainties. The comparison of the $z^{\rm ch}$ distributions in the intervals $20 < p_{\rm T,jet}^{\rm ch} < 30$ GeV/c and $40 < p_{\rm T,jet}^{\rm ch} < 60$ GeV/c shown in Fig. 22 (bottom right) indicates that the $z^{\rm ch}$ distribution follows a scaling behaviour with $p_{\rm T,jet}^{\rm ch}$ within systematic uncertainties.

9.4. *Summary*

We have presented the measurement of charged-particle jet properties in minimum bias p–Pb collisions at $\sqrt{s_{\rm NN}} = 5.02$ TeV in ALICE. Results are compared with DPMJET (GRV94) predictions, which reproduces both the measured distributions ($\langle N_{\rm ch}\rangle$ and $z^{\rm ch}$) within uncertainties except for $\langle N_{\rm ch}\rangle$ at very low $p_{\rm T,jet}^{\rm ch}$ (< 30

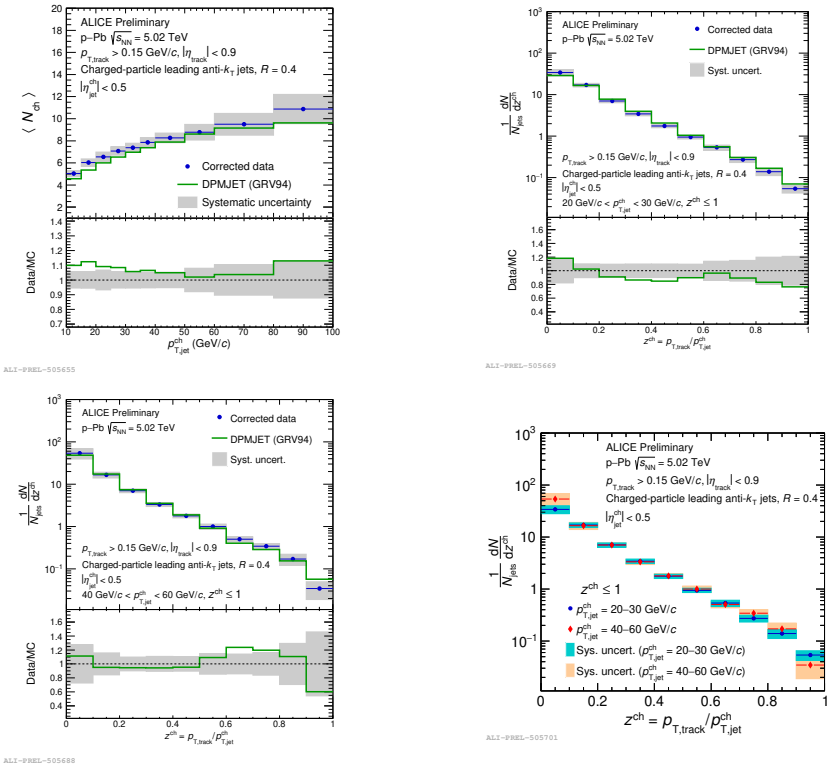


Fig. 22: Top panels: (top left) $\langle N_{\rm ch} \rangle$ distribution as a function of leading jet $p^{\rm ch}_{\rm T,jet}$. (top right) and (bottom left) $z^{\rm ch}$ distributions for leading jets with $20 < p^{\rm ch}_{\rm T,jet} < 30$ GeV/c and $40 < p^{\rm ch}_{\rm T,jet} < 60$ GeV/c respectively. Bottom panels: ratio between the data and MC results. (Bottom right) $z^{\rm ch}$ distributions for leading jets with $20 < p^{\rm ch}_{\rm T,jet} < 30$ GeV/c and $40 < p^{\rm ch}_{\rm T,jet} < 60$ GeV/c.

GeV/c). A scaling of jet fragmentation with leading charged-particle jet $p_{\rm T}$ is observed within systematic uncertainties.

10. Strange particles femtoscopic correlation in PbPb collisions at $\sqrt{s_{\rm NN}}$= 5.02 TeV

Raghunath Pradhan

Two-particle correlations as a function of relative momentum are measured for $\rm K^0_S$, Λ, and $\overline{\Lambda}$ strange hadrons. The data were obtained for PbPb collisions at $\sqrt{s_{\rm NN}}$= 5.02 TeV using the CMS detector at the LHC. Such correlations are sensitive to quantum statistics and to possible final-state interactions between the particles. The source radii are extracted from $\rm K^0_S K^0_S$ correlations in different centrality regions and are found to decrease from central to peripheral collisions. The strong-interaction scattering parameters (i.e., scattering length and effective range) are extracted from $\Lambda \rm K^0_S \oplus \overline{\Lambda} K^0_S$ and $\Lambda\Lambda \oplus \overline{\Lambda\Lambda}$ correlations using the Lednicky-Lyuboshits model and compared with other

experimental and theoretical results.

10.1. *Introduction*

Identical and nonidentical particle short-range correlations in relative momentum, known as "femtoscopic" correlations, can be used to study the space-time extent of the particle emitting source created in relativistic heavy ion collisions.[116] The identical particle correlations are sensitive to quantum statistics (QS) and to possible final-state interactions (FSI), while nonidentical particle correlations are only sensitive to final state interactions. The correlations among the neutral $\mathrm{K^0_S}$, Λ, and $\overline{\Lambda}$ particles, collectively referred to as $\mathrm{V^0}$ particles, are of specific interest. They can be used to extract the size of the particle-emitting source, and, in a way complementary to dedicated scattering experiments, the strong-interaction parameters, i.e., the scattering length and the effective range. Because of their heavy mass and absence of Coulomb interactions, femtoscopy based on neutral kaon particles ($\mathrm{K^0_S}$) complements the more commonly studied pion and charged kaon femtoscopy. By studying $\Lambda\mathrm{K^0_S} \oplus \overline{\Lambda}\mathrm{K^0_S}$ and $\Lambda\Lambda$ correlations, it is possible to extract the strong interaction scattering parameters for baryon-meson and baryon-baryon systems, which can shed light on the nature of the strong interaction.

This note presents the $\mathrm{K^0_S K^0_S}$, $\Lambda\mathrm{K^0_S} \oplus \overline{\Lambda}\mathrm{K^0_S}$ and $\Lambda\Lambda \oplus \overline{\Lambda\Lambda}$ femtoscopic correlations in lead-lead (PbPb) collisions at center-of-mass energy per nucleon pair of $\sqrt{s_{\mathrm{NN}}}$ = 5.02 TeV using the data recorded by "the CMS[63] experiment" at the LHC. The $\mathrm{K^0_S K^0_S}$ correlations were measured in the extended range of centrality bin (0–60%), where centrality is defined as the fraction of the total nucleus-nucleus cross section, with 0% denoting the maximum overlap of the colliding nuclei. The $\Lambda\mathrm{K^0_S} \oplus \overline{\Lambda}\mathrm{K^0_S}$ and $\Lambda\Lambda \oplus \overline{\Lambda\Lambda}$ correlations were measured in centrality range 0–80%. The size of the particle emitting source is extracted from $\mathrm{K^0_S K^0_S}$, $\Lambda\mathrm{K^0_S} \oplus \overline{\Lambda}\mathrm{K^0_S}$, and $\Lambda\Lambda \oplus \overline{\Lambda\Lambda}$ correlations. The strong interaction scattering parameters are extracted from $\Lambda\mathrm{K^0_S} \oplus \overline{\Lambda}\mathrm{K^0_S}$ and $\Lambda\Lambda \oplus \overline{\Lambda\Lambda}$ correlations using Lednicky-Lyuboshits fit[117] and compared with theoretical calculations and results from other experiments.

10.2. $\mathbf{K^0_S K^0_S}$ *femtoscopic correlation*

The left plot of figure 23 shows the $\mathrm{K^0_S K^0_S}$ correlation measurement as a function of relative momenta of the particles pair q_{inv}[116,117] in 20–30% centrality with $0 < k_T < 2.5$ GeV, where $k_T \equiv |\vec{p}_{\mathrm{T},1} + \vec{p}_{\mathrm{T},2}|/2$ is the average transverse momentum of the pair.[117] The size of the particle-emitting source R_{inv} (right) extracted from $\mathrm{K^0_S K^0_S}$ correlation using the Lednicky-Lyuboshits fit[118] together with nonfemtoscopic background[117] for different centrality ranges and plotted in the right plot of figure 23.[117] It can be seen that R_{inv} decreases from central (0–10%) to peripheral (50–60%) collisions. The values of R_{inv} as extracted by considering only the QS effect are larger than those found from considering both QS and FSI effects, which suggests that the FSI effects needs to be consider for the accurate measurement of R_{inv}.

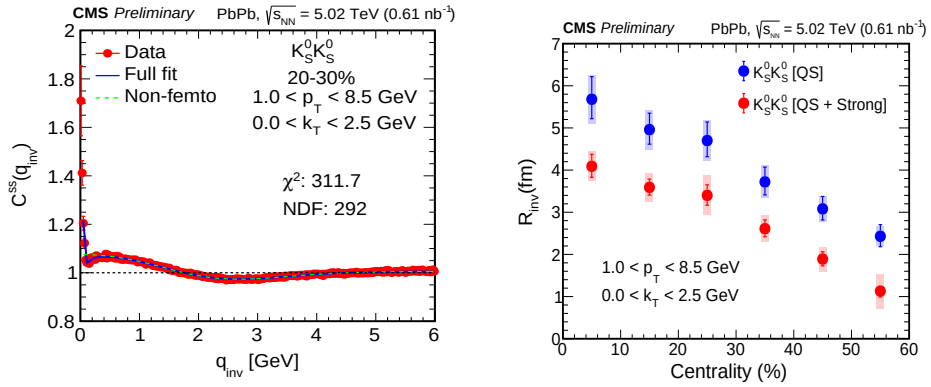


Fig. 23: Left: An example of correlation measurement and their fit for $K^0_S K^0_S$ in 20–30% centrality. In this plots, red filled circles are the experimental results, the blue solid line is the full fit,[117] and the green dotted line is the nonfemtoscopic background.[117] Right: $R_{\rm inv}$ as a function of centrality by considering only the QS (blue circle) and both the QS and strong FSI effects (red circles). For each data point, the line and shaded area indicate the statistical and systematic uncertainty, respectively.

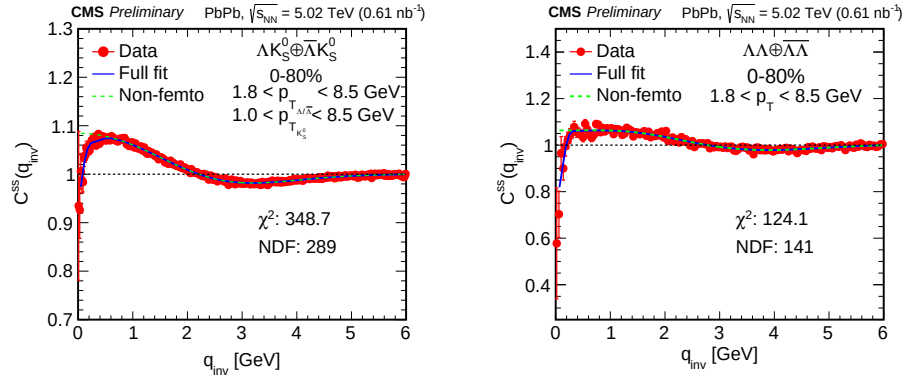


Fig. 24: The correlation measurements and their fits for $\Lambda K^0_S \oplus \overline{\Lambda} K^0_S$ (left) and $\Lambda\Lambda \oplus \overline{\Lambda\Lambda}$ (right)in 0–80% centrality. In these plots, red circles are the experimental results, the blue solid line is the full fit, and the green dotted line is the nonfemtoscopic background fit.[117] For each data point, the line and shaded area indicate the statistical and systematic uncertainty, respectively.

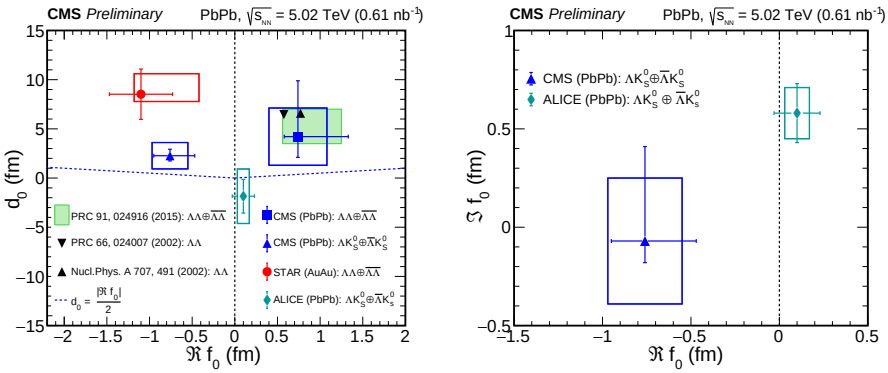


Fig. 25: Figure shows the values of d_0 and $\Re f_0$ (left) and the values of $\Im f_0$ and $\Re f_0$ (right). In the left plot, the blue triangle and square marker are for $\Lambda K^0_S \oplus \overline{\Lambda} K^0_S$ and $\Lambda\Lambda \oplus \overline{\Lambda\Lambda}$ correlations, respectively, and are compared with the $\Lambda\Lambda \oplus \overline{\Lambda\Lambda}$ results from STAR experiment[120] and $\Lambda K^0_S \oplus \overline{\Lambda} K^0_S$ result from ALICE experiment.[119] A reanalysis of STAR data for $\Lambda\Lambda \oplus \overline{\Lambda\Lambda}$ correlations is shown in the shaded area.[121] Theory calculations of the $\Lambda\Lambda$ interaction parameters are shown as black triangles.[122,123] In the right plot, the triangle is for $\Lambda K^0_S \oplus \overline{\Lambda} K^0_S$ correlation, and is compared with ALICE $\Lambda K^0_S \oplus \overline{\Lambda} K^0_S$ results.[119]For each data point, the two lines and the box indicate the (one-dimensional) statistical and systematic uncertainties, respectively.

10.3. $\Lambda K^0_S \oplus \overline{\Lambda} K^0_S$ *and* $\Lambda\Lambda \oplus \overline{\Lambda\Lambda}$ *femtoscopic correlations*

Figure 24 shows the $\Lambda K^0_S \oplus \overline{\Lambda} K^0_S$ (left) and $\Lambda\Lambda \oplus \overline{\Lambda\Lambda}$ (right) correlation measurements in $0-80\%$ centrality with no restriction on k_T.[117] The $R_{\rm inv}$ and strong-interaction scattering parameters: real scattering length ($\Re f_0$), imaginary scattering length ($\Im f_0$), and effective range (d_0) are extracted from the $\Lambda K^0_S \oplus \overline{\Lambda} K^0_S$ and $\Lambda\Lambda \oplus \overline{\Lambda\Lambda}$ correlations using Lednicky-Lyuboshits fit[118] are listed in Table 1 and plotted in Fig. 25. Figure 25 shows d_0 versus $\Re f_0$ (left) and $\Im f_0$ versus $\Re f_0$ (right). Comparisons are shown to theoretical calculations and results from other experiments.[119–123] The negative value of $\Re f_0$ in $\Lambda K^0_S \oplus \overline{\Lambda} K^0_S$ correlations suggests that the ΛK^0_S ($\overline{\Lambda} K^0_S$) interaction is repulsive while $\Im f_0$ is consistent with zero within their uncertainty, preventing us from drawing any conclusion about inelastic processes.[117] A positive $\Re f_0$ value for the $\Lambda\Lambda \oplus \overline{\Lambda\Lambda}$ correlations indicates that the $\Lambda\Lambda(\overline{\Lambda\Lambda})$ interaction is attractive.

10.4. *Summary*

The $K^0_S K^0_S$, $\Lambda K^0_S \oplus \overline{\Lambda} K^0_S$, and $\Lambda\Lambda \oplus \overline{\Lambda\Lambda}$ femtoscopic correlations are presented in PbPb collisions at a center-of-mass energy per nucleon pair of $\sqrt{s_{\rm NN}} = 5.02$ TeV, as measured by the CMS experiment at the LHC. This is the first report of $\Lambda\Lambda \oplus \overline{\Lambda\Lambda}$ correlations in PbPb collisions. The source size R_{inv} is extracted for $K^0_S K^0_S$

Table 1: Extracted values of the $R_{\rm inv}$, $\Re f_0$, $\Im f_0$, and d_0 from $\Lambda\mathrm{K}^0_\mathrm{S} \oplus \overline{\Lambda}\mathrm{K}^0_\mathrm{S}$ and $\Lambda\Lambda \oplus \overline{\Lambda\Lambda}$ correlations in the 0–80% centrality.

Parameter	$\Lambda\mathrm{K}^0_\mathrm{S} \oplus \overline{\Lambda}\mathrm{K}^0_\mathrm{S}$	$\Lambda\Lambda \oplus \overline{\Lambda\Lambda}$
R_{inv} (fm)	$2.09^{+1.42}_{-0.50}$ (stat) $\pm$ 0.65 (syst)	$1.33^{+0.37}_{-0.23}$ (stat) $\pm$ 0.25 (syst)
$\Re f_0$ (fm)	$-0.76^{+0.29}_{-0.19}$ (stat) $\pm$ 0.21 (syst)	$0.74^{+0.59}_{-0.16}$ (stat) $\pm$ 0.34 (syst)
$\Im f_0$ (fm)	$-0.07^{+0.48}_{-0.11}$ (stat) $\pm$ 0.31 (syst)	—
d_0 (fm)	$2.27^{+0.66}_{-0.53}$ (stat) $\pm$ 1.31 (syst)	$4.21^{+5.68}_{-2.11}$ (stat) $\pm$ 2.91 (syst)

correlations in six centrality bins from 0–60% centrality and found to decrease toward more peripheral collisions. The values of $R_{\rm inv}$, based on $\Lambda\mathrm{K}^0_\mathrm{S} \oplus \overline{\Lambda}\mathrm{K}^0_\mathrm{S}$ and $\Lambda\Lambda \oplus \overline{\Lambda\Lambda}$ correlations, are also presented for the 0–80% centrality range . The Lednicky-Lyuboshits model fit to the data suggests that the $\Lambda\Lambda \oplus \overline{\Lambda\Lambda}$ interaction is attractive, whereas the $\Lambda\mathrm{K}^0_\mathrm{S} \oplus \overline{\Lambda}\mathrm{K}^0_\mathrm{S}$ interaction is repulsive.

11. Measurement of exclusive vector meson photoproduction in pPb and PbPb collisions with the CMS experiment

Subash Chandra Behera

The exclusive photoproduction of vector mesons provides a unique opportunity to constrain the gluon distribution function within protons and nuclei. Measuring vector mesons of various masses over a wide range of rapidity and as a function of transverse momentum provides important information on the evolution of the gluon distribution within nuclei. A variety of measurements, including the exclusive J/ψ, ρ, and Υ meson production in pPb (at nucleon-nucleon center of mass energies of 5.02 and 8.16 TeV) and PbPb (5.02 TeV) collisions, are presented as a function of squared transverse momentum and the photon-proton center of mass energy. Finally, compilations of these data and previous measurements are compared to various theoretical predictions.

11.1. *Introduction*

This article presents the measurement of the exclusive photoproduction of Υ and J/ψ mesons from protons in pPb collisions at a nucleon–nucleon centre-of-mass energy of $\sqrt{s_{\rm NN}}$ = 5.02 TeV with the CMS detector.[63] Ultraperipheral collisions (UPCs) of protons or ions occur at the impact parameter is larger than the sum of their radii, therefore it is largely suppressed by hadronic interaction.[124] In UPCs, one of the incoming hadron emits quasi real photon and they converted into vector meson state by a color singlet gluon exchange process with the other hadrons. Since incoming hadrons remain intact in the process and vector meson is produced in the event, the process is called "exclusive". The study of exclusive quarkonia photoproduction can provide a unique probe of the target hadron structure, with the large mass of the J/ψ and Υ mesons providing a hard scale for calculations based

on perturbative quantum chromodynamics (pQCD).[125] The study of the photoproduction of Υ and ρ^0 mesons from proton is sensitive to the generalized parton distributions (GPDs), which can be approximated by the square of the gluon density in the proton. Exclusive vector photoproduction is very interesting because the Fourier transform of the t distribution is related to the two-dimensional distribution of the struck partons in the transverse plane. Here, t indicates the squared four-momentum transfer at the proton vertex. In this proceedings, the $|t| \approx p_{\mathrm{T}}^2$ distributions of Υ and ρ^0 are presented.

In this talk, we discuss the exclusive photoproduction of ρ^0 that decay to $\pi^+\pi^-$ and Υ decay to $\mu^+\mu^-$ channel in ultra-peripheral pPb collisions at $\sqrt{s_{\mathrm{NN}}} = 5.02$. The cross section is measured as a function of photon-proton center-of-mass energy, $W_{\gamma p}$ and t. This note is organized as follows. In section 11.2 discusses the invariant mass of the vector meson. Section 11.3 presents the differential cross section as a function of rapidity, transverse momentum and $W_{\gamma p}$.

11.2. *Invariant mass*

Figure 1 shows the invariant mass distribution for dimuon in the range between 8 and 12 GeV that satisfies the selection criteria described in Ref.[126] An unbinned likelihood fit to the spectrum is performed using ROOFIT [52] with a linear function to describe the QED $\gamma+\gamma \to \mu+\mu^-$ continuum background, where the background slope parameter is fixed to the STARLIGHT $\gamma + \gamma \to \mu+\mu^-$ simulation, with three Gaussian functions for the three Υ signal peaks.

Figure 26 (right plot) presents the fit of the unfolded distribution with the modifed Soding model. A least squares fit is performed for the interval $0.6 < M_{\pi^+\pi^-} < 1.1$ GeV, with the quantities, $M_{\rho(770)^0}$, $M_{\omega(783)}$, $\Gamma\rho(770)^0$, $\Gamma_{\omega(783)}$, A, B, C, $\phi_{\omega(783)}$ treated as free parameters.

11.3. *Differential cross section measurement*

The differential cross section of the exclusive Υ(nS) is measured as a function of p_{T}^2 and y over $|y| < 2.2$, are shown in Figure 27. The p_{T}^2-differential cross section is fitted with an exponential function in the region $0.01 < p_{\mathrm{T}}^2 < 1.0$ GeV^2, using a χ^2 goodness-of-fit minimization technique. The slope parameter $b = 6.0 \pm 2.1$ (stat) ± 0.3 (syst) GeV^{-2} is extracted, and in agreement with $b = 4.3^{2.0}_{-1.3}$ (stat) $^{0.5}_{-0.6}$ (syst) GeV^{-2}, is measured by the ZEUS in the photon–proton centre-of-mass energy range $60 < W_{\gamma p} < 220$ GeV. The measured results are consistent with the predictions of pQCD-based models.

Figure 28 (left plot) shows the rapidity distribution of the Υ(1S). Our results are compared with the various theoretical predictions, and they are consistent with the data within the relatively large experimental uncertainties. The JMRT-LO[127] results being systematically above the data points as well as all the other calculations.

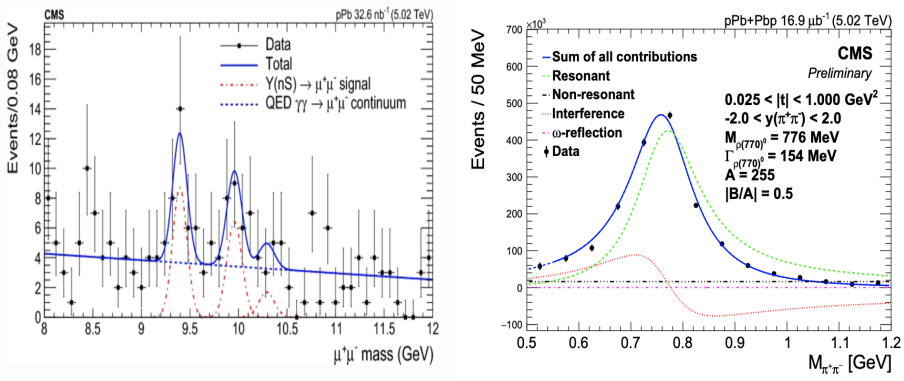


Fig. 26: Left side figure shows the invariant mass distribution of the exclusive dimuon candidates in the range $8 < m_{\mu^+\mu^-} < 12$ GeV that satisfied all the selection criteria, fitted to a linear function for the two-photon QED continuum (blue dashed line) plus three Gaussian distributions corresponding to the $\Upsilon(1S), \Upsilon(2S), \Upsilon(3S)$ mesons (dashed-dotted-red curves). Right side figure shows unfolded $\pi^+\pi^-$ invariant mass distribution in the pion pair rapidity interval $|y_{\pi^+\pi^-}| < 2$ fitted with the Soding model. The green dashed line indicates resonant $\rho(770)^0$ production, the red dotted line represents the interference term, the magenta dash-dotted line corresponds to the background from $\omega \to \pi^+\pi^-\pi^0$, the black dash-dotted line represents the no resonant contribution, and the blue solid line represents the sum of all these contributions.

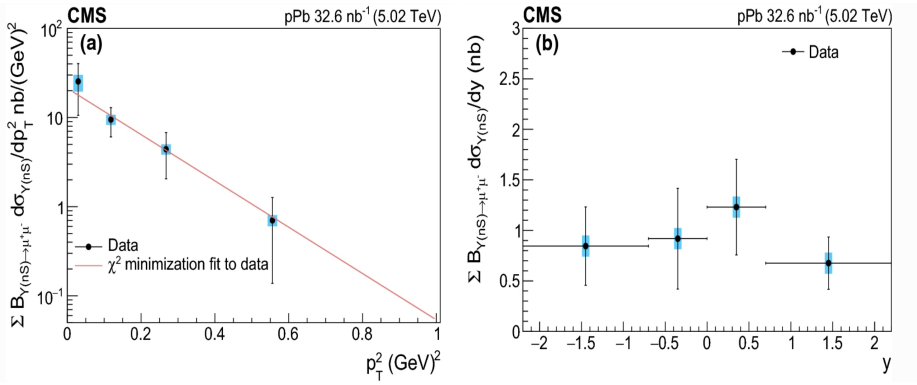


Fig. 27: Left side shows the differential $\Upsilon(\mathrm{nS}) \to \mu+\mu^-$ as a function of p_{T}^2 and rapidity y in pPb collisions. The data points are placed along the abscissa following the prescription, and the solid line is an exponential fit. In the right plot, the horizontal bars are indicating the width of each y bin.

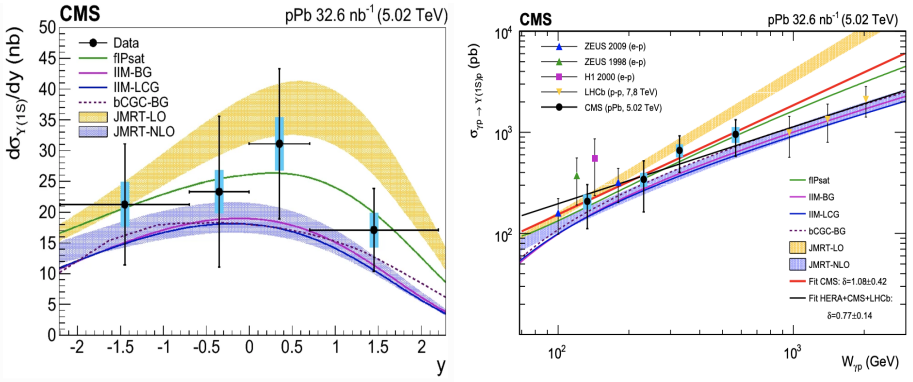


Fig. 28: Left plot is the differential cross section as a function of rapidity measured in pPb collisions. Right plot is the $W_{\gamma p}$ dependence of cross section for the exclusive photo production.

The data are compared to the various theoretical predictions. A fit with the power-law function in the entire $W_{\gamma p}$ range of data yields $\delta = 1.30$ and $\delta = 0.84$ for the LO and NLO calculations, respectively. We significantly reduced the uncertainty compared to ZEUS[128] and covered a wide range of W.

11.4. *Summary*

The study of the exclusive photoproduction of Υ and $\rho(770)^0$ are measured in UPC pPb collisions at $\sqrt{s_{\rm NN}} = 5.02$ TeV with the CMS. The differential cross section as a function of rapidity, p_T^2 and $W_{\gamma p}$ are calculated and compared with the previous experiment at H1, LHCb and ZEUS. The data, within their currently large statistical uncertainties, are consistent with various pQCD approaches that model the behaviour of the low-x gluon density, and provide new insights on the gluon distribution in the proton in this poorly explored region.

12. Investigation of jet quenching effects due to different energy loss mechanisms in heavy-ion collisions using JETSCAPE framework

Rohan V S

Heavy ion collisions produced at relativistic high energies generate a hot, dense medium of strongly interacting nuclear matter known as a quark–gluon plasma (QGP). The jets produced in the QGP medium lead to the expulsion of a large number of particles in a parton shower. The quantity of energy lost by the jet and the shape of the underlying transverse momentum p_T spectrum are the objects of interest to determine the nuclear modification factor (R_{AA}) of jets. Jet Energy-loss Tomography with a Statistically and Computationally Advanced Program Envelope (JETSCAPE) is a multi-stage jet evolution framework that provides an integrated depiction of jet quenching which could be

used to analyze the multi-stage high-energy jet evolution in QGP medium in great detail. In this work, Pb-Pb collisions at $\sqrt{s_{NN}} = 5.02$ TeV and Au-Au collisions at 200 GeV were selected for various combinations of jet energy loss models including MATTER, LBT, Martini, and AdSCFT and are examined. For centrality classes ranges from 0 to 10%, 30 to 40% and 60 to 80% for the different energy loss models were compared in both QGP medium and vacuum to study the nuclear modification factor.

12.1. *Introduction*

Heavy ion collisions at relativistic high energies results in the production of a fireball that creates the QGP.[129] When a jet is produced in a heavy ion collision, the partons in the shower must traverse through the droplet of QGP produced in the same collision. The evolution of jets produced in the early stages of collisions provide crucial information about the short-distance-scale interactions of high energy partons within the QGP medium. The jets originating from the collision of ions pass through the QGP medium and lose energy due to jet-medium interactions, a phenomenon termed as jet quenching.[130] The energy lost by the partons while propagating through the QGP medium result in the suppression of yield at different transverse momentum values. In this proceeding, we present the nuclear modification factor of inclusive jets.

Simulations of high energy heavy-ion collisions require a multitude of interacting elements, ranging from simulations of the incoming nuclei, to the thermalization of the deposited energy-momentum, viscous fluid dynamical expansion, as well as the production of hard partons, their propagation and interaction with the dense medium, hadronization and freeze-out, escape and fragmentation into jets.[131] To compare with high-statistics experimental data, one requires a modular and extendable event generator, with state-of-the-art components modeling of each aspect of the collision. The JETSCAPE[132] used in this study is such a framework for general purpose event generation. It contains modules that runs simulations of each sector of high energy heavy-ion collisions. This framework includes an initial soft sector event generator for simulations of the incoming nuclei, viscous fluid dynamical model for the medium expansion, hadronization model and freeze-out model. Four different energy loss modules are available; The Modular All Twist Transverse-scattering Elastic-drag and Radiation (MATTER)[133] for modeling high virtuality and high energy parton evolution, Linear Boltzmann Transport (LBT)[134] for modeling low virtuality and high energy evolution, Modular Algorithm for Relativistic Treatment for heavy Ion Interactions (MARTINI)[135] for modeling low virtuality and high-energy evolution using a gluon radiation process and AdS/CFT for modeling a low virtuality and low energy parton shower. Initial hard partons generated by PYTHIA are fed into MATTER and propagated with a virtuality-ordered shower.

12.2. *Jet Observable (Nuclear modification factor)*

The nuclear modification factor (R_{AA}) is the ratio of the jet yields in heavy-ion collisions (Pb-Pb or Au-Au) to those in p-p collisions as a function of transverse

momentum, normalised by the mean nuclear thickness function.

$$R_{AA} = \frac{\frac{1}{N_{\rm ev}} \frac{d^2 N_{\rm jet}}{dp_T dy}}{\langle T_{AA} \rangle \frac{d^2 \sigma_{\rm jet}}{dp_T dy}} \tag{62}$$

where $N_{\rm ev}$ is the number of hard scattering events, $N_{\rm jet}$ is the number of jets in heavy-ion collisions, $p_{\rm T}$ is the transverse momentum, y is the rapidity, σ_{jet} is the jet cross section in p-p collisions and $\langle T_{AA} \rangle$ is the mean nuclear thickness function.

12.3. *Results and Summary*

In this work, we have used the JETSCAPE framework to produce Pb-Pb collisions at $\sqrt{s_{NN}}$ = 5.02 TeV and Au-Au collisions at $\sqrt{s_{NN}}$ = 200 GeV. We have compared the results obtained using the JETSCAPE framework to the corresponding results from ATLAS[136] and STAR[137] experiments. Initial state model TRENTO[138] was added, in which, we set the corresponding geometric and kinematic properties of ions i.e. Pb-Pb at 5.02 TeV, cross-section, normalization and centrality etc. A free streaming module Milne was used for bulk evolution. The hard scattering was carried out using the PYTHIA 8[139] gun with initial state radiation and multi parton interaction turned on and final state radiation turned off.The hydrodynamic module MUSIC[140–142] was used; subsequently, the jets were hadronized using the hadronization module.

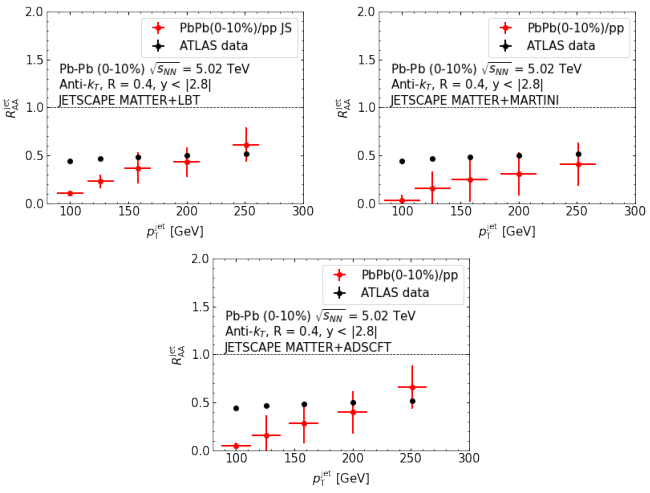


Fig. 29: The dependence of different energy loss modules on R_{AA} for Pb-Pb at 5.02 TeV

The dependence of different energy loss modules on R_{AA} was studied using Pb-Pb collisions at 0-10% centrality. Fig. 29 (left plot) shows R_{AA} with MATTER

and LBT energy loss modules. Fig. 29 (middle plot) uses MATTER and MARTINI energy loss modules and Fig. 29 (right plot) uses MATTER and ADSCFT for the same centrality interval. The hadrons that are formed were then reconstructed using the anti-kt algorithm[143] with radius of cone R = 0.4, minimum p_T of jets = 100 GeV, $y < |2.8|$ and minimum track p_T = 4 GeV. Figure 29 shows that for p_T above 150 GeV, the results are consistent with the experimental results for all the three energy loss modules, and for the low p_T region the JETSCAPE results under predict the data (more quenching in this region).

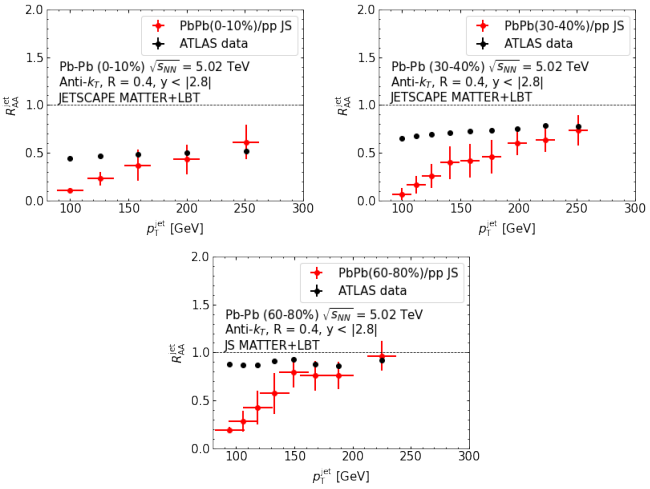


Fig. 30: Centrality dependence of R_{AA} for Pb-Pb collisions at 5.02 TeV

Fig. 30 shows the centrality dependence of R_{AA} for Pb-Pb collisions for 0-10% 30-40% and 60-80% centrality intervals simulated using the MATTER + LBT energy loss modules. The switching virtuality was set to 2 GeV and the strong coupling constant $\alpha_s = 3.0$ Here we can observe that the energy lost due to jet quenching is the highest for the central collisions 0-10% (left plot) and less for the mid-central collisions 30-40% (middle plot) and it is least for the peripheral collisions 60-80% (right plot). However, we can also see that in Fig. 30, the JETSCAPE results under predict the data in the lower p_T region.

The Au–Au heavy-ion collisions were simulated for the jets of transverse momentum from 5-30 GeV with TRENTO initial conditions and PYTHIA 8 hard scattering mechanism. The partons evolved from this are sent to MATTER and LBT energy loss modules with the switching virtuality set to 1 GeV and α_s = 3. The MUSIC module was used to describe the hydrodynamic evolution of bulk medium. The hadrons formed were reconstructed with the jet cone radius R = 0.4, minimum p_T of jets = 5 GeV, $y < |1|$ and minimum track p_T = 0.5 GeV.

The centrality dependence of R_{AA} for Au-Au collisions for centrality classes

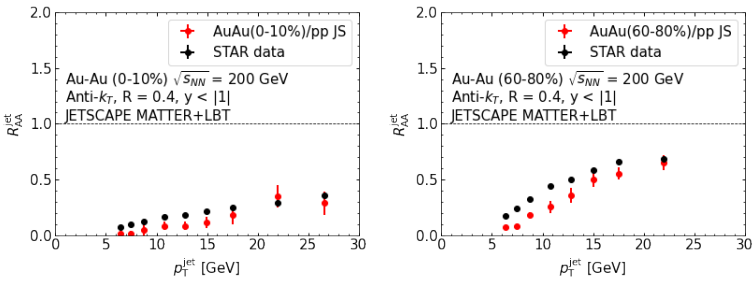


Fig. 31: Centrality dependence of R_{AA} for Au-Au collisions at 200 GeV

0-10% and 60-80% is shown in Fig. 31. The JETSCAPE results are consistent with the STAR experimental data and qualitatively explains the data in both the centrality classes. Fig. 31 shows that the jet quenching is more in the most central collisions 0-10% (left plot) as compared to peripheral collisions 60-80% (right plot) and the quenching gradually decreases with the transverse momentum of the jets as expected.

13. Recent Results from STAR and ALICE Experiments

Lokesh Kumar

We report recent selected results on particle production and fluctuations from the STAR and ALICE experiments. The results from the ALICE include baryon-to-meson ratios, elliptic flow v_2, and rapidity asymmetry. The results from the STAR are presented on kinetic freeze-out parameters at lower energy, and observables related to search of critical point and transition temperature. The physics implications of these results are discussed.

13.1. *Introduction*

The Solenoidal Tracker At RHIC (STAR)[144] at Relativistic Heavy-Ion Collider (RHIC), Brookhaven National Laboratory (BNL), USA and A Large Ion Collider Experiment (ALICE)[145] at Large Hadron Collider (LHC), CERN, Switzerland, are dedicated experiments for the heavy-ion collisions. They are built to study the properties of Quark Gluon Plasma (QGP), quark-hadron phase transition, and critical point in the phase diagram of Quantum Chromodynamics (QCD). The energy range ($\sqrt{s_{NN}}$ = 2.76 – 5.44 TeV)) at which ALICE experiment works is towards the region where $\mu_B \sim 0$, while STAR covers the energy range ($\sqrt{s_{NN}}$ = 3.0 – 200 GeV) from small $\mu_B \sim 20$ MeV up to the ∼720 MeV that includes the data collected in the fixed target mode of the STAR experiment. The higher energies will lead to QGP with longer lifetime and hene allow for the detailed study of QGP while the lower energy ranges help to look for the expected first order phase transition and critical point in the conjectured QCD phase diagram. In this way, both STAR and ALICE experiments provide important information regarding the

study of QGP and QCD phase diagram. In addition, the results from small systems (pp or pA) help in understanding the particle production and the baseline studies. We present selected results from the ALICE and STAR experiments.

13.2. *Results from the ALICE*

Recently, ALICE has collected data for Xe-Xe collisions at $\sqrt{s_{NN}} = 5.44$ TeV. The Xe is a medium sized nucleus and bridges the gap between p-Pb and Pb-Pb systems. Moreover, the detailed comparison of Xe-Xe and Pb-Pb allows to investigate the results for the systems at a similar multiplicity but with different initial eccentricity. Figure 32 (left) shows the p/π ratio (top panel) and v_2 (bottom panel) comparison

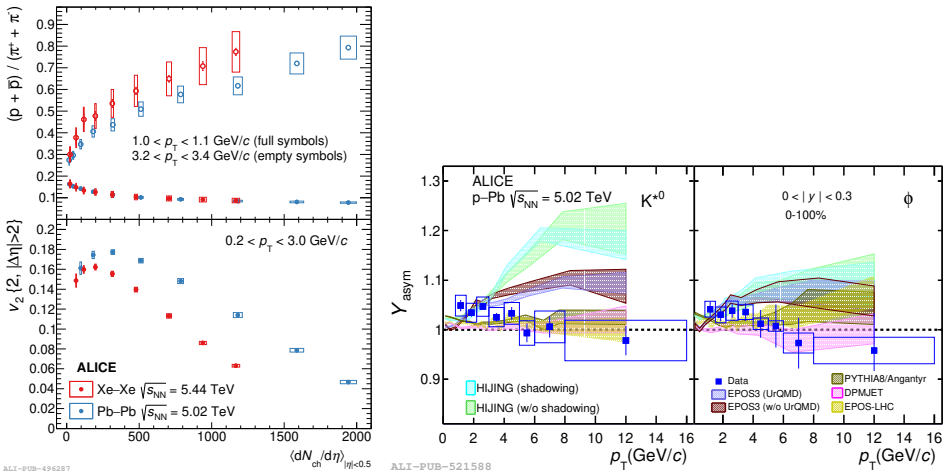


Fig. 32: Left: Comparison of proton-to-pion ratio (top panel) and v_2 (bottom panel) as a function of charged particle multiplicity density between Xe–Xe at $\sqrt{s_{NN}} = 5.44$ TeV sand Pb-Pb at $\sqrt{s_{NN}} = 5.02$ TeV. Right: The $Y_{\rm asym}$ for K^{*0} and ϕ meson as a function of p_T in the rapidity range $0 < |y| < 0.3$ in p–Pb collisions at $\sqrt{s_{NN}} = 5.02$ TeV. The results are compared with various models.

between Xe-Xe at $\sqrt{s_{NN}} = 5.44$ TeV and Pb-Pb at $\sqrt{s_{NN}} = 5.02$ TeV,[146] as a function of charged particle multiplicity density $\langle dN_{\rm ch}/d\eta\rangle$. The p/π ratio is plotted for the low-transverse momentum p_T (1.0–1.1 GeV/c) and intermediate-p_T (3.2–3.4 GeV/c) ranges. Both Xe-Xe and Pb-Pb show depletion of p/π ratio at low-p_T while enhancement of this ratio at intermediate-p_T. The enhancement of this ratio at intermediate-p_T is associated with quark-recombination and radial flow.[147,148] One observes that at a similar charged particle multiplicity density, the magnitude of p/π ratio is similar in both Xe-Xe and Pb-Pb systems. This suggests that this ratio depends on the final state multiplicity. However, the lower panel shows that for a given $\langle dN_{\rm ch}/d\eta\rangle$ (except for very low multiplicity), the v_2 in Pb-Pb is higher than that in Xe-Xe. Since, the v_2 originates from the hydrodynamical expansion which

in turn depends on the initial eccentricity, the results here suggests that Pb-Pb and Xe-Xe have different initial eccentricities.

The hadron production depends on various effects such as nuclear modification of parton distribution functions (nuclear shadowing) and possible parton saturation, multiple scattering, and radial flow. These effects depend on the rapidity of produced particles. The p-Pb collisions provide an opportunity to study the rapidity asymmetry ($Y_{\rm asym}$) of hadron production. Figure 32 (right) shows the $Y_{\rm asym}$ for K^{*0} and ϕ mesons as a function of p_T for 0–100% collision centrality in p–Pb collisions at $\sqrt{s_{NN}} = 5.02$ TeV.[149] The rapidity asymmetry is defined as: $Y_{\rm asym}(p_T) = \frac{[d^2N/(dp_T dy)]_{-0.3<y<0}}{[d^2N/(dp_T dy)]_{0<y<0.3}}$. It is observed that the $Y_{\rm asym}$ deviates from unity for both K^{*0} and ϕ at low-p_T whereas at high p_T it is consistent with unity. The deviations from unity at low-p_T suggests that there is rapidity dependence of nuclear effects in p-Pb collisions. The HIJING and EPOS3 model calculations suggest $Y_{\rm asym}$ at low-p_T but significantly overestimate the data at high-p_T.

13.3. *Results from the STAR*

The blast wave (BW), a hydrodynamic based model, has been successful in explaining the p_T spectra of various produced particles in heavy-ion collisions. It provides information on the kinetic freeze-out temperature $T_{\rm kin}$ and average radial flow velocity $\langle\beta\rangle$ of the system produced in these collisions. STAR recently has collected data in a fixed target mode in Au+Au collisions at $\sqrt{s_{NN}} = 3.0$ GeV. It is interesting to note if the blast wave model could explain the data at such a low energy. Figure 33 (left) shows the variation of $T_{\rm kin}$ as a function of $\langle\beta\rangle$ for various energies.[151]

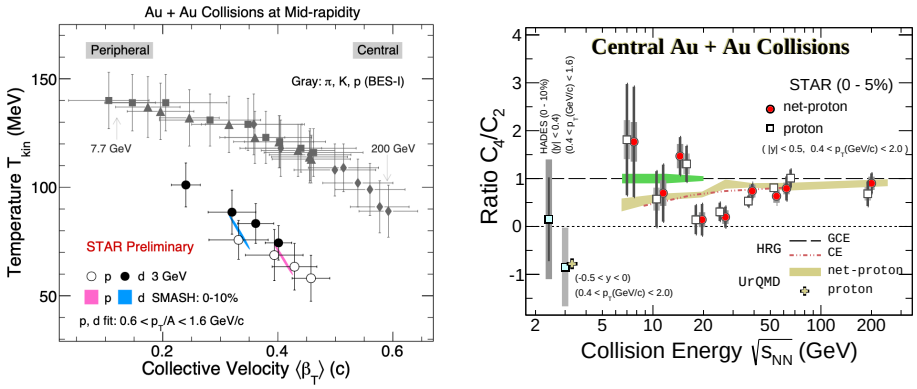


Fig. 33: Left: Variation of $T_{\rm kin}$ as a function of $\langle\beta\rangle$ for various energies.[151] Right: Ratios of cumulants, C4/C2, for protons (squares) and net-protons (red circles) as a function of collision energy. The vertical black and gray bars are the statistical and systematic uncertainties, respectively. Comparison with the HRG model (Canonical Ensemble (CE) and Grand-Canonical Ensemble (GCE)), and transport model UrQMD are also shown.

The results from $\sqrt{s_{NN}} = 3.0$ GeV are obtained by fitting protons and deuterons using the BW model. The results shown for other STAR energies are obtained by fitting pion, kaon, and proton and their antiparticles' spectra simultaneously with BW model. The $T_{\rm kin}$ and $\langle\beta\rangle$ exhibit an anticorrelation behavior. It is observed that the kinetic freeze-out parameters at $\sqrt{s_{NN}} = 3.0$ GeV are drastically different compared to other higher energies. This may suggest a different equation of state prevailing at 3 GeV compared to that at higher energies. It is also observed that the $T_{\rm kin}$ ($\langle\beta\rangle$) is higher (lower) for deuterons as compared to protons. The SMASH model, a hadronic transport model, shows similar results as data at 3 GeV.

One of the main goals of heavy-ion collisions is to investigate the phase structure of the QCD matter. At $\mu_B \sim 0$, the lattice QCD calculations suggest a smooth crossover transition from hadronic medium to the QGP phase and the transition temperature is about 155 MeV. At finite μ_B, a critical point followed by a first order phase transition is expected. At critical point, the correlation length of the system diverges and can be studied through the higher moments (skewness $S = \langle(\delta N)^3\rangle/\sigma^3$ and kurtosis $\kappa = [\langle(\delta N)^4\rangle/\sigma^4] - 3$, where $\delta N = N - \langle N\rangle$) of conserved quantities such as net-baryon (or net-proton) number which are sensitive to the correlation length. A non-monotonic behavior of higher moments of conserved quantities as a function of $\sqrt{s_{NN}}$ has been proposed as an experimental signature of critical point. To study the shape of the event-by-event net-proton distribution, the cumulants

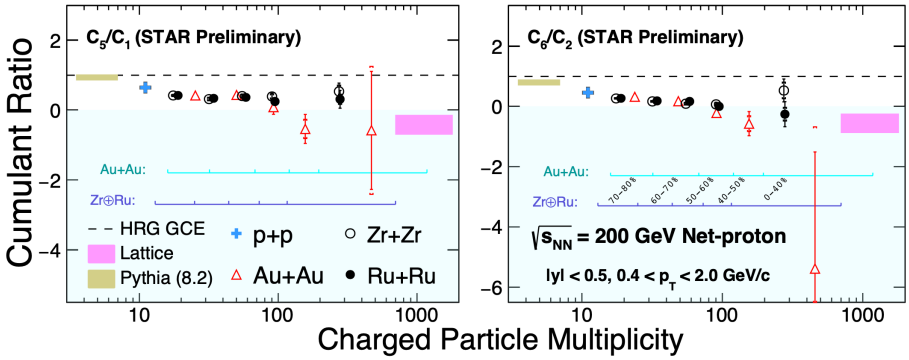


Fig. 34: C_5/C_1 (left panel) and C_6/C_2 (right panel) as a function of charged particle multiplicity for various systems pp, Au+Au, Ru+Ru, and Zr+Zr at $\sqrt{s_{NN}} = 200$ GeV.

(C_n) of various orders, $C_1 = M, C_2 = \sigma^2, C_3 = S\sigma^3$, and $C_4 = \kappa\sigma^4$, are calculated. The ratios of these cumulants such as $C_3/C_2 = S\sigma$, and $C_4/C_2 = \kappa\sigma^2$, lead to the cancelation of volume effects and are also related to the ratio of baryon-number susceptibilities computed in lattice QCD. Recent results from the STAR in the energy range $\sqrt{s_{NN}}$ =7.7–27 GeV for 0-5% central collisions, on net-proton fluctuation measurements C_4/C_2 show a non-monotonic behavior as a function of $\sqrt{s_{NN}}$ with a significance of 3.1σ as shown in Fig. 33 (right).[152] The calculations from hadron

resonance gas models (HRG) and Ultra Relativistic Molecular Dynamics (UrQMD) show a smooth energy dependence. These models have the baryon number conservation and do not include the critical point in their calculations. New results from STAR for proton cumulant ratios in Au+Au collisions at $\sqrt{s_{NN}}$ = 3.0 GeV are also shown in Fig. 33 (right).[153] The C_4/C_2 value at 3.0 GeV is around -1 and is reproduced by the transport model UrQMD. The results at 3.0 GeV are also consistent with those from HADES experiment. These results can be explained by fluctuations driven by baryon number conservation at high baryon density where hadronic interactions are dominant. It is expected that if the critical point exists, it can be observed in the region of $\sqrt{s_{NN}} > 3.0$ GeV to 19.6 GeV. The high statistics beam energy scan-II (BES-II) data will provide a definite answer in this regard.

Figure 34 shows the cumulant ratios C_5/C_1 (left panel) and C_6/C_2 (right panel) as a function of charged particle multiplicity for various systems pp, Au+Au, Ru+Ru, and Zr+Zr at $\sqrt{s_{NN}}$ = 200 GeV.[154] Results from HRG GCE model, Pythia (8.2), and lattice QCD calculation that include smooth crossover phase transition at $\mu_B = 0$, are compared with the experimental data. Both cumulant ratios decrease as a function of multiplicity and the most central Au+Au collisions results are consistent with the lattice results for the thermalized QCD matter and smooth crossover.

13.4. *Summary*

We have reported the latest results from the STAR and ALICE experiments. The measurement of p/π ratio and v_2 in Xe-Xe collisions at $\sqrt{s_{NN}}$ = 5.44 TeV compared to that in Pb-Pb collisions at $\sqrt{s_{NN}}$ = 5.02 TeV suggests that p/π ratio is sensitive to final state effect while v_2 is sensitive to initial effect, and Xe-Xe collisions have different initial eccentricity compared to Pb-Pb collisions. The K^{*0} and ϕ production in p-Pb collisions show a rapidity asymmetry at low-p_T. The matter produced in Au+Au collisions at $\sqrt{s_{NN}} = 3.0$ GeV shows different equation of state compared to that at higher energies. Results on net-proton cumulant ratios C_4/C_2 at $\sqrt{s_{NN}}$ = 3.0 GeV suggests that fluctuations at this energy are consistent with expectation of baryon number conservation at high baryon density where hadronic interactions are dominant. The higher cumulant ratios C_5/C_1 and C_6/C_2 results suggest that most central Au+Au collisions at $\sqrt{s_{NN}}$ = 200 GeV are consistent with the lattice results for thermalized QCD matter and smooth crossover.

14. Impact of Time Varying Electromagnetic Field on Electrical Conductivity of Hot QCD Matter

K K Gowthama, Manu Kurian, and Vinod Chandra

The impact of the time dependence of the electromagnetic fields and collisional aspects of the medium on the induced electric and Hall current densities have been explored using the relativistic Boltzmann equation. The effect of momentum anisotropy on electric

charge transport has also been studied. The electric response of the medium is seen to be significantly affected by the inhomogeneity of the fields and the anisotropy of the medium.

14.1. *Introduction*

Experiments at Relativistic Heavy Ion Collider (RHIC) and Large Hadron Collider (LHC) have indicated the existence of the strongly interacting matter-Quark Gluon plasma (QGP)[144] and strong magnetic fields in the heavy-ion collision process.[155,156] Transport coefficients of the hot QCD matter serve as the input parameters for the hydrodynamical description of the evolution of the created medium and act as a key ingredient in exploring the critical properties of the medium.[157] The response of the QCD medium to the time varying external electromagnetic fields can be quantified in terms of induced electric and Hall current densities and associated conductivities. Here, we have explored (i) a general formalism to study the electric charge transport in the presence of time-varying electromagnetic fields,[158] (ii) medium response in an anisotropic QCD medium.[158] To that end, we have estimated the general form of quark degrees of freedom in the presence of time dependent fields within the kinetic theory framework for both isotropic and anisotropic cases.

14.2. *Formalism*

The induced vector current in the QCD medium with a finite quark chemical potential μ can be defined as,

$$\mathbf{j} = 2N_c \sum_f \int \frac{d^3\mathbf{p}}{(2\pi)^3}\, \mathbf{v}\left(q_q f_q - q_{\bar{q}} f_{\bar{q}}\right), \tag{63}$$

where $f_k = f_k^0 + \delta f_k$ (the subscript k incidates the particle species) is the quark/antiquark distribution function with f_k^0 being the fermi Dirac distribution function for quarks and antiquarks, $\mathbf{v}$ the velocity vector, and N_c is number of colors. We chose the following ansatz for non-equilibrium part of the distribution function δf_k due to the inhomogeneous fields,

$$\delta f_k = (\mathbf{p}.\mathbf{\Xi})\frac{\partial f_k^0}{\partial \epsilon}, \tag{64}$$

where the vector $\mathbf{\Xi}$ is related to the strength of electric and magnetic fields and their derivatives and has the form as follows,

$$\begin{aligned}\mathbf{\Xi} =& \alpha_1\mathbf{E} + \alpha_2\dot{\mathbf{E}} + \alpha_3(\mathbf{E}\times\mathbf{B}) + \alpha_4(\dot{\mathbf{E}}\times\mathbf{B}) + \alpha_5(\mathbf{E}\times\dot{\mathbf{B}})\\ &+ \alpha_6(\boldsymbol{\nabla}\times\mathbf{E}) + \alpha_7\mathbf{B} + \alpha_8\dot{\mathbf{B}} + \alpha_9(\boldsymbol{\nabla}\times\mathbf{B}).\end{aligned} \tag{65}$$

With $\alpha_i (i = (1, 2, .., 9))$ are the unknown functions that relate to the respective transport coefficients associated with the electric charge transport. The transport

equation that describes the dynamics of the momentum distribution function can be defined as,

$$\frac{\partial f_k}{\partial t} + \mathbf{v}.\frac{\partial f_k}{\partial \mathbf{x}} + q_{f_k}[\mathbf{E} + \mathbf{v} \times \mathbf{B}].\frac{\partial f_k}{\partial \mathbf{p}} = -\frac{\delta f_k}{\tau_R}, \tag{66}$$

where $\mathbf{E}$ and $\mathbf{B}$ are the electric and magnetic fields, using the relaxation time approximation (RTA) for the collision kernal with τ_R being the relaxation time. We have obtained the α's for various cases of electromagnetic fields by solving the Boltzmann equation.[158,159]

14.3. *Time varying electromagnetic fields*

In the presence of time-varying electromagnetic fields, the current density take the form as $\mathbf{j} = j_e\hat{\mathbf{e}} + j_H(\hat{\mathbf{e}} \times \hat{\mathbf{b}})$ with,

$$j_e = j_e^{(0)} + j_e^{(1)}, \qquad\qquad j_H = j_H^{(0)} + j_H^{(1)} + j_H^{(2)}, \tag{67}$$

where j_e corresponds to the electric current in the direction of the electric field $\hat{\mathbf{e}}$ and j_H is the electrical current in the direction perpendicular to both electric and magnetic fields, $(\hat{\mathbf{e}} \times \hat{\mathbf{b}})$ are given in detail in Ref. 5. In the present analysis we have conisdered the form of the electric and magnetic fileds to be exponentially decaying fields with the decay parameters, τ_E and τ_B respectively.[160]

14.4. *Effects of momentum anisotropy*

Momentum anisotropy can be modeled by compressing or expanding the isotropic distribution function f_k^0 as,

$$f_{(\text{aniso})_k} = \sqrt{1+\xi}\, f_k^0\Big(\sqrt{p^2 + \xi(\mathbf{p}\cdot\mathbf{n})^2}\Big), \tag{68}$$

where ξ is the anisotropic parameter and $\mathbf{n}$ is the direction of anisotropy. The electric and Hall currents develop additional components due to the anisotropy as,

$$(j_e)_{\text{aniso}} = j_e^{(0)} + \delta j_e^{(0)} + j_e^{(1)} + \delta j_e^{(1)}, \tag{69}$$

$$(j_H)_{\text{aniso}} = j_H^{(0)} + \delta j_H^{(0)} + j_H^{(1)} + \delta j_H^{(1)} + j_H^{(2)} + \delta j_H^{(2)}.$$

The forms of the additional components are described in detail in Ref. 5.

14.5. *Results and Observations*

To analyze the impact of time-dependence of the electromagnetic fields on the QCD medium response, we define the following ratios,

$$R_e = \frac{j_e^{(0)}}{ET} + \frac{j_e^{(1)}}{ET}, \qquad\qquad R_H = \frac{j_H^{(0)}}{EBT} + \frac{j_H^{(1)}}{EBT} + \frac{j_H^{(2)}}{EBT}.$$

For the case with anisotropy we have, $(R_e)_{aniso} = \frac{(j_e)_{aniso}}{ET}$ and $(R_H)_{aniso} = \frac{(j_H)_{aniso}}{EBT}$. In the limiting case of constant electromagnetic fields, the term

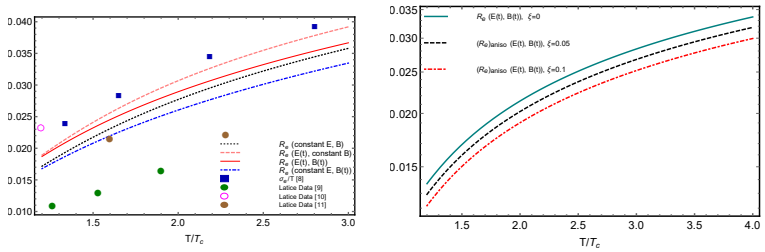


Fig. 35: The temperature dependence of R_e (left panel) for various choices of the external electromagnetic fields. For constant magnetic field case $eB = 0.03$ GeV^2 and we choose $\tau_B = 9$ fm, $\tau_E = 7$ fm for the time-varying cases. The effects of aniotropy and equation of state vs temperatre (right panel) for time dependent fields with $\tau_B = 9$ fm.

$j_e^{(0)}/(ET) = \sigma_e/T$ and the term $j_e^{(1)}/(ET)$ denotes the correction due to the time dependence of the electric field. In the similar way, $j_H^{(0)}$ describes the leading order term and the quantities $j_H^{(1)}$ and $j_H^{(2)}$ denote the corrections to the current density in the direction $(\hat{\mathbf{e}} \times \hat{\mathbf{b}})$. The strength of the time dependence of the fields is quantified in terms of decay time, τ_B, τ_E. We have depicted the effect of the inhomogeneity of time of the external electromagnetic fields on the temperature dependence of R_e in Fig. 1. The time dependence of the fields is seen to have a visible impact on the QCD medium response. For the case of a time-varying electric field and a constant magnetic field, the value of R_e is higher in comparison with the case of constant fields due to the additional contribution from $\dot{\mathbf{E}}$. The inclusion of time inhomogeneity of the magnetic field further introduces back current in the QGP medium. The same observation holds for R_H. In addition, we have observed that $j_e\hat{\mathbf{e}}$ and $j_H(\hat{\mathbf{e}} \times \hat{\mathbf{b}})$ decrease with an increase in momentum anisotropy of the medium. The additional components to current densities may play a vital role in the magnetohydrodynamical framework for the QCD medium in the collision experiments.

14.6. *Summary*

In summary, we have observed that the time dependent electromagnetic fields and momentum anisotropy of the medium play a significant role in the electric charge transport of the hot QCD medium.

15. Study of Electromagnetic Effect by Charged-dependent Directed Flow in Isobar Collisions at $\sqrt{s_{NN}} = 200$ GeV using STAR at RHIC

Dhananjaya Thakur (for the STAR collaboration)

In non-central heavy-ion collisions, it is predicted that an initial strong but transient magnetic field ($\sim 10^{18}$ Gauss) can be generated. The charge-dependent directed flow (v_1) can serve as the probe to detect this initial magnetic field. In addition, v_1 of several identified hadron species with different constituent quarks will help to disentangle the role of produced and transported quarks. In this proceedings, we present the measurements of v_1 for $\pi^{\pm}$, $K^{\pm}$, $p(\bar{p})$ in Ru+Ru and Zr+Zr collisions at $\sqrt{s_{NN}} = 200$ GeV as a function of transverse momentum, rapidity, and centrality. The difference of v_1 slope ($\Delta \mathrm{d}v_1/\mathrm{dy}$) between protons and anti-protons is observed and is studied as a function of centrality. While the contribution from transported quarks can give positive $\Delta \mathrm{d}v_1/\mathrm{dy}$, the electromagnetic field is predicted to give negative $\Delta \mathrm{d}v_1/\mathrm{dy}$. The significant negative $\Delta \mathrm{d}v_1/\mathrm{dy}$ of protons in peripheral collisions is consistent with the prediction from initial strong magnetic field in heavy-ion collisions.

15.1. *Introduction*

A collision of two ultra-relativistic nuclei forms a strongly interacting matter called the Quark-Gluon Plasma (QGP).[168] Anisotropic flow is quantified by Fourier coefficients of particle's distribution in azimuthal angle measured with respect to the reaction plane. The first coefficient of Fourier expansion is termed as directed flow (v_1),[169]

$$v_1 = \langle cos(\phi - \Psi_R) \rangle, \tag{70}$$

where ϕ denotes the azimuthal angle of an outgoing particle and Ψ_R is the orientation of the reaction plane defined by the beam axis and the impact parameter vector. The rapidity-odd component of directed flow v_1(y) has been argued to be sensitive to initial strong electromagnetic (EM) fields.[167]

In the early stages of the collisions, an ultra strong magnetic field is expected to be created (eB $\sim m_{\pi}^2$ at top Relativistic Heavy Ion Collider (RHIC) energy)[170] . This magnetic field is generated by the incoming spectator protons in the collision, and may be captured if the medium produced has finite electric conductivity. As the spectator protons recede from the collision zone the produced magnetic field decays with time. This time-varying magnetic field induces an electric field due to the Faraday effect. The Lorentz force results in an electric current perpendicular to expansion velocity of medium and magnetic field, akin to the classical Hall effect. The interplay of competing Faraday and Hall effects can influence the v_1. In other words, the EM fields are expected to drive positively-charged and negatively-charged particles in opposite ways, leading to a splitting of v_1(y)[167] .

The UrQMD calculations[172] at RHIC energies have shown that the transported protons and the spectator nucleons have the same sign of v_1 and hence they have a positive v_1 slope ($dv_1/dy > 0$) at the mid-rapidity. On the other hand, the produced protons and anti-protons can have negative v_1 ($dv_1/dy < 0$) slope due to contribution other than transported quarks, e.g. the tilted source[171] . This results in a positive splitting between protons and anti-protons [$\Delta dv_1/dy = dv_1/dy(p) - dv_1/dy(\bar{p}) > 0$]. Therefore, the transport will affect the splitting between any particle and anti-particle pairs having transported quark content, e.g splitting between $\pi^+(u\bar{d})$ and $\pi^-(d\bar{u})$, and also between $K^+(u\bar{s})$ and $K^-(\bar{u}s)$. Fi-

nally, the interplay between the EM field and transported quark effect determines the sign and magnitude of splitting between particle and anti-particle pairs.

15.2. *Method and Analysis*

This analysis uses Ru+Ru and Zr+Zr collisions at $\sqrt{s_{NN}}$ = 200 GeV, collected by Solenoidal Tracker at RHIC (STAR) during 2018. Details about the event cuts and track selections can be found in Ref[173] . In this analysis, the first order event plane angle is determined using Zero Degree Calorimeter (ZDC)[174] . The description of measuring v_1 using the ZDC event plane can be found in Ref[173] . The Time Projection Chamber (TPC)[175] was used for charged-particle tracking within pseudorapidity $|\eta| < 1$, with full 2π azimuthal coverage. After the vertex selection, we analysed about 1.7 billion Ru+Ru events and 1.8 billion Zr+Zr events. Centrality is defined from the number of charged particles detected by the TPC within $|\eta| <$ 0.5. The directed flow analyses were carried out on tracks that have transverse momenta, $p_T > 0.2$ GeV/c for $\pi^{\pm}$ and $K^{\pm}$, and $p_T > 0.4$ GeV/c for $p(\bar{p})$. The tracks should pass a requirement to be within 3 cm of distance of closest approach (DCA) to the primary vertex (V_z), and have at least 15 space points (N_{hits}) in the main TPC acceptance. The $\pi^{\pm}$, $K^{\pm}$, p and $\bar{p}$ are identified based on the truncated mean value of the track energy loss ($\langle dE/dx \rangle$) in the TPC and we select $|n\sigma| < 2$ ($n\sigma = \frac{1}{\sigma_R} ln(\langle dE/dx \rangle / \langle dE/dx \rangle_{[\pi/K/p]}$, σ_R is the $\langle dE/dx \rangle$ resolution). To ensure the purity of identified particles, we select particles with momentum smaller than 2 GeV/c for protons, and 1.6 GeV/c for pions and kaons. The time-of-flight detector (TOF)[176] was used to improve the particle identification and we select particles within mass-square (m^2) range, -0.01 $< m^2 <$ 0.1 ((GeV/c^2)^2) for pions, 0.2 $< m^2 <$ 0.35 ((GeV/c^2)^2) for kaons and 0.8 $< m^2 <$ 1.0 ((GeV/c^2)^2) for protons.

The systematic uncertainties of the v_1 measurements are calculated by varying DCA, V_z, N_{hits}, $n\sigma$ etc. within a reasonable maximum range. The absolute difference ($|\Delta_i|$) between default cut with the cut variation is taken as systematic uncertainty. In addition, the absolute difference between the $v_1(y)$ slopes between forward and backward rapidities is also considered as a source of systematic uncertainty. The final systematic error is the quadrature sum of the systematic errors from all the sources, which are calculated as $|\Delta_i|/\sqrt{12}$ assuming uniform probability distribution.

15.3. *Results*

Figure 36 presents $v_1(y)$ for protons and anti-protons in Au+Au collisions at $\sqrt{s_{NN}}$ = 27 and 200 GeV and isobar collisions at $\sqrt{s_{NN}}$ = 200 GeV in the centrality range of 50–80%. Linear fits within -0.8 $< y <$ 0.8 (solid lines) that passing through (0, 0) is used to extract the slope ($\Delta dv_1/dy$). We observe a significant negative slope of proton and antiproton difference in the peripheral collisions which is inline with the prediction of dominance of the Faraday/Coulomb effect over the Hall

and transported-quark effects, as transported quarks only provide positive contributions to the proton $\Delta dv_1/dy$ [172] . The extracted $\Delta dv_1/dy$ values for each particle species using the same linear-function fit are plotted as a function of centrality and is presented in Fig. 37 for $\pi^{\pm}$, $K^{\pm}$, p and $\bar{p}$ in Au+Au at $\sqrt{s_{NN}} = 27$ and 200 GeV and isobar collisions at $\sqrt{s_{NN}} = 200$ GeV.

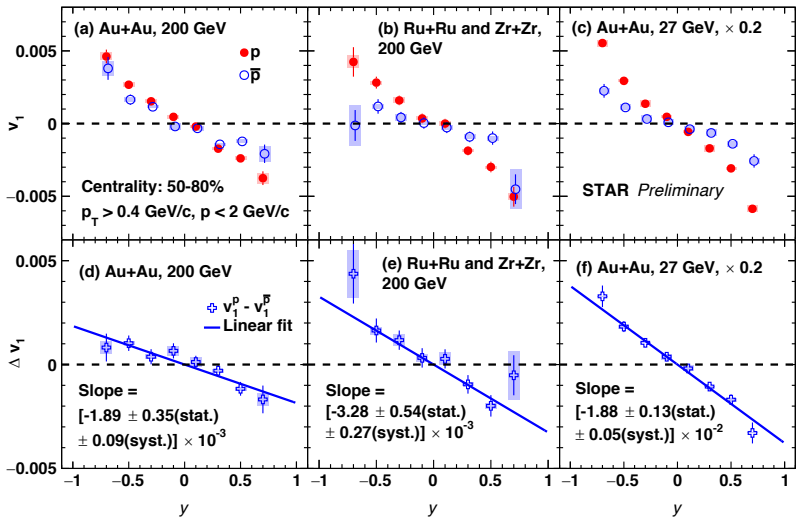


Fig. 36: Directed flow of protons and anti-protons and their difference ($v_1^p - v_1^{\bar{p}}$) as a function of rapidity for Au+Au collisions at $\sqrt{s_{NN}} = 27$ and 200 GeV, and Ru+Ru and Zr+Zr collisions at $\sqrt{s_{NN}} = 200$ GeV for 50-80 % centrality[165] . The systematic uncertainties are indicated with shaded bands and the slopes are obtained with linear fits (solid lines).

It is clear from Fig. 37 that $\Delta dv_1/dy$ for protons shows decreasing trend, i.e positive to negative when going from central to peripheral collisions. The electromagnetic effect is weak in central collisions due to the lack of spectator protons. Therefore, the transported-quark effect can contribute to the positive v_1 splitting. Towards the peripheral collisions the electromagnetic effect can be dominant and we see a sign change of $\Delta dv_1/dy$. The solid curve represented in the figure shows the quantitative calculation of electromagnetic-field contributions to the proton $\Delta dv_1/dy$ in Au+Au collisions at $\sqrt{s_{NN}} = 200$ GeV [166] . Similar decreasing trend of $\Delta dv_1/dy$ is also observed for K^+ and K^-, but less significant compared to protons. This could be due to the fact that kaons have lower mean transverse momentum ($\langle p_T \rangle$) than protons and hence weaker electromagnetic field effects[166] .

The v_1 splitting between π^+ and π^- is consistent with zero within uncertainty at $\sqrt{s_{NN}} = 200$ GeV. The transported quarks should give negative $\Delta dv_1/dy$ between

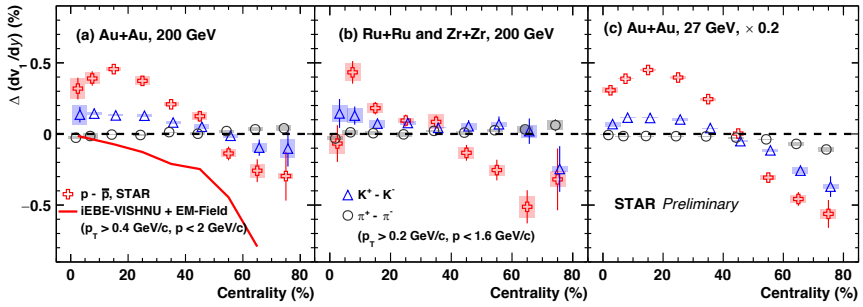


Fig. 37: Slope difference ($\Delta dv_1/dy$) between positively and negatively charged pions, kaons and protons as a function of centrality for Au+Au collisions at $\sqrt{s_{NN}}$ = 27 and 200 GeV and isobar collisions at $\sqrt{s_{NN}}$ = 200 [165] . The systematic uncertainties are represented by shaded bands. The solid line is the electromagnetic field prediction for v_1 splitting between protons and anti-protons in Au+Au collisions at $\sqrt{s_{NN}}$ = 200 GeV [166] .

π^+ and π^-. Also, the electromagnetic effect gives negative $\Delta dv_1/dy$. Since π^+ and π^- numbers are almost symmetric at the top RHIC energy, the transported-quark effect is negligible. The electromagnetic effect can be diluted from neutral resonance decay. At $\sqrt{s_{NN}}$ = 27 GeV, we can see a small negative $\Delta dv_1/dy$ at peripheral collisions which can have both transported-quark and electromagnetic effect.

15.4. *Summary and Outlook*

The study of charged-dependent v_1 can provide information about transported quark and electromagnetic (Hall, Faraday, and Coulomb etc.) effects in heavy-ion collisions. We have presented the v_1 measurements of $\pi^{\pm}$, $K^{\pm}$, p and $\bar{p}$ for Au+Au collisions at $\sqrt{s_{NN}}$ = 27 and 200 GeV, and Ru+Ru and Zr+Zr collisions at $\sqrt{s_{NN}}$ = 200 GeV. The splitting between protons and anti-protons changes sign from positive value in central collisions to negative value in peripheral collisions. The positive value of $\Delta dv_1/dy$ in central collisions could be accommodated by transported quark contribution where as significant negative $\Delta dv_1/dy$ in peripheral collisions is consistent with expectation from dominance of the Faraday/Coulomb effects over Hall effect.

16. Suppressed Charmonium production in *pp* Collisions at the LHC Energies

Captain R. Singh, Suman Deb, Raghunath Sahoo, and Jan-e Alam

We investigate the possibility of formation of a deconfined QCD matter in *pp* collisions at LHC. A 1+1D viscous hydrodynamical expansion is considered to study the evolution of the medium formed in *pp* collisions. Here we present a theoretical study to investigate the

presence of a QGP-like medium through charmonium suppression in such a small system. Our theoretical prediction for the normalized J/ψ yield as a function of normalized multiplicity agrees well with ALICE data at mid-rapidity.

16.1. *Introduction*

High energy heavy-ion collisions offer an opportunity to explore the properties of hot and dense thermalized and deconfined QCD matter known as Quark-Gluon Plasma (QGP), considering no QGP-like medium formation in proton-proton (pp) collisions. Therefore, pp collisions are usually considered as benchmark for investigating the existence of such a medium in the heavy-ion (AA) collisions. Nevertheless, what if ultra-relativistic pp collisions start showing similar behaviour like AA. Recent experimental findings for pp collisions at $\sqrt{s} = 7$ & 13 TeV have provided some hints towards the existence of QGP-like medium. More precisely, collective phenomena and strangeness enhancement observed in ultra-relativistic pp collisions at the LHC energies press to retrospect small systems more comprehensively.[68,177] However, investigating such an exotic medium in these collisions is challenging, and the reasons are obvious from the physics perspective. Due to its unique features, quarkonium suppression is proposed as one of the important probes to look for the existence of a QGP-like medium in the heavy-ion collision. In this work Unified Model of Quarkonia Suppression (UMQS) is used to study the multiplicity ($dN_{ch}/d\eta$) dependent suppression of J/ψ and ψ(2S) in pp collisions at mid-rapidity.[178,179]

16.2. *UMQS Model Formulation: in brief*

The UMQS formulation includes the in-medium dissociation and regeneration effects like color screening, gluonic dissociation, collisional damping, and regeneration due to the correlated $c\bar{c}$ pair.[178] It finally estimates the multiplicity ($dN_{ch}/d\eta$) dependent net charmonium yield in terms of survival probability, S_P. Charmonium kinematics in the QGP medium is governed by medium expansion rate, which can be obtained using hydrodynamics. To apply hydrodynamical evolution on a medium local thermalization is a necessary and sufficient condition. Therefore it is a must to check whether thermalization is achieved in pp collisions or not. The initial temperature (T_0) obtained for pp collisions at all the multiplicities is larger than the critical temperature (T_c) required for QCD phase transition.[178] Based on this motivation, we assume that the system formed in pp collisions achieve thermalization and find its consequences by contrasting the theoretical results with experimental data. The assumption of thermalization permits us to apply hydrodynamics to study its evolution. However, it is somewhat hard to estimate the initial thermalization time precisely. The attainment of thermalization in a classical system depends on two crucial factors: (i) the number of particles present in the system and (ii) the strength of interaction between the particles. A weakly interacting system with a high number density will take a long time to thermalize. On the other hand, a strongly interacting system with a small number of particles may quickly

thermalize. However, from the first principle, it is impossible to state how many partons are required to produce a system which will thermalize within a time scale set by strong interaction $\approx 1/\Lambda_{QCD}$. In the absence of the first principle-based estimate of thermalization time of a strongly interacting partonic system and based on the above mentioned approach, we assume the initial thermalization time $\tau_0 = 0.1$ fm. Further, we obtained the temperature cooling rate using second-order viscous hydrodynamical equations under 1+1D evolution:

$$\frac{dT}{d\tau} = -\frac{T}{3\tau} + \frac{T^{-3}\phi}{12a\tau} \tag{71}$$

$$\frac{d\phi}{d\tau} = -\frac{2aT\phi}{3b} - \frac{1}{2}\phi\left[\frac{1}{\tau} - \frac{5}{\tau}\frac{dT}{d\tau}\right] + \frac{8aT^4}{9\tau} \tag{72}$$

The ϕ appearing in Eqs. 71 and 72 is given by $\phi = 4\eta/(3\tau)$. We have taken the initial value of ϕ that is $\phi(\tau_0) = \phi_0 = s_0/(3\pi\tau_0)$ by using the relation $\eta/s = 1/4\pi$. The value of $\phi_0 = 0.1709\ GeV^4$ obtained, is comparable with $\phi_0 \sim 2p_0$ and $\phi_0 < 4p_0$ as discussed in Ref.[182] It may be noted that we have taken $\eta/s = 1/4\pi$ to set only the initial condition for ϕ because its initial value is not known from QCD. Moreover, apart from η, the value of τ_0 (which is not known precisely) is also required to get ϕ_0, therefore, we have taken $\eta/s = 1/4\pi$ to estimate the initial value of ϕ. The cooling rate obtained using second-order viscous hydrodynamical equations is shown in Fig.38. It shows including the viscosity of the medium cooling becomes slower and that can lead to the particles suppression if $T > T_c = 155$ MeV. In

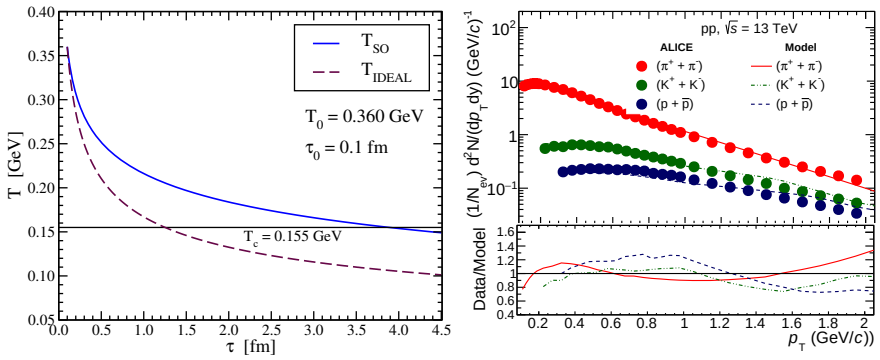


Fig. 38: **Left:** The temperature cooling rate as function of proper time (τ) is shown here for ideal (T_{IDEAL}) and second-order viscous hydrodynamics (T_{SO}). **Right:** The p_T-spectra of identified particles obtained from hydrodynamical study are compared with experimental data.

order to validate our theoretical prediction, we produced the identified soft-hadron spectra using 1+1D second-order viscous hydrodynamics. Fig. 38 Right shows, that

proposed hydro-model quantitatively explains the transverse momenta (p_T) spectra of identified particle obtained from experiments.[183] The temperature (T) versus proper time (τ) shown in Fig.38 depicts that medium created in pp collisions cool down below $T < T_c$ at $\tau = 3 \sim 4$ fm. In this time scale, the charmonium suppression is expected, as the kinematics of quarkonia gets modified in the presence of the QGP medium. The transport equation that governs the charmonium kinematics in the QGP medium is given as;

$$\frac{dN_{J/\psi}}{d\tau} = \Gamma_{F,nl} N_c \; N_{\bar{c}} \; [V(\tau)]^{-1} - \Gamma_{D,nl} N_{J/\psi} \tag{73}$$

here, $\Gamma_{F,nl}$ and $\Gamma_{D,nl}$ represent the formation and dissociation of the $c\bar{c}$ bound states, respectively. The solution of this transport equation gives the net number of charmonia by considering gluonic dissociation, collision damping, and regeneration mechanisms. Color screening is another mechanism that does not allow charmonium to form if $T > T_D$, (here T_D is the dissociation temperature of charmonia). Using this approach, we obtain the normalized J/ψ yield compared with experimental data and show that it is qualitatively explaining the normalized J/ψ yield plotted against the normalized multiplicity yield (see Fig. 39). Finally, charmonia suppression is measured in terms of the survival probability (S_P) of the resonance state propagating through deconfined QCD matter. Fig. 39 also shows that suppression of charmonium states increases with the multiplicity, and it further increases with increasing centre-of-mass energy from $\sqrt{s} = 5.02$ to 13 TeV.

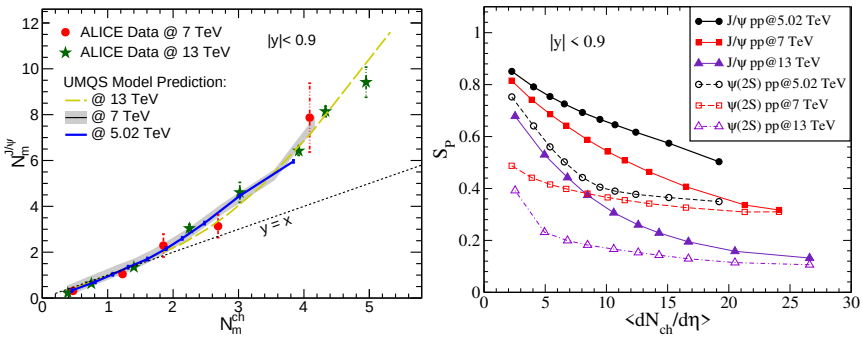


Fig. 39: **Left:** Normalized yield as a function of normalized multiplicity at mid-rapidity is compared with ALICE data corresponding to V0M selection. A prediction for the same at $\sqrt{s} = 5.02$ TeV is also shown.[178] **Right:** Model predictions for J/ψ and ψ(2S) suppression as a function of multiplicity corresponding to various pp collision energies.[178]

16.3. *Summary*

Our current study shows a QGP-like behaviour at all the multiplicity intervals in ultra-relativistic pp collisions at $\sqrt{s} = 5.02, 7$ & 13 TeV LHC energies. The formation of a QGP-like medium in such a small system requires a new baseline to analyze QGP effects in AA collisions at LHC energies.

- We have found that second-order temperature cooling enables effective suppression of charmonium at all the multiplicities.
- In our study, we obtained more suppression for $\psi(2S)$ than J/ψ and the effect of regeneration is also marginal for $\psi(2S)$. Therefore, higher resonances like $\psi(2S)$ could be a cleaner probe to investigate QGP in small systems.
- As the cold nuclear environment is absent in the pp collisions, any modification in the charmonium yield can be considered as a pure effect of a hot QCD medium.
- These observations challenge the previous findings on QGP existence, where most of the QGP signatures are measured considering pp as a baseline. Therefore, it requires comparative theoretical and experimental studies aiming to investigate a QGP-like medium in pp collisions.

17. Spatial Diffusion of Heavy Quarks in Magnetic Field

Sudipan De, Sarthak Satapathy, Jayanta Dey, Chitrasen Jena, Sabyasachi Ghosh

Heavy quarks are one of the most important tools to probe Quark Gluon Plasma (QGP) due to their large masses, which are significantly higher than the quantum chromodynamics (QCD) energy scale and the temperature at which QGP is created. In the recent years, off-central heavy ion collisions have gained a lot of attention owing to the possibility of the creation of strong magnetic fields of the order of 10^{18} Gauss at the Relativistic Heavy-Ion collider (RHIC) and $\sim 10^{19}$ Gauss at the Large Hadron Collider (LHC). In presence of this strong magnetic field, spatial diffusion coefficient of heavy quark splits into two components viz. transverse and longitudinal components. In the present work, we have estimated spatial diffusion of heavy quarks as a function of magnetic field and temperature.

17.1. *Introduction*

During the collisions of two nuclei at relativistic energies it is expected to form a hot and dense state of matter known as Quark Gluon Plasma (QGP) which is governed by light quarks and gluons.[184] Heavy quarks, namely charm (c) and bottom (b) quarks are considered one of the fine probes of quark gluon plasma (QGP). Due to the fact that their masses (M) are significantly larger than the QCD energy scale ($\Lambda_{\rm QCD}$) and the temperature (T) at which QGP is created i.e $M >> \Lambda_{\rm QCD}, T$. Unlike the light quarks they do not thermalize quickly and witness the entire evolution of the fireball. Currently, it is admitted that a very strong magnetic field is created at very early stage of heavy-ion collisions.[185,186] The estimated

values of the intensity of the strong magnetic field created at RHIC and LHC is of the order of 10^{18} to 10^{19} Gauss.[2] The effects of such a strong magnetic field is discussed in different cases such as jet quenching coefficient $\hat{q}$,[187] elliptic flow,[188] chiral magnetic effect[189] etc. The effect has also been studied to diffusion coefficients of charm quarks.[190,191] As heavy quarks produced early in the heavy-ion collisions their dynamics can be affected by such strong magnetic field. In this article we aim to study the longitudinal and transverse components of diffusion coefficients of heavy quarks in a QGP medium in the presence of a background magnetic field $\vec{B}$ in z-direction.

17.2. *Formulation*

Let us consider a background magnetic field $\vec{B} = B\ \hat{k}$ pointing in the z-direction which magnetizes a relativistic fluid. In presence of magnetic field anisotropic properties of the fluid is considered which leads to multi-component structure of the electrical conductivity tensor such as, σ_{xx}, $\sigma_{xy} = -\sigma_{yx}$ and σ_{zz}. In this article we obtained diffusion coefficient in two different approaches, one is classical based Relaxation Time Approximation (RTA) method and another is Quantum Mechanical (QM) approximation. According to Einstein's relation the spatial diffusion coefficient (D) can be expressed as a ratio of electrical conductivity (σ) and susceptibility (χ) of the medium. These become anisotropic in the presence of magnetic field thus taking a 3×3 matrix structure given by

$$D_{ij} = \frac{\sigma_{ij}}{\chi}, \quad i,j = x,y,z \tag{74}$$

where D_{ij} is the spatial diffusion matrix, σ_{ij} is the electrical conductivity matrix, and χ is the susceptibility. According to RTA approach we obtain

$$\sigma_{zz} = \sigma_{\parallel} = \frac{gq^2\beta}{3}\int \frac{d^3k}{(2\pi)^3}\frac{(k_z)^2}{\omega_k^2}\tau_c f\big[1-f\big] \tag{75}$$

$$\sigma_{xx} = \sigma_{yy} = \sigma_{\perp} = \frac{gq^2\beta}{3}\int \frac{d^3k}{(2\pi)^3}\frac{(k_{x,y})^2}{\omega_k^2}\frac{\tau_c}{1+\frac{\tau_c^2}{\tau_B^2}} f\big[1-f\big], \tag{76}$$

where, f represents the distribution function such as,

$$f = \begin{cases} \big[e^{\beta(\omega_k-\mu)}+1\big]^{-1}, & \text{for Fermions} \\ \big[e^{\beta\omega_k}-1\big]^{-1}, & \text{for Bosons} \end{cases}, \tag{77}$$

$\omega_k = \sqrt{\vec{k}^2+m^2}$ is the energy with momentum $\vec{k}$ and mass m, $\beta = T^{-1}$, where T is the temperature, μ is the chemical potential, q is the charge and τ_c is the relaxation time. Here, g is the degeneracy factor and $\tau_B = \frac{m}{qB}$ is the inverse of classical cyclotron frequency. σ_{zz} (or $\sigma_{\parallel}$) is the parallel component of the electrical conductivity i.e. parallel to the magnetic field and σ_{xx} (or $\sigma_{\perp}$) is the perpendicular component of the electrical conductivity. The absence of Landau quantization over energies in RTA expressions prompts us to call them as classical results. On the

other hand, on applying Landau quantization of energies and quantizing the phase space part of the momentum integral we obtain

$$\chi_{\rm QM} = \beta \sum_{n=0}^{\infty} (2-\delta_{n,0}) \frac{qB}{2\pi} \int_{-\infty}^{+\infty} \frac{dk_z}{2\pi}\ f(1-f). \tag{78}$$

$$\sigma_{\perp}^{\rm QM} = \frac{2q^2}{T} \sum_{n=0}^{\infty} (2-\delta_{n,0}) \frac{qB}{2\pi} \int_{-\infty}^{+\infty} \frac{dk_z}{2\pi} \frac{lqB}{\omega_l^2} \tau^{\perp} f(1-f) \tag{79}$$

$$\sigma_{\parallel}^{\rm QM} = \frac{2q^2}{T} \sum_{n=0}^{\infty} (2-\delta_{n,0}) \frac{qB}{2\pi} \int_{-\infty}^{+\infty} \frac{dk_z}{2\pi} \frac{k_z^2}{\omega_l^2} \tau^{\parallel} f(1-f), \tag{80}$$

where the superscript QM denotes quantum theoretical results, $\tau^{\parallel} = \tau_c$, $\tau^{\perp} = \frac{\tau_c}{1+\frac{\tau_c^2}{\tau_B^2}}$, τ_c is the relaxation time.

17.3. *Results*

The left figure of the upper panel of Fig. 40 shows the results of longitudinal diffusion as a function of temperature by plotting $2\pi TD_{zz}$ with T which basically shows how the heavy quarks can diffusively travel in a direction parallel to the background magnetic field. In this figure the solid lines are for the isotropic case calculated via RTA formalism for $\tau_c = 6\ fm$ and $eB = 0.2$ and 0.4 GeV^2. The dotted lines are the results of $2\pi TD_{zz}$ for QM case where Landau quantization were employed, thus providing an expression of spatial diffusion as a sum over Landau levels. The increasing trend of diffusion coefficient with temperature can be attributed to the fact that an increase in kinetic energy contributes to an increase in diffusion along the direction parallel to magnetic field. The right figure of the upper panel of Fig. 40 shows the results of longitudinal diffusion as a function of magnetic field by plotting $2\pi TD_{zz}$ with eB at two different temperatures 0.2 GeV and 0.4 GeV for both RTA and QM formalisms. At low magnetic field the RTA and QM results coincide with each other whereas at high magnetic fields we see a clear deviation of QM results from RTA results which implies the universal behaviour of spatial diffusion at low magnetic field. The longitudinal component of diffusion calculated via RTA formalism, does not depend on the magnetic field since along the direction of magnetic field the heavy quarks do not experience Lorentz force. Contrary to the RTA case, the QM results depend on the magnetic field. Here we see that for the QM case the diffusion increases with increasing magnetic field. To understand this we note that spatial diffusion is the ratio of electrical conductivity and static susceptibility. In the QM approach the Landau level summation appears in the expression of σ and χ due to which quantum effects come into play and thus we observe a deviation relative to RTA results. The left figure of the lower panel of Fig. 40 shows the results of perpendicular component of spatial diffusion coefficient as a function of temperature for two different magnetic field strength, $eB = 0.2$

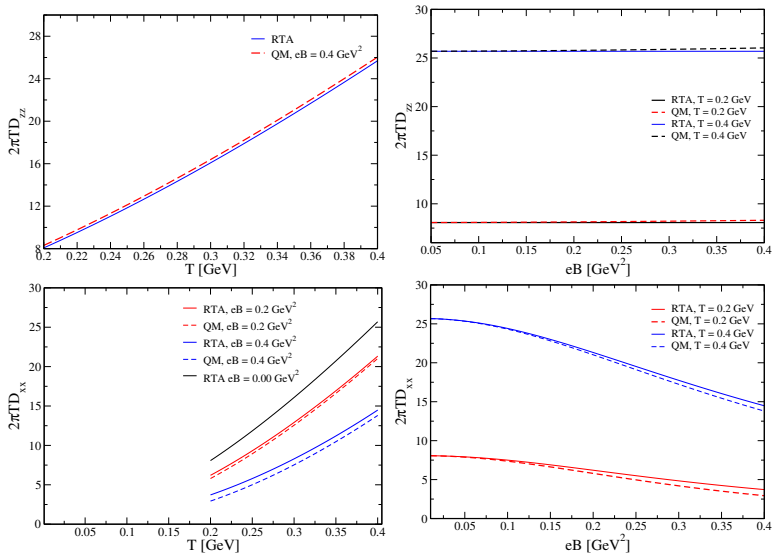


Fig. 40: Upper panel: solid line shows the result from RTA calculation and dotted line shows results from QM approximation. Lower Panel: Black solid line represents the RTA result without magnetic field. Solid and dotted lines represent the results from RTA and QM respectively. Different colors represent the results at different magnetic fields as well as at different temperatures.

GeV^2 and 0.4 GeV^2 along with the RTA results without presence of magnetic field. It is observed that in presence of strong magnetic field diffusion decreases. The right figure of the lower panel of Fig. 40 shows the behaviour of D_{xx} with magnetic field for different values of temperatures. At low magnetic field the RTA and QM results coincide implying the universal nature of diffusion at low magnetic field whereas at high magnetic field they are different due to Landau level summation present in QM expressions.

The aim of our present work is not the comparison between classical and quantum estimation of heavy quark diffusion at finite magnetic field, rather addressed them systemically step by step, which was missing in literature. However, for application point of view, they should be used in the weak and strong magnetic field domains respectively.

17.4. *Summary*

The spatial component of diffusion coefficient for heavy quarks was calculated in presence of strong background magnetic field using the well known Einstein relation. As diffusion coefficient becomes anisotropic in presence of magnetic field, both parallel and perpendicular components of diffusion coefficient were obtained.

It is found that diffusion coefficient increases with increasing temperature both for parallel and perpendicular components. This behaviour can be attributed to the increase in kinetic energy of heavy quarks with increasing temperature. The difference between RTA and QM results is higher at higher magnetic field due to Landau level summation present in QM expression. Parallel component of diffusion coefficient is independent of magnetic field in case of RTA formulation contrary to the results obtained in QM formalism. Perpendicular component of diffusion coefficient decreases with increasing magnetic field both for RTA and QM. In summary, different behaviour of parallel and perpendicular component of spatial diffusion coefficient of heavy quarks in presence of strong initial magnetic field may lead us to interesting directions in recent future.

18. Weak Interaction driven bulk viscosity of hot and dense plasma

Sreemoyee Sarkar

We present the formalism of bulk viscosity coefficient of baryonic matter in presence of trapped neutrinos. In neutron star at temperature $T \sim 5$ MeV, neutrino mean free path remains small in comparison to the dimension of the star which results in non-vanishing neutrino chemical potential. This directs modified URCA process for the beta equilibration rate to produce maximum bulk viscosity at temperature larger than the neutrino-trapped temperature. The calculation has been performed considering beta non-equilibration of modified URCA process. The resonant behaviour of the bulk viscosity is dependent on the particle interaction rate and thermodynamic susceptibilities of the medium. The susceptibilities have been calculated considering free Fermi gas equation of state of hadrons. The bulk viscosity coefficient attains its maximum at $T \sim 9$ MeV. The bulk-viscous dissipation time scale for compression-rarefaction oscillation is found out to be 50 millisecond. These results imply the relevance of the formalism in high temperature, highly dense medium produced in binary neutron star merger.

18.1. *Introduction*

Time scale for damping of stellar vibrations of neutron stars and maximum rotation rate of millisecond pulsars are greatly influenced by the bulk viscosity of the stars. For a vibrating star density changes due to vibrational and rotational instabilities and these change the concentrations of different species mainly through URCA and modified URCA (MURCA) processes. This results in dissipation and the dissipation becomes maximum once the rate of the above microscopic reactions become comparable to the rate of the oscillation of the chemical potential.

Over the last decade the theory of bulk viscosity coefficient (ξ) has been studied in the field of heavy ion collision experiment[192,193] as well as in the isolated neutron stars and in the quark stars.[194–198] In Ref.[199] it has been shown that the value of average contribution of ξ in heavy ion collision experiment is comparable to that of in binary neutron star (BNS) merger. Recently, authors in Ref.[200] have revealed the fact that ξ, driven by MURCA process in the neutrino transparent regime gives rise to dissipation time scale of the order of survival time period (millisecond) of BNS

merger. In connection to this the bulk viscosity coefficient due to URCA process in the neutrino trapped domain has been evaluated in Ref.[201] All these current findings motivate us to estimate the bulk viscous dissipation due to MURCA process in the high temperature and high density plasma in presence of trapped neutrinos relevant for BNS merger.

18.2. *Bulk Viscosity of dense matter with trapped neutrinos*

In this paper we consider a system of baryonic matter consists of neutrons, protons, electrons, neutrinos. In neutron star due to rotational and vibrational motion fluid elements undergo continuous compression and rarefaction and this leads to bulk viscous dissipation. We consider the MURCA as beta equilibration process which contributes maximum in bulk viscosity at high temperature in comparison to the URCA process.[197] The MURCA processes are $n+N \leftrightarrow N+p+e+\bar{\nu}$, $N+p+e \leftrightarrow N+n+\nu_e$. In chemical equilibrium the forward and backward reactions occur at the same rate and the sum of the incoming chemical potentials remain the same as that of the backward reaction. Volumetric fluid element oscillations give rise to non-equilibrium scenario when equality of forward and backward chemical equilibration does not happen.

In a neutron star with large temperature, typically $T \sim 5$ MeV the mean free path of neutrinos remain small and they remain trapped in side the star and hence non-zero chemical potential. Subtracting the final state chemical potential from the initial state the fluctuation in chemical potential is $\mu_\Delta = \sum_i \mu_i - \sum_f \mu_f \neq 0$. The time derivative of μ_Δ gives a linear equation in μ_Δ, $\frac{d\mu_\Delta}{dt} = C\omega\frac{\delta n_\star}{\bar{n}_\star}cos(\omega t) + Bn_\star\frac{dx}{dt}$. $\delta n_\star$ is the deviation of baryon density and δx is the deviation of the baryon density fraction from the equilibrium value. C is defined as the beta non-equilibration baryon density susceptibility and B is the beta non-equilibration proton fraction susceptibility, ω is the oscillation frequency, $n_\star$ is the equilibrium baryon density. Susceptibilities are defined as, $C \equiv n_* \left.\frac{\partial\mu_\Delta}{\partial n_*}\right|_x$, $B \equiv \frac{1}{n_*}\left.\frac{\partial\mu_\Delta}{\partial x}\right|_{n_*}$.

The differential equation for the chemical fluctuation can be written as

$$\frac{dA}{d\phi} = d\cos(\phi) + \frac{B\Gamma^{\leftrightarrow}}{\omega T}. \tag{81}$$

where, $\phi = \omega t$, $A = \mu_\Delta/T$, the prefactors $d \equiv \frac{C}{T}\frac{\delta n_\star}{n_\star}$, $f \equiv \frac{B\tilde{\Gamma}T^6}{\omega}$, $\Gamma^{\leftrightarrow} = n^\star\frac{\partial x}{\partial t}$. The details of $\Gamma^{\leftrightarrow}$ we present later in this paper. The bulk viscosity of a given system is defined to be the response of the system to an oscillating compression and rarefaction of the medium. The energy dissipation rate per volume in the fluid due to oscillation is $\frac{d\epsilon}{dt} = \xi(\vec{\nabla}.\vec{v})^2$, v is the local fluid velocity of the conserved baryon density. In the hydrodynamic limit after averaging the energy dissipation rate per volume over one time period the bulk viscosity can be expressed as,

$$\xi = \frac{TC}{\pi\omega B}\frac{\bar{n}_\star}{\delta n_\star}\int_0^{2\pi} A(\phi)cos(\phi)d\phi \tag{82}$$

The detailed calculation of obtaining ζ can be found in Ref.[197] $A(\phi)$ can be evaluated by solving Eq.(81).

Now, we present the microphysics of re-equilibration rate $\Gamma^{\leftrightarrow} \equiv \Gamma^{\rightarrow} - \Gamma^{\leftarrow}$, where, $\Gamma^{\rightarrow}$ is the rate of the forward and $\Gamma^{\leftarrow}$ is the backward reaction. For MURCA process,[202]

$$\Gamma^{\rightarrow} - \Gamma^{\leftarrow} = \int \frac{d^3p_n}{(2\pi)^3}\frac{d^3p_N}{(2\pi)^3}\frac{d^3p'_N}{(2\pi)^3}\frac{d^3p_p}{(2\pi)^3}\frac{d^3p_e}{(2\pi)^3}\frac{d^3p_{\nu_e}}{(2\pi)^3} \tag{83}$$

$$(2\pi)^4|\mathcal{M}^2_{fi}|[\delta^4(p_n + p_N - p'_N - p_e - p_{\nu_e})]\mathcal{P} \tag{84}$$

The scattering matrix element $\mathcal{M}_{fi}$ is given in Ref.[203] $\mathcal{P}$ is the phase space factor and I is the energy integral.

$$\mathcal{P} = [f_N f_p f_e f_{\bar{\nu}_e}(1-f_N)(1-f_n) - f_N f_n(1-f_N)(1-f_p)(1-f_e)(1-f_{\bar{\nu}_e})] \tag{85}$$

After performing angular integration we obtain,

$$\Gamma^{\rightarrow} - \Gamma^{\leftarrow} = \mathcal{C}\,(I_4 - I_5(\nu) - I_6(\nu)) \tag{86}$$

where, I_4, I_5 and I_6 are given below,[196]

$$I_4 - I_5(\nu) = \frac{1}{4!(1+e^{-x_{\bar{\nu}_e}+\frac{\mu_\nu}{T}})}\frac{1}{1+e^{(x_{\bar{\nu}_e}+\frac{\delta\mu}{T})}}\left[(x_{\bar{\nu}_e}+\frac{\delta\mu}{T})^4 + 10\pi^2(x_{\bar{\nu}_e}+\frac{\delta\mu}{T})^2 + 9\pi^4\right] \tag{87}$$

$$I_6(\nu) = \frac{1}{4!(1+e^{x_{\bar{\nu}_e}-\frac{\mu_\nu}{T}})}\frac{1}{1+e^{(x_{\bar{\nu}_e}+\delta\mu/T)}}\left[(x_{\bar{\nu}_e}+\frac{\delta\mu}{T})^4 + 10\pi^2(x_{\bar{\nu}_e}+\frac{\delta\mu}{T})^2 + 9\pi^4\right] \tag{88}$$

We write $x_i = \beta(E_i - \mu_i)$,$i = n, N, p, e$ and $x_{\nu_e} = \beta(E_{\nu_e} - \mu_{\nu_e})$ for neutrinos and $x_{\nu_e} = \beta(E_\nu + \mu_{\nu_e})$ for anti-neutrinos. Now, after evaluating the beta equilibration rate, we solve the integro-differential Eq.(81) to obtain $\mathcal{A}$. Inserting $\mathcal{A}$ in Eq.(82) we obtain the final expression for ξ.

18.3. *Result*

To quantify the amount of dissipation due to bulk viscosity in the medium we first estimate the susceptibilities of the medium. We compute the susceptibilities in free Fermi gas model of neutron star. In this model the system is made up of noninteracting neutrons, protons and electrons.[204] We calculate the susceptibilities considering beta equilibrium and charge neutrality condition to obtain , $B = \frac{4m_N^2}{3(3\pi^2)^{\frac{1}{3}}n^{\frac{4}{3}}}$ and $C = \frac{(3\pi^2 n)^{\frac{2}{3}}}{6m_N}$. This has been obtained after expanding in the powers of n_B/m_N^3 (n_B the total baryon density, m_N mass of neutron). In the left panel of Fig. (41) we present the density variation of B and C in the medium at zero temperature. C increases with density whereas B decreases with density. From the plot it is evident that the variation of C with density is much prominent in contrast to the variation of B with density. From the right panel of Fig.(41) the density dependence of ξ can be observed. Calculation of ξ reveals that interaction rate has very little

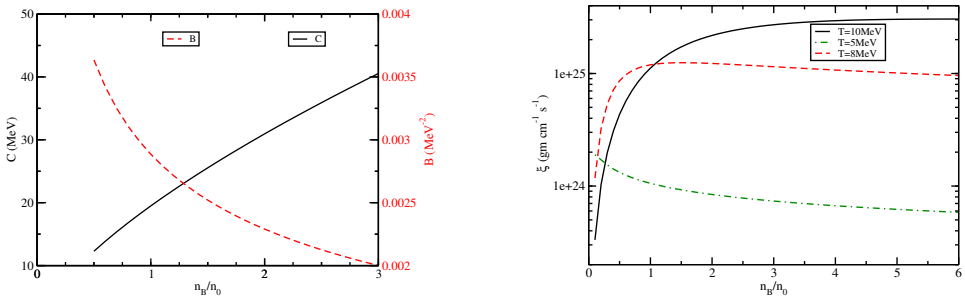


Fig. 41: Left: Density variation of susceptibilities. Right: Variation of ξ with density for different temperatures for neutrino-trapped matter

density dependence whereas the susceptibilities are density dependent only. Hence, the nature of the ξ plots with density is equivalent to the combined nature of both B and C. In Fig.(42) we present the temperature dependence of the bulk viscosity coefficient. In the left panel of Fig.(42) temperature dependence of ξ in neutrino transparent matter has been presented. The plots are for different baryonic densities $n_B = n_0$, $2n_0$, $3n_0$. In the right panel we plot the same for neutrino-trapped matter. From both the plots it can be seen that bulk viscosity shows resonant behaviour and the maximum of the curve appears at different temperatures. For the neutrino transparent medium the maximum appears at $T \sim$ 4MeV and for the neutrino trapped matter this happens at $T \sim$ 9MeV. From both the plots one can infer that incorporating neutrino in the interaction rate changes the position of the maximum of the curves but does not change the maxima of the curve. In the same plot with change in density the maxima of the curve increases since the height of the maxima is dependent on equation of state. For both temperature and density dependent plots we consider the frequency of density oscillation as 8.4 kHz. The dissipation time scale is calculated considering $\tau = K n_B t_{dns}^2/(36\pi^2 \xi_{max})$, $\tau \sim 50$ ms if we consider K is the nuclear compressibility ~ 250 MeV, $t_{dns} \sim 1/\omega \sim 1ms$ and ξ_{max} is the maximum of the bulk viscosity.

18.4. *Discussion*

In this paper we have computed bulk viscosity coefficient of neutrino trapped baryonic matter in high temperature high density plasma. For the neutron stars when the temperature is high enough $T \sim 5$ MeV mean free path of neutrinos remain small in comparison to the radius of the neutron star. Hence, we incorporate neutrinos in the medium along with neutrons, protons and electrons. Bulk viscosity coefficient is significantly dependent upon the underlying equation of state of the medium. We have not considered neutrinos in the equation of state. Apart from equation of state the viscosity coefficient also requires the rate of interaction of constituent particles in the medium. We have calculated the phase space of interaction

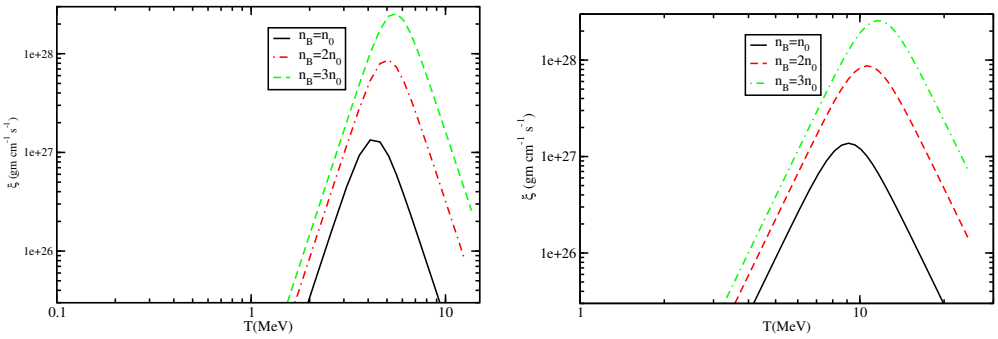


Fig. 42: Left: Temperature variation of bulk viscosity for various density for neutrino-transparent matter. Right: Temperature variation of bulk viscosity for various density for neutrino-trapped matter

rate for the MURCA process considering neutrinos in the medium. The calculation considers explicit beta non-equilibration and does not consider the small amplitude oscillation approximation. The resonant behaviour of the bulk viscosity with temperature has its maximum at $T \sim 9$ MeV and the time scale during which dissipation remains effective is found out to be $\tau \sim 50$ ms. These two indicate that neutrino trapped MURCA process could become a possible reaction for bulk viscous dissipation in BNS merger since the maximum temperature attained in BNS merger is of the order of $T \sim 10$ MeV and survival time period of the merged object is millisecond. We will report more realistic calculation of bulk viscous dissipation in BNS merger soon with a comparative study of ξ in heavy ion collision and BNS merger.

19. Study of jet fragmentation functions at RHIC and LHC energies using the JETSCAPE framework

Vaishnavi Desai

Jet-medium interactions in the Quark-Gluon Plasma (QGP) created in high-energy heavy-ion collisions not only reduces the total energy of the reconstructed jets but also change the energy and momentum distributions among the jet constituents. This work focuses on the modification of jet fragmentation function in relativistic heavy-ion collisions. Using the JETSCAPE framework, events produced in Au-Au collisions at $\sqrt{s_{NN}}$ = 200 GeV and Pb-Pb collisions at $\sqrt{s_{NN}}$ = 5.02 TeV are investigated to explore the dependence of modifications based on centrality and in combination with different energy loss modules such as MATTER and LBT for partons with high and low virtuality respectively. The JETSCAPE framework is a modular and versatile Monte-Carlo event generation tool for the simulation of high energy nuclear collisions. Jet fragmentation function results based on MATTER and LBT indicate medium-induced modifications in heavy-ion collisions.

19.1. *Introduction*

It is now widely accepted that jet quenching is a multi-stage phenomenon.[205–207] Simulations of high energy heavy-ion collisions requires a unified framework that implements all stages of heavy ion collisions namely: initial state hard scattering, expansion of QGP, hadronization as well as the production of hard partons, their propagation, interaction with the dense medium and fragmentation into jets. To compare with high-statistics, event-by-event experimental data, requires a modular and extendable event generator, with state-of-the-art components modeling each aspect of the collision. The Jet Energy-loss Tomography with a Statistically and Computationally Advanced Program Envelope (JETSCAPE)[208,209] is such a framework which is used in this work to study jet fragmentation function.

Pb-Pb and pp data at $\sqrt{s_{NN}} = 5.02$ TeV recorded by the ATLAS collaboration[210] and Au-Au data at $\sqrt{s_{NN}} = 200$ GeV recorded by the STAR collaboration[210] are used to compare with the studies of jet fragmentation function. Centrality dependent comparisons between different energy loss modules, Modular All Twist Transverse-scattering Elastic-drag and Radiation (MATTER)[210] and Linear Boltzmann Transport (LBT)[139,211] are carried out to explore the effect of each approach in the full history of parton evolution in heavy-ion collisions.

19.2. *Multi-stage Jet Evolution in JETSCAPE*

Simulation of jet events in Pb-Pb and Au-Au are performed within JETSCAPE (JS) framework. Initial hard partons generated by PYTHIA 8[139] are fed into MATTER for modeling high virtuality evolution, $Q^2 >> \sqrt{\hat{q}E}$, and propogated with a virtuality-ordered splittings in the medium. If the virtuality of a given parton drops below a specified separation scale, Q_0 , the low-virtuality energy loss modules, one of the LBT, MARTINI,[214] or AdS/CFT[215] take the parton over for time-ordered evolution. Switching between different energy loss modules is done independently for each parton. The separation scale Q_0 is set to 2 GeV. Colourless hadronization is performed by the Lund String Model as implemented in PYTHIA 8. The soft products in Au-Au collisions is generated using fluctuating TRENTO[138] initial conditions evolved hydrodynamically using the (3+1)D MUSIC[139,141,142] viscous hydrodynamic module.

19.3. *Jet Fragmentation Function*

The longitudinal momentum distribution of charged particles inside a reconstructed jets is calculated using the jet fragmentation function. It is measured as a function of both the charged-particle transverse momentum, p_{T} , and $z = \frac{p_{\mathrm{T}}^{\mathrm{ch}}}{p_{\mathrm{T}}^{\mathrm{jet}}}$ is the transverse momentum fraction between the charged particle and the jet. The fragmentation function is calculated as

$$D(z) = \frac{1}{N_{\mathrm{jet}}} \frac{dN_{\mathrm{ch}}}{dz} \tag{89}$$

and

$$D(p_T) = \frac{1}{N_{\rm jet}} \frac{dN_{\rm ch}}{dp_T} \tag{90}$$

where $N_{\rm ch}$ is the number of charged particles inside jets, $N_{\rm jet}$ is the number of jets under consideration. D(z) and D(p_T) distributions are closely related to each other, differing, primarily, in the normalization by $p_{\rm T}^{\rm jet}$ in the definition of z. Therefore, a comparison of the modifications of the fragmentation functions as a function of $p_{\rm T}^{\rm jet}$ can show whether the size of modifications scales with charged-particle z or with p_T. The former would be expected for fragmentation effects, and the latter might indicate some scale in the QGP.

19.4. *Results and Discussion*

In this work, JETSCAPE results based on energy loss modules MATTER and LBT are discussed. In order to determine the centrality dependence of ratio of fragmentation function on p_T^{jet}, the fragmentation functions from three p_T^{jet} intervals are compared. Fig.43 (top panel) shows the ratio of jet fragmentation functions for 40-

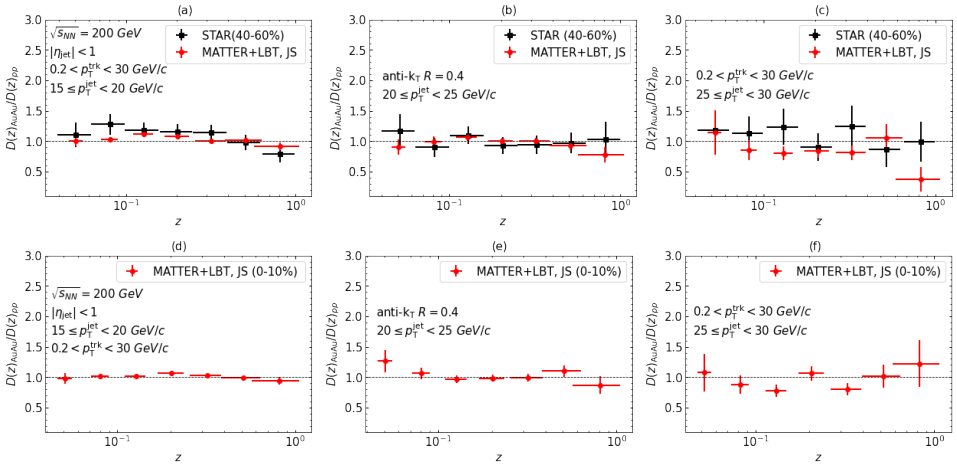


Fig. 43: (top panel) Shows the ratio of jet fragmentation function between 40-60% central Au-Au collisions for three p_T^{jet} ranges for JETSCAPE calculations compared with STAR experimental data.[208] (bottom panel) Shows the ratio of jet fragmentation function between 0-10% central Au-Au collisions for three p_T^{jet} ranges for JETSCAPE calculations.

60% Au-Au collisions to those in pp collisions. These calculations are extended to the most central 0-10% Au-Au collisions as shown in Fig. 43 (bottom panel). The JETSCAPE results are consistent with STAR experimental data for mid-central

collisions at 40-60% as shown in Fig. 43 (a) and (b). In Fig. 43(c), MATTER + LBT under predicts the experimental data. In Fig. 43(f), for 0-10% centrality class, MATTER + LBT shows marginal suppression at low z, the ratio is close to unity at intermediate z and small enhancement at high z values. Fragmentation function shows no modifications in Au-Au collisions at 0-10% and 40-60% centrality classes for $15 \leq p_{\mathrm{T}}^{\mathrm{jet}} < 20$ GeV and $20 \leq p_{\mathrm{T}}^{\mathrm{jet}} < 25$ GeV as seen from Fig. 43 (a),(b),(d) and (e). Fig. 44 shows the ratio of the jet fragmentation function as a function of z and p_T for Pb-Pb and pp collisions at 0-10% (top panel) and 30-40% (bottom panel) centrality classes respectively. In Fig. 44(a), no apparent modification of fragmentation function is seen. This could be attributed to lack of recoils in MATTER + LBT. In Fig. 44(b), JS results are in agreement with ATLAS data for $p_T > 10$ GeV, this indicates that the size of modification scales with p_T, while it exhibits much smaller dependence on D(z) ratio. Enhancement at high p_T region suggests re-distribution of energy inside the jet cone. In Fig. 44(c), at low-z region, JS under predicts the data whereas JS results are consistent in intermediate z region. In high z-region, JS results are not consistent, partly due to statistical fluctuations and uncertainty. In Fig. 44(d), JS results shows consistency with the ATLAS data at intermediate to high p_T region.

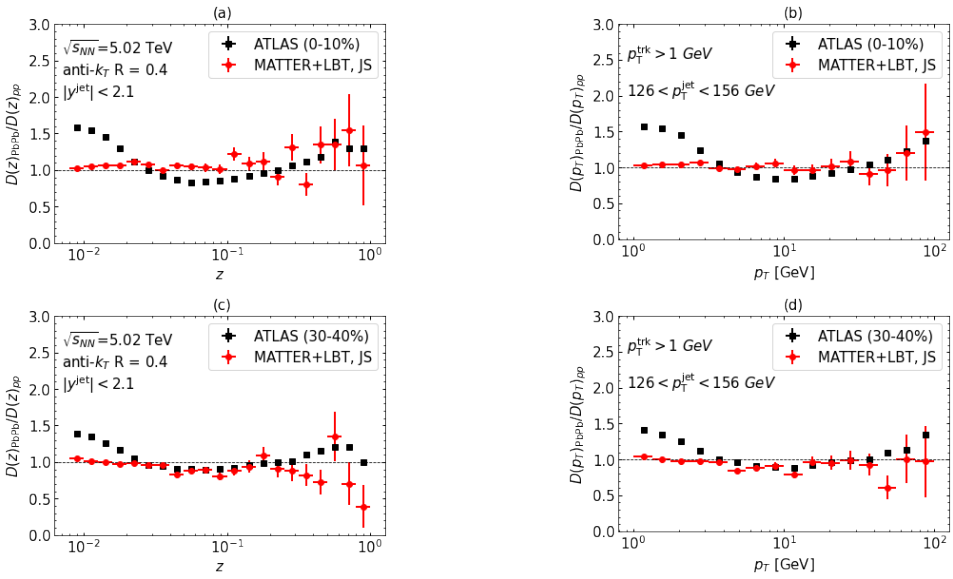


Fig. 44: The jet fragmentation distribution ratio of Pb-Pb to pp measured using the JS with MATTER + LBT at 0-10% centrality (top panel) and 30-40% centrality (bottom panel) compared with the ATLAS experimental data.[207]

20. First-order stable and causal hydrodynamics from kinetic theory

Rajesh Biswas

We derived a stable and causal relativistic first-order hydrodynamics from the relativistic Boltzmann equation. General hydrodynamic frame are introduced to incorporate the arbitrariness of hydrodynamics fields. The system interactions are included by momentum-dependent relaxation time in the relativistic Boltzmann equation. The hold the causality and stability of the first-order hydrodynamics, the system interactions play a crucial role along with the general frame.

20.1. *Introduction*

Relativistic Hydrodynamics is an effective theory; it has been proved to be reasonably successful in describing various systems' collective (long wavelength) behavior ranging from relativistic heavy-ion collision to condensed matter system. Relativistic hydrodynamical theory can be expressed as the gradient expansion of the hydrodynamic variable around the local equilibrium state. The theory with zeroth-order gradients is called ideal hydrodynamics, and with first-order gradients is called first-order hydrodynamics, and so on. Relativistic Navier-Stokes equations show superluminal signal propagation as well as instability.[216,217] The second-order hydrodynamic theory is introduced to resolve the stability and causality problem of NS equations.[218,219] Recently, the solution to the stability and causality of first-order hydrodynamics have proposed by Bemfica, Disconzi, Noronha, and Kovtun (BDNK) theory[52,57,58] by introducing a general hydrodynamic frame.

Here we derive a first-order stable and causal theory from the underlying microscopic kinetic theory for a general frame or general matching condition. We have calculated the transport coefficients that appeared in the constitutive relations. By studying the analysis of the modes in a linear regime, we show that microscopic interaction plays an important role along with general matching conditions to get a stable and causal, first-order theory. We have calculate the transport coefficients that appeared in the constitutive relations. By studying the modes analysis in linear regime, we show that to get a stable and causal, first-order theory microscopic interaction is play a important role along with general matching conditions.

20.2. *General form of first-order field correction from Boltzmann equation*

To estimate the entire distribution function $f(x,p)$ $(= f_p)$, we starting from the relativistic Boltzmann equation

$$p^\mu \partial_\mu f_p = C[f] = -\mathcal{L}[\phi] \ , \tag{91}$$

here, p^μ is the particle four-momentum, $C[f]$ is the collision kernel. The distribution function can be written as $f_p = f_p^0 + f_p^0 \left(1 \pm f_p^0\right) \phi_p$, here f_p^0 is the equilibrium distribution function and ϕ_p is the out-of-equilibrium deviation. The collision operator

in linear order becomes $C[f] = -\mathcal{L}[\phi] = -\int d\Gamma_{p_1} d\Gamma_{p'} d\Gamma_{p'_1} f^{(0)} f_1^{(0)} (1 \pm f'^{(0)})(1 \pm f_1'^{(0)})\{\phi + \phi_1 - \phi' - \phi'_1\}\mathcal{W}(p'p'_1|pp_1)$, with $d\Gamma_p = \frac{d^3p}{(2\pi)^3 p^0}$ and $\mathcal{W}$ is the transition rate that depends on the cross-section of the interactions.

The out-of-equilibrium distribution function is expressed by the linear combination of the gradients of hydrodynamic variables with appropriate tensor combinations. To extract out the values of unknown coefficients, we expand it on a polynomial basis as Ref.[61] For the properties of linearized collision operator ($\mathcal{L}[1]$ and $\mathcal{L}[p^\mu]$), one can't determine the first two coefficients from scalar sector and one from vector sector. These coefficient are called the homogeneous solution and the rest of the coefficients are called inhomogeneous or interaction solutions. Here we introduced the general matching conditions

$$\int dF_p \tilde{E}_p^i \phi = 0, \quad \int dF_p \tilde{E}_p^j \phi = 0, \quad \int dF_p \tilde{E}_p^k \tilde{p}^{\langle\mu\rangle} \phi = 0 \ , \tag{92}$$

with $i \neq j$, i, j, k are non-negative integers and $\tilde{E}_p = \frac{u\cdot p}{T}$. Employing the general matching conditions one can calculate the homogeneous solutions in terms of inhomogeneous solutions.

We employ the relativistic Boltzmann equation to extract the inhomogeneous part of the out-of-equilibrium distribution function. Here we choose the Anderson-Witting type collision kernel[220] with momentum-dependent relaxation-time (MDRTA). The relaxation time is expressed as $\tau_R = \tau_R^0 \tilde{E}_p^\Lambda$, here τ_R^0 is momentum independent.[47–49,55,221,222] To ensure the microscopic conservation of energy-momentum and particle four-current, we propose a linearized collision operator[47]

$$\begin{aligned}\mathcal{L}_{\rm MDRTA}[\phi] =& \frac{(p\cdot u)}{\tau_R} f^{(0)}(1 \pm f^{(0)}) \Bigg[\phi - \frac{\langle \frac{\tilde{E}_p}{\tau_R}\tilde{E}_p^2\rangle\langle \frac{\tilde{E}_p}{\tau_R}\phi\rangle - \langle \frac{\tilde{E}_p}{\tau_R}\tilde{E}_p\rangle\langle \frac{\tilde{E}_p}{\tau_R}\phi\tilde{E}_p\rangle}{\langle \frac{\tilde{E}_p}{\tau_R}\rangle\langle \frac{\tilde{E}_p}{\tau_R}\tilde{E}_p^2\rangle - \langle \frac{\tilde{E}_p}{\tau_R}\tilde{E}_p\rangle^2} \\ & - \tilde{E}_p \frac{\langle \frac{\tilde{E}_p}{\tau_R}\tilde{E}_p\rangle\langle \frac{\tilde{E}_p}{\tau_R}\phi\rangle - \langle \frac{\tilde{E}_p}{\tau_R}\rangle\langle \frac{\tilde{E}_p}{\tau_R}\phi\tilde{E}_p\rangle}{\langle \frac{\tilde{E}_p}{\tau_R}\tilde{E}_p\rangle^2 - \langle \frac{\tilde{E}_p}{\tau_R}\rangle\langle \frac{\tilde{E}_p}{\tau_R}\tilde{E}_p^2\rangle} - \tilde{p}_{\langle\nu\rangle} \frac{\langle \frac{\tilde{E}_p}{\tau_R}\phi\tilde{p}^{\langle\nu\rangle}\rangle}{\frac{1}{3}\langle \frac{\tilde{E}_p}{\tau_R}\tilde{p}^{\langle\mu\rangle}\tilde{p}_{\langle\mu\rangle}\rangle}\Bigg] . \end{aligned} \tag{93}$$

From the relativistic Boltzmann equation Eq. (91), the first-order out-of-equilibrium distribution function written as[222]

$$\begin{aligned}\phi^{(1)}_{\rm int} =& -\tau_R^0 \tilde{E}_p^{\Lambda-1}\Bigg[\tilde{E}_p^2 \frac{\dot{T}}{T} + \tilde{E}_p \dot{\tilde{\mu}} + \left(\frac{\tilde{E}_p^2}{3} - \frac{z^2}{3}\right)(\partial\cdot u) + \tilde{E}_p \tilde{p}^{\langle\mu\rangle}\left(\frac{\nabla_\mu T}{T} - \dot{u}_\mu\right) \\ & + \tilde{p}^{\langle\mu\rangle}\nabla_\mu\tilde{\mu} - \tilde{p}^{\langle\mu}\tilde{p}^{\nu\rangle}\sigma_{\mu\nu}\Bigg], \end{aligned} \tag{94}$$

where $D = u^\mu\partial_\mu$, $\dot{A} = DA$, $\nabla^\mu = \Delta^{\mu\nu}\partial_\nu$, and $\sigma_{\mu\nu} = \nabla_{\langle\mu}u_{\nu\rangle}$.

Using the entire out-of-equilibrium distribution function upto first order, the

dissipative currents can be written as[52,57,58]

$$\delta n^{(1)}, \delta\epsilon^{(1)}, \delta P^{(1)} = \nu_1, \varepsilon_1, \pi_1 \frac{\dot{T}}{T} + \nu_2, \varepsilon_2, \pi_2 \left(\partial \cdot u\right) + \nu_3, \varepsilon_3, \pi_3 \dot{\tilde{\mu}} \ , \tag{95}$$

$$W^{(1)\mu}, V^{(1)\mu} = \theta_1, \gamma_1 \left[\frac{\nabla^\mu T}{T} - \dot{u}^\mu\right] + \theta_3, \gamma_3 \nabla^\mu \tilde{\mu} \ . \tag{96}$$

The details expression of the transport coefficients ($\epsilon_i, \nu_i, \theta_i$, etc.) given in Ref.[61]

20.3. *Resuts*

After derive the transport coefficients we studied the stability ad causality of theory in linear regime. We linearizing the conservation equations for small perturbations of fluid variables around their equilibrium $\epsilon(t,x) = \epsilon_0 + \delta\epsilon(t,x)$, $n = n_0 + \delta n(t,x),, P(t,x) = P_0 + \delta P(t,x)$, $u^\mu(t,x) = (1,\vec{0}) + \delta u^\mu(t,x)$ and find out the different modes.

For the shear channel the group velocity of the perturbation turns out to be $v_g = \sqrt{\eta/\theta}$. Here $\eta = \tau_R^0 T^2 K_{\Lambda-1}/2$ and we define $\theta = -\theta_1 = \tau_R^0 T^2 \left(J_{\Lambda+1} + \frac{\epsilon_0+P_0}{T^2}\frac{J_{k+\Lambda}}{J_k}\right)$ with $J_n = \int dF_p \tilde{p}^{\langle\mu\rangle}\tilde{p}^{\langle\nu\rangle}\tilde{E}_p^n$ and $\Delta^{\alpha\beta\mu\nu}K_n = \int dF_p \tilde{p}^{\langle\mu}\tilde{p}^{\nu\rangle}\tilde{p}^{\langle\alpha}\tilde{p}^{\beta\rangle}\tilde{E}_p^n$. So the causality criteria of the shear channel is $v_g < 1$ and the stability criteria turns out to be $\theta > 0$.

Using Routh-Hurwitz criteria, we find the following conditions for stability of the non-hydro modes,

$$A_6 > 0 \ , \ A_5 > 0 \ , \ A_3^0 > 0 \ , B_2 = (A_4^0 A_5 - A_3^0 A_6)/A_5 > 0 \ , \tag{97}$$

here A_i's are the are function of the transport coefficients[61] appeared in Eqs. (95) and (96).

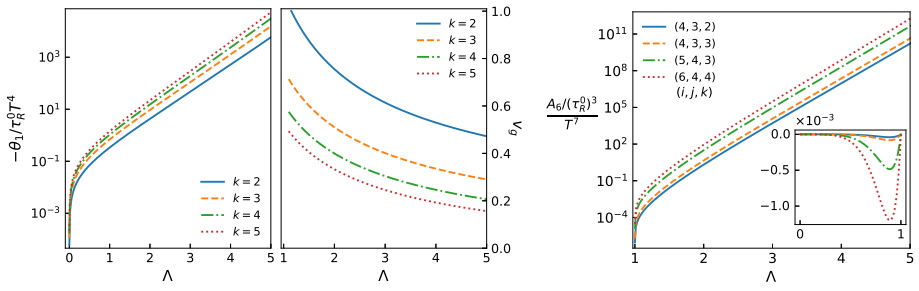


Fig. 45: (Color online) The stability and causality criteria. Left panel two plots is for shear channel and right panel plot is for sound channel.

From the first two plots of Fig. (45) it is clear that the shear channel is stable with different vector matching conditions (k). However, the group velocity of the

shear channel becomes superluminal for $\Lambda < 1$. Also, from the right plot, the stability criteria for sound channel (A_6) are not held.

20.4. *Summary and conclusion*

In this work, we derive a first-order, relativistic stable, and causal hydrodynamic theory from the relativistic Boltzmann equation in general matching conditions. We propose a collision operator for MDRTA to obey the microscopic conservation equations. We have shown that to get a first-order stable and causal theory, not only the general frame but also the system interactions play a crucial role. The conventional momentum-independent RTA leads to superluminal signal propagation in the general frame.

21. Hydrodynamical Attractor and Signals from Quark-Gluon Plasma

Lakshmi J. Naik, Sunil Jaiswal, K. Sreelakshmi, Amaresh Jaiswal, and V. Sreekanth

We study the analytical attractor solutions of third-order viscous hydrodynamics by considering thermal particle production from heavy-ion collisions within the longitudinal boost-invariant expansion. Using these analytical solutions, the allowed initial states are constrained by demanding positivity and reality of energy density throughout the evolution. Further, we calculate the thermal dilepton spectra within the framework of hydrodynamic attractors. It has been observed that the evolution corresponding to attractor solution leads to maximum production of thermal particles.

21.1. *Introduction*

Quark-Gluon Plasma (QGP), state of hot and dense deconfined nuclear matter has been realized in the relativistic heavy ion collision experiments at RHIC and LHC. Relativistic hydrodynamics has been extremely successful in describing the QGP created in these experiments and this has led to the development of several causal dissipative theories of hydrodynamics. The formulation of relativistic viscous hydrodynamics usually proceeds with the assumption that system is in local thermodynamic equilibrium. However, hydrodynamical simulations have showed unexpected success in explaining the flow data from small collisional systems (far from equilibrium) and this has generated much interest in the foundational aspects of causal relativistic hydrodynamics. We investigate an important aspect which manifests in causal boost invariant relativistic viscous hydrodynamics, the *hydrodynamical attractor*[223,224] and study its phenomenological consequences through thermal particle production.[225] We consider thermal dileptons and photons, since their interaction with quark-gluon matter is less and can be detected easily. We calculate the thermal particle production rate in the presence of first order Chapman-Enskog type viscous correction. The spectra of particles are obtained by employing the recently developed analytical solutions of higher order dissipative hydrodynamics under Björken expansion.

21.2. *Hydrodynamical attractor*

Considering longitudinal boost-invariant Björken flow[226] in the Milne coordinates $x^\mu = (\tau, r, \varphi, \eta_s)$, the evolution equations for energy density and shear stress tensor can be written in the generic form:[224]

$$\frac{d\epsilon}{d\tau} = -\frac{1}{\tau}\left(\frac{4}{3}\epsilon - \pi\right),$$
$$\frac{d\pi}{d\tau} = -\frac{\pi}{\tau_\pi} + \frac{1}{\tau}\left[\frac{4}{3}\beta_\pi - \left(\lambda + \frac{4}{3}\right)\pi - \chi\frac{\pi^2}{\beta_\pi}\right], \tag{98}$$

where $\pi \equiv -\tau^2\pi^{\eta_s\eta_s}$, with τ and η_s being the proper time and space-time rapidity of the system. The coefficients γ and χ appearing in the above equations are tabulated in Ref. 224 for the three different causal theories considered here. In the present work, we consider the coefficients corresponding to third-order theory as it shows better agreement with the exact solution of kinetic theory.[227] Also, since we consider a conformal system, we have $\beta_\pi = 4P/5$. The above equations can be solved analytically by considering certain approximations for τ_π. Analytical solutions of these equations were obtained in Ref. 224 for a conformal system and by considering the relation $T\tau_\pi = 5(\eta/s) = \text{const.}$, for three cases : T is either a constant or has proper time evolution following ideal or Navier-Stokes solutions. These analytical solutions can be written in a generic form as :

$$\bar{\pi}(\bar{\tau}) = \frac{(k+m+\frac{1}{2})M_{k+1,m}(w) - \alpha\, W_{k+1,m}(w)}{\gamma|\Lambda|\left[M_{k,m}(w) + \alpha\, W_{k,m}(w)\right]},$$
$$\epsilon(\bar{\tau}) = \epsilon_0\left(\frac{w_0}{w}\right)^{\frac{4}{3}\left(|\Lambda| - \frac{k}{\gamma}\right)} e^{-\frac{2}{3\gamma}(w-w_0)}\left(\frac{M_{k,m}(w) + \alpha\, W_{k,m}(w)}{M_{k,m}(w_0) + \alpha\, W_{k,m}(w_0)}\right)^{\frac{4}{3\gamma}}, \tag{99}$$

where $\bar{\pi} \equiv \pi/(\epsilon + P)$ is the normalized shear stress tensor. Here $M_{k,m}(w)$ and $W_{k,m}(w)$ are the Whittaker functions and α is the integration constant which encodes the initial energy density ϵ_0 and normalized shear stress tensor $\bar{\pi}_0$. The parameters of Whittaker functions appearing in the above equations are tabulated in Ref. 224 for the three cases of τ_π. From the above analytical solutions, the hydrodynamic attractor solution can be obtained for $\alpha = 0$ and repulsor curve correspond to $\alpha = \infty$.

21.3. *Thermal particles from expanding QGP*

Thermal particles, such as dileptons and photons are emitted throughout the expansion of the QGP. The major source of dileptons in a QGP medium is from the $q\bar{q}-$annihilation process. The rate of dilepton production for this process is given by

$$\frac{dN_{l^+l^-}}{d^4x d^4p} = g^2 \int \frac{d^3\mathbf{p}_1}{(2\pi)^3}\frac{d^3\mathbf{p}_2}{(2\pi)^3} f(E_1, T) f(E_2, T) v_{rel}\sigma(M^2)\delta^4(p - p_1 - p_2). \tag{100}$$

$f(E,T)$ represents the viscous modified quark (anti-quark) distribution function and is given by

$$f(E,T) = f_0(E,T)\left(1 + \frac{\beta}{\beta_\pi}\frac{p^\alpha p^\beta \pi_{\alpha\beta}}{2(u\cdot p)}\right), \tag{101}$$

where $f_0(E,T) \approx e^{-E/T}$ denotes the ideal part in the Maxwell-Boltzmann limit, $\beta = 1/T$ and $\beta_\pi = (\epsilon + P)/5$. We have considered the form of viscous correction due to Chapman-Enskog method. Substituting Eq. (101) in Eq. (100) and keeping the terms upto second order in momenta, we can write the total dilepton rate as $\frac{dN_{l^+l^-}}{d^4xd^4p} = \frac{dN^0_{l^+l^-}}{d^4xd^4p} + \frac{dN^\pi_{l^+l^-}}{d^4xd^4p}$, where the ideal and viscous contributions respectively are obtained as[225]

$$\begin{aligned}
\frac{dN^0_{l^+l^-}}{d^4xd^4p} &= \frac{1}{2}\frac{M^2g^2\sigma\left(M^2\right)}{(2\pi)^5}e^{-E/T},\\
\frac{dN^\pi_{l^+l^-}}{d^4xd^4p} &= \frac{dN^0_{l^+l^-}}{d^4xd^4p}\left\{\frac{\beta}{2\beta_\pi|\mathbf{p}|^5}\left[\frac{E|\mathbf{p}|}{2}\left(2|\mathbf{p}|^2 - 3M^2\right) + \frac{3M^4}{4}\ln\left(\frac{E+|\mathbf{p}|}{E-|\mathbf{p}|}\right)\right]p^\alpha p^\beta\pi_{\alpha\beta}\right\}.
\end{aligned} \tag{102}$$

Similarly, we calculate the photon production rate due to Compton scattering: $q(\bar{q})g \to q(\bar{q})\gamma$ and $q\bar{q}$-annihilation $q\bar{q} \to g\gamma$. The ideal and viscous contributions to photon rate are given as[225]

$$\begin{aligned}
E\frac{dN^0_\gamma}{d^4xd^3p} &= \frac{5}{9}\frac{\alpha_e\alpha_s}{2\pi^2}f_0(E,T)T^2\left[\ln\left(\frac{12E}{g^2T}\right) + \frac{C_{\rm ann}+C_{\rm Comp}}{2}\right],\\
E\frac{dN^\pi_\gamma}{d^4xd^3p} &= E\frac{dN^0_\gamma}{d^4xd^3p}\left\{\frac{\beta}{\beta_\pi}\frac{p^\alpha p^\beta\pi_{\alpha\beta}}{2E}\right\},
\end{aligned} \tag{103}$$

respectively. The constants have the values $C_{\rm ann} = -1.91613$, $C_{\rm Comp} = -0.41613$ and $g = \sqrt{4\pi\alpha_s}$; with α_s denoting the strong coupling constant. Thermal particle yields are calculated by numerically integrating the rate equations obtained above over the space-time history of the collisions. Considering the Björken expansion, four-dimensional volume element becomes $d^4x = \pi R_A^2 d\eta_s \tau d\tau$, with R_A being the radius of the colliding nuclei.

21.4. *Results and discussions*

We study the impact of viscous effects on thermal particle yields by constructing the ratios : $R_{l^+l^-} = \left(\frac{dN_{l^+l^-}}{dM^2d^2p_Tdy}\right)\Big/\left(\frac{dN^i_{l^+l^-}}{dM^2d^2p_Tdy}\right)$ and $R_\gamma = \left(\frac{dN_\gamma}{d^2p_Tdy}\right)\Big/\left(\frac{dN^i_\gamma}{d^2p_Tdy}\right)$, where the superscript i denotes the ideal yield and is obtained by integrating the ideal rate expressions ($\delta f = 0$) over the ideal Björken evolution. In Figs. 46 and 47, we plot the ratio of viscous to ideal dilepton and photon yields respectively for the $\tau_\pi \sim 1/T_{id}$ case. The dashed grey curves in the figures represent the ratios corresponding to the viscous evolution for the α values ranging from 10 to 5000. We observe that the thermal particle yields are maximum for the attractor solution

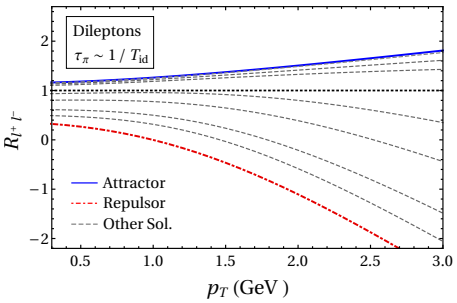


Fig. 46: Ratio of viscous to ideal thermal dilepton yields for $\tau_\pi \sim 1/T_{id}$ approximation.

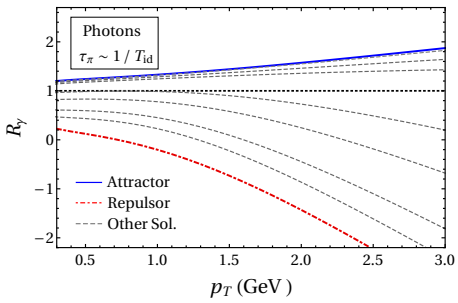


Fig. 47: Ratio of viscous to ideal thermal photon spectra for $\tau_\pi \sim 1/T_{id}$ approximation.

and minimum for the repulsor. Viscous contributions for non-zero values of α tend to approach the repulsor one with increase in α value. Also, it can be noted that the large α values suppress the spectra considerably over the entire p_T regime.

22. Dependence of anisotropic flow and particle production on particlization models and nuclear equation of state

Sumit Kumar Kundu, Yoshini Bailung, Sudhir Pandurang Rode, Partha Pratim Bhaduri, and Ankhi Roy

We investigate the effect of particlization models on particle production for the various equation of states in heavy-ion collisions using the UrQMD event generator. We study anisotropic flow coefficients and particle ratios for mid-central (b=5-9 fm corresponds to approximately 10-40% central) Au-Au collisions for beam energies 1A-158A GeV. UrQMD provides different equations of state in a hybrid mode: chiral EoS, hadron gas EoS, and bag model EoS. Three different particlization models to convert fluid dynamic description to the transport description using various hypersurface criteria are provided by the UrQMD event generator. The results are also compared with available experimental results.

22.1. *Introduction*

Different heavy-ion collision experiments around the globe are being operated to explain the QCD phase diagram in different temperature and baryon density regions. Large Hadron Collider (LHC)[228] and Relativistic Heavy Ion Collider (RHIC)[144] experiments are exploring the high temperature and zero net baryon density region up to a greater extent. Several new experimental facilities like Facility for Anti-proton and Ion Research (FAIR)[229] and Nuclotron-based Ion Collider fAcility (NICA)[230] are trying to explore the intermediate temperature and non-zero net baryon density region of the QCD phase diagram. Until these experimental facilities become operational, several simulation packages and phenomenological models

can be employed to provide predictions at the corresponding regime of temperature and baryon density.

22.2. *UrQMD Model Description*

The ultrarelativistic quantum molecular dynamic (UrQMD)[231–233] model provides different hybrid modes and particlization scenarios to replicate the hydrodynamic effect. UrQMD involves a hybrid mode with the pure transport approach for a better understanding of hot and dense stages of collision. It provides three hybrid modes; Chiral EoS, Hadron Gas EoS, and Bag Model EoS. Chiral and Bag Model EoS have a partonic degrees of freedom, while Hadron Gas EoS involves a hadron degrees of freedom. Chiral, Hadron Gas, and Bag Model EoS include crossover, no phase transition, and first-order phase transition respectively. Besides that, UrQMD provides three different freeze-out or particlization models for the fluid to the particle transition process. First is gradual freeze-out (GF) hypersurface, where particlization takes place slice by slice of 0.2 fm thickness each when the energy density of all cells of that slice falls below the critical energy density, which is five times the nuclear ground state energy density, i.e., $5\epsilon_0$ ($\sim 730 MeV/fm^3$).[234] The second is isochronous freeze-out (ICF), where particlization takes place at the time when the energy density of all cells drops below the critical energy density value. The third is the iso-energy density particlization scenario (IEF), where the hypersurface for particlization is developed numerically using the Cornelius routine[234] which is a freeze-out hypersurface finder code used to generate 3D hypersurface in four dimensions.

22.3. *Results and Discussion*

We show the effect of different EoS on the anisotropic flow and particle production[239] in noncentral Au-Au collisions for beam kinetic energies in the range 1A-158A GeV. Figure 48 shows the effect of the equation of states on the slope of the directed flow of protons. Up to 10A GeV, the employed equations of state show a similar outcome. However, Bag Model EoS shows a split, which may be due to the first-order phase transition. Overall, all EoS overestimate the experimental results. Other observables such as elliptic flow (v_2), particle ratios, and net-proton rapidity spectra are also studied, and for detailed information on the findings, the reader is referred to Ref.[239] In every case, we see the sensitivity for different EoS. However, we cannot predict which EoS is most suitable for reproducing experimental measurements.

Furthermore, in another study,[240] we attempt to investigate the effect of different particlization models provided by UrQMD. Figure 49 compares the slope of the directed flow of protons to see the effect of these particlization models. It is observed that Iso-Energy hypersurface (IEF) with any EoS predicts the experimental measurements much better compared to other freeze-out scenarios. The similar observations are seen in other measurements[240] and are shown in Figure 50 in case

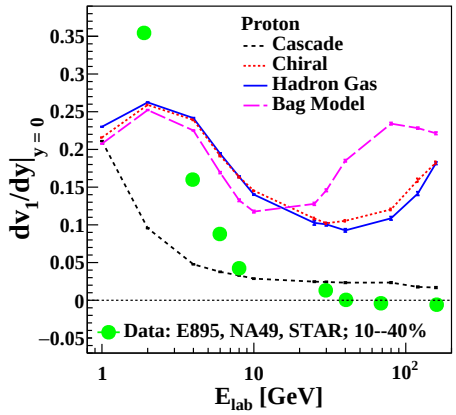


Fig. 48: The slope of directed flow of protons w.r.t. the beam energy in a lab frame at midrapidity region for various configurations of UrQMD with default gradual freeze-out hypersurface for noncentral Au-Au collisions with E895[235] and STAR[236] experimental measurements in Au-Au collisions and with NA49[237] experimental measurements in Pb-Pb collisions. Reprinted from Ref.[239]

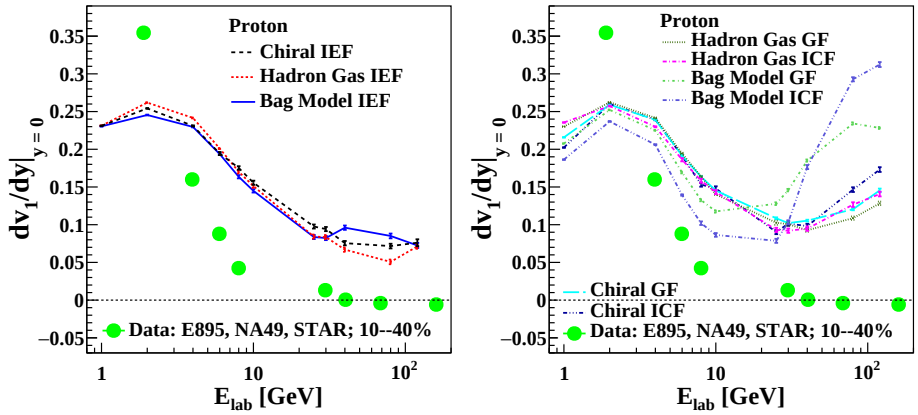


Fig. 49: The slope of directed flow of protons w.r.t. the beam energy in a lab frame at midrapidity region for various configurations of UrQMD for noncentral Au-Au collisions with E895[235] and STAR[236] experimental measurements in Au-Au collisons and with NA49[237] experimental measurements in Pb-Pb collisions. Reprinted from Ref.[240]

of ratio, $\overline{P}/\pi^-$. Observations are in line with ones made in the case of dv_1/dy that iso-energy density particlization scenario explains the experimental measurements

reasonably well.

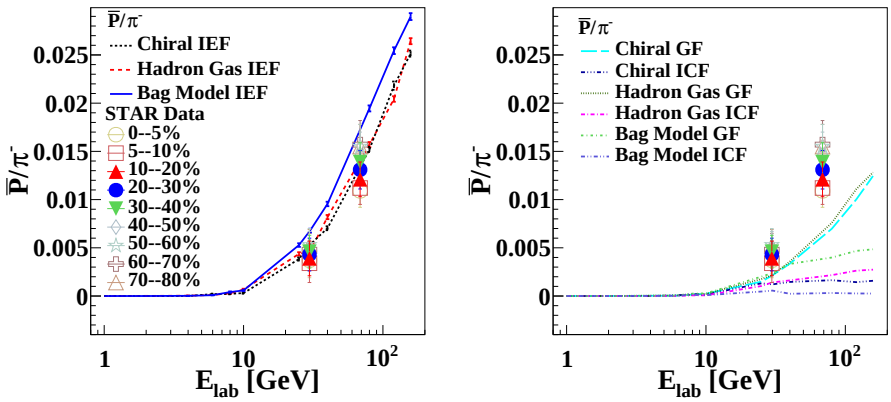


Fig. 50: $\overline{P}/\pi^-$ ratio w.r.t. the beam energy in a lab frame for various configurations of UrQMD for noncentral Au-Au collisions and comparison with STAR[238] experimental measurements in Au-Au collisions for all available centralities. Reprinted from Ref.[240]

22.4. *Summary*

The IEF scenario reproduces the experimental results much better than the other two freeze-out scenarios. However, no such noticeable difference is observed for the different EoS. It will be interesting to employ these different variants of EoS and particlization models in the higher beam energy range.

23. Conductivity of massless quark matter for its lowest possible relaxation time

Cho Win Aung, Thandar Zaw Win, Sabyasachi Ghosh

We have calculated microscopically electrical conductivity of massless quark matter by using relaxation time approximation of kinetic theory framework. The lowest possible quark relaxation time, tuned from the quantum lower bound of shear viscosity to entropy density ratio for massless matter, is used to obtain its corresponding (normalized by temperature T) electrical conductivity $\sigma/T = 0.0135$. By comparing with earlier existing numerical values of electrical conductivity, we marked roughly $(0.25 - 15) \times 0.0135$ as strongly and beyond 20×0.0135 as weakly quark gluon plasma domain.

23.1. *Introduction*

According to the Biot and Savart law, when two heavy nuclei are doing peripheral or non-central collisions in heavy ion collisions (HIC) experiments, a huge magnetic

field can be produced. Its values are expected approximately m_π^2 in RHIC energy and $10m_\pi^2$ in LHC energy.[2] The order of magnitude of this magnetic field ($1 - 10m_\pi^2 \approx 10^{18} - 10^{19}G$) is perhaps the strongest magnetic field that has ever existed in nature. However, it will decay with time, whose detailed time profile (including space profile) are investigated in Refs.[2,170,185] The decay time with respect to QGP life time will basically fix whether QGP face strong[2] or weak[170,247] magnetic field which is not approached towards converging conclusion probably.

The electrical conductivity of QGP becomes an important quantity, which controls the decay profile.[2] So present work has explored its existing numerical values, calculated from different microscopic models and their corresponding effective relaxation time scales. We have guidance on the shear relaxation time scale (τ_c) from the experimental direction, which is expected to be close to its lower bound $\tau_c = 5/(4\pi T)$ (for massless QGP) as shear viscosity (η) to entropy density (s) ratio of QGP is experimentally expected to be close to its quantum lower bound $\eta/s = 1/(4\pi)$. Present work has tried to explore the numerical bands of the electric charge relaxation time scale in terms of the lower bound of shear relaxation time.

Article is organized as follows. After brief addressing of kinetic theory framework of electrical conductivity of relativistic matter in Sec. (24.2), we have estimated its values for massless QGP with lowest possible relaxation time in the Sec. (24.3), where estimations of earlier works are included. We have analysed possible numerical bands of conductivity in terms of corresponding band relaxation time in Sec. (23.4).

23.2. *Framework*

The dissipative current density J_D due to external electric field $\tilde{E}$ can be expressed in macroscopic relation $J_D^i = \sigma^{ij}\ \tilde{E}_j$ (Ohm's law) and microscopic relation

$$J_D^i = g\sum_{u,d} e_Q \int \frac{d^3\mathbf{p}}{(2\pi)^3}\frac{p^i}{E}\delta f_\sigma\ , \tag{104}$$

where $g = 12$ is total degeneracy factor of quark, coming from its spin, particle-anti-particle and color degeneracy factors. The quark flavor are summed as electric charge of u and d quarks are different. The δf is the deviation from equilibrium distribution function $f_0 = 1/[exp(\beta E)+1]$ of quark. To know this δf, we will use the relaxation time approximation(RTA) of Boltzmann transport equation with force term $F^i = e_Q\tilde{E}^i$ and we will get

$$e_Q\tilde{E}^i\frac{\partial f}{\partial p^i} = -\frac{\delta f}{\tau_c}, \Longrightarrow \delta f = \Big[e_Q\big(\frac{p^i}{E}\big)\tau_c\beta f_0(1-f_0)\Big]\tilde{E}_i\ . \tag{105}$$

The Eq.(104) becomes

$$J^i = g\sum_{u,d}\int e_Q^2\frac{d^3\mathbf{p}}{(2\pi)^3}\frac{p^ip^j}{E^2}\tau_c\beta f_0(1-f_0)\tilde{E}_j\ . \tag{106}$$

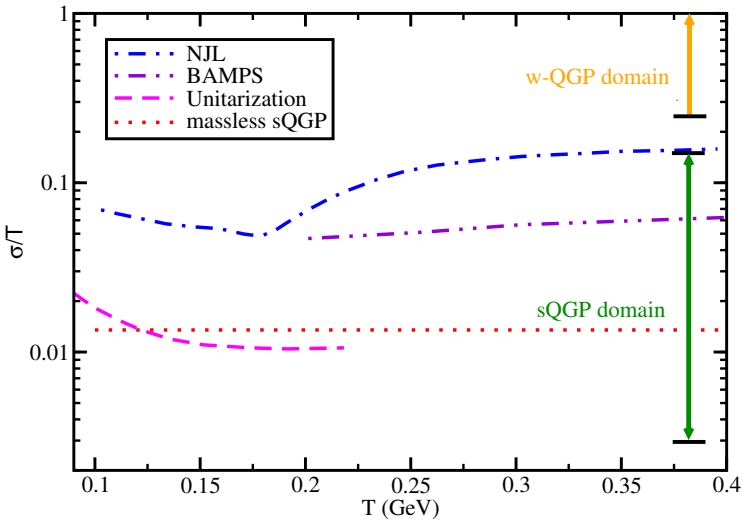


Fig. 51: Normalised conductivity of different estimations with temperature, based on NJL (blue dash-dotted line), BAMPS (violet dash-double dotted line) and uniterization (pink dash line) methodologies with respect to the massless sQGP estimation (red dotted line)

Comparison with the macroscopic description, $J^i = \sigma^{ij}\tilde{E}_j$, we get

$$\sigma = \frac{g}{T}\sum_{u,d} e_Q^2 \int \frac{d^3\mathbf{p}}{(2\pi)^3}\frac{p^2}{3E^2}\tau_c f_0(1-f_0)\ . \tag{107}$$

23.3. *Results and discussion*

For generating results, let us use massless limit $E = p$ in Eq. (107)[241] and then we get

$$\sigma = \frac{10}{27}\ e^2\tau_c T^2, \tag{108}$$

where $\sum e_Q^2 = \left(+\frac{2}{3}e\right)^2 + \left(-\frac{1}{3}e\right)^2 = \left(\frac{5}{9}\right)e^2$. Now, lower bound of η/s for massless medium can provide lower bound of (shear) relaxation time,[241]

$$\frac{\eta}{s} = \frac{\tau_c T}{5} = \frac{1}{4\pi}, \Longrightarrow \tau_c = \frac{5}{4\pi T}. \tag{109}$$

Using this lowest possible (shear) relaxation time, we will get conductivity

$$\sigma(T) = \frac{25}{54}\ \frac{e^2}{\pi}T \approx 0.0135T\ . \tag{110}$$

Assuming $\sigma/T = 0.0135$ as lowest reference point, we have plotted it by red dotted line in Fig.(51) and marked as massless strongly quark gluon plasma (sQGP).

The results of electrical conductivity from Refs.[242] ,[243] ,[244] are also included in the figure, which covers a large numerical band of electrical conductivity. Ref.[242] is based on the transport quark model and its estimated values are approximately 5 times larger than the massless sQGP values. Ref.[243] is based on an effective QCD model, called Nambu-Jona-Lasinio (NJL) model and its estimated values located in the range 5-15 times larger than the massless sQGP values. Interestingly hadronic conductivity estimation, based on unitarization methodology, is close to the massless sQGP values. On the other hand, lattice quantum chromodynamics (LQCD) calculations by Amato et al.[162] provide values from 0.003 to 0.015. It means that 4 times smaller than the massless sQGP values (0.0135) should have to be considered also within the numerical band of σ/T. Now this entire numerical band of σ/T from 0.003 to 0.2 might be considered as sQGP domain for electrical conductivity because weakly QGP (w-QGP) estimation from perturbative QCD (pQCD) calculation[245,252] provides more than 20 times larger values of η/s with respect to its quantum lower bound $1/(4\pi) \approx 0.08$. So corresponding (shear) relaxation time may be larger than $25/(\pi T)$ and using that relaxation time range for electrical conductivity, one can expect $\sigma/T \geq 20 \times 0.0135$ as wQGP domain. Our exploration of sQGP and wQGP domain of σ/T might be very important information for knowing the corresponding domain of decay profile of magnetic field, produced in heavy ion collision experiments.

23.4. *Summary*

In summary, with the help of the relaxation time approximation of the kinetic theory framework, we have calculated microscopically electrical conductivity of massless quark matter. Based on the knowledge of quantum lower bound for shear viscosity to entropy density ratio, one can get the lowest possible (shear) relaxation time for massless matter. Present work has tried to understand electric charge transportation in terms of that quantum bound. So, we have used that relaxation time to obtain electrical conductivity by temperature ratio $\sigma/T = 0.0135$, which might be considered as a reference point for charge transportation of QGP. Comparing with earlier existing numerical values of electrical conductivity, we noticed that LQCD estimations of σ/T can be 4 times smaller to 3 times larger than the reference value 0.0135. When we considered some earlier model calculations like NJL, BAMPS, and unitarization, we find the ratio may go up to 15 times larger than 0.0135. In this angle, we may assign roughly $\sigma/T = (0.25 - 15) \times 0.0135$ as our known range of microscopic calculations, which might be connected to the strongly quark-gluon plasma domain. On the other hand, beyond 20×0.0135 as weakly quark gluon plasma domain because earlier perturbative QCD calculation by Arnold et al. indicate that range for shear viscosity to entropy density ratio. We believe that these strongly and weakly interacting domains of electrical conductivity will be very important inputs to investigate the corresponding detailed decay profile of magnetic field, produced in heavy ion collision experiments.

24. Exploring the numerical bands of electrical conductivity of quark gluon plasma and decay profile of magnetic field

Thandar Zaw Win, Cho Win Aung, Sabyasachi Ghosh

In heavy ion collision experiments, a huge magnetic field can be produced in peripheral collisions, owing to Ampere's law. The quark-gluon plasma, produced in the heavy ion collision experiments, will face this field, which will decay with time. This exponential decay profile will be controlled by the electrical conductivity of expanding quark-gluon plasma. Present work has explored that connection by using different earlier works, predicting the values of electrical conductivity for quark-gluon plasma.

24.1. *Introduction*

When two heavy nuclei are colliding in peripheral collision in heavy ion collisions experiments (HIC), a huge magnetic field can be produced according to Biot Savart law. The field strengths can approximately be m_π^2 in RHIC energy and $10m_\pi^2$ in LHC energy[2] . It can decay with time, whose detailed space-time profile are investigated recently in many references. The reader may see Refs.[2,170,247] and references therein. This decay time may[170,247] or may not[2] be smaller than lifetime of QGP. Fact is still a matter of debate. The decay profile of the magnetic field[2] can be controlled by the electrical conductivity of the QGP medium. In this context, the present work has explored its existing numerical values, calculated from different microscopic models, and then use them for generating corresponding decay profiles of magnetic field.

The article is organized as follows. Next, in the Formalism section (24.2), we have briefly addressed the formalism of magnetic field decay, as prescribed by Tuchin. Then, we have generated their curves in the result section (24.3) along with a detailed discussion. At the end, Sec (24.4) provides summary of our findings.

24.2. *Framework*

Here, we are adopting the formalism, prescribed by Tuchin[248] , which is briefly described below.

The parameter that controls the strength of the matter effect on the field evolution is $\sigma\gamma b$, where σ is the electrical conductivity, γ is the Lorentz boost factor, and b is the characteristic transverse size of matter. Let us start with Maxwell's equations for EM field created by a point charge e moving along the positive z-axis with velocity v[248] :

$$\nabla\cdot\mathbf{B}=0, \qquad \nabla\times\mathbf{E}=-\frac{\partial\mathbf{B}}{\partial t}$$
$$\nabla\cdot\mathbf{D}=e\delta(z-vt)\delta(b), \qquad \nabla\times\mathbf{H}=\frac{\partial\mathbf{D}}{\partial t}+\sigma E+ev\hat{z}\delta(z-vt)\delta(b)\ .$$

Performing Fourier transform, we get the magnetic field part

$$H(t,r)=\int_{-\infty}^{\infty}\frac{d\omega}{2\pi}\int_{-\infty}^{\infty}\frac{dk_z}{2\pi}\int\frac{d^2k_\perp}{(2\pi)^2}e^{-i\omega t+ik_z z+ik_\perp b}H_{\omega k}\ , \tag{111}$$

whose solution becomes

$$H_{\omega k} = -2\pi iev\frac{|k\times\hat{z}|}{\omega^2\tilde{\epsilon}\mu - k^2}\delta(\omega - k_z v)\ . \tag{112}$$

Substituting the Eq.(112) into the Eq.(111) and taking integral over k, we get[248]

$$H(t,r) = \frac{e}{2\pi\sigma}\int_0^\infty \frac{J_1(k_\perp b)k_\perp^2}{\sqrt{1+\frac{4k_\perp^2}{\gamma^2\sigma^2}}} e^{\left\{\sigma\gamma^2 x_-/2(1-\sqrt{1+\frac{4k_\perp^2}{\gamma^2\sigma^2}}\right\}} dk_\perp\ . \tag{113}$$

If $\gamma\sigma b \gg 1$, the Eq.(113) becomes,[248]

$$H = \frac{e}{2\pi}\frac{b\sigma(t)}{4x_-^2}e^{-\frac{b^2\sigma(t)}{4x_-}}\ , \tag{114}$$

where, $x_- = t - z/v$, hence the magnetic field is given by the solution (114). This Eq. (114) will be our working formula for generating results.

24.3. *Results*

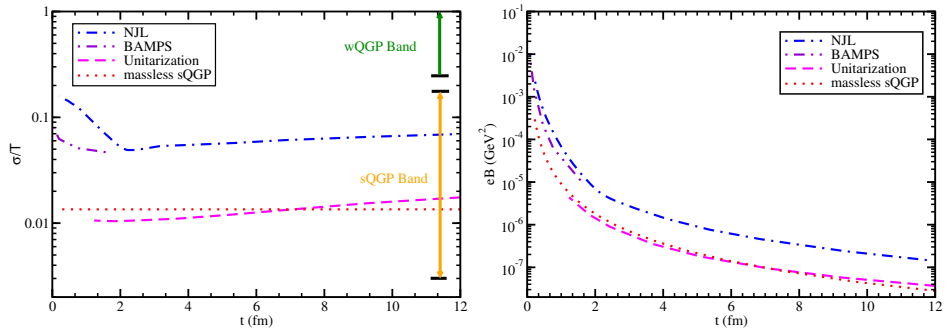


Fig. 52: The electrical conductivity (Left) and corresponding magnetic field decay (Right) of different calculations, based on NJL[250] (blue dash-dotted iine), BAMPS[242] (violet dash-double dotted line) and uniterization[251] (pink dash line) methodologies, and for the massless sQGP case (red dotted line).

If we explore the long list of earlier references, which have provided estimations of electrical conductivity for QGP by using different microscopic model calculations, then we will get a rough numerical range of its values. Lattice quantum chromodynamics (LQCD) calculations[32,88,246,249] mostly provide temperature-independent values and electrical conductivity by temperature ratio remains within $0.003 - 0.03$ approximately. However, different microscopic model calculations can go towards larger values. To cover that broad numerical band, we have selected a few Refs.[250] ,[242] ,[251] , which have provided temperature-dependent conductivity values. To convert from temperature to time, we use the standard cooling law of

QGP $T^3t = T_i^3 t_i \approx 0.0128$, where the initial temperature and time of expanding QGP are considered as $T_i = 400$ MeV and $t_i = 0.2$ fm respectively. We get the electrical conductivity in terms of time, as shown in the left panel of Fig. (52). If we notice the NJL model calculations, given in Ref.[250] , then we can recognize the minimum values of σ/T near transition temperature. So, the blue dash-dotted line in the left panel of Fig. (52), presenting σ/T along the time axis, also exhibit a minimum value. According to the present version of simple T-t mapping via cooling law, we can identify $t \leq 2$ fm as expanding QGP and $t \geq 2$ fm as expanding hadronic matter up to freeze out time. This time ranges of QGP and hadronic matter is bit of sensitive on initial values of time, temperature. Hence, we should consider them as gross ranges instead of exact quantitative values. These ranges can also be seen from BAMPS[242] and unitarization[251] results, whose predicted values are confined within QGP and hadronic matter temperature respectively. Let us try to understand these results, predicted from earlier microscopic model calculations, in terms of simple massless QGP conductivity $\sigma = \frac{10}{27}\ e^2\tau_c T^2$ for lowest possible (shear) relaxation time $\tau_c = \frac{5}{4\pi T}$, which can be tuned by imposing quantum lower bound of fluid property[241] . So we may call this $\sigma = \frac{25}{54}\ \frac{e^2}{\pi} T \approx 0.0135T$ as massless sQGP, whose time dependent expression will be $\sigma = 0.0032/t^{1/3}$, as plotted by red dotted line in Fig. (52)(Left). This result may be called as conductivity of massless strongly QGP (sQGP), where strongly interacting behaviour is linked with the lowest possible shear relaxation time. If one compare existing literature for σ/T, then with respect to massless sQGP, then they will be within the ranges from 1/4 to 15 times larger than the massless sQGP. This band may be considered as sQGP bands of conductivity (marked in Fig. (52)(Left)) because perturbative QCD (pQCD) calculations[245,252] give more than 20 times larger values of shear relaxation, marked as weakly QGP (wQGP) domain in Fig. (52)(Left).

Now, considering this sQGP bands of $\sigma(t)$ in Eq. (114), we will get magnetic field decay profile as shown in Fig. (52)(Right), where $b = 1$ fm, $z = 0$ and $v = 0.99$ are considered. Changing those b, z and v, decay profile will be modified but our aim is to show corresponding bands of the decay profile by using existing sQGP conductivity band.

24.4. *Summary*

In summary, we have extracted the temperature-dependent conductivity data of earlier references and converted them to time-dependent data by using the standard cooling law of expanding QGP. Then, using those data in Tuchin's decay expression of the magnetic field, we have plotted different decay curves for constant values of other parameters like the Lorenz factor, transverse characteristic size, etc. In terms of massless sQGP values of conductivity, we have realized that the existing estimations of earlier work locate within 0.25 to 15 times larger values, which may be considered as its sQGP bands as wQGP cover 20 times larger and beyond values. Present work provided the numerical band of magnetic field decay profiles due to

the sQGP conductivity band.

25. Causal hydrodynamics based on effective kinetic theory and particle yield from QGP

Lakshmi J. Naik and V. Sreekanth

We investigate thermal particle production and evolution of QGP created in heavy ion collisions in presence of viscosities, by employing the recently formulated second order dissipative hydrodynamics estimated within the effective fugacity quasi-particle model of hot QCD medium. We employ the viscous corrections to the parton distribution functions obtained from the Chapman-Enskog method in the relaxation time approximation. We analyze the sensitivity of shear and bulk viscous pressures to the temperature dependence of relaxation time within one dimensional boost invariant flow. Particle emission yields are quantified for the longitudinal expansion of QGP with different temperature dependent relaxation times. Our results indicate that the particle spectra computed using this formalism is well behaved and is sensitive to the relaxation times.

25.1. *Introduction*

Relativistic dissipative hydrodynamics has been successfully employed to study the evolution of Quark-Gluon Plasma (QGP), created in the relativistic heavy ion collisions at RHIC, LHC. The evolution of QGP has to be studied with higher order viscous hydrodynamics as the first order Navier-Stokes theory shows acausal behaviour. Several causal hydrodynamic theories have been developed and have been applied in the context of heavy ion collisions. Recently, a causal second order viscous hydrodynamic formulation was developed[253] by employing the effective fugacity quasi-particle model (EQPM)[254] for the thermal QCD medium. This model incorporates the QCD medium interactions into the analysis through thermal effective fugacity parameters in the distribution functions. The hydrodynamic equations in this formulation have been estimated by employing the covariant kinetic theory for EQPM.[255] The viscous corrections to the distribution functions have been determined by the Chapman-Enskog (CE) expansion in RTA. We intend to employ this hydrodynamic framework to study the thermal dilepton and photon production from heavy ion collisions under boost invariant Björken expansion of QGP.

25.2. *Second Order hydrodynamics based on EQPM*

We present the formalism to derive the second order causal hydrodynamics within the EQPM description of thermal QCD medium. EQPM incorporates the hot QCD medium effects into the analysis through temperature dependent effective fugacity parameters z_k ($k \equiv (q, g)$ stands for quarks and gluons respectively). The equilibrium momentum distribution function within this model is given by[254]

$$f_k^0 = \frac{z_k \exp[-\beta(u_\mu p_k^\mu)]}{1 \pm z_k \exp[-\beta(u_\mu p_k^\mu)]}, \tag{115}$$

where $\beta = 1/T$ is the inverse of temperature. It must be noted that the quantity z_k in this model represents the interaction between the partons and is not associated with any conservation laws. Here, $p_k^\mu = (E_k, \vec{p}_k)$ is the bare four-momenta of the particles and this is related to the quasi-particle four-momenta through the dispersion relation $\tilde{p}_{g,q}^\mu = p_{g,q}^\mu + \delta\omega_{g,q}u^\mu$; where $\delta\omega_{g,q} = T^2\partial_T \ln(z_{g,q})$ denotes the modified part of energy dispersion relation due to the interaction. The dissipative hydrodynamic equations is derived by quantifying the non-equilibrium corrections in the system. The viscous corrections to the momentum distribution functions are estimated by considering the effective Boltzmann equation within EQPM description in RTA[255]

$$\tilde{p}_k^\mu \partial_\mu f_k^0(x, \tilde{p}_k) + F_k^\mu \partial_\mu^{(p)} f_k^0 = -\frac{\delta f_k}{\tau_R}\omega_k. \tag{116}$$

In the above equation, τ_R denotes the relaxation time and δf_k is the non-equilibrium part of the distribution function. Presence of non-trivial dispersion relation in the theory gives the mean field force term $F_k^\mu = -\partial_\nu(\delta\omega_k u^\nu u^\mu)$ in the effective transport equation and the same is obtained from energy-momentum and particle flow conservation.[255] We use the form of distribution function derived from the Chapman-Enskog like expansion of effective Boltzman equation in RTA,

$$\delta f_q = \tau_R\left[\tilde{p}_q^\mu\partial_\mu\beta + \frac{\beta\,\tilde{p}_q^\mu\,\tilde{p}_q^\nu}{u\cdot\tilde{p}_q}\partial_\mu u_\nu - \beta\Theta(\delta\omega_q) - \beta\dot{\beta}\left(\frac{\partial(\delta\omega_q)}{\partial\beta}\right)\right] f_q^0\,\bar{f}_q^0, \tag{117}$$

where $\bar{f}_q^0 = 1 - f_q^0$. The expressions for $\pi^{\mu\nu}$ and Π within the effective kinetic theory are obtained as,[255]

$$\begin{aligned}\pi^{\mu\nu} &= \sum_k g_k\Delta_{\alpha\beta}^{\mu\nu}\int d\tilde{P}_k\tilde{p}_k^\alpha\tilde{p}_k^\beta\delta f_k + \sum_k g_k\delta\omega_k\Delta_{\alpha\beta}^{\mu\nu}\int d\tilde{P}_k\tilde{p}_k^\alpha\tilde{p}_k^\beta\frac{\delta f_k}{E_k},\\ \Pi &= -\frac{1}{3}\sum_k g_k\Delta_{\alpha\beta}\int d\tilde{P}_k\tilde{p}_k^\alpha\tilde{p}_k^\beta\delta f_k - \frac{1}{3}\sum_k g_k\delta\omega_k\Delta_{\alpha\beta}\int d\tilde{P}_k\tilde{p}_k^\alpha\tilde{p}_k^\beta\frac{\delta f_k}{E_k}.\end{aligned} \tag{118}$$

Following Ref. 253, the evolution equations for $\pi^{\mu\nu}$ and Π are obtained as given below

$$\begin{aligned}\dot{\pi}^{\langle\mu\nu\rangle} + \frac{\pi^{\mu\nu}}{\tau_R} &= 2\beta_\pi\sigma^{\mu\nu} + 2\pi_\phi^{\langle\mu}\omega^{\nu\rangle\phi} - \delta_{\pi\pi}\pi^{\mu\nu}\theta - \tau_{\pi\pi}\pi_\phi^{\langle\mu}\sigma^{\nu\rangle\phi} + \lambda_{\pi\Pi}\Pi\sigma^{\mu\nu},\\ \dot{\Pi} + \frac{\Pi}{\tau_R} &= -\beta_\Pi\theta - \delta_{\Pi\Pi}\Pi\theta + \lambda_{\Pi\pi}\pi^{\mu\nu}\sigma_{\mu\nu}.\end{aligned} \tag{119}$$

Now, we solve the above equations for various temperature dependent relaxation times by considering the longitudinal boost-invariant expansion of Björken.[226] The space-time coordinates are parameterized as $t = \tau\cosh\eta_s$ and $z = \tau\sinh\eta_s$, with $\tau = \sqrt{t^2 - z^2}$ and $\eta_s = \frac{1}{2}\ln\frac{t+z}{t-z}$ respectively being the proper time and space-time rapidity of the system. Four−velocity of the fluid is given by the ansatz $u^\mu = (\cosh\eta_s, 0, 0, \sinh\eta_s)$. Considering the boost-invariance, the above equations reduce

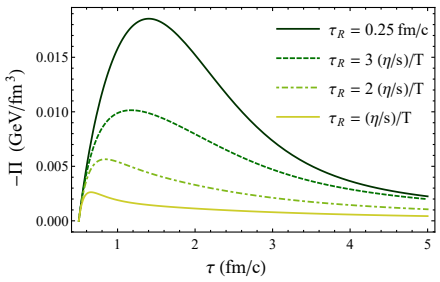


Fig. 53: Proper time evolution of bulk viscous pressure.

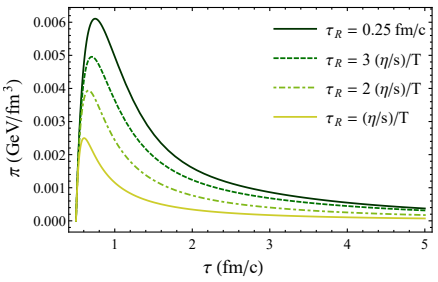


Fig. 54: Proper time evolution of shear viscous pressure.

to the following first order coupled equations in τ :[253]

$$\begin{aligned}
\frac{d\epsilon}{d\tau} &= -\frac{1}{\tau}\left(\epsilon + P + \Pi - \pi\right), \\
\frac{d\pi}{d\tau} + \frac{\pi}{\tau_\pi} &= \frac{4}{3}\frac{\beta_\pi}{\tau} - \left(\frac{1}{3}\tau_{\pi\pi} + \delta_{\pi\pi}\right)\frac{\pi}{\tau} + \frac{2}{3}\lambda_{\pi\Pi}\frac{\Pi}{\tau}, \\
\frac{d\Pi}{d\tau} + \frac{\Pi}{\tau_\Pi} &= -\frac{\beta_\Pi}{\tau} - \delta_{\Pi\Pi}\frac{\Pi}{\tau} + \lambda_{\Pi\pi}\frac{\pi}{\tau};
\end{aligned} \tag{120}$$

where $\pi = \pi^{00} - \pi^{zz}$. The expressions for the transport coefficients can be found in Ref. 253. Now, we analyze the evolution of π and Π by choosing three different forms of relaxation times : $\tau_R = 3(\eta/s)/T, 2(\eta/s)/T$ and $(\eta/s)/T$. In Figs. (53) and (54), we plot the bulk and shear viscous pressures respectively as a function of proper time for different temperature dependent relaxation times. We choose the initial temperature and proper time to be $T_0 = 0.31$ GeV and $\tau_0 = 0.5$ fm/c respectively. It is observed that both π and Π have strong dependency on the value of τ_R. The effect due to viscous contributions increases with increase in τ_R. We also plot the evolution corresponding to a constant relaxation time, $\tau_R = 0.25$ fm/c (as taken in Ref. 253) for comparison. It can be noted that the viscous effects are maximum for this constant value compared to the temperature dependent cases considered here.

25.3. *Thermal particle spectra from heavy ion collisions*

In this section, we calculate the thermal particle spectra from heavy ion collisions by employing the second order hydrodynamic formulation discussed above. We consider dileptons from $q\bar{q}-$annihilation process, $q\bar{q} \longrightarrow \gamma^* \longrightarrow l^+l^-$. The rate of dilepton production within EQPM in the presence of viscous modified distribution function $f(\vec{p}) = f_0(\vec{p}) + \delta f$ is given by

$$\frac{dN}{d^4x d^4p} = \iint \frac{d^3\vec{p}_1}{(2\pi)^3}\frac{d^3\vec{p}_2}{(2\pi)^3}\frac{M_{\rm eff}^2 g^2\,\sigma(M_{\rm eff}^2)}{2\omega_1\omega_2} f(\vec{p}_1) f(\vec{p}_2)\delta^4(\tilde{p} - \tilde{p}_1 - \tilde{p}_2). \tag{121}$$

We consider the viscous correction upto first order in momenta, obtained from Chapman-Enskog method :

$$\delta f = \delta f_\pi + \delta f_\Pi = \frac{\beta}{2\beta_\pi (u\cdot\tilde{p})}\tilde{p}^\mu\tilde{p}^\nu\pi_{\mu\nu} + \frac{\beta\Pi}{\beta_\Pi}\Big[\xi_1 - \xi_2(u\cdot\tilde{p})\Big], \tag{122}$$

where

$$\xi_1 = \beta c_s^2\frac{\partial\delta\omega_q}{\partial\beta} + \delta\omega_q; \qquad \xi_2 = \left(c_s^2 - \frac{1}{3}\right) + \frac{\delta\omega_q}{3(u\cdot\tilde{p})^2}\left[2(u\cdot\tilde{p}) - \delta\omega_q\right]. \tag{123}$$

Keeping the terms upto second order in momenta, we can write the total dilepton rate as sum of ideal and viscous contributions. The ideal part of dilepton rate, within EQPM is given by

$$\frac{dN^{(0)}}{d^4xd^4p} = \frac{z_q^2}{2}\frac{M_{\rm eff}^2\, g^2\,\sigma(M_{\rm eff}^2)}{(2\pi)^5}e^{-(u\cdot\tilde{p})/T}. \tag{124}$$

The contribution to the dilepton rate due to shear and bulk viscosities are obtained respectively as[256]

$$\begin{aligned}
\frac{dN^{(\pi)}}{d^4xd^4p} &= \frac{dN^{(0)}}{d^4xd^4p}\Bigg\{\frac{\beta}{\beta_\pi}\frac{1}{2|\vec{p}|^5}\Bigg[\frac{(u\cdot\tilde{p})|\vec{p}|}{2}\left(2|\vec{p}|^2 - 3M_{\rm eff}^2\right)\\
&\quad + \frac{3}{4}M_{\rm eff}^4\ln\left(\frac{(u\cdot\tilde{p}) + |\vec{p}|}{(u\cdot\tilde{p}) - |\vec{p}|}\right)\Bigg]\tilde{p}^\mu\tilde{p}^\nu\pi_{\mu\nu}\Bigg\},\\
\frac{dN^{(\Pi)}}{d^4xd^4p} &= \frac{dN^{(0)}}{d^4xd^4p}\frac{2\beta\Pi}{\beta_\Pi}\Bigg\{\beta c_s^2\frac{\partial\delta\omega_q}{\partial\beta} - \frac{2}{3}\delta\omega_q - \left(c_s^2 - \frac{1}{3}\right)\frac{(u\cdot\tilde{p})}{2}\\
&\quad + \frac{\delta\omega_q^2}{6|\vec{p}|^5}\Bigg[\frac{(u\cdot\tilde{p})|\vec{p}|}{2}\left(2|\vec{p}|^2 - 3M_{\rm eff}^2\right) + \frac{3}{4}M_{\rm eff}^4\ln\left(\frac{(u\cdot\tilde{p}) + |\vec{p}|}{(u\cdot\tilde{p}) - |\vec{p}|}\right)\Bigg]\Bigg\},
\end{aligned} \tag{125}$$

where $|\vec{p}| = \sqrt{(u\cdot\tilde{p})^2 - M_{\rm eff}^2}$. Similarly, we determine the photon production rate expressions in the presence of modified distribution functions. The ideal, shear and bulk viscous contributions to the photon production rate are obtained as[256]

$$\begin{aligned}
\omega_0\frac{dN_\gamma^{(0)}}{d^3pd^4x} &= \frac{5}{9}\frac{\alpha_e\alpha_s}{2\pi^2}T^2 f(\vec{p})\left[\ln\left(\frac{12\,(u\cdot\tilde{p})}{g^2T}\right) + \frac{C_{\rm ann}+C_{\rm Comp}}{2}\right]\\
\omega_0\frac{dN_\gamma^{(\pi)}}{d^3pd^4x} &= \omega_0\frac{dN_\gamma^{(0)}}{d^3pd^4x}\left\{\frac{\beta}{2\beta_\pi(u\cdot\tilde{p})}\right\},\\
\omega_0\frac{dN_\gamma^{(\Pi)}}{d^3pd^4x} &= \omega_0\frac{dN_\gamma^{(0)}}{d^3pd^4x}\left\{\frac{\beta\Pi}{\beta_\Pi}\Big[\xi_1 - \xi_2(u\cdot\tilde{p})\Big]\right\}.
\end{aligned} \tag{126}$$

25.4. *Results and discussions*

We calculate thermal particle spectra by numerically integrating the above particle rate expressions over the space-time history of the collisions under boost invariant Björken flow. We use the viscous and temperature evolutions of the QGP obtained

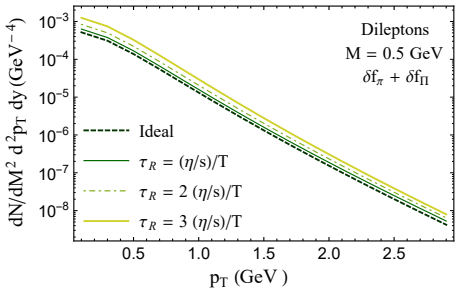


Fig. 55: Thermal dilepton spectra in the presence of viscous corrections for different τ_R and with $M = 0.5$ GeV.

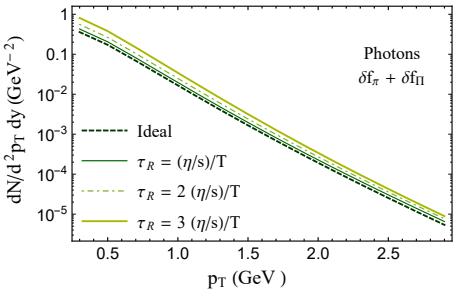


Fig. 56: Thermal photon spectra in the presence of viscous corrections by varying τ_R.

in the previous section. We choose the initial conditions : $T_0 = 0.31$ GeV and $\tau_0 = 0.5$ fm/c and temperature is evolved till $T_c = 0.17$ GeV. In Figs. 55 and 56, we plot the thermal dilepton and photon yields respectively for different temperature dependent relaxation times. It can be seen that the particle yields increase with increase in magnitude of τ_R. As expected (from figs. 53 and 54), we observe maximum enhancement in the spectra with evolution corresponding to $\tau_R = 3(\eta/s)/T$ and minimum with $\tau_R = 3(\eta/s)/T$. Our results indicate that the particle spectra obtained by employing this second order hydrodynamics is well behaved and is sensitive to τ_R. We note that the Björken expansion employed here overestimates the yields and a quantitative study requires employing $2+1$ or $3+1$ dimensional hydrodynamic simulations for the evolution.

26. Relativistic Dissipative Magnetohydrodynamic from Kinetic Theory

Ankit kumar panda and Victor Roy

We derive the second-order magnetohydrodynamics evolution equations of the dissipative stresses for both non-resistive and resistive cases from kinetic theory using the relaxation time approximation for the collision kernel. We found new transport coefficients that were not present in an earlier study by a different group using the 14-moment method. Also, we calculate the anisotropic transport coefficients pertaining to this. We further show the temperature and hadronic mass dependence of the two newly derived leading order transport coefficients δ_{VB} and $\delta_{\pi B}$.

26.1. *Introduction*

The magnetic field seems to play an important role in the working of our present-day universe. They find a lot of applications, from the laboratory systems to the very large systems like the astrophysical objects. The strength of the magnetic field in these cases can vary by several orders of magnitudes; for example, Earth's magnetic fields on the surface have typical values 10^{-4}T, whereas one of the strongest

fields $\sim 10^{14}$-10^{15}T ever known can be found in the high energy heavy-ion collision experiments at RHIC and LHC. Along with the magnetic field produced in the initial stages of the heavy-ion collisions (primarily due to the spectators), a new form of very hot and dense matter known as quark-gluon plasma (QGP) is also formed. QGP can also be found in astrophysical objects such as in the core of superdense neutron stars. Considering that the QGP evolves in a strong background magnetic field, we can study its dynamical evolution within the framework of the Relativistic magnetohydrodynamics (RMHD).

It is well known that a straightforward extension of the Navier-Stokes equations for viscous fluids leads to unacceptable acausal behavior. Israel and Stewart (IS) were the first who develop a causal and stable relativistic version of the dissipative hydrodynamics known as the second-order hydrodynamics, as it contains dissipative terms proportional to the second-order gradients of the fluid variables. IS equations are applicable for ordinary (uncharged) fluids. Only recently, second-order evolution equations for charged fluids, i.e., the second-order causal magnetohydrodynamics equations, were derived for non-resistive in Ref.[257] and resistive case in Ref.[258] for a single component system of spinless particles (no antiparticle) using a 14-moment approximation. In our recent work, Refs.[259, 260] we consider the contribution from both particles and antiparticles. We derive the RMHD equations for the non-resistive and resistive cases using the Chapman-Enskog-like gradient expansion of the single-particle distribution function within relaxation time approximation (RTA). Also, the anisotropic transport coefficients pertaining to this case have been evaluated. In this proceeding, we further study the temperature and hadronic mass dependence of the two newly derived leading order transport coefficients δ_{VB} and $\delta_{\pi B}$.

26.2. *Formalism*

In this section, we discuss the essential part of the formalism, for details see Refs.[259, 260]. The relativistic Boltzmann equation (RBE) in the presence of a non-zero force $\mathcal{F}^\nu$ is given by:

$$p^\mu \partial_\mu f + \mathcal{F}^\nu \frac{\partial}{\partial p^\nu} f = C[f], \tag{127}$$

where $f(\mathbf{x}, \mathbf{p}, t)$ is the one particle distribution function characterising the phase space density of the particles, $C[f]$ is the collision kernel. Here we simply the collision kernel using the RTA, that is we choose $C[f] = -\frac{u.p}{\tau_c}\delta f$. In this approach we calculate off-equilibrium distribution f order-by-order as :

$$f = \sum_{n=0}^{\infty} (-1)^n \left(\frac{\tau_c}{u.p}\right)^n \left(p^\mu \partial_\mu + qF^{\mu\nu} p_\nu \frac{\partial}{\partial p^\mu}\right)^n f_0. \tag{128}$$

We use Kn $= \tau_c \partial_\mu$,$\chi = qB\tau_c/T$ and $\xi = qE\tau_c/T$ as small parameters for the order-by-order expansion. Truncating this series upto the second-order we get:

$$f = f_0 + \delta f^{(1)} + \delta f^{(2)}. \tag{129}$$

We evaluate the dissipative part of the energy-momentum tensor (which includes the shear, bulk viscosity, and diffusion) using $\delta\tilde{f}^{(1,2)}$ and $\delta\tilde{\tilde{f}}^{(1,2)}$ in the following expressions,

$$\pi^{\mu\nu} = \Delta^{\mu\nu}_{\alpha\beta}\int dpp^{\alpha}p^{\beta}\left(\delta\tilde{f}+\delta\tilde{\tilde{f}}\right), \tag{130}$$

$$\Pi = -\frac{\Delta_{\mu\nu}}{3}\int dpp^{\mu}p^{\nu}\left(\delta\tilde{f}+\delta\tilde{\tilde{f}}\right), \tag{131}$$

$$V^{\mu} = \Delta^{\mu}_{\alpha}\int dpp^{\alpha}\left(\delta\tilde{f}-\delta\tilde{\tilde{f}}\right). \tag{132}$$

Using the above definitions along with the conservation equations for energy-momentum we get the magnetohydrodynamics evolution equations for the dissipative quantities.

26.3. *Second order Evolution equations for dissipative stresses*

From the above formalism we derive all the set of equations for non-resistive and resistive mhd for the dissipative stresses. First for the non-resistive case we have :

$$\begin{aligned}\frac{\pi^{\mu\nu}}{\tau_c} =& -\dot{\pi}^{\mu\nu}+2\beta_{\pi}\sigma^{\mu\nu}+2\pi_{\gamma}^{\langle\mu}\omega^{\nu\rangle\gamma}-\tau_{\pi\pi}\pi_{\gamma}^{\langle\mu}\sigma^{\nu\rangle\gamma}-\delta_{\pi\pi}\pi^{\mu\nu}\theta+\lambda_{\pi\Pi}\Pi\sigma^{\mu\nu}\\ &-\tau_{\pi V}V^{\langle\mu}\dot{u}^{\nu\rangle}+\lambda_{\pi V}V^{\langle\mu}\nabla^{\nu\rangle}\alpha+l_{\pi V}\nabla^{\langle\mu}V^{\nu\rangle}+\delta_{\pi B}\Delta^{\mu\nu}_{\eta\beta}qBb^{\gamma\eta}g^{\beta\rho}\pi_{\gamma\rho}\\ &-\tau_c qB\lambda_{\pi VB}V_{\gamma}b^{\gamma\langle\mu}\nabla^{\nu\rangle}\alpha-q\tau_c\delta_{\pi VB}\nabla^{\langle\mu}\left(B^{\nu\rangle\gamma}V_{\gamma}\right)-\tau_c qB\tau_{\pi VB}\dot{u}^{\langle\mu}b^{\nu\rangle\sigma}V_{\sigma},\\ \frac{\Pi}{\tau_c} =& -\dot{\Pi}-\delta_{\Pi\Pi}\Pi\theta+\lambda_{\Pi\pi}\pi^{\mu\nu}\sigma_{\mu\nu}-\tau_{\Pi V}V\cdot\dot{u}-\lambda_{\Pi V}V\cdot\nabla\alpha-l_{\Pi V}\partial\cdot V-\beta_{\Pi}\theta\\ &+\tau_c\tau_{\Pi VB}\dot{u}_{\alpha}qBb^{\alpha\beta}V_{\beta}-\tau_c q\delta_{\Pi VB}\nabla_{\mu}\left(Bb^{\mu\beta}V_{\beta}\right)-\tau_c qB\lambda_{\Pi VB}b^{\mu\beta}V_{\beta}\nabla_{\mu}\alpha,\end{aligned}$$

$$\begin{aligned}\frac{V^{\mu}}{\tau_c} =& -\dot{V}^{\langle\mu\rangle}-V_{\nu}\omega^{\nu\mu}-\lambda_{VV}V^{\nu}\sigma^{\mu}_{\nu}-\delta_{VV}V^{\mu}\theta+\lambda_{V\Pi}\Pi\nabla^{\mu}\alpha-\lambda_{V\pi}\pi^{\mu\nu}\nabla_{\nu}\alpha\\ &-\tau_{V\pi}\pi^{\mu}_{\nu}\dot{u}^{\nu}+\tau_{V\Pi}\Pi\dot{u}^{\mu}+l_{V\pi}\Delta^{\mu\nu}\partial_{\gamma}\pi^{\gamma}_{\nu}-l_{V\Pi}\nabla^{\mu}\Pi+\beta_V\nabla^{\mu}\alpha-qB\delta_{VB}b^{\mu\gamma}V_{\gamma}\\ &+\tau_c qBl_{V\pi B}b^{\sigma\mu}\partial^{\kappa}\pi_{\kappa\sigma}+\tau_c qB\tau_{V\Pi B}b^{\gamma\mu}\Pi\dot{u}_{\gamma}-\tau_c qBl_{V\Pi B}b^{\gamma\mu}\nabla_{\gamma}\Pi\\ &-q\tau_c\delta_{VVB}Bb^{\mu\nu}V_{\nu}\theta-q\tau_c\lambda_{VVB}Bb^{\gamma\nu}V_{\nu}\sigma^{\mu}_{\gamma}-q\tau_c\rho_{VVB}Bb^{\gamma\nu}V_{\nu}\omega^{\mu}_{\gamma}\\ &-\tau_c q\tau_{VVB}\Delta^{\mu}_{\gamma}D\left(Bb^{\gamma\nu}V_{\nu}\right),\end{aligned}$$

Here we can see that along with all the usual transport coefficients in ordinary hydro we have co-efficients like $\delta_{\pi B}$, $\lambda_{\pi VB}$, $\delta_{\pi VB}$, $\tau_{\pi VB}$, $\tau_{\Pi VB}$, $\delta_{\Pi VB}$, $\lambda_{\Pi VB}$, δ_{VB} , $l_{V\pi B}$, $\tau_{V\pi B}$, $l_{V\Pi B}$, δ_{VVB}, λ_{VVB}, ρ_{VVB}, τ_{VVB} are arising from the external magnetic field.

Similarly for resistive case we get :

$$\begin{aligned}
\frac{\Pi}{\tau_c} &= -\dot{\Pi} - \delta_{\Pi\Pi}\Pi\theta + \lambda_{\Pi\pi}\pi^{\mu\nu}\sigma_{\mu\nu} - \tau_{\Pi V}V\cdot\dot{u} - \lambda_{\Pi V}V\cdot\nabla\alpha - l_{\Pi V}\partial\cdot V - \beta_\Pi\theta \\
&\quad -qB\lambda_{\Pi VB}b^{\mu\beta}V_\beta V_\mu + \tau_c\tau_{\Pi VB}\dot{u}_\alpha qBb^{\alpha\beta}V_\beta - q\delta_{\Pi VB}\nabla_\mu\left(\tau_c Bb^{\mu\beta}V_\beta\right) \\
&\quad -q^2\tau_c\chi_{\Pi EE}E^\mu E_\mu. \\
\frac{V^\mu}{\tau_c} &= -\dot{V}^{\langle\mu\rangle} - V_\nu\omega^{\nu\mu} + \lambda_{VV}V^\nu\sigma^\mu_\nu - \delta_{VV}V^\mu\theta + \lambda_{V\Pi}\Pi\nabla^\mu\alpha - \lambda_{V\pi}\pi^{\mu\nu}\nabla_\nu\alpha \\
&\quad -\tau_{V\pi}\pi^\mu_\nu\dot{u^\nu} - qB\delta_{VB}b^{\mu\gamma}V_\gamma + \tau_{V\Pi}\Pi\dot{u^\mu} + l_{V\pi}\Delta^{\mu\nu}\partial_\gamma\pi^\gamma_\nu - l_{V\Pi}\nabla^\mu\Pi + \beta_V\nabla^\mu\alpha \\
&\quad +\tau_c qBl_{V\pi B}b^{\sigma\mu}\partial^\kappa\pi_{\kappa\sigma} - q\tau_c\lambda_{VVB}Bb^{\gamma\nu}V_\nu\sigma^\mu_\gamma + \tau_c qB\tau_{V\Pi B}b^{\gamma\mu}\Pi\dot{u}_\gamma \\
&\quad -\tau_c qBl_{V\Pi B}b^{\gamma\mu}\nabla_\gamma\Pi - q\tau_c\delta_{VVB}Bb^{\mu\nu}V_\nu\theta - q\tau_c\rho_{VVB}Bb^{\gamma\nu}V_\nu\omega^\mu_\gamma \\
&\quad +\chi_{VE}qE^\mu + q\Delta^\mu_\alpha\chi_{VE}D\left(\tau_c E^\alpha\right) - q\tau_c\rho_{VE}E^\mu\theta - q\tau_{VVB}\Delta^\mu_\gamma D\left(\tau_c Bb^{\gamma\nu}V_\nu\right). \\
\frac{\pi^{\mu\nu}}{\tau_c} &= -\dot{\pi}^{\langle\mu\nu\rangle} + 2\beta_\pi\sigma^{\mu\nu} + 2\pi^{\langle\mu}_\gamma\omega^{\nu\rangle\gamma} - \tau_{\pi\pi}\pi^{\langle\mu}_\gamma\sigma^{\nu\rangle\gamma} - \delta_{\pi\pi}\pi^{\mu\nu}\theta + \lambda_{\pi\Pi}\Pi\sigma^{\mu\nu} \\
&\quad -\tau_{\pi V}V^{\langle\mu}\dot{u}^{\nu\rangle} - \tau_c qB\tau_{\pi VB}\dot{u}^{\langle\mu}b^{\nu\rangle\sigma}V_\sigma + \lambda_{\pi V}V^{\langle\mu}\nabla^{\nu\rangle}\alpha - l_{\pi V}\nabla^{\langle\mu}V^{\nu\rangle} \\
&\quad +\delta_{\pi B}\Delta^{\mu\nu}_{\eta\beta}qBb^{\gamma\eta}g^{\beta\rho}\pi_{\gamma\rho} - qB\lambda_{\pi VB}V_\gamma b^{\gamma\langle\mu}V^{\nu\rangle} - q\delta_{\pi VB}\nabla^{\langle\mu}\left(\tau_c B^{\nu\rangle\gamma}V_\gamma\right) \\
&\quad +q^2\tau_c\chi_{\pi EE}\Delta^{\mu\nu}_{\sigma\rho}E^\sigma E^\rho.
\end{aligned}$$

In resistive case we have $\chi_{\Pi EE}$, χ_{VE}, ρ_{VE}, $\chi_{\pi EE}$ as the new transport co-efficients.

26.4. *Anisotropic transport co-efficients*

As we have external electromagnetic field so the isotropic transport coefficients will now split in different directions of the applied force and hence become anisotropic. For anisotropic diffusion co-efficients are :

$$\begin{aligned}
\kappa_\parallel &= \beta_V\tau_c, \\
\kappa_\perp &= \frac{\beta_V\tau_c}{1+\left(qB\tau_c\delta_{VB}\right)^2}, \\
\kappa_\times &= \frac{\beta_V qB\tau_c^2\delta_{VB}}{1+\left(qB\tau_c\delta_{VB}\right)^2} = \kappa_\perp qB\tau_c\delta_{VB}.
\end{aligned}$$

We can see that there is no magnetic field dependence along the direction of B (magnetic field) which is expected and others are $k_\perp$ and $k_\times$ which are the perpendicular component and the hall coefficient respectively. For the shear case we

have:

$$\eta_0 = 2\beta_\pi \tau_c,$$
$$\eta_1 = \frac{2\beta_\pi \tau_c}{1 + (2qB\tau_c \delta_{\pi B})^2},$$
$$\eta_2 = \frac{4\beta_\pi qB\tau_c^2 \delta_{\pi B}}{1 + (2qB\tau_c \delta_{\pi B})^2} = 2\eta_1 qB\tau_c \delta_{\pi B},$$
$$\eta_3 = \frac{2\beta_\pi \tau_c}{1 + (qB\tau_c \delta_{\pi B})^2},$$
$$\eta_4 = \frac{2\beta_\pi qB\tau_c^2 \delta_{\pi B}}{1 + (qB\tau_c \delta_{\pi B})^2} = \eta_3 qB\tau_c \delta_{\pi B}.$$

In this case η_0 is the coefficient along the direction of applied field, whereas η_1, η_3 are perpendicular components, with η_2 and η_4 being the hall coefficients.

Lastly for anisotropic coefficients for conductivity we have:

$$\sigma_E^{\parallel} = q^2 \tau_c \beta \beta_V,$$
$$\sigma_E^{\perp} = \frac{q^2 \tau_c \beta \beta_V}{1 + (qB\tau_c \delta_{VB})^2},$$
$$\sigma_E^{\times} = \frac{q^3 B\tau_c^2 \beta \beta_V \delta_{VB}}{1 + (qB\tau_c \delta_{VB})^2}.$$

Here also we have the same interpretation for the said notations as in case of the diffusion. The leading contributors to the anisotropy are $\delta_{\pi B}$ and δ_{VB} and its variation with mass and temperature has been studied below in Figs.[57,58] .

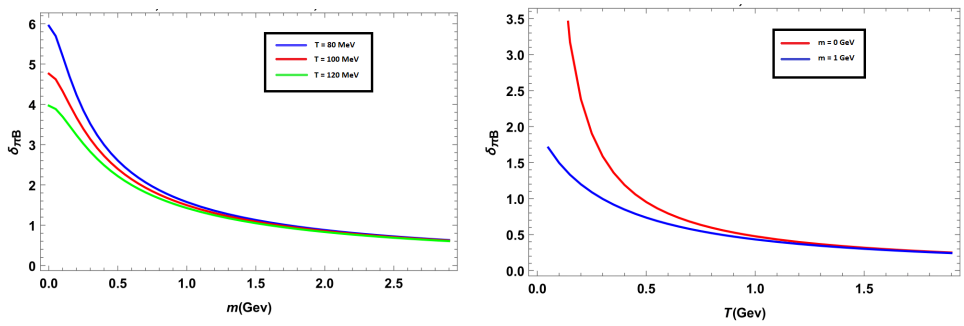


Fig. 57: Here left plot shows variation of $\delta_{\pi B}$ with mass for different values of temperature. Right plot shows variation of $\delta_{\pi B}$ with temperature for different values of masses.

Here we can see that $\delta_{\pi B}$ and δ_{VB} are sensitive to different temperature at low mass region Fig.[57 (left),58 (left)] and sensitive to different mass at low temperature region in Fig.[57 (right),58 (right)].

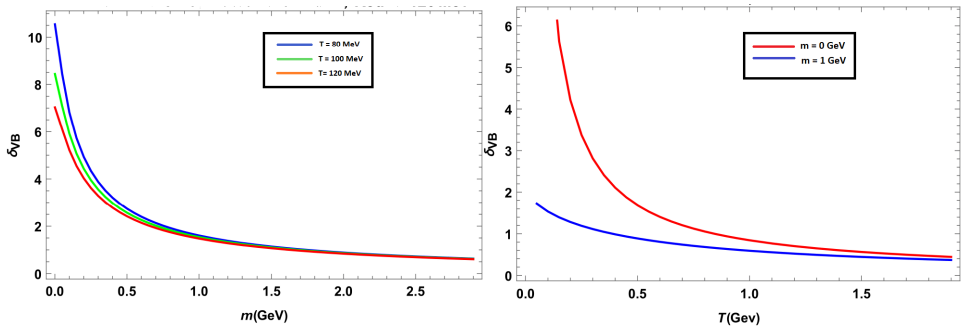


Fig. 58: Here left plot shows variation of δ_{VB} with mass for different values of temperature. Right plot shows variation of δ_{VB} with temperature for different values of masses.

27. Parameters estimation of the Viscous Blast-Wave model using Machine learning techniques

Nachiketa Sarkar and Amaresh Jaiswal

Recently different statistical-based Machine learning techniques are being used vastly in the field of computational heavy-ion physics to overcome the need for immense computational power. We have developed a general machine learning code using the bayesian statistics that enables us to quantify the multi-parameters model by comparing multiple experimental observables simultaneously. Though this framework is universal and can be applied to any model or data set, in this study, we have implemented this framework in the Viscous Blast-Wave model, which has six parameters, including the η/s. We have calibrated the model to reproduce experimental data and extracted all the model parameters and their correlation simultaneously.

27.1. *Introduction*

The primary goal of the ultra-relativistic heavy-ion experiments is to inspect the properties of quark-gluon plasma (QGP) produced in such collisions. In the absence of a smoking-gun signal, a general approach to understand the QGP properties is to compare experimental results with model predictions. Numerical descriptions of heavy-ion physics are very complex and need huge CPU time, sometimes beyond our reach. Different phases of the heavy-ion collision, i.e., from collision geometry to final state hadron production, are described by different physics models. The model often takes multiple inputs and produces multiple observables that usually have complex correlations. Recently, efficient implementation of the bayesian techniques has been done in[261,262] to overcome the massive computational challenges of quantifying the properties of QGP by extracting model parameters via comparing the model to data. Following the prescription in,[261,262] we have developed our parameter-estimation code using different machine learning techniques. This framework is wholly based on the data-driven approach and can be applied to any data or model.

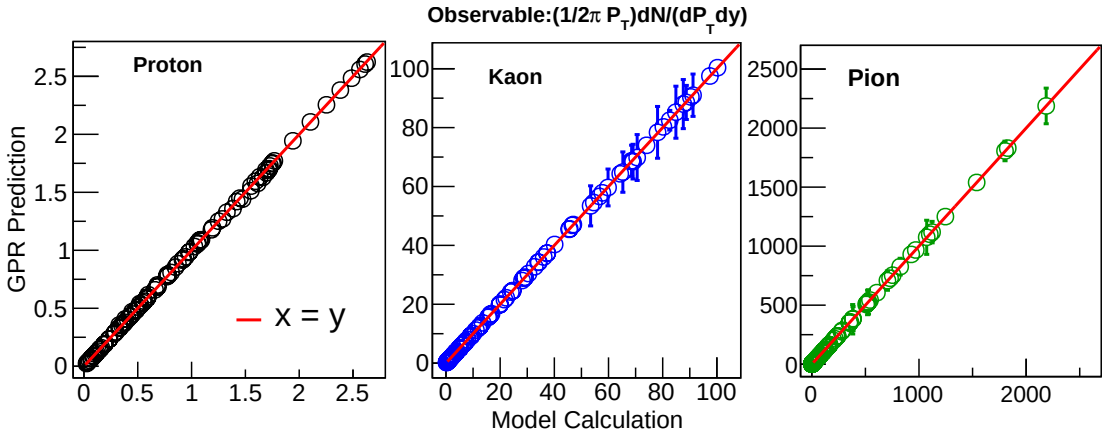


Fig. 59: The emulator validation plots, represent the comparison between the emulator predictions and VBW model outputs for fifty randomly generated points in the parameter space.

The present work is dedicated to estimating the Viscous Blast-Wave (VBW) model parameters. For the constraints of space, we will not discuss the VBW model here, details can be found in the ref.[263] The VBW model has six input parameters, including freeze-out temperature T_f, the radial velocity β_0 at the freeze-out surface, and η/s. The other three parameters, m, κ, and α_0 related to the freeze-out radius and flow harmonics. For detailed information about parameters see ref.[263] Our goal is the quantitative-estimation of these parameters by simultaneous fitting the experimental p_T spectrum of different hadrons for different centrality classes.

27.2. *Model Description and Result*

We have performed our analyses in two phases. In the first step, using the Gaussian Process(GP) emulator, we have built a surrogate model of the given physics model of interest, i.e., fast model prediction for any arbitrary set of parameters without explicitly executing the VBW-code. In the next phase, using bayesian statistics, we extracted the posterior probability distribution of the model parameters by comparing the experimental result.

27.3. *Gaussian Process Emulator*

Gaussian Process (GP),[264] is a supervised learning algorithm based on bayesian statistics. The posterior distribution is obtained from the prior distribution through the training data set. To create the training data set we generate 300 (m = 300) points $X[x_1, x_2....x_m]$ in the six-dimensional (n = 6) parameter space using Latin Hypercube sampling algorithm[265] and then produce m model outputs

$Y[y_1, y_2....y_m]$ at the each point by executing VBW-code. Finally, we trained the emulator using this data set. For a given test point x_*, the posterior distribution of the emulator outputs y_* is the multivariate gaussian distribution, completely defined by mean, μ, and covariance matrix, Σ, i.e.,

$$\begin{aligned} y_* &\sim \mathcal{N}(\mu, \Sigma) \\ \mu &= \sigma(X_*, X)\sigma(X_*, X)^{-1} y, \\ \Sigma &= \sigma(X_*, X_*) - \sigma(X_*, X)\sigma(X_*, X)^{-1}\sigma(X, X_*) \end{aligned} \tag{133}$$

Where, σ's are the square matrices whose each element represents the covariance function between pairs of points.

$$\sigma(X, X) = \begin{pmatrix} \sigma(x_1, x_1) & \cdots & \sigma(x_1, x_m) \\ \vdots & \ddots & \vdots \\ \sigma(x_m, x_1) & \cdots & \sigma(x_m, x_m) \end{pmatrix} \tag{134}$$

In the present work, we have chosen the following covariance function,

$$\sigma(x, x\prime) = \sigma_{GP}^2 \exp\left[-\sum_{k=1}^{n} \frac{(x_k - x_k\prime)^2}{2l_k^2} \right] + \sigma_n^2 \delta_{xx\prime}. \tag{135}$$

σ_{GP}^2, l_k, and σ_n are known as *hyperparameters*, related to the total variance of the GP, correlation length between pairs of points, and statistical noise, respectively. The *hyperparameters* are tuned during the tanning process.

Finally, to validate emulator prediction, we generate fifty random points in the parameter space and compare emulator predictions with VBW model outputs at each point. We have presented our validation check in Figure (59). It is clear from Figure (59), that the emulator faithfully reproduces the VBW model outputs. One should note that, the errors in Figure (59), represent emulator prediction error which depends on the relative position of the prediction and training point in the parameter space. The emulator error increase if the distance between the nearest training point and the prediction point increases. Thus some points which are far away from training points have larger errors than others.

Here we like to mention that we have performed Principal Component Analyses (PCA)[266] to reduce the dimensionality. All the analyses are done on the reduced PCA space and finally performed the reverse transformation to get the results in the physical space.

27.4. *Model Calibration*

After building a faithful emulator, the final task left is the model calibration, thereby extracting the posterior distributions of model parameters by comparing experimental data.[267] According to bayesian statistics, if x_* represents the desired set of input that reproduces the experimental results, then the posterior distribution is,

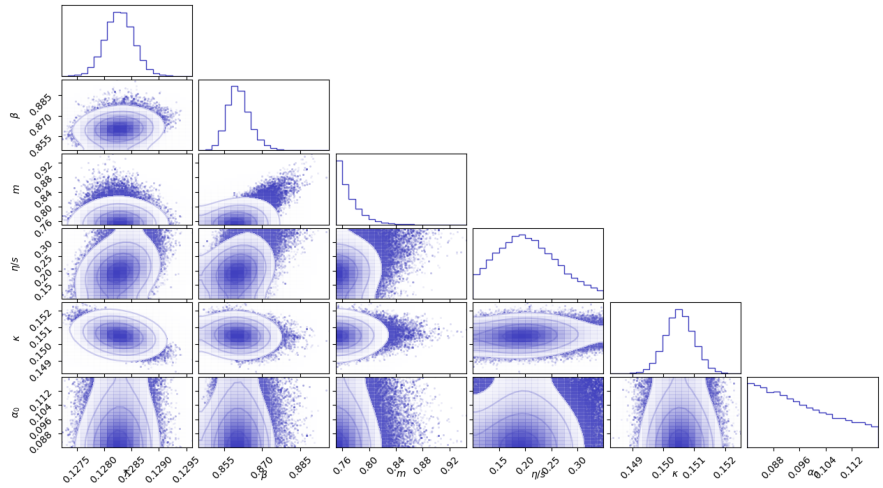


Fig. 60: The corner plot generated from the MCMC samples represents the posterior marginal and joint probability distribution of the VBW model parameters.

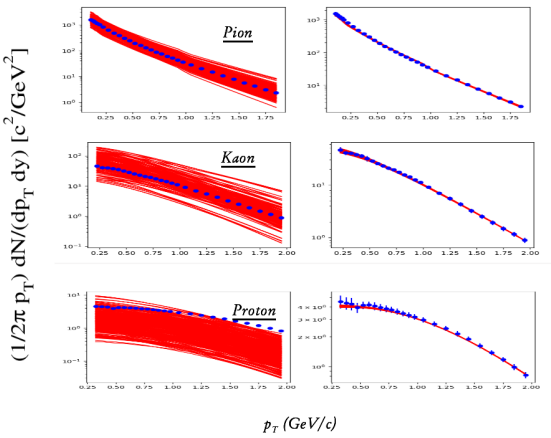


Fig. 61: Comparison of the transverse momentum distribution of the hadrons in the Pb+Pb collision for the most central events $(0-5\%)$ between the experimental results and emulator predictions with prior and posterior parameter sets. The symbols represent experimental data.[267]

$$P(x_*|X,Y,y_{exp}) \propto P(X,Y,y_{exp}|x_*)P(x_*) \tag{136}$$

For the Bayesian analysis, we used Markov chain Monte Carlo (MCMC) based on affine-invariant ensemble sampling algorithm[268] employing the following likeli-

Table 2: Quantitative estimated parameters values of the VBW model from the posterior distribution. C.I. represents the confidence interval.

C.I.	T_F	β_0	m	η/s	κ	α_0
99%	126.6-129.0	0.85-0.88	0.75- 0.84	0.16- 0.32	0.149-0.152	0.08-0.12
95%	126.8-128.8	0.84-0.87	0.75- 0.81	0.15- 0.30	0.149-0.151	0.08-0.12

hood and prior distribution function.

$$P(x_*|X,Y,y_{exp}) \propto \exp\Big[-1/2(z_*-z_{exp})^T\Sigma_z^{-1}(z_*-z_{exp})\Big] \tag{137}$$

$$P(x_*) = \begin{cases} 1 & min(x_i) \leq x_i \leq max(x_i), \forall i \\ 0 & otherwise. \end{cases} \tag{138}$$

z_* and z_{exp} are the principal components of emulator outputs, y_* and experimental data y_{exp} respectively. Σ_z is the covariance or the uncertainty matrix, for this work we take $\Sigma_z = diag(\sigma_z^2 z_{exp})$ with $\sigma_z^2 = 0.10$.[262]

The final results of our analyses are presented in Figure (60) and (61). Figure (60) is the well-known corner plot, where the diagonal plots are the marginal distributions of the parameters and off-diagonal plots represent contour plots of the correlations between the pair of parameters. The estimated values of different parameters are given in Table (2). Figure (61) represents the comparison between the experimental data with emulator predication for the prior and posterior parameter sets. Figures in the right column represent the visualization confirmation that the posterior parameters sets truly represent the experimental data.

27.5. *Summary and Future plan*

In summary, we have presented the Viscous Blast-Wave model parameters estimation analyses using bayesian technique and different machine learning tools. This is our preliminary analyses using the machine learning techniques. We are working to incorporate different flow coefficients as well as different centrality classes in our future analyses.

28. Charge and heat transport properties of a weakly magnetized hot QCD matter at finite density

Shubhalaxmi Rath

The effect of weak magnetic field on the transport of charge and heat in hot and dense QCD matter has been explored by calculating electrical ($\sigma_{\rm el}$) and thermal (κ) conductivities in kinetic theory approach. The interactions among partons have been encoded

in their thermal masses. We have noticed that both $\sigma_{\rm el}$ and κ decrease with magnetic field, whereas, these transport coefficients increase with chemical potential. Further, we have observed the effects of weak magnetic field and chemical potential on the Knudsen number. We have observed a reduction of the Knudsen number in a weak magnetic field, contrary to its enhancement at finite chemical potential. However, its value remains below unity, so, the hot and dense QCD matter remains in the equilibrium state in the presence of a weak magnetic field.

28.1. *Introduction*

Strong evidences for the production of quark-gluon plasma (QGP) have been found in heavy ion collisions at Relativistic Heavy Ion Collider (RHIC) and Large Hadron Collider (LHC). High temperature and/or high density can facilitate the production of QGP. In addition, for noncentral collisions, strong magnetic fields are produced with strength varying between $eB = m_\pi^2$ ($\simeq 10^{18}$ Gauss) at RHIC and $eB = 15\ m_\pi^2$ at LHC. These magnetic fields are transient, so, there are two scenarios of magnetic field: strong magnetic field ($eB \gg T^2$) and weak magnetic field ($T^2 \gg eB$). However, the electrical conductivity can noticeably elongate the lifetimes of such magnetic fields.[2,269] In the presence of a magnetic field, charge and heat transport coefficients acquire multicomponent structures.[270] Out of different components, our present analysis focuses on the study of electrical ($\sigma_{\rm el}$) and thermal (κ) conductivities using kinetic theory approach in the relaxation time approximation, where thermal masses of particles encode the interactions among them. Previously, thermal mass of quark in the strong magnetic field regime had been calculated and used in the study of transport coefficients.[269,271] In weak magnetic field limit, we assume that the phase space and the single particle energies are not affected by the magnetic field through Landau quantization,[272] rather, the main contribution of the magnetic field enters through the cyclotron frequency. As an application, we also study the Knudsen number (Ω) to understand the local equilibrium property in the presence of weak magnetic field and finite chemical potential.

28.2. *Charge transport coefficient*

The external electric field disturbs the system infinitesimally, thus resulting an induced electric current density, which is written as

$$J^\mu = \sum_f g_f \int \frac{d^3{\rm p}}{(2\pi)^3} \frac{p^\mu}{\omega_f} [q\delta f_f(x,p) + \bar{q}\delta \bar{f}_f(x,p)] \ , \tag{139}$$

where g_f is the degeneracy factor of quark with flavor f, $g_f = 6$. According to the Ohm's law, the longitudinal component of the spatial part of four-current density is directly proportional to the electric field with the proportionality factor being the electrical conductivity ($\sigma_{\rm el}$),

$$J^i = \sigma_{\rm el} \delta^{ij} E_j \ . \tag{140}$$

The δf_f is calculated from the relativistic Boltzmann transport equation in the relaxation time approximation,

$$p^\mu \frac{\partial f_f(x,p)}{\partial x^\mu} + \mathcal{F}^\mu \frac{\partial f_f(x,p)}{\partial p^\mu} = -\frac{p_\nu u^\nu}{\tau_f} \delta f_f(x,p) \ , \tag{141}$$

where $f_f = \delta f_f + f_f^0$, $\mathcal{F}^\mu = qF^{\mu\nu}p_\nu = (p^0 \mathbf{v}\cdot\mathbf{F}, p^0\mathbf{F})$ with $F^{\mu\nu}$ being the electromagnetic field strength tensor and the Lorentz force, $\mathbf{F} = q(\mathbf{E} + \mathbf{v}\times\mathbf{B})$. The relaxation time for quark (antiquark), τ_f ($\tau_{\bar{f}}$) is written[273] as

$$\tau_{f(\bar{f})} = \frac{1}{5.1 T \alpha_s^2 \log(1/\alpha_s)\left[1 + 0.12(2N_f+1)\right]} \ . \tag{142}$$

For a spatially homogeneous distribution function with steady-state condition ($\frac{\partial f_f}{\partial \mathbf{r}} = 0$ and $\frac{\partial f_f}{\partial t} = 0$), and for $\mathbf{E} = E\hat{x}$ and $\mathbf{B} = B\hat{z}$, Eq. (141) becomes

$$\tau_f q E v_x \frac{\partial f_f}{\partial p_0} + \tau_f q B v_y \frac{\partial f_f}{\partial p_x} - \tau_f q B v_x \frac{\partial f_f}{\partial p_y} = f_f^0 - f_f - \tau_f q E \frac{\partial f_f^0}{\partial p_x} \ . \tag{143}$$

To solve the above equation, the following ansatz has been used,

$$f_f = f_f^0 - \tau_f q \mathbf{E}\cdot\frac{\partial f_f^0}{\partial \mathbf{p}} - \mathbf{\Gamma}\cdot\frac{\partial f_f^0}{\partial \mathbf{p}} \ , \tag{144}$$

where $\mathbf{\Gamma}$ depends on magnetic field. Using ansatz (144), Eq. (143) becomes

$$\tau_f q E v_x \frac{\partial f_f}{\partial p_0} + \beta f_f^0 \mathbf{\Gamma}\cdot\mathbf{v} - qB\tau_f \left(v_x \frac{\partial f_f}{\partial p_y} - v_y \frac{\partial f_f}{\partial p_x} \right) = 0 \ . \tag{145}$$

From Eq. (145) and ansatz (144), we calculate δf_f and $\delta \bar{f}_f$ and then by substituting them in Eq. (139) and comparing with Eq. (140), we get $\sigma_{\rm el}$[274] as

$$\sigma_{\rm el} = \frac{\beta}{3\pi^2} \sum_f g_f q_f^2 \int d\mathrm{p} \frac{\mathrm{p}^4}{\omega_f^2} \left[\frac{\tau_f f_f^0 \left(1 - f_f^0\right)}{1 + \omega_c^2 \tau_f^2} + \frac{\tau_{\bar{f}} \bar{f}_f^0 \left(1 - \bar{f}_f^0\right)}{1 + \omega_c^2 \tau_{\bar{f}}^2} \right] . \tag{146}$$

28.3. *Heat transport coefficient*

The heat flow four-vector is the difference between the energy diffusion and the enthalpy diffusion,

$$Q_\mu = \Delta_{\mu\alpha} T^{\alpha\beta} u_\beta - h \Delta_{\mu\alpha} N^\alpha, \tag{147}$$

where $\Delta_{\mu\alpha} = g_{\mu\alpha} - u_\mu u_\alpha$ and the enthalpy per particle $h = (\varepsilon + P)/n$ with the particle number density $n = N^\alpha u_\alpha$, the energy density $\varepsilon = u_\alpha T^{\alpha\beta} u_\beta$ and the pressure $P = -\Delta_{\alpha\beta} T^{\alpha\beta}/3$. The spatial component of the heat flow is given by

$$Q^i = \sum_f g_f \int \frac{d^3\mathrm{p}}{(2\pi)^3} \frac{p^i}{\omega_f} \left[(\omega_f - h_f)\delta f_f(x,p) + (\omega_f - \bar{h}_f)\delta \bar{f}_f(x,p) \right] . \tag{148}$$

According to the Navier-Stokes equation, we have

$$Q^i = -\kappa \delta^{ij} \left[\partial_j T - \frac{T}{\varepsilon + P} \partial_j P \right] , \tag{149}$$

where κ is thermal conductivity. With the help of ansatz (144), Eq. (141) becomes

$$\tau_f \frac{\partial f_f^0}{\partial t} + \frac{\tau_f \mathbf{p}}{p_0} \cdot \frac{\partial f_f^0}{\partial \mathbf{r}} + \beta f_f^0 \mathbf{\Gamma} \cdot \mathbf{v} + \tau_f q E v_x \frac{\partial f_f}{\partial p_0} - qB\tau_f \left(v_x \frac{\partial f_f}{\partial p_y} - v_y \frac{\partial f_f}{\partial p_x} \right) = 0. \quad (150)$$

From Eq. (150) and ansatz (144), we calculate δf_f and $\delta \bar{f}_f$. Substituting them in Eq. (148) and then comparing with Eq. (149), we get κ[274] as

$$\kappa = \frac{\beta^2}{6\pi^2} \sum_f g_f \int d\mathrm{p} \frac{\mathrm{p}^4}{\omega_f^2} \left[\frac{\tau_f \left(\omega_f - h_f\right)^2 f_f^0 \left(1 - f_f^0\right)}{1 + \omega_c^2 \tau_f^2} + \frac{\tau_{\bar{f}} \left(\omega_f - \bar{h}_f\right)^2 \bar{f}_f^0 \left(1 - \bar{f}_f^0\right)}{1 + \omega_c^2 \tau_{\bar{f}}^2} \right]. \quad (151)$$

28.4. *Knudsen number*

The Knudsen number (Ω) gives the information about the local equilibrium property of the medium and is defined by the ratio of the mean free path (λ) to the characteristic length scale of the medium (l). Since λ is related to the thermal conductivity ($\lambda = \frac{3\kappa}{vC_V}$), one can write Ω in terms of κ as

$$\Omega = \frac{\lambda}{l} = \frac{3\kappa}{lvC_V} \ , \quad (152)$$

where v is relative speed and $C_V = \partial(u_\mu T^{\mu\nu} u_\nu)/\partial T$ is specific heat at constant volume. In our calculation, we have set $v \simeq 1$ and $l = 4$ fm.

The aforementioned transport coefficients and application are studied by using the thermal masses of charged particles. The thermal mass (squared) of quark is given[275] by $m_{fT}^2 = \frac{g^2 T^2}{6}\left(1 + \frac{\mu_f^2}{\pi^2 T^2}\right)$. We have taken the chemical potentials for all flavors to be the same, i.e. $\mu_f = \mu$.

28.5. *Results and discussions*

From Fig. 62a, it is observed that, σ_{el} gets decreased in the presence of a weak magnetic field, which can be understood as follows: σ_{el} is directly proportional to the current along the direction of electric field. But, due to the emergence of magnetic field, the direction of moving quarks gets deflected and it causes a reduction of current along the direction of electric field, thus decreasing the electrical conductivity. On the other hand, an increase of σ_{el} is observed at finite chemical potential, which is mainly due to the increase of distribution function at finite chemical potential. Thus, weak magnetic field reduces the charge conduction in QCD medium, whereas finite chemical potential facilitates this. From Fig. 62b, it is found that the weak magnetic field reduces κ too, whereas its increase is observed at finite chemical potential. The increase of κ with temperature is mainly due to the increase of both enthalpy per particle and distribution function with temperature. Thus, like charge conduction, heat conduction also gets waned in a weak magnetic field, whereas finite chemical potential enhances this.

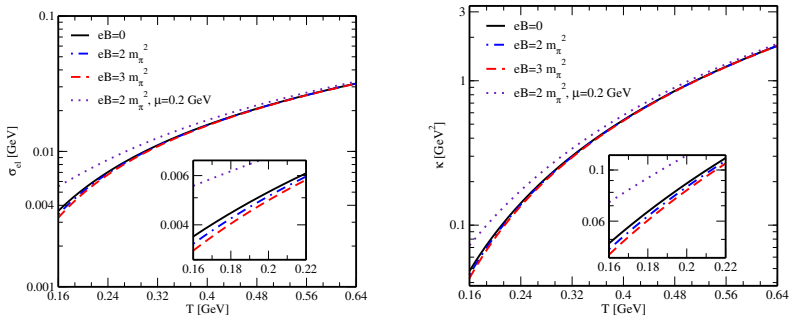


Fig. 62: Variations of (a) $\sigma_{\rm el}$ and (b) κ with temperature for different weak magnetic fields and chemical potentials.

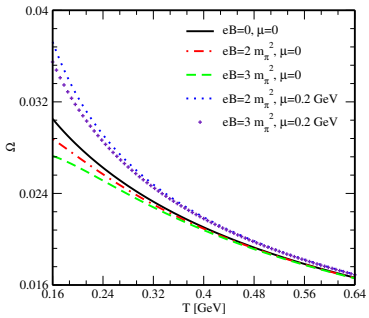


Fig. 63: Variation of Ω with temperature for different weak magnetic fields and chemical potentials.

Figure 63 depicts the variation of the Knudsen number with the temperature. The Ω retains its magnitude much below unity, but in the presence of weak magnetic field it gets decreased, whereas the emergence of chemical potential increases its magnitude. The behavior of Ω at finite eB and finite μ corroborates the behavior of κ in the similar environment. Throughout the variation, the Knudsen number remains much below unity, indicating that the macroscopic length scale prevails over the microscopic length scale. Thus, the hot QCD matter remains in local equilibrium state even in the presence of both weak magnetic field and finite chemical potential.

28.6. *Conclusions*

In this work, we studied the effects of weak magnetic field and finite chemical potential on the electrical and thermal conductivities of hot and dense QCD matter, which were determined by following the kinetic theory. It is observed that both $\sigma_{\rm el}$

and κ get decreased in a weak magnetic field, whereas the finite chemical potential increases their magnitudes. Further, we studied the Knudsen number and found that it retains its value below unity, so, the characteristic length scale remains larger than the mean free path and the hot QCD matter stays in the equilibrium state even in the presence of both weak magnetic field and finite chemical potential.

29. Multiplicity dependent study of Λ(1520) production in pp collisions at $\sqrt{s} = 5$ and 13 TeV

Sonali Padhan (For the ALICE collaboration)

We present the measurement of the baryonic resonance particle Λ(1520) (mass = 1520 MeV/c^2) at mid-rapidity ($|y| < 0.5$) in pp collisions at 5.02 and 13 TeV as a function of charged-particle multiplicity. Λ(1520) is reconstructed using its hadronic decay channel Λ(1520) ($\bar{\Lambda}$(1520)) $\rightarrow pK^-(\bar{p}K^+)$ with branching ratio (BR = 22.5 ± 1%). Λ(1520) has a lifetime of around 13 fm/c, which lies between the lifetimes of K^* and ϕ resonances. The multiplicity dependence of the Λ(1520)/Λ ratio for pp collisions can serve as a baseline for heavy-ion collisions.

29.1. *Introduction*

Hadronic resonances are short-lived particles having lifetime comparable to QGP fireball. They are valuable tools to study the hadronic phase in ultrarelativistic heavy-ion collisions. Most of the hadrons' measured yields are constant between the chemical and kinetic freeze-out. In the case of resonance particles, their yields and transverse momenta may be affected by pseudo-elastic rescattering or regeneration effects due to interactions with hadrons in the hadron gas phase .[276] The rescattering suppresses the measured yield, while the regeneration enhances the resonance yield.

The ratio of hadronic resonances to the stable particles' yields could provide information on the in-medium properties of the hadronic phase. The Λ(1520)/Λ ratio in pp collisions can serve as a baseline for heavy-ion collisions. We present the transverse-momentum spectra, the integrated yields ($\mathrm{d}N/\mathrm{d}y$), the mean transverse-momentum ($\langle p_{\mathrm{T}} \rangle$) and the Λ(1520)/Λ yield ratio and the multiplicity dependence of Λ(1520) production as a function of the charged-particle multiplicity in pp collisions at $\sqrt{s} = 5.02$ and 13 TeV with ALICE.

29.2. *Analysis Procedure*

This analysis is carried out by the data collected using the ALICE detector.[277] The details on the performance of the ALICE detector can be found in .[111] The Inner Tracking System (ITS) is responsible for the tracking and vertex finding. The tracking and particle identification can be done by using the Time Projection Chamber (TPC). The Time of Flight (TOF) detector is used for the PID of relativcely high momentum particles. The identification of protons and kaons is carried out using

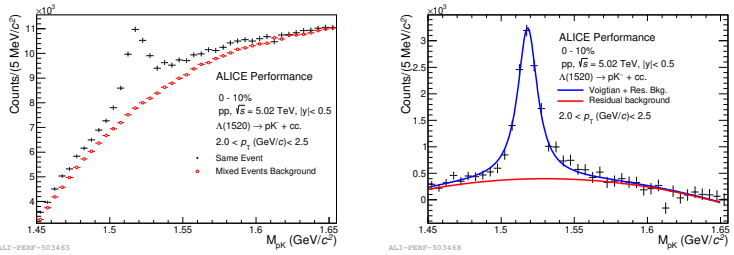


Fig. 64: The invariant mass distribution before (left panel) and after (right panel) subtracting the normalized mixed-event background distribution.The black histograms are the data. The signal is described by the blue line which is the Voigtian function plus a second order polynomial and the red line is the second order polynomial describing the residual background.

the TPC dE/dx energy loss measurement. For event selection, it is required to have a reconstructed primary vertex within 10 cm of the interaction point.

The $\Lambda(1520)$ production has been measured by invariant mass reconstruction of its decay daughters through the hadronic decay channel: $\Lambda(1520)$ ($\bar{\Lambda}(1520)$) $\rightarrow pK^-(\bar{p}K^+)$. $\Lambda(1520)$ resonance is reconstructed by computing the invariant mass spectrum of all the pK primary track pairs. Then the combinatorial background is subtracted, which is estimated by mixed-event techniques. The signal of the invariant mass distribution is fitted with a voigtian function (convolution of non-relativistic Briet-Wigner and a gaussian detector resolution) plus a 2nd order polynomial for the residual background. The invariant mass plot of $\Lambda(1520)$ is given in Fig. 64. The fully corrected $p_{\rm T}$ spectrum is obtained by correcting the raw yield with branching ratio, re-weighted efficiency, vertex correction factor, signal loss correction factor, and trigger efficiency factor.

29.3. *Results*

We present the $p_{\rm T}$ spectra of $\Lambda(1520)$ for five V0 multiplicity classes (0–10%, 10–30%, 30–50%, 50–70%, 70–100%) as shown in Fig. 65. The ratio to 0-100% multiplicity class is shown in the bottom panel. We observed the hardening of $p_{\rm T}$ spectra with the increasing multiplicity classes, and similar behaviour is observed for other resonances in pp, p–Pb, and Xe–Xe collisions.

A Levy-Tsallis function is fitted to the $p_{\rm T}$-spectra to obtain integrated yields dN/dy and average transverse momentum $\langle p_{\rm T}\rangle$. $\Lambda(1520)$ $p_{\rm T}$ Integrated yield and mean transverse momentum have been calculated as a function of charged particle multiplicity in various V0 multiplicity classes as shown in Fig. 66. The $p_{\rm T}$ Integrated yield and mean transverse momentum increase with multiplicity and are independent of the collisions systems and energies.

The $\Lambda(1520)/\Lambda$ ratio as a function of charged particle multiplicity in pp collisions

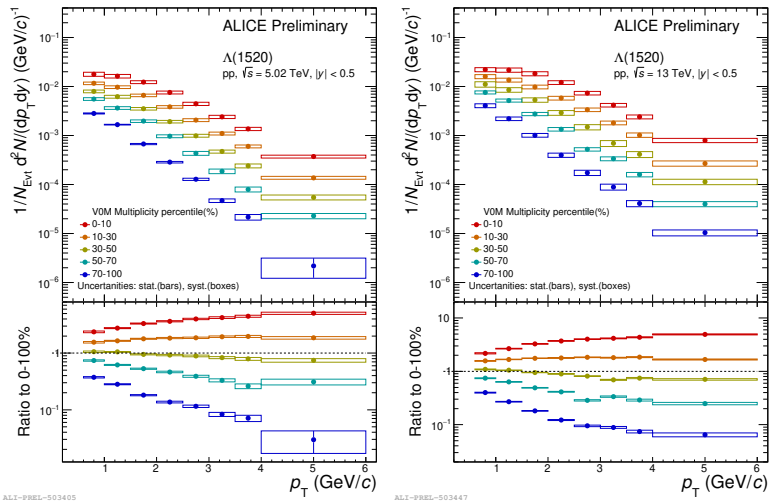


Fig. 65: $\Lambda(1520)$ p_{T} spectra for different multiplicity classes in mid rapidity pp collisions at $\sqrt{s} = 5.02$ TeV (left panel)and 13 TeV (right panel).Bars show statistical errors and boxes show the systematic errors.

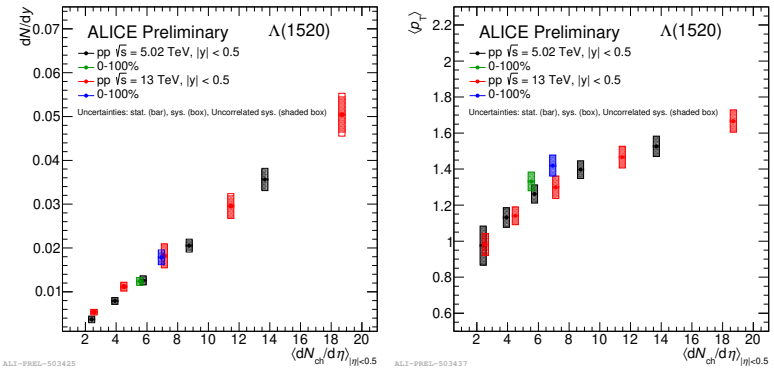


Fig. 66: Integrated yield(left panel) and mean transverse momentum(right panel) of $\Lambda(1520)$ as a function of charged particle multiplicity in pp collisions at $\sqrt{s} = 5.02$ TeV and 13 TeV in various multiplicity classes. Bars, boxes, and shaded boxes are the statistical errors, systematics errors and uncorrelated errors respectively .

at $\sqrt{s} = 5.02$ and 13 TeV is shown in the Fig. 67(left panel). Right panel shows the comparison of this ratio with other systems and energies [279 , 280] . There is a suppression of the $\Lambda(1520)/\Lambda$ ratio in Pb–Pb collisions at $\sqrt{s_{\mathrm{NN}}} = 2.76$ TeV as a function of centrality with respect to peripheral Pb–Pb collisions.[279] But no such significance suppression is observed in case of p–Pb collisions at $\sqrt{s_{\mathrm{NN}}} = 5.02$ TeV

.[280] We observed that $\Lambda(1520)/\Lambda$ ratio is almost flat in pp collisions at $\sqrt{s} = 5.02$ and 13 TeV and is independent of multiplicity.

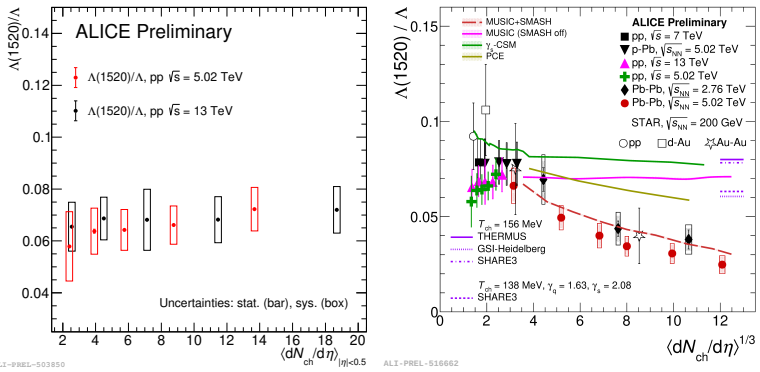


Fig. 67: $\Lambda(1520)/\Lambda$ ratio as a function of charged particle multiplicity in pp collisions at $\sqrt{s} = 5.02$ and 13 TeV (left panel) and compared with previous measurement (right panel).

29.4. *Conclusion*

The resent results on the measurement of baryonic resonance $\Lambda(1520)$ in pp collisions at $\sqrt{s} = 5.02$ TeV and 13 TeV obtained from ALICE detector have been presented. Both p_{T} Integrated yield and mean transverse momentum increase with multiplicity and are independent of collisions systems and energies. The $\Lambda(1520)/\Lambda$ ratio is flat as a function of charged particle multiplicity in pp collisions.

30. Non-identical particle femtoscopy in Pb–Pb collisions at $\sqrt{s_{\mathrm{NN}}} = 5.02$ TeV with ALICE

Pritam Chakraborty (for the ALICE Collaboration)

The pion-kaon femtoscopic correlation functions are obtained in Pb–Pb collisions at $\sqrt{s_{\mathrm{NN}}} = 5.02$ TeV with ALICE at the LHC and femtoscopic parameters are extracted. The spherical harmonics representations of the correlation function are investigated. The results are compared with the predictions from (3+1)D Lhyquid + THERMINATOR 2 model.

30.1. *Introduction*

Femtoscopy has been used to measure the space–time dimensions of the particle-emitting source created in heavy-ion collisions using two-particle correlations. With non-identical particle femtoscopy, one can measure the size of source as well as the

average pair-emission asymmetry that are directly related to the collectivity of the system and transverse mass of the particles. The measurement of femtoscopic correlations between charged pion and kaon pairs for different charge combinations obtained in Pb–Pb collisions at $\sqrt{s_{\rm NN}} = 5.02$ TeV with ALICE at the LHC is presented.

30.2. *Formalism of Femtoscopy*

The femtoscopic correlation function (CF) can be constructed experimentally using Eq. 153

$$C(k^*) = A(k^*)/B(k^*) \tag{153}$$

where, k^* is the pair-relative momentum, $A(k^*)$ and $B(k^*)$ are the distribution of particle-pairs selected from same events (signal) and different events (background), respectively. Theoretically, the CF can be interpreted as the convolution of emission probability of particle-pair, namely source function, $S(k^*, r^*)$ and the final state interaction between particles, $\Psi(k^*, r^*)$, as given in Eq: 154 281.

$$C(k^*) = \int S(k^*, r^*)|\Psi(k^*, r^*)|^2 d^3r^* \tag{154}$$

For pion-kaon pairs, $\Psi(k^*, r^*)$ includes the Coulomb and Strong interaction as given in Eq: 155 281.

$$\Psi(k^*, r^*) = \sqrt{A_C(\eta)}\left[e^{-ik^*r^*}F(-i\eta, 1, i\zeta) + f_C(k^*)\frac{G(\rho, \eta)}{r^*}\right] \tag{155}$$

where, $\mathbf{r}^*$ and $\mathbf{k}^*$ are the pair-relative separation and half of pair-relative momentum at Pair Rest Frame (PRF, where total momentum of the pair is zero), respectively, A_C is the Gamow factor, $\eta = 1/k^*a_C$, F is the confluent hypergeometric function, G is the combination of the regular and singular s-wave Coulomb functions, $\zeta = k^*r^*(1 + cos\theta^*)$, f_C is the strong scattering amplitude, θ^* is the angle between the pair relative momentum k^* and relative position r^* in PRF, a_C is the Bohr radius of the pair which is equal to 248.52 fm for like-sign and -248.52 fm 281 for unlike-sign pion-kaon pair.

In this analysis, the spherical harmonics representations (SH) of the correlation function have been analysed since most of the femtoscopic information can be extracted using the lower harmonics of CF and lesser statistics of pair-particles compared to the conventional method. The coordinate system used in this analysis consists of 3 axes, *out*, *side* and *long*, where, *out* is along the pair-transverse momentum, *long* is along the beam direction and *side* is perpendicular to other two axes. Using C_0^0 and ReC_1^1, the system-size ($R_{\rm out}$) and the pair-emission asymmetry along the *out* direction ($\mu_{\rm out}$), respectively, can be estimated.

To extract the $R_{\rm out}$ and $\mu_{\rm out}$, the experimental correlation function is parameterised using Eq. 154. The source function is assumed to be a 3 dimensional Gaussian

function with sizes $R_{\rm out}$, $R_{\rm side}$ and $R_{\rm long}$ in *out*, *side* and *long* directions and the pair emission asymmetry $\mu_{\rm out}$ along *out* direction as given in Eq. 156 281.

$$S(\mathbf{r}) = exp\left(-\frac{(r_{\rm out}-\mu_{\rm out})^2}{R^2_{\rm out}} - \frac{r^2_{\rm side}}{R^2_{\rm side}} - \frac{r^2_{\rm long}}{R^2_{\rm long}}\right) \tag{156}$$

While parameterising S, it is assumed that $R_{\rm side} = R_{\rm out}$ and $R_{\rm long} = 1.3R_{\rm out}$ based on the results from identical particle 3D femtoscopy for pions from RHIC 281.

30.3. *Analysis details*

The femtoscopic correlation functions of pion-kaon pairs, produced in Pb−Pb collisions at $\sqrt{s_{\rm NN}}$ = 5.02 TeV with ALICE at the LHC have been analysed for 0-5% to 40-50% central events. The events with vertex-z positions $|{\rm z_{vtx}}| < 7.0$ cm are selected. The pions and kaons are selected within $|\eta| < 0.8$ having $0.19 < p_{\rm T}({\rm GeV/c}) < 1.5$ with Time Projection Chamber and Time Of Flight detectors. The CFs for all charged pion-kaon pairs for 20-30% centrality are shown in the left plot of Fig. 68. The C_0^0 for unlike and like-signed pion-kaon pairs go above and below 1, respectively at lower k* due to Coulomb interaction. Similarly, ReC_1^1's deviation from the flat region at lower k*, signals the existence pair-emission asymmetry along the *out* direction. However, at higher k* region, the C_0^0 and ReC_1^1 is not flat which implies the presence of non-femtoscopic background due to the elliptic flow, residual correlation functions, resonance decays etc. The background function is similar for all combinations of pion-kaon pairs and assumed to be 6^{th} order polynomial as shown in the left plot of Fig. 68.

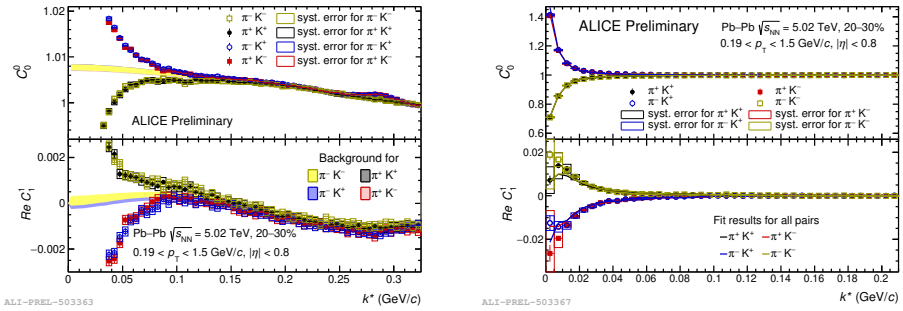


Fig. 68: Correlation functions for pion-kaon pairs with 6^{th} order polynomial function as the non-femtoscopic background (left) and background minimised femtoscopic correlation functions for 20-30% for all charge-pair combinations of pion and kaon, together with their fits calculated using CorrFit software (right) for Pb−Pb collisions at $\sqrt{s}_{\rm NN} = 5.02$ for 20-30% centrality

The right plot of Fig. 68 shows the background minimised correlation functions

with fit results, obtained using CorrFit package based on the process described in section 30.2.

30.4. *Results and discussions*

The $R_{\rm out}$ and $\mu_{\rm out}$, extracted from the background minimised femtoscopic correlation functions of pion-kaon pairs from 0-5% to 40-50% centrality are as the function of charge particle multiplicity density ($\langle {\rm d}N_{ch}/{\rm d}\eta\rangle^{1/3}$) in Fig. 69. The $R_{\rm out}$ is observed to be increasing with multiplicity due to the increase of system size with increasing number of participants. The $\mu_{\rm out}$ has been observed to be negative indicating that pions are emitted closer to the center of system than kaons and the finite value of $\mu_{\rm out}$ indicates the presence of radial flow in the system. The results are compatible with the pion-kaon femtoscopic analysis in Pb−Pb collisions at $\sqrt{s_{\rm NN}} =$ 2.76 TeV with ALICE and no energy dependence of $R_{\rm out}$ and $\mu_{\rm out}$ has been found so far. By comparing the results with predictions from (3 + 1)D viscous hydrodynamics coupled to decay code THERMINATOR 2 with different hypotheses of the extra delay ($\Delta\tau$) in emission for kaons, it is observed that the measured and predicted radii are in well agreement for peripheral events. The trend of measured $\mu_{\rm out}$ almost matches with the predicted ones with $\Delta\tau = 1.0$ fm/c, which indicates the presence of rescattering phase in the system along with the radial flow.

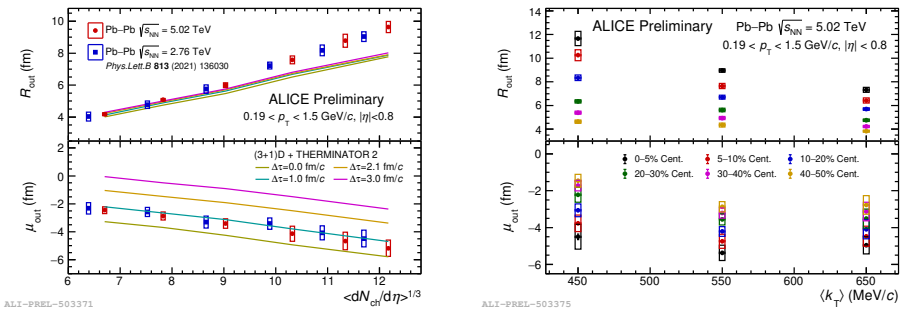


Fig. 69: $R_{\rm out}$ and $\mu_{\rm out}$ vs. $\langle {\rm d}N_{ch}/{\rm d}\eta\rangle^{1/3}$ with predictions from (3+1)D + THERMINATOR 2 model (left)) and $R_{\rm out}$ and $\mu_{\rm out}$ vs. $\langle k_{\rm T}\rangle$ as the function of centrality (right)

In the right plot of Fig. 69, the $R_{\rm out}$ and $\mu_{\rm out}$ are plotted as the function of average pair-transverse momentum ($\langle k_{\rm T}\rangle$) and centrality. The radii are found to be decreasing with $\langle k_{\rm T}\rangle$ in all centralities, indicating the presence of collectivity in the system. The $\mu_{\rm out}$ is lowest in the $k_{\rm T}$ range: 400-500 MeV/c in every centrality. To understand the effect of $k_{\rm T}$ on $\mu_{\rm out}$, further investigation is needed.

30.5. *Summary*

The analysis of pion-kaon femtoscopic correlation function in Pb−Pb collision at $\sqrt{s_{\rm NN}}$ =5.02 TeV shows that the source-size increases with multiplicity as the number of participants increase from low to high multiplicity events. Also, source-size decreases with increasing k_T due to the collective expansion of the system. The observed negative pair emission asymmetry signals that pions are emitted closer to the center of system than kaons. The predictions of pair emission asymmetry from theoretical model indicates the presence hadronic rescattering phase in the system. Also, no beam-energy dependence of the femtoscopic parameters is found.

31. Estimation of hadronic phase lifetime and locating the QGP phase boundary

Dushmanta Sahu, Sushanta Tripathy, Girija Sankar Pradhan, Raghunath Sahoo

Resonances are very useful probes to understand the various phases of the system evolution in ultra-relativistic collisions. A simple toy model is adopted to estimate the hadronic phase lifetime of the systems produced in ultra-relativistic collisions at RHIC and LHC by taking advantage of the short lifetime of K^{*0}, which is a resonance particle. With this model, we estimate the lower limit of the hadronic phase lifetime as a function of charged particle multiplicity for various collision systems and collision energies. On the other hand, ϕ, a long-lived resonance, can be used to locate the Quark-Gluon Plasma (QGP) phase boundary. We fit the Boltzmann-Gibbs blast-wave function and estimate the effective temperature of ϕ mesons, which gives information about the location of the QGP phase boundary.

31.1. *Introduction*

Estimating the hadronic phase lifetime of any collision system is not trivial. Although we know that the hadronic phase lifetime would be in the order of a few fermis in high-energy heavy-ion collisions, a proper phenomenological study as a function of charged particle multiplicity is of utmost importance. Furthermore, this can be taken as inputs in event generators such as a multi phase transport model (AMPT), where hadronic phase lifetime is usually set randomly. We have used K^{*0} produced in high energy collisions to estimate the hadronic phase lifetime,[284,285] which we have studied as a function of event multiplicity across various collision energies and system sizes. In addition, we have also used long-lived hadronic resonances like ϕ mesons to locate the QGP phase boundary with the information of effective temperature, which can be extracted from fitting the transverse momentum spectra with the Boltzmann-Gibbs blast wave function.[284]

31.2. *Results and discussion*

Hadronic resonances, which are produced in high-energy collisions, can decay while traveling through the medium. The decay daughters can then interact with other particles in the medium and lose momentum, suppressing resonances during their

invariant mass reconstructions. This process is called rescattering. In addition, resonances can be regenerated within the hadronic phase due to pseudoelastic collisions, enhancing the resonance yields. The suppression of K^{*0}/K ratio thus hints at the domination of rescattering over the regeneration effect. This can help us to estimate the hadronic phase lifetime. A simple toy model like the nuclear decay formula can be taken and modified for this purpose. K^{*0}/K ratio for low multiplicity pp collisions can be taken as the ratio at chemical freeze-out temperature, and the K^{*0}/K ratio at different event multiplicities for different collision systems can be taken as the ratio at the kinetic freeze-out temperature. Thus, the hadronic phase lifetime can be estimated by the following relation,[284, 285]

$$[\mathrm{K}^{*0}/\mathrm{K}]_{\mathrm{kinetic}} = [\mathrm{K}^{*0}/\mathrm{K}]_{\mathrm{chemical}} \times \mathrm{e}^{-\Delta \mathrm{t}/\tau}. \tag{157}$$

Here τ is K^0 lifetime and Δt is defined as the hadronic phase lifetime multiplied by the Lorentz factor.

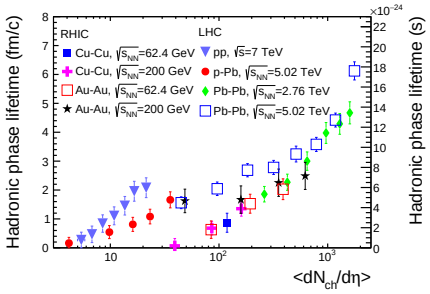


Fig. 70: Hadronic phase lifetime as a function of charged particle multiplicity for RHIC and LHC energies.[284]

In fig. 70, we have plotted the hadronic phase lifetime as a function of charged particle multiplicity for various collision systems and collision energies. The detailed framework and results can be found in ref.[284] We observe strong dependencies of the hadronic phase lifetime on the multiplicity and the collision energies. We also observe that in high-multiplicity pp collisions, the hadronic phase lifetime is around two fm/c. However, the most central Pb-Pb collisions it is around six fm/c.[284]

Resonances with a relatively higher lifetime might not go through the rescattering and regeneration processes. Thus, in contrast to K^{*0}, ϕ meson can act as a tool to locate the QGP phase boundary. The transverse momentum (p_{T}) spectra of ϕ meson will not be distorted during the hadronic phase. Hence, by using the p_{T} spectra of ϕ meson, we can extract information about the location of the QGP phase boundary. To do this, we fit the ϕ meson p_{T} spectra with the Boltzmann-Gibbs blast-wave (BGBW) function up to $p_{\mathrm{T}} \sim 3$ GeV/c.[67, 286] From this, we can get the

freeze-out temperature ($T_{\rm th}$) and the average velocity of the medium ($\langle\beta\rangle$), which can then help us to estimate the effective temperature ($T_{\rm eff}$) by the formula;[284]

$$T_{\rm eff} = T_{\rm th} + \frac{1}{2} m \langle\beta\rangle^2. \tag{158}$$

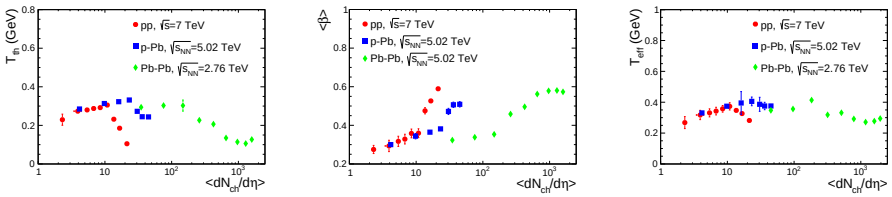


Fig. 71: Kinetic freezeout temperature, radial flow velocity and effective temperature of ϕ meson as functions of charged particle multiplicity for pp, p-Pb and Pb-Pb collisions at LHC energies.[284]

From the BGBW fits, we extract the values of $T_{\rm th}$ and $\langle\beta\rangle$ and have plotted them as functions of charged particle multiplicity in fig. 71. We observe a sudden decrease and increase in $T_{\rm th}$ and $\langle\beta\rangle$ respectively at $\langle dN_{\rm ch}/d\eta\rangle \sim 10$ - 20. This can be because, for low charged-particle multiplicity, the system freezes out early. It means the system freezes out at high $T_{\rm th}$. However, as the charged-particle multiplicity increases, the system is supposed to have gone through a QGP phase, which results in the system taking a long time to attain the kinetic freeze-out, thus a lower $T_{\rm th}$. This is also the reason for a higher average velocity of the system after certain charged-particle multiplicity.[284] Moreover, as ϕ meson keeps the information of the QGP phase boundary intact, from the right-hand side panel of fig. 71, we can observe that $T_{\rm eff}$, and the location of the QGP phase boundary, in turn, is independent or weakly dependent on charged-particle multiplicity. This observation is supported by earlier reports of the chemical freeze-out temperature independent of final-state charged-particle multiplicity.

31.3. *Summary*

In summary, we have presented a possible way to estimate the hadronic phase lifetime by considering a nuclear decay formula-like toy model and studied the hadronic phase lifetime as a function of final state event multiplicity. The hadronic phase lifetime is found to be strongly dependent on the charged particle multiplicity and the collision energy. In addition, we have also made an attempt to locate the QGP phase boundary by taking ϕ meson as our probe.

32. First deep learning based estimator for elliptic flow in heavy-ion collisions

N. Mallick, S. Prasad, A. N. Mishra, R. Sahoo, and G. G. Barnaföldi

We propose deep learning techniques such as the feed-forward deep neural network (DNN) based estimator to predict elliptic flow (v_2) in heavy-ion collisions at RHIC and LHC energies. A novel method is designed to process the final state charged particle kinematics information as input to the DNN model. The model is trained with Pb-Pb collisions at $\sqrt{s_{\rm NN}} = 5.02$ TeV minimum bias events simulated with a multiphase transport model (AMPT). The trained model is successfully applied to estimate centrality and transverse momentum ($p_{\rm T}$) dependence of v_2 for both RHIC and LHC energies. A noise sensitivity test is also performed to estimate the systematic uncertainty of this method by adding the model response to uncorrelated noise. Results of the proposed estimator are compared to both simulation and experiment, which confirms the model's accuracy.

32.1. *Introduction*

Relativistic heavy-ion collisions have been studied extensively in experiments at the Large Hadron Collider (LHC), CERN, Switzerland, and Relativistic Heavy Ion Collider (RHIC), BNL, USA for quite some time now and have established the fact that an extremely hot and dense state of strongly interacting matter is produced in such collisions. This thermalized deconfined state of matter is known as the quark-gluon plasma (QGP). One of the crucial signatures for QGP is the presence of transverse collective exapansion.[287] This transverse flow is anisotropic following the almond-shaped nuclear overlap region in noncentral heavy-ion collisions. The anisotropic flow of different orders can be expressed as the Fourier expansion coefficients of the produced final state particles' azimuthal momentum distribution as follows.[288]

$$\frac{{\rm d}N}{{\rm d}\phi} = \frac{1}{2\pi}\left[1 + \sum_{n=1}^{\infty} 2v_n \cos\left[n(\phi - \psi_n)\right]\right]. \tag{159}$$

Here, $v_n = \langle \cos\left[n(\phi - \psi_n)\right]\rangle$ is the nth order harmonic flow coefficient, ϕ is the azimuthal angle and ψ_n is the nth harmonic symmetry plane angle.[288] Existence of finite anisotropic flow, mainly the elliptic flow (v_2) in heavy-ion collisions is observed in experiments.[289,290] For the first time, we propose a machine learning based deep learning estimator for elliptic flow in heavy-ion collisions.[291] Machine learning algorithms are well known for their capabilities to exploit features and correlation from data for mapping complex nonlinear functions. In recent works,[292–294] deep neural network based studies are quite successful in heavy-ion physics. The motivation of this work is to prepare a deep learning framework to estimate v_2 from final state charged particle kinematics information and also learn the centrality and transverse momentum dependence of v_2 for RHIC and LHC energies. For this study, we have used AMPT with string melting mode (AMPT version 2.26t9b)[295] to obtain the required data sets.

32.2. *Deep learning estimator*

The primary input to the model comes from the binned $(\eta-\phi)$ distribution of all the charged particles in an event. Additionally, these $(\eta-\phi)$ layers are weighted with transverse momentum $(p_{\rm T})$, mass of the charged particles, and a term related to collision energy, *i.e.*, $\log(\sqrt{s_{\rm NN}/s_0})$ separately. $\sqrt{s_0}=1$ GeV makes $\sqrt{s_{\rm NN}/s_0}$ unitless. The grid size is 32×32 for each layer, which makes the total number of input features 3072. All charged particles with transverse momentum cut, $0.2<p_{\rm T}<5.0$ GeV/c in pseudorapidity, $|\eta|<0.8$ are considered for the training of the minimum bias regression model. The input is normalized using the *L2-Norm* to make a more meaningful representation for the training algorithm. This step is crucial as it helps faster convergence of the regression estimator and keeps the model's coefficients small.

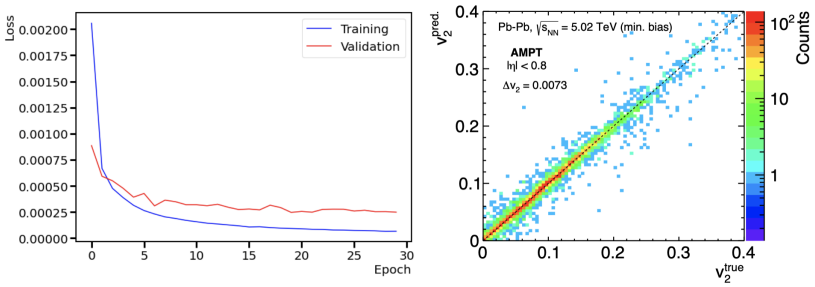


Fig. 72: (Color online) Left: The evaluation of loss function against the epochs during the training and validation runs. Right: Prediction of v_2 from the DNN estimator versus the true values from simulation for 10K minimum bias events of Pb-Pb collisions at $\sqrt{s_{\rm NN}}=5.02$ TeV. (Fig. 72 and 73[291])

The feed-forward deep neural network used in this work has four dense layers having 128-256-256-256 nodes each. All the layers have ReLU activation. The output layer has a single node as v_2 with linear activation. The role of activation function is to bring nonlinearity to the network. The network is trained with Pb-Pb collisions at $\sqrt{s_{\rm NN}}=5.02$ TeV minimum bias events using the *adam* optimizer with mean-squared-error (MSE) loss function.[291] The model is trained with a maximum of 60 epochs with a fixed batch size of 32. An early stopping callback is used with a patience level of 10 epochs to reduce overfitting. In Fig. 72, the left plot shows the performance of the DNN model during the training and validation runs as a function of epochs. The right plot shows the comparison of the model prediction with the true value of v_2. The model seems to perform quite nicely when subjected to a noise sensitivity test by adding uncorrelated noise to the feature space.[291] The systematic uncertainty is estimated by taking the MAE from this exercise for a given centrality bin.

32.3. *Results and discussion*

The trained model is successfully applied to predict the centrality dependence of v_2 for Pb-Pb collisions at $\sqrt{s_{\rm NN}}$ = 5.02, 2.76 TeV and Au-Au collisions at $\sqrt{s_{\rm NN}}$ = 200 GeV as shown in Fig. 73. The experimental results from ALICE[296] and PHENIX[297] are also shown. There is a good agreement between AMPT values and DNN predictions, as seen in the bottom ratio plots. In Fig. 73, the quadratic sum of statistical and systematic uncertainty is shown in a solid red band in the upper panel. In contrast, on the bottom panel, a solid band and a dashed band are used separately for the statistical and systematic uncertainty, respectively. By training the model with minimum bias Pb-Pb collisions at $\sqrt{s_{\rm NN}}$ = 5.02 TeV, we allow the machine to learn physics for a larger and more complex system. The DNN model is thus shown to preserve the centrality and energy dependence of v_2.[291]

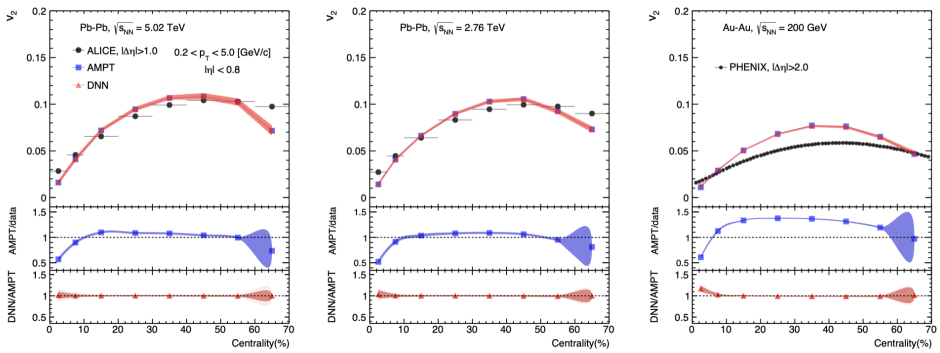


Fig. 73: (Color online) Prediction of v_2 versus centrality in Pb-Pb collisions at $\sqrt{s_{\rm NN}}$ = 5.02 TeV, 2.76 TeV and Au-Au collisions at $\sqrt{s_{\rm NN}}$ = 200 GeV from AMPT using the DNN estimator. Experimental results are added for comparison. (Fig. 6[291])

32.4. *Summary*

We propose a DNN-based estimator for elliptic flow in heavy-ion collisions at RHIC and LHC energies. The model is trained with Pb-Pb collisions at $\sqrt{s_{\rm NN}}$ = 5.02 TeV minimum bias events simulated with AMPT by taking input from particle kinematics information. The model is shown to preserve the centrality, energy, and transverse momentum dependence of v_2.[291] When subjected to uncorrelated noise added to the simulation, the model seems to preserve the prediction accuracy up to a reasonable extent. Current work is being taken up for testing and implementing this model with experimental data.

33. Thermoelectric response in a thermal QCD medium with chiral quasiparticle masses

Debarshi Dey and Binoy Krishna Patra

The lifting of the degeneracy between L- and R-modes of massless flavors in a weakly magnetized thermal QCD medium leads to a novel phenomenon of chirality dependence of the thermoelectric tensor, whose diagonal and non-diagonal elements are the Seebeck and Hall-type Nernst coefficient, respectively. Both coefficients in L-mode have been found to be greater than their counterparts in R-mode, however the disparity is more pronounced in the Nernst coefficient.

33.1. *Introduction*

The deconfined hot QCD medium created in relativistic heavy ion collision experiments may be exposed to magnetic fields (B) arising from non-central nucleus-nucleus collisions.[185,299] Depending on the time-scale of evolution, magnetic field could be strong or weak. Whereas a strong B provides the ground for probing the topological properties of QCD vacuum,[189,300] a weak B leads to some novel phenomenological consequences, such as the lifting of degeneracy between left and right handed quarks. Our aim is to explore the consequence of this mass splitting of chiral quasiparticle modes on the thermoelectric response of the medium.

In the weak B regime ($m_0^2 \ll eB \ll T^2$), the thermoelectric response of the thermal QCD medium is quantified by the Seebeck (S) and Nernst ($N|\boldsymbol{B}|$) coefficients, which, respectively are the measures of induced electric fields in the longitudinal and transverse directions with respect to the direction of temperature gradient. Large fluctuations in the initial energy density in the heavy-ion collisions[301] translate to significant temperature gradients between the central and peripheral regions of the produced fireball, providing the ideal ground to study thermoelectric phenomena.

33.2. *Dispersion Relations for quarks in weak B: Chiral modes*

The dispersion relation of quarks is obtained from the zeros of the inverse resummed quark propagator, which is related to the bare propagator and the self energy via the Dyson-Schwinger equation:

$$S^{-1}(P) = S_0^{-1}(P) - \Sigma(P), \tag{160}$$

The one loop quark self energy is then given by

$$\Sigma(P) = g^2 C_F T \sum_n \int \frac{d^3k}{(2\pi)^3} \gamma_\mu \left(\frac{\not{K}}{(K^2 - m_f^2)} - \frac{\gamma_5[(K.b)\not{u} - (K.u)\not{b}]}{(K^2 - m_f^2)^2} (|q_f B|) \right) \gamma^\mu \frac{1}{(P-K)^2},$$

with $u^\mu = (1,0,0,0)$ and $b^\mu = (0,0,0,1)$ being the fluid four-velocity in the rest frame of the heat bath and the direction of magnetic field, respectively.

The full propagator (and the self energy) can eventually be expressed in terms of projection operators $P_L = (\mathbb{I} - \gamma_5)/2$ and $P_R = (\mathbb{I} + \gamma_5)/2$ as

$$S(P) = \frac{1}{2}\Big[P_L \frac{\not{L}}{L^2/2} P_R + \frac{1}{2} P_R \frac{\not{R}}{R^2/2} P_L\Big], \tag{161}$$

where, L and R are combinations of structure constants that appear in the general expression of self energy in a tensor basis.[302] The $p_0 = 0$, $\mathbf{p} \to 0$ limit of the denominator of the effective propagator yields the quasiparticle masses as[303,304]

$$m_L^2 = \frac{L^2}{2}|_{p_0=0,|\mathbf{p}|\to 0} = m_{th}^2 + 4g^2 C_F M^2, \tag{162}$$

$$m_R^2 = \frac{R^2}{2}|_{p_0=0,|\mathbf{p}|\to 0} = m_{th}^2 - 4g^2 C_F M^2, \tag{163}$$

thus lifting the degeneracy. Here,

$$M^2 = \frac{|q_f B|}{16\pi^2}\left(\frac{\pi T}{2m_f} - \ln 2 + \frac{7\mu^2\zeta(3)}{8\pi^2 T^2}\right), \tag{164}$$

$$m_{th}^2 = \frac{1}{8} g^2 C_F \left(T^2 + \frac{\mu^2}{\pi^2}\right). \tag{165}$$

33.3. *The thermoelectric coefficients*

We make use of the Boltzmann transport equation to calculate the infinitesimal deviation of the single particle distribution function from equilibrium caused by the temperature gradient.

$$p^\mu \frac{\partial f_i(x,p)}{\partial x^\mu} + q_i F^{\mu\nu} p_\nu \frac{\partial f_i(x,p)}{\partial p^\mu} = \left(\frac{\partial f_i}{\partial t}\right)_{\text{coll}} \tag{166}$$

The highly non linear collision integral on the R.H.S. can be linearized using the relaxation time approximation which reads (suppressing the flavor index i)

$$\left(\frac{\partial f}{\partial t}\right)_{\text{coll}} \simeq -\frac{p^\mu u_\mu}{\tau}\delta f = -\frac{f - f_0}{\tau} = -\frac{\delta f}{\tau}, \tag{167}$$

where, τ is the relaxation time[273] and f_0 is the Fermi-Dirac distribution function. δf is then used to calculate the induced current which is set to zero (enforcing the equilibrium condition) to evaluate the relevant response functions[305] (Seebeck and Nernst coefficients).

We use the following Ansatz[272] to solve for δf from Eq.(166)

$$f^{L/R} = f_0^{L/R} - \tau q \boldsymbol{E} \cdot \frac{\partial f_0^{L/R}}{\partial \boldsymbol{p}} - \boldsymbol{\chi} . \frac{\partial f_0^{L/R}}{\partial \boldsymbol{p}}, \tag{168}$$

where, the effect of $\mathbf{B}$ is encoded in $\boldsymbol{\chi}$.

The induced 4-current of the system consisting of u and d quarks is given by:

$$J^\mu = \sum_{a=u,d} q_a g_a \int \frac{d^3\mathrm{p}}{(2\pi)^3 \epsilon_a} p^\mu \left[\delta f_a - \overline{\delta f_a}\right], \tag{169}$$

where, $\overline{\delta f}$ denotes the contribution from antiparticles. For $\boldsymbol{\nabla T} = \frac{\partial T}{\partial x}\hat{\boldsymbol{x}} + \frac{\partial T}{\partial y}\hat{\boldsymbol{y}}$ the equilibrium condition $J_x = J_y = 0$ finally yields:

$$\begin{pmatrix} E_x \\ E_y \end{pmatrix} = \begin{pmatrix} S & N|\boldsymbol{B}| \\ -N|\boldsymbol{B}| & S \end{pmatrix} \begin{pmatrix} \frac{\partial T}{\partial x} \\ \frac{\partial T}{\partial y} \end{pmatrix}, \tag{170}$$

with

$$S = -\frac{\sum\limits_{a=u,d}(C_1)_a \cdot \sum\limits_{a=u,d}(C_3)_a + \sum\limits_{a=u,d}(C_2)_a \cdot \sum\limits_{a=u,d}(C_4)_a}{\left(\sum\limits_{a=u,d}(C_1)_a\right)^2 + \left(\sum\limits_{a=u,d}(C_2)_a\right)^2},$$

$$N|\boldsymbol{B}| = \frac{\sum\limits_{a=u,d}(C_2)_a \cdot \sum\limits_{a=u,d}(C_3)_a - \sum\limits_{a=u,d}(C_1)_a \cdot \sum\limits_{a=u,d}(C_4)_a}{\left(\sum\limits_{a=u,d}(C_1)_a\right)^2 + \left(\sum\limits_{a=u,d}(C_2)_a\right)^2}.$$

where,

$$C_{1/2} = q\int \mathrm{d}p\, p^4 \frac{\tau(\omega_c\tau)^{0/1}}{\epsilon^2(1+\omega_c^2\tau^2)}\{f_0(1-f_0) \pm \bar{f}_0(1-\bar{f}_0)\},$$

$$C_{3/4} = \beta\int \mathrm{d}p\, p^4 \frac{\tau(\omega_c\tau)^{0/1}}{\epsilon^2(1+\omega_c^2\tau^2)}\{\pm(\epsilon+\mu)\bar{f}_0(1-\bar{f}_0) - (\epsilon-\mu)f_0(1-f_0)\}.$$

33.4. *Results*

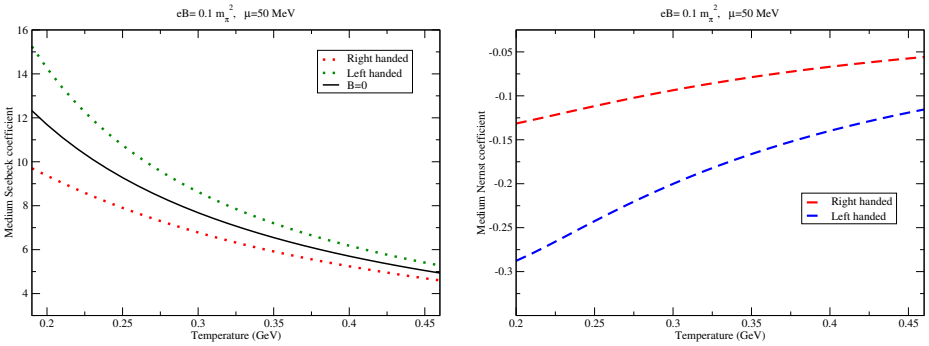


Fig. 74: Variation of Seebeck (left) and Nernst coefficients (right) with temperature.

Figures (74) left and (74) right show the variation of Seebeck and Nernst coefficients of the medium with temperature. The coefficient magnitudes show similar trends as far as variation with temperature is considered; for both the modes, the magnitudes decrease with temperature. Also, for both the coefficients, the L mode elicits a larger comparative response.

Coefficient	% change between L and R modes	
	Max	Min
Seebeck	57.1	13.9
Nernst	118.6	105.7

Table 3: Comparative response strength of L and R modes.

The difference between the L and R mode responses is amplified significantly for the Nernst coefficient, as can be seen from Table 3. Also, the temperature sensitivity of the Seebeck coefficient is much greater than that of the Nernst coefficient. For comparison, the $B = 0$ case is also shown for the Seebeck coefficient. The Nernst coefficient is, however zero for $B = 0$, as should be the case.

34. Charge and heat transport in hot quark matter with chiral dependent quark masses

Pushpa Panday and Binoy Krishna Patra

The generation of nondegeneracy in the mass of left-handed (L) and right-handed (R) chiral modes of quarks is noticed in a weak magnetic field (B), which is in contrast to the case of the strong magnetic field. Therefore, we have studied the impact of nondegenerate mass on longitudinal and Hall components of charge and heat transport coefficients.

34.1. *Introduction*

The generation of fast decaying and strong magnetic field during the initial stage of heavy-ion collisions[306] brings the new aspects for the study of quark-gluon plasma. The lifetime of magnetic field gets enhanced due to the charge properties of the medium.[248,307,308] Therefore, the study of transport coefficients in weak magnetic field is of great interest, where these coefficients serve as input parameters for the hydrodynamical study of QGP. Furthermore, the lifting up of degeneracy in mass of chiral modes of quarks in the ambience of weak magnetic field can give more insight to the study of medium properties of QGP.

34.2. *Effective Mass of quark in weakly magnetized thermal medium*

The effective quark mass for fth flavor in presence of magnetic field can be written in terms of current quark mass and medium generated mass as[309]

$$m_f^2 = m_{f0}^2 + \sqrt{2} m_{f0} m_{fth,B} + m_{fth,B}^2. \tag{171}$$

$m_{fth,B}$ can be obtained by taking the static limit of denominator of the dressed quark propagator in magnetic field. The inverse of dressed quark propagator using Schwinger-Dyson can be written in terms of bare inverse propagator ($S^{-1}(P)$) and quark self energy ($\Sigma(P)$) as

$$S^{*-1}(P) = S^{-1}(P) - \Sigma(P). \tag{172}$$

The one-loop quark self energy upto $\mathcal{O}(q_f B)$ in hot and weakly magnetized medium can be written as

$$\Sigma(P) = g^2 C_F T \sum_n \int \frac{d^3k}{(2\pi)^3} \gamma_\mu \left(\frac{\not{K}}{(K^2 - m_{f0}^2)} - \frac{\gamma_5[(K.b)\not{u} - (K.u)\not{b}]}{(K^2 - m_{f0}^2)^2}(q_f B) \right) \times \gamma^\mu \frac{1}{(P-K)^2}. \tag{173}$$

We will employ the general covariant structure of quark self energy[303] in terms of chiral projection operator to obtain the effective quark propagator as

$$S^*(P) = \frac{1}{2}\left[P_L \frac{\not{L}}{L^2/2} P_R + P_R \frac{\not{R}}{R^2/2} P_L \right]. \tag{174}$$

The static limit ($p_0 = 0, |\mathbf{p}| \to 0$) of $L^2/2$ and $R^2/2$ will give the different medium generated mass for L and R mode thus lifting up the degeneracy in mass.

$$m_L^2 = m_{th}^2 + 4g^2 C_F M^2, \tag{175}$$

$$m_R^2 = m_{th}^2 - 4g^2 C_F M^2. \tag{176}$$

34.3. *Charge and heat transport coefficients*

34.4. *Ohmic and Hall conductivity*

The Boltzmann transport equation governs the evolution of phase space density $f(x,p)$ associated with partons in our system. The relativistic Boltzmann transport equation (RBTE) in presence of external electromagnetic field ($F^{\mu\nu}$) is[310]

$$p^\mu \partial_\mu f(x,p) + qF^{\mu\nu} p_\nu \frac{\partial f(x,p)}{\partial p^\mu} = C[f], \tag{177}$$

where, f is the distribution function deviated slightly from equilibrium distribution function (f_0) with $f = f_0 + \delta f$ ($\delta f << f_0$). $C[f]$ is the collision integral whose general form consists of absorption and emission terms in phase space volume element. This leads to complicated nonlinear integro-differential equation which can be solved easily under relaxation-time approximation (RTA). To solve RBTE for static and spatially uniformed medium, we take the following *ansatz* of $f(p)$ as[272]

$$f(p) = f_0 - \tau q \mathbf{E}.\frac{\partial f_0}{\partial \mathbf{p}} - \boldsymbol{\xi}.\frac{\partial f_0}{\partial \mathbf{p}}, \tag{178}$$

and hence $f(p)$ for quarks simplifies to

$$f(p) = f_0 - \frac{qEv_x\tau}{(1+\omega_c^2\tau^2)}\left(\frac{\partial f_0}{\partial \varepsilon}\right) + \frac{qEv_y\omega_c\tau^2}{(1+\omega_c^2\tau^2)}\left(\frac{\partial f_0}{\partial \varepsilon}\right). \tag{179}$$

Similarly, we can solve for antiquarks. The induced current due to external electromagnetic field is $j^i = \sigma_{\rm Ohmic}\delta^{ij}E_j + \sigma_{\rm Hall}\epsilon^{ij}E_j$, where $\sigma_{\rm Ohmic}$ is the response along the direction of electric field and $\sigma_{\rm Hall}$ is the transverse response to the electric field. Further, the induced current can be written in terms of deviation δf and $\delta \bar{f}$ as

$$\mathbf{j} = g_f \int \frac{d^3p}{(2\pi)^3} \mathbf{v}\left(q\delta f(p) + \bar{q}\delta\bar{f}(p)\right). \tag{180}$$

Hence, $\sigma_{\rm Ohmic}$ and $\sigma_{\rm Hall}$ comes out to be

$$\sigma_{\rm Ohmic} = \frac{1}{6\pi^2 T}\sum_f g_f q_f^2 \tau_f \int dp \frac{p^4}{\varepsilon_f^2}\frac{1}{(1+\omega_c^2\tau_f^2)}[f_f^0(1-f_f^0)+\bar{f}_f^0(1-\bar{f}_f^0)], \quad (181)$$

$$\sigma_{\rm Hall} = \frac{1}{6\pi^2 T}\sum_f g_f q_f^2 \tau_f^2 \int dp \frac{p^4}{\varepsilon_f^2}\frac{\omega_c}{(1+\omega_c^2\tau_f^2)}[f_f^0(1-f_f^0)-\bar{f}_f^0(1-\bar{f}_f^0)], \quad (182)$$

34.5. *Thermal and Hall-type thermal conductivity*

We will express the RBTE in terms of gradients of flow velocity and temperature under RTA as

$$p^\mu \partial_\mu T\left(\frac{\partial f}{\partial T}\right) + p^\mu \partial_\mu (p^\nu u_\nu)\left(\frac{\partial f}{\partial p^0}\right) + q\Bigg(F^{0j}p_j\frac{\partial f}{\partial p^0} + F^{j0}p_0\frac{\partial f}{\partial p^j} + F^{ij}p_j\frac{\partial f}{\partial p^i} + F^{ji}p_i\frac{\partial f}{\partial p^j}\Bigg) = -\frac{p^\mu u_\mu}{\tau}\delta f. \quad (183)$$

We will choose the *ansatz* for δf as $(\mathbf{p}.\boldsymbol{\chi})\frac{\partial f_0}{\partial \varepsilon}$, where $\boldsymbol{\chi}$ is related to thermal driving forces and magnetic field in the medium. The spatial heat flow in terms of δf and $\delta \bar{f}$ can be written as

$$\mathbf{Q} = \sum_f g_f \int \frac{d^3p}{(2\pi)^3}\frac{\mathbf{p}}{\varepsilon_f}\left[(\varepsilon_f - h_f)\,\delta f_f + \left(\varepsilon_f + \bar{h}_f\right)\delta \bar{f}_f\right] \quad (184)$$

Comparing Eq.(184) with $\mathbf{Q} = -\kappa_0 T\mathbf{Y} - \kappa_1 T(\mathbf{Y}\times\mathbf{c})$, where $\mathbf{Y} = \frac{\boldsymbol{\nabla} T}{T} - \frac{\boldsymbol{\nabla} P}{nh}$ and $\mathbf{c} = \frac{\mathbf{B}}{|\mathbf{B}|}$, thermal ($\kappa_0$) and Hall-type thermal conductivity (κ_1) obtained to be as

$$\kappa_0 = \sum_f \frac{g_f\tau_f}{6\pi^2T^2}\int dp\frac{p^4}{\varepsilon_f^2}\left[\frac{(\varepsilon_f - h_f)^2}{(1+\omega_c^2\tau_f^2)}f_f^0(1-f_f^0) + \frac{(\varepsilon_f+\bar{h}_f)^2}{(1+\omega_c^2\tau_f^2)}\bar{f}_f^0(1-\bar{f}_f^0)\right], \quad (185)$$

$$\kappa_1 = \sum_f \frac{g_f\tau_f^2}{6\pi^2T^2}\int dp\frac{p^4}{\varepsilon_f^2}\left[\frac{(\varepsilon_f - h_f)^2\omega_c}{(1+\omega_c^2\tau_f^2)}f_f^0(1-f_f^0) - \frac{(\varepsilon_f+\bar{h}_f)^2\omega_c}{(1+\omega_c^2\tau_f^2)}\bar{f}_f^0(1-\bar{f}_f^0)\right]. \quad (186)$$

34.6. *Results and Discussion*

The magnitude of R mode $\sigma_{\rm Ohmic}/T$ and $\sigma_{\rm Hall}/T$ is higher than L mode as shown in Fig. (75). This can be attributed to the different mass of L and R mode. The normalized Ohmic conductivity increases with temperature due to the Boltzmann factor in the distribution function whereas normalized Hall conductivity decreases with temperature due to the factor $\omega_c\tau$ in the numerator of Eq.(182). Similarly, the variation of κ_0/T and κ_1/T with temperature is shown in Fig. (76) where magnitude for R mode is higher than L mode. κ_0/T increases with temperature due to the factor $(\varepsilon - h)^2$, $(\varepsilon + h)^2$ and distribution function in Eq.(185). Considering the absolute value of the ratio κ_1/T, we infer that κ_1/T also increases with temperature due to $(\varepsilon + h)^2$ factor in the numerator of Eq.(186). Moreover, Hall component for both charge and heat transport will vanish for zero magnetic field.

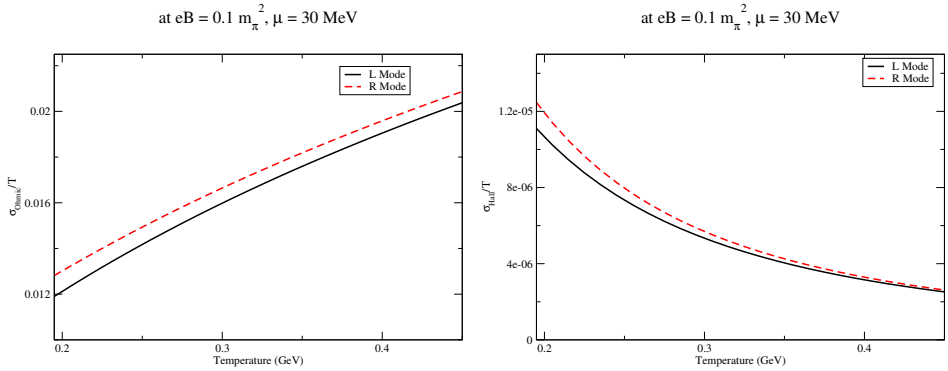


Fig. 75: Variation of $\sigma_{\rm Ohmic}/T$ (a) and $\sigma_{\rm Hall}/T$ (b) with temperature.

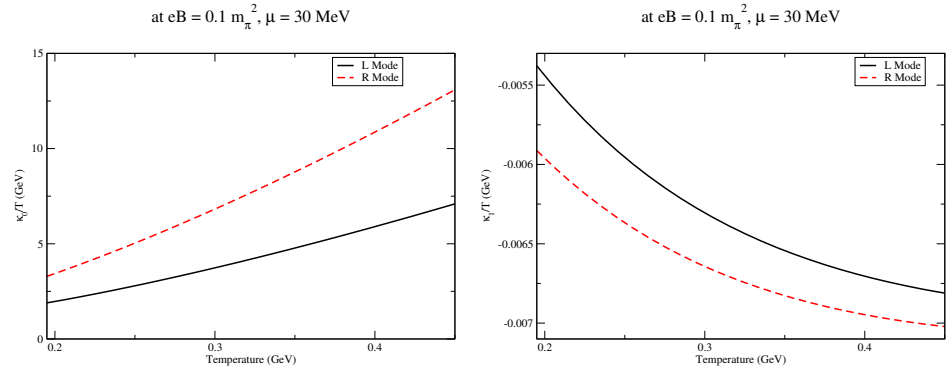


Fig. 76: Variation of κ_0/T (a) and κ_1/T (b) with temperature.

35. NLO quark self-energy and dispersion relation using the hard thermal loop resummation

Sumit, Najmul Haque, and Binoy Krishna Patra

Using the hard-thermal-loop (HTL) resummation in real-time formalism, we study the next-to-leading order (NLO) quark self-energy and corresponding NLO dispersion laws. We calculate the momentum integrals in the transverse part of the NLO quark self-energy numerically and plot them as a function of the ratio of momentum and energy. Using that, we plot the transverse contribution of NLO dispersion laws.

35.1. *Introduction*

The standard perturbative loop expansion in quantum chromodynamics (QCD) encounters several issues at finite temperatures. One of those issues is that the physical quantities, for example, dispersion laws, become gauge-dependent. Another critical point is that Debye screening in the chromoelectric mode does occur in

the leading order in the one-loop calculation, but chromomagnetic screening does not.[311]

The issue related to the gauge dependence of the gluon damping rates, which have been calculated up to one-loop order, particularly at zero momentum, in different gauges and schemes, has been studied, and different outcomes have been obtained.[312] Later, it was concluded that the lowest order result is not complete, and higher-order diagrams can contribute to lower orders in powers of the QCD coupling.[313] Braaten and Pisarski developed a systematic theory for an effective perturbative expansion that sums the higher-order terms into effective propagators and effective vertices[314] and is known as hard-thermal loop (HTL) resummation. Using the effective HTL propagators and vertices, the transverse part of the gluon damping rate $\gamma_t(0)$ at vanishing momentum was calculated,[315] and it was found to be finite, positive, and gauge independent.

Using the HTL resummed propagators and vertices, the pressure and quark number susceptibilities up to three-loop order have been studied using the thermodynamic potential.[316] Using the HTL summation, it has been found that massless quarks and gluons acquire the thermal masses of order gT, m_q, and m_g respectively,[317] which shows that for the lowest order gT in effective perturbation, the infrared region is 'okay.' However, the static chromomagnetic field does not screen at the lowest order; instead, it gets screened at the next order, so-called magnetic screening.[311] Thus, if we want to demonstrate the infrared sector of the HTL perturbative expansion, we need to go beyond the leading-order calculations.

35.2. *NLO Formalism*

The lowest order dispersion relation can be summarized in the equation:

$$p_0 \mp p - \Sigma_{\pm}(P) = 0. \tag{187}$$

For on shell quarks, we write the (complex) quark energy $p_0 \equiv \Omega(p)$ as

$$\Omega(p) = \Omega^{(0)}(p) + \Omega^{(1)}(p) + \cdots \ . \tag{188}$$

A similar kind of approach is also relevant for self-energy Σ, as well

$$\Sigma(P) = \Sigma_{\rm HTL}(P) + \Sigma^{(1)}(P) + \cdots , \tag{189}$$

where $\Sigma_{\rm HTL}$ is the lowest-order quark self-energy having gT order, whereas $\Sigma^{(1)}$ the NLO contribution of quark self-energy, with order g^2T.

Thus, eq. (187) will take the form as

$$\Omega^{(0)}_{\pm}(p) + \Omega^{(1)}_{\pm}(p) + \cdots = \pm p + \Sigma_{\rm HTL\pm}\left(\omega, p\right)|_{\omega\to\Omega_{\pm}(p)} + \Sigma^{(1)}_{\pm}\left(\omega, p\right)\Big|_{\omega\to\Omega_{\pm}(p)} + \dots \ . \tag{190}$$

After simplification, for slow-moving quarks ($p \sim gT$), we get

$$\Omega^{(1)}_{\pm}(p) = \frac{{\Omega^{(0)}_{\pm}}^2(p) - p^2}{2m_q^2}\Sigma^{(1)}_{\pm}\left(\Omega^{(0)}_{\pm}(p), p\right). \tag{191}$$

To calculate the NLO quark self-energy, we have to consider two one-loop graphs with effective vertices, shown in figure 77.



Fig. 77: Feynman graphs for the NLO HTL resummed quark self-energy $\Sigma_{\pm}^{(1)}$. The black blobs indicate HTL effective quantities. All momenta are soft.

The final compact expressions for the NLO one-loop HTL-summed quark self-energy as[318]

$$\Sigma_{\pm}^{(1)}(P) = -\frac{ig^2 C_F}{2}\int \frac{d^4K}{(2\pi)^4}\left[F^{\rm SR}_{\pm;0}(P,K) + F^{\rm AS}_{\pm;0}(P,K) + 2F^{\rm SR}_{\pm;--}(P,K) + F^{\rm AS}_{\pm;--}(P,K)\right.$$
$$\left. +\ F^{\rm AS}_{\pm;-+}(P,K) + F^{\rm SR}_{\pm;--;--}(P,K) + F^{\rm AS}_{\pm;--;+-}(P,K) + G^{\rm S}_{\pm;--}(P,K)\right]. \quad (192)$$

35.3. *Evaluation of NLO quark self-energy*

In order to evaluate eq. (192), we need retarded transverse $D_T^R(k,k_0,\varepsilon)$, retarded longitudinal $D_L^R(k,k_0,\varepsilon)$ gluon propagators which we have derived.[319] The retarded transverse gluon propagator comes out to be

$$D_T^{R(-1)}(k,k_0,\varepsilon) = -\left[\frac{4k_0^2}{k^2} + \left(k^2-k_0^2\right)\left\{1 - \frac{k_0}{k^3}\ln\frac{(k_0-k)^2+\varepsilon^2}{(k_0+k)^2+\varepsilon^2}\right\}\right]$$
$$- i\left[\frac{2k_0}{k^3}\left(k_0^2-k^2\right)\left\{\tan^{-1}\left(\frac{\varepsilon}{k_0-k}\right) - \tan^{-1}\left(\frac{\varepsilon}{k_0+k}\right)\right\} - \varepsilon\Theta(k_0)\right],$$

Here, we show how the terms in eq. (192) have been evaluated. For example, in the third term of eq. (192), we will get the following lines of discontinuity.

$$k_0 = 0; \quad k_0 = \pm k;$$
$$k_0 = p_0 \pm \sqrt{p^2+k^2-2pkx};$$
$$k = k_t \equiv \frac{1}{2}\frac{p_0^2-p^2}{p_0-xp} = \frac{1}{2t}\frac{1-t^2}{1-xt}\sqrt{\frac{t}{1-t} - \frac{1}{2}\ln\left(\frac{1+t}{1-t}\right)} \quad (193)$$

These domains are shown in figure 78. We numerically evaluated this term in each of the domains of the figure 78 and summed up the results.[319] Similar technique has been used to evaluate the other terms[319] of eq. (192).

35.4. *Results and Discussion*

All the terms of NLO quark self-energy in eq. (192) have a non-trivial dependence on ε. So, we have checked the stability for each term by plotting them as a function

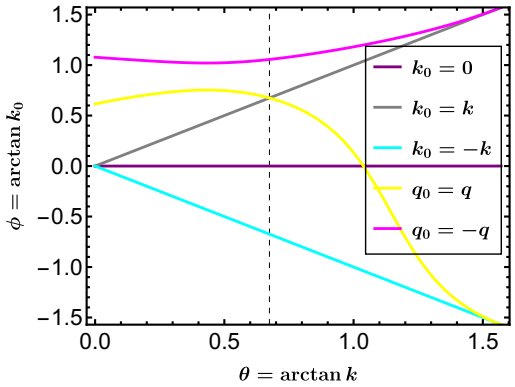


Fig. 78: Domains in (k, k_0) plane at which the third term of eq. (192) has sharp jumps. Here we used $t = \frac{p}{p_0} = 0.45$ and $x = 0.8$

of $m = -\log_{10}\varepsilon$. This is an essential task because different terms have different stability regions, and if one does the integration beyond those regions, then numerical values lose reliability. After calculating each term's transverse part separately, we added all terms to plot the transverse contribution of NLO quark self-energy w.r.t ratio of momentum and energy. Using eq. (191), we plotted the transverse contribution of NLO damping rate and NLO mass for each quark mode shown in Figure 79 and figure (80). The important outcome of the results shown is that one can handle the instabilities that arise, at least in part arising from the gluon propagator's transverse component.[319] The infrared divergence in the longitudinal part[319] can be handled by introducing an infrared cut-off or resumming a specific class of diagrams.

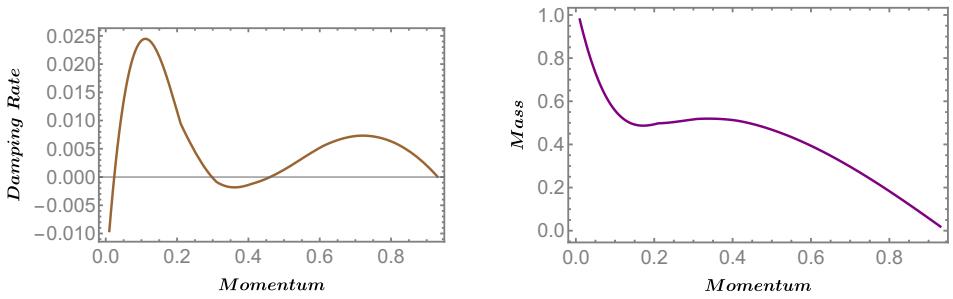


Fig. 79: Damping rate and quark energy variation with soft momentum p for '+' mode with a coefficient $4\pi g$.

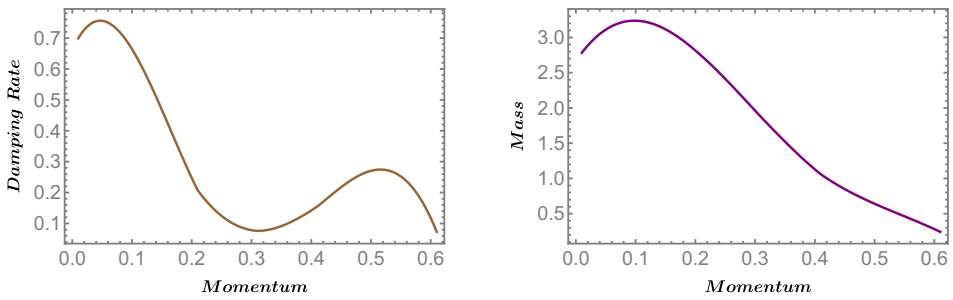


Fig. 80: Damping rate and quark energy variation with soft momentum p for '-' mode with a coefficient $4\pi g$.

36. Overview of experimental results

Nihar Ranjan Sahoo

In this conference, variety of topics related to the QCD and its hot-dense medium—known as Quark-Gluon Plasma—were discussed. Different experimental results pertaining to the particle production and bulk properties of the medium to the hard probes of the QGP medium were presented. In this proceedings, I summarize succinctly all these results from the LHC and RHIC experiments shown at this conference.

36.1. *Introduction*

In heavy-ion collisions, neutrons and protons inside heavy ions melt, due to extreme temperature and pressure, into a state of matter where the color degrees of freedom plays an important role—this state of matter is known as Quark-Gluon Plasma(QGP). Dedicated heavy-ion experiments at the Large Hadron Collider (LHC) at CERN and Relativistic Heavy-Ion Collider (RHIC) at BNL observed different signatures of QGP created in heavy-ion collisions. In this proceedings, I discuss some recent results presented at this conference.

Hard probes: The hard probes such as jets and heavy-flavors are produced in the early stages of the heavy-ion collisions and hence carry full space-time evolution of the medium. The J/ψ, Υ, and D-mesons are measured in the heavy-ion experiments to study the energy loss of heavy-flavors by comparing with its vacuum reference in proton+proton collisions and their collectivity in the QGP medium. The ratio of production yield in nucleus-nucleus collisions and the production cross-section in proton-proton collisions normalized by the average number of nuclear thickness function is known as the nuclear modification factor, $R_{\rm AA}$. The $R_{\rm AA}$ as a function of transverse momentum ($p_{\rm T}$) enables a way to measure the energy loss in heavy-ion collisions. In the ALICE experiment,[320] a clear difference of $R_{\rm AA}$ between D-mesons, J/ψ, and charged pions at low $p_{\rm T}$ suggesting the colour charge and the quark mass dependence of in-medium parton energy loss. The measurement of second order coefficient, v_2, called elliptic flow, provides information about the

heavy quark interaction with the medium and their thermalization. D-mesons show a finite elliptic flow as a function of p_T whereas CMS results[321] show zero Υ(1S) v_2 and non-zero J/ψ v_2 suggesting different medium effects for charmonia and bottomonia. However, different model comparisons suggest that most of the models fail the simultaneous description of D-meson $R_{\rm AA}$ and v_2 in central and peripheral collisions.[320] We need a further study to constrain different model parameters, interaction processes, and hadronization mechanisms in the hot-dense QCD medium.

Jets are collimated spray of hadrons fragmented from an energetic parton (quark or gluon) originating from a hard scattering. Jet measurement is an important tool to study the energetic parton in heavy-ion and proton-proton collisions. In this conference, jet-fragmentation function in p+p and p+Au collisions were presented at $\sqrt{s}$=13 TeV and $\sqrt{S}_{\rm NN}$ = 5.02 TeV, respectively. In $p+p$ collisions, jet fragmentation function is softer in high-multiplicity events than the minimum bias events in the ALICE experiment.[322] A further detailed study is ongoing to investigate the multiplicity dependence of jet production and fragmentation at the LHC.

Collectivity in heavy-ion collisions: Different flow harmonic measurements in heavy-ion collisions measure the collectivity in the QGP. The elliptic flow measurement in the STAR Beam Energy Scan pase-I (BES-I) experiment observes the scaling of v_2 as a function of p_T with the number of constituent quarks (NCQ) for different hadrons.[323] This observation concludes that elliptic flow develops in the early stage of heavy-ion collision where partonic degrees of freedom play an important role. The recent BES phase-II high statistics data at $\sqrt{S}_{\rm NN}$ = 19.6 GeV show the NCQ scaling holds better for anti-particles than for particles.[324] The light nuclei and hyper-nuclei v_2 measurements show that a systematic deviation from mass number scaling of v_2 (v_2/A) as a function $p_{\rm T}/A$ where A is the mass number of nuclei. The first order coefficient of the Fourier-expansion of momentum azimuthal distribution, known as the directed flow v_1, provides sensitive information on early nuclear collisions. In the STAR experiment, observation of hyper-nuclei ${}^{3}_{\Lambda}H$ and ${}^{4}_{\Lambda}H$ v_1 at $\sqrt{s_{\rm NN}}$ = 3 GeV is seen.[324] More detailed studies and analyses for other energies from BES-II are underway in the STAR experiment.

Particle production in heavy-ion collisions: In heavy-ion collisions, different species of particles are produced at both mid- and forward-rapidity. The preliminary result from inclusive photon yield measurement was presented at forward rapidity in p+Pb collisions at $\sqrt{S_{\rm NN}}$=5.02 TeV using Photon Multiplicity Detector (PMD) in the ALICE experiment.[326] The pseudorapidity dependence of photon yield are comparable with that of the charged particles at forward rapidity at this collision energy. On the other hand, in the ALICE experiment, the yield ratio of Λ(1520) over Λ as function of average multiplicity for $p+p$ collisions at $\sqrt{s}$=5.02 and 13 TeV are comparable, and the ratio lies between 0.05-0.07.[325] In the STAR experiment, the ratio of ϕ/K^- and ϕ/Ξ^- in Au+Au collisions at $\sqrt{S_{\rm NN}}$= 3 GeV from fixed

target configuration and compared with different statistical model predictions. The anti-hyper-hydrogen-4 ($^{4}_{\bar{\Lambda}}H$) state is observed in the STAR experiment by combining all heavy-ion data from Au+Au, (U+U) Ru+Ru, and Zr+Zr collisions at $\sqrt{S_{\rm NN}}$=200 (193) GeV in STAR.[324]

Correlations and fluctuations: In heavy-ion collisions, the two-particle correlation function provides the information about the distribution of separation of emission sources and the final-state interactions. At the LHC and RHIC, the $\Lambda\Lambda$ correlation measurements where performed. The STAR experiment results and model comparison suggest that the $\Lambda\Lambda$ interaction is weak in nature.[327] However, this contradicts the observation by the recent CMS measurement.[328]

Search for the QCD critical point is one of the main goals of the BES program at RHIC. The recent net-proton number $\kappa\sigma^2$ values as a function of beam energy shows 3.1σ non-monotonic variation in central Au+Au collisions.[152,329] In addition, the recent STAR measurement at $\sqrt{s_{\rm NN}}$ = 3 GeV with fixed-target configuration, the net-proton number $\kappa\sigma^2$ value is negative (-0.85$\pm$0.09(stat)$\pm$0.82(sys)).[153] At this collision energy, the results are consistent with the baryon number conservation. High precision measurements with large acceptance are ongoing using BES-II data for incisive understanding in the direction of QCD critical point search by the STAR collaboration.

Summary and outlook: Many results were presented at this conference primarily on the particle production, freeze-out parameters obtained in heavy-ion collsions, correlation measurements, collectivity in heavy-ion collisions and the small system, hard probes, etc. I try to shed light on those results briefly in this proceedings. At its nascent stage, this conference foresees a reassuring future sequel providing a suitable environment and forum for the discussions between young and senior researchers in Goa, India.

Acknowledgments

This writeup is a compilation of the contributions presented at the "Hot QCD Matter 2022 conference" held from May 12–14, 2022, in Goa, India. This first national conference on "HOT QCD Matter 2022" was jointly organized by the School of Physical Sciences, Indian Institute of Technology Goa, and the School of Physical and Applied Sciences, Goa University. This conference's academic activities took place inside the Goa University, situated at the heart of Goa, from 12th to 14th May 2022. This conference attracted 62 participants from different institutes and universities all over India. Prof. B. K. Mishra, Director, IIT Goa, and Prof. H. B. Menon, Vice-Chancellor, Goa University, inaugurated the conference and delighted the event with their inspirational speeches. An energetic and vibrant group of Ph.D. students made this event lively by active contribution to the lively discussion. The scientific program consisted of 24 invited plenary talks by renowned scientists from all over India and 24 contributed talks by Ph.D. students. After each presentation, there was a discussion session to discourse on that topic. At the end of the conference, two overview talks were scheduled to summarize all the presentations and discussions. The six contributed talks (three from experiment and three from theory) presented by the Ph.D. students were facilitated as the best presentations. The conference organizers, Santosh K. Das, Prabhakar Palani, Jhuma Sannigrahi, and Kaustubh R.S. Priolkar, are greatly indebted to the sponsors' generous support: IOP Publishing, Balani Infotech (Library and information services) and San Instruments. The organizers would like to acknowledge all the administrative staff from IIT Goa and Goa University associated with this conference. They worked behind the screen with lots of dedication and enthusiasm to ensure that "HOT QCD Matter 2022" ran smoothly, technically as well as socially. Saumen Datta's research is supported by the Department of Atomic Energy, Government of India, under Project Identification No. RTI 4002. Santosh K. Das and Marco Ruggieri acknowledge the support by the National Science Foundation of China (Grant Nos. 11805087 and 11875153). Santosh K. Das acknowledges the support from DAE-BRNS, India, Project No. 57/14/02/2021-BRNS. Pooja acknowledges IIT Goa and MHRD for funding her research. J. Prakash would like to acknowledge support from IIT Goa and MHRD for funding this project. Debjani Banerjee would like to acknowledge the DST INSPIRE research grant [DST/INSPIRE Fellowship/2018/IF180285] and the ALICE project grant [SR/MF/PS-02/2021-BI (E-37125)], and the computing facility at Bose Institute. Prottoy Das would like to acknowledge the Institutional Fellowship of Bose Institute, the ALICE project grant [SR/MF/PS-02/2021-BI (E-37125)], and the computing server facility at Bose Institute. Rohan V S would like to acknowledge JETSCAPE collaboration and simulation framework. The support from the DST project No. SR/MF/PS-02/2021-PU (E-37120) is acknowledged by Lokesh Kumar. Sudipan De and Sarthak Satapathy acknowledge financial support from the DST INSPIRE Faculty research grant (IFA18-PH220), India. Sreemoyee Sarkar would like to thank Dr. Rana Nandi for fruitful discussions of the topic.

Vaishnavi Desai would like to acknowledge JETSCAPE collaboration, its simulation framework, Goa University for seed money grant support and Param computing facility. Lakshmi J. Naik thanks the Department of Science and Technology, Govt. of India for the INSPIRE Fellowship. Sumit Kumar Kundu would like to acknowledge the financial support provided by the Council of Scientific and Industrial Research (CSIR) (File No. 09/1022(0051)/2018-EMR-I). Cho Win Aung and Thandar Zaw Win deeply thank to DIA-Programme funded by Ministry of Education, India. Ankit Kumar Panda acknowledges the CSIR-HRDG financial support. Victor Roy acknowledges support from the DAE, Govt. of India and the DST Inspire faculty research grant (IFA-16-PH-167), India. Shubhalaxmi Rath is thankful to the Indian Institute of Technology Bombay for the Institute postdoctoral fellowship. Sonali Padhan and Pritam Chakraborty would like to thank the Department of Science and Technology (DST), Government of India, for supporting the present work. S.P. acknowledges the doctoral fellowship from UGC, Government of India. Raghunath Sahoo acknowledges the financial support under the CERN Scientific Associateship and the financial grants under DAE-BRNS Project No. 58/14/29/2019-BRNS. Aditya Nath Mishra and Gergely Gábor Barnaföldi gratefully acknowledge the Hungarian National Research, Development and Innovation Office (NKFIH) under the contract numbers OTKA K135515, K123815, and NKFIH 2019-2.1.11-TET-2019-00078, 2019-2.1.11-TET-2019-00050 and Wigner Scientific Computing Laboratory (WSCLAB, the former Wigner GPU Laboratory). The authors gratefully acknowledge the MoU between IIT Indore and WRCP, Hungary, under which this work has been carried out as a part of the techno-scientific international cooperation. Nihar Ranjan Sahoo is supported by the Fundamental Research Funds of Shandong University and National Natural Science Foundation of China, Grant number:12050410235.

References

1. F. Becattini, F. Piccinini and J. Rizzo, Phys. Rev. C **77**, 024906 (2008) doi:10.1103/PhysRevC.77.024906 [arXiv:0711.1253 [nucl-th]].
2. K. Tuchin, Adv. High Energy Phys. **2013**, 490495 (2013) doi:10.1155/2013/490495 [arXiv:1301.0099 [hep-ph]].
3. Z. T. Liang and X. N. Wang, Phys. Rev. Lett. **94**, 102301 (2005) [erratum: Phys. Rev. Lett. **96**, 039901 (2006)] doi:10.1103/PhysRevLett.94.102301 [arXiv:nucl-th/0410079 [nucl-th]].
4. Z. T. Liang and X. N. Wang, Phys. Lett. B **629**, 20-26 (2005) doi:10.1016/j.physletb.2005.09.060 [arXiv:nucl-th/0411101 [nucl-th]].
5. S. A. Voloshin, [arXiv:nucl-th/0410089 [nucl-th]].
6. L. Adamczyk *et al.* [STAR], Nature **548**, 62-65 (2017) doi:10.1038/nature23004 [arXiv:1701.06657 [nucl-ex]].
7. J. Adam *et al.* [STAR], Phys. Rev. C **98**, 014910 (2018) doi:10.1103/PhysRevC.98.014910 [arXiv:1805.04400 [nucl-ex]].

8. J. Adam *et al.* [STAR], Phys. Rev. Lett. **123**, no.13, 132301 (2019) doi:10.1103/PhysRevLett.123.132301 [arXiv:1905.11917 [nucl-ex]].
9. J. Adam *et al.* [STAR], Phys. Rev. Lett. **126**, no.16, 162301 (2021) doi:10.1103/PhysRevLett.126.162301 [arXiv:2012.13601 [nucl-ex]].
10. M. S. Abdallah *et al.* [STAR], Phys. Rev. C **104**, no.6, L061901 (2021) doi:10.1103/PhysRevC.104.L061901 [arXiv:2108.00044 [nucl-ex]].
11. S. Acharya *et al.* [ALICE], Phys. Rev. Lett. **125**, no.1, 012301 (2020) doi:10.1103/PhysRevLett.125.012301 [arXiv:1910.14408 [nucl-ex]].
12. H. Li, H. Petersen, L. G. Pang, Q. Wang, X. L. Xia and X. N. Wang, Nucl. Phys. A **967**, 772-775 (2017) doi:10.1016/j.nuclphysa.2017.04.008 [arXiv:1704.03569 [nucl-th]].
13. S. Bhadury, W. Florkowski, A. Jaiswal, A. Kumar and R. Ryblewski, Phys. Rev. D **103**, no.1, 014030 (2021) doi:10.1103/PhysRevD.103.014030 [arXiv:2008.10976 [nucl-th]].
14. S. Bhadury, W. Florkowski, A. Jaiswal, A. Kumar and R. Ryblewski, Phys. Lett. B **814**, 136096 (2021) doi:10.1016/j.physletb.2021.136096 [arXiv:2002.03937 [hep-ph]].
15. S. Bhadury, W. Florkowski, A. Jaiswal, A. Kumar and R. Ryblewski, [arXiv:2204.01357 [nucl-th]].
16. D. Vasak, M. Gyulassy and H. T. Elze, Annals Phys. **173**, 462-492 (1987) doi:10.1016/0003-4916(87)90169-2
17. H. T. Elze, M. Gyulassy and D. Vasak, Phys. Lett. B **177**, 402-408 (1986) doi:10.1016/0370-2693(86)90778-1
18. H. T. Elze, M. Gyulassy and D. Vasak, Nucl. Phys. B **276**, 706-728 (1986) doi:10.1016/0550-3213(86)90072-6
19. N. Weickgenannt, X. L. Sheng, E. Speranza, Q. Wang and D. H. Rischke, Phys. Rev. D **100**, no.5, 056018 (2019) doi:10.1103/PhysRevD.100.056018 [arXiv:1902.06513 [hep-ph]].
20. N. Weickgenannt, E. Speranza, X. l. Sheng, Q. Wang and D. H. Rischke, Phys. Rev. Lett. **127**, no.5, 052301 (2021) doi:10.1103/PhysRevLett.127.052301 [arXiv:2005.01506 [hep-ph]].
21. X. L. Sheng, N. Weickgenannt, E. Speranza, D. H. Rischke and Q. Wang, Phys. Rev. D **104**, no.1, 016029 (2021) doi:10.1103/PhysRevD.104.016029 [arXiv:2103.10636 [nucl-th]].
22. Y. Dokshitzer & D. Kharzeev, *Phys. Lett.* B 519 (2001) 199.
23. G. D. Moore and D. Teaney, *Phys. Rev.* C 71 (2005) 064904.
24. B. Svetitsky, *Phys. Rev.* D 37 (1988) 2484.
25. M. G. Mustafa, D. Pal & D. K. Srivastava, *Phys. Rev.* C 72 (2005) 014905.
H. van Hees & R. Rapp, *Phys. Rev.* C 71 (2005) 034907.
26. X. Dong, Y-J. Lee & R. Rapp, Ann. Rev. Nucl. Part. Sci. 69 (2019) 417.
27. S. Caron-Huot & G. Moore, *J. H. E. P.* 0802 (2008) 081.
28. S. Cao, et al., *Phys. Rev.* C 99 (2019) 054907.
29. S. K. Das, F. Scardina, S. Plumari & V. Greco, *Phys. Lett.* B 747 (2015) 260.
30. Y. Xu, J. Bernhard, S. Bass, M. Nahrgang & S. Cao, *Phys. Rev.* C 97 (2018) 014907.
31. J. Kapusta & C. Gale, Finite Temperature Field Theory: Principles and Applications, 2nd Edition. Cambridge University Press, 2006.
32. H. Ding, *et al.*, *Phys. Rev.* D 104 (2021) 114508.
33. J. Casalderrey-Solana and D. Teaney, *Phys. Rev.* D 74 (2006) 085012.
34. S. Caron-Huot, M. Laine & G. Moore, *J. H. E. P.* 04 (2009) 053.
35. A. Bouttefeux and M. Laine, *J. H. E. P.* 12 (2020) 150.
36. D. Banerjee, S. Datta, R. Gavai & P. Majumdar, *Phys. Rev.* D 85 (2012) 014510.

37. A. Francis, O. Kaczmarek, M. Laine, T. Neuhaus & H. Ohno, *Phys. Rev.* D 92 (2015) 116003.
38. N. Brambilla, V. Leino, P. Petreczky & A. Vairo, *Phys. Rev.* D 102 (2020) 074503.
39. L. Altenkort, A. Eller, O. Kaczmarek, L. Mazur, G. Moore & H.-T. Shu, *Phys. Rev.* D 103 (2021) 014511.
40. N. Brambilla, V. Leino, J. Mayer-Steudte & P. Petreczky, arXiv:2206.02861.
41. D. Banerjee, S. Datta, R. Gavai & P. Majumdar, arXiv:2206.15471.
42. Y. Burnier, M. Laine, J. Langelage, L. Mether, *J. H. E. P.* 08 (2010) 094.
43. D. Banerjee, S. Datta & M. Laine, arXiv:2204.14075.
44. L. Altenkort, talk in Quark Matter 2022.
45. D. Teaney and L. Yan, Phys. Rev. C **89** (2014) no.1, 014901.
46. A. Kurkela and U. A. Wiedemann, Eur. Phys. J. C **79** (2019) no.9, 776.
47. G. S. Rocha, G. S. Denicol and J. Noronha, Phys. Rev. Lett. **127** (2021) no.4, 042301.
48. S. Mitra, Phys. Rev. C **103** (2021) no.1, 014905.
49. S. Mitra, Phys. Rev. C **105** (2022) no.1, 014902.
50. S. Mitra, Phys. Rev. C **105** (2022), 054910.
51. S. R. De Groot, W. A. Van Leeuwen and C. G. Van Weert, *Relativistic Kinetic Theory, Principles And Applications* (North-holland, Amsterdam, 1980).
52. P. Kovtun, JHEP **10** (2019), 034.
53. A. Jaiswal, Phys. Rev. C **87** (2013) no.5, 051901.
54. A. El, Z. Xu and C. Greiner, Phys. Rev. C **81** (2010), 041901.
55. K. Dusling, G. D. Moore and D. Teaney, Phys. Rev. C **81** (2010), 034907.
56. Z. Xu and C. Greiner, Phys. Rev. C **71** (2005), 064901.
57. F. S. Bemfica, M. M. Disconzi and J. Noronha, Phys. Rev. D **98** (2018) no.10, 104064.
58. F. S. Bemfica, M. M. Disconzi and J. Noronha, Phys. Rev. D **100** (2019) no.10, 104020.
59. R. E. Hoult and P. Kovtun, JHEP **06** (2020), 067.
60. F. S. Bemfica, M. M. Disconzi and J. Noronha, Accepted in Phys. Rev. X, [arXiv:2009.11388 [gr-qc]].
61. R. Biswas, S. Mitra and V. Roy, Phys. Rev. D **106**, no.1, L011501 (2022).
62. CMS Collaboration, Phys. Rev. C **100**, 024902 (2019).
63. CMS Collaboration, **JINST 3**, S08004 (2008).
64. CMS Collaboration, Phys. Lett. B **06**, 028 (2013).
65. CMS Collaboration, Phys. Lett. B **718**, 795 (2013).
66. CMS Collaboration, Phys. Lett. B **768**, 103 (2017).
67. E. Schnedermann *et al.*, Phys. Rev. C **48**, 2462 (1993).
68. CMS Collaboration, Phys. Lett. B **765**, 193 (2017).
69. CMS Collaboration, Phys. Rev. Lett. **120**, 092301 (2018).
70. CMS Collaboration, Phys. Rev. Lett. **121**, 082301 (2018).
71. STAR Collaboration, Phys. Rev. C **75**, 054906 (2007).
72. PHENIX Collaboration, Phys. Rev. C **85**, 064914 (2012).
73. K. Werner *et al.*, Phys. Rev. Lett. **112**, 232301 (2014).
74. B. Schenke *et al.* Phys. Rev. Lett. **117**, 162301 (2016).
75. CMS Collaboration, Phys. Lett. B. **791**, 172 (2019).
76. CMS Collaboration, Phys. Rev. Lett. **115**, 012301 (2015).
77. T. Lappi, L. McLerran, *Nucl. Phys. A* **772** (2006) 200-212.
78. R. Rapp, P. B. Gossiaux, A. Andronic, R. Averbeck, S. Masciocchi, A. Beraudo, E. Bratkovskaya, P. Braun-Munzinger, S. Cao and A. Dainese, *et al.* Nucl. Phys. A **979** (2018), 21-86.
79. F. Scardina, S. K. Das, V. Minissale, S. Plumari and V. Greco, Phys. Rev. C **96**

(2017) no.4, 044905
80. S. K. Das, J. e. Alam and P. Mohanty, Phys. Rev. C **82** (2010), 014908
81. M. Ruggieri, S. K. Das, *Phys. Rev. D* **98**(9) (2018) 094024.
82. S. K. Das, F. Scardina, S. Plumari, V. Greco, *Phys. Rev. C* **90** (2014) 044901.
83. P. Khowal, S. K. Das, L. Oliva, M. Ruggieri, *Eur. Phys. J. Plus* **137** (2022) 307.
84. S. K. Wong, *Nuovo Cim. A* **65** (1970) 689-694.
85. J. H. Liu, S. Plumari, S. K. Das, V. Greco, M. Ruggieri, *Phys. Rev. C* **102**(4) (2020) 044902.
86. J. H. Liu, S. K. Das, V. Greco, M. Ruggieri, *Phys. Rev. D* **103**(3) (2021) 034029.
87. Y. Sun, G. Coci, S. K. Das, S. Plumari, M. Ruggieri and V. Greco, Phys. Lett. B **798** (2019), 134933
88. G. Aarts, J. Aichelin, C. Allton, R. Arnaldi, S. A. Bass, C. Bedda, N. Brambilla, E. Bratkovskaya, P. Braun-Munzinger and G. E. Bruno, *et al.* Eur. Phys. J. A **53** (2017) no.5, 93
89. S. Plumari, V. Minissale, S. K. Das, G. Coci and V. Greco, Eur. Phys. J. C **78** (2018) no.4, 348
90. M. Ruggieri, Pooja, J. Prakash and S. K. Das, *[arXiv:2203.06712 [hep-ph]].*
91. Viñales, A. D. and Despósito, M. A. *Physical Review E*, **75**, 042102, 2007.
92. S. K. Das, J. M. Torres-Rincon, L. Tolos, V. Minissale, F. Scardina and V. Greco, Phys. Rev. D **94** (2016) no.11, 114039
93. ALICE (P. Cortese et al.), tech. rep., 9, 2004.
94. ALICE (J. Alme et al.), Nucl. Instrum. Meth. A622 (2010) 316–367, arXiv:1001.1950.
95. ALICE (K. Aamodt et al.), JINST 5 (2010) P03003, arXiv:1001.0502.
96. Matteo Cacciari et. al., "FastJet User Manual", Eur.Phys.J.C 72 (2012) 1896.
97. G. D'Agostini, Nucl. Instrum. Meth. A 362, 487-498 (1995).
98. T. Adye, arXiv:1105.1160 [physics.data-an].
99. ALICE (B. B. Abelev et al.), Phys. Rev. D 91 112012 (2015).
100. J. Cleymans, J. Phys. G **35**, 044017 (2008)11.
101. K. Fukushima, Y. Hidaka, Phys. Rev. Lett. **117**, 102301 (2016).
102. M. Hasan, B. Chatterjee, B. K. Patra, Eur. Phys. J. C **77**, 767 (2017).
103. M. Hasan, B. K. Patra, B. Chatterjee, P. Bagchi, Nucl. Phys. A **995**, 121688 (2020).
104. M. Hasan, B. K. Patra Phys. Rev. D **102**, 036020 (2020).
105. J. Alford and M. Strickland, Phys. Rev. D **88**, 105017 (2013).
106. C. Bonati, M. D'Elia, and A. Rucci, Phys. Rev. D **92**, 054014 (2015).
107. B. Singh, L. Thakur, H. Mishra, Phys. Rev. D **97**, 096011 (2018).
108. Adrian Dumitru, Yun Guo, and Michael Strickland Phys. Rev. D **79**, 114003 (2009).
109. B. Karmakar, A. Bandyopadhyay, N. Haque and M. G. Mustafa, Eur. Phys. J. C. **79**, 658, (2019).
110. Armesto, Néstor, EPJ Web Conf. 171 11001 (2018).
111. ALICE (B. B. Abelev et al.), Int. J. Mod. Phys. A 29, 1430044 (2014).
112. Matteo Cacciari et. al., JHEP04(2008)063.
113. RooUnfold, `https://gitlab.cern.ch/RooUnfold/RooUnfold`.
114. Roesler et al., `https://doi.org/10.1007/978-3-642-18211-2_166`.
115. A. Vogt (DESY), https://doi.org/10.48550/arXiv.hep-ph/9507241.
116. M. A. Lisa, S. Pratt, R. Soltz, and U. Wiedeman, *Ann. Rev. Nucl. Part. Sci.* **55** (2005) 357.
117. CMS Collaboration, CMS-PAS-HIN-21-006
118. R. Lednicky and V. Lyuboshits, *Sov. J. Nucl. Phys.* **35** (1982) 770.
119. ALICE Collaboration, *Phys. Rev. C* **114** (2021) 055201.
120. STAR Collaboration, *Phys. Rev. Lett.* **103** (2015) 022301.

121. K. Morita, T. Furumoto, and A. Ohnishi, *Phys. Rev. C* **91** (2015) 024916.
122. E. Hiyama et al., *Phys. Rev. C* **66** (2002) 024007.
123. I. N. Filikhin and A. Gal, *Nucl. Phys. A* **707** (2002) 491.
124. A BALTZ and G BAUR and D DENTERRIA and L FRANKFURT and F GELIS and V GUZEY and K HENCKEN and Y KHARLOV and M KLASEN and S KLEIN, *Ann. Rev. Nucl. Part. Sci.* **1** (2008) 458.
125. Stanley J. Brodsky and L. Frankfurt and J. F. Gunion and A. H. Mueller and M. Strikman, *Physical Review D* **50** (1994) 3134.
126. CMS Collaboration, *The European Physical Journal C* **277** (2019) 4005.
127. Jones, S. P. and Martin, A. D. and Ryskin, M. G. and Teubner, T., *JHEP* **11** (2019) 085.
128. A. M. Sirunyan and et al, *Physics Letters B* **1** (2009) 680.
129. E. V. Shuryak, Phys. Lett. B 78, 150 (1978).
130. A. Majumder and M. Van Leeuwen, Prog. Part. Nucl. Phys. 66,**41**(2011),
131. M. L. Miller, K. Reygers *et al.* Rev. Nucl. Part. Sci. 57 (2007) 205.
132. J. H. Putschke, K. Kauder, E. Khalaj, *et al.* [arXiv:1903.07706 [nucl-th]].
133. A. Kumar *et al.* [JETSCAPE], [arXiv:2204.01163 [hep-ph]].
134. Y. He, T. Luo, X.-N. Wang, and Y. Zhu, Phys. Rev. C91, 054908 (2015).
135. S. Cao, T. Luo, G.-Y. Qin, and X.-N. Wang, Phys. Rev.C94, 014909 (2016).
136. M. Aaboud et al. (ATLAS), Phys.Lett. B 790, 108 (2019), arXiv:1805.05635 [nucl-ex].
137. J. Adam et al. (STAR), Phys. Rev. C 102, 054913 (2020), arXiv:2006.00582 [nucl-ex]
138. J. S. Moreland, J. E. Bernhard, and S. A. Bass, APhys. Rev. C 92, 011901 (2015).
139. T. Sjostrand,Phys. Commun. 178 (2008) 852, arXiv: 0710.3820 [hep-ph].
140. B. Schenke, S. Jeon, and C. Gale, Phys. Rev. C 82, 014903 (2010).
141. B. Schenke, S. Jeon, C. Gale., Phys. Rev. Lett. 106, 042301 (2011).
142. J.-F. Paquet, *et al.*. Phys. Rev. C 93, 044906 (2016).
143. M. Cacciari, G. P. Salam, and G. Soyez, JHEP 04, 063, arXiv:0802.1189 [hep-ph].
144. J. Adams *et al.* [STAR], Nucl. Phys. A **757**, 102-183 (2005).
145. K. Aamodt *et al.* [ALICE], JINST **3**, S08002 (2008).
146. S. Acharya *et al.* [ALICE], Eur. Phys. J. C **81**, no.7, 584 (2021).
147. S. Acharya *et al.* [ALICE], Phys. Rev. C **101**, no.4, 044907 (2020).
148. J. V. Greco, C. M. Ko, and P. Levai, Phys. Rev. Lett. **90**, 202302 (2003); R. J. Fries, B. Müller, C. Nonaka, and S. A. Bass, Phys. Rev. Lett. **90**, 202303 (2003).
149. S. Acharya *et al.* [ALICE], [arXiv:2204.10263 [nucl-ex]].
150. S. Acharya *et al.* [ALICE], JHEP **01**, 106 (2022).
151. H. Lui [for STAR Collaboration], Quark Matter (2022).
152. J. Adam *et al.* [STAR], Phys. Rev. Lett. **126**, no.9, 092301 (2021).
153. M. S. Abdallah *et al.* [STAR], Phys. Rev. Lett. **128**, no.20, 202303 (2022).
154. Ho-San Ko [for STAR Collaboration], Quark Matter (2022).
155. S. Acharya *et al.* (ALICE), *Phys. Rev. Lett.* **125** 0220301 (2020).
156. J. Adam *et al.* (STAR), *Phys. Rev. Lett.* **123** 162301 (2019).
157. A. Jaiswal *et al.*, *Int. J. Mod. Phys. E* **E 30**, 2130001 (2021).
158. K. K. Gowthama, M. Kurian, and V. Chandra, *Phys. Rev. D* **104**, 094037 (2021).
159. K. K. Gowthama, M. Kurian, and V. Chandra, *Phys. Rev. D* **103**, 074017 (2021).
160. M. Hongo, Y. Hirono, and T. Hirano, *Phys. Lett. B* **775**, 266 (2017).
161. L. Thakur and P. Srivastava, *Phys. Rev. D* **100**, 076016 (2019).
162. A. Amato, G. Aarts, C. Allton, P. Giudice, S. Hands, and J.-I. Skullerud, *Phys. Rev. Lett.* **111**, 172001 (2013).
163. G. Aarts, C. Allton, J. Foley, S. Hands, and S. Kim, *Phys. Rev. Lett.* **99**, 022002 (2007).

164. H.-T. Ding, A. Francis, O. Kaczmarek, F. Karsch, E. Laermann, and W. Soeldner, *Phys. Rev. D* **83**, 034504 (2011).
165. Observation of the electromagnetic field effect via charge-dependent directed flow in Au+Au, Ru+Ru, and Zr+Zr collisions at $\sqrt{s_{NN}} = 200$ GeV (In preparation by STAR collaboration).
166. U. Gürsoy, D. Kharzeev, E. Marcus, K. Rajagopal and C. Shen, "Charge-dependent Flow Induced by Magnetic and Electric Fields in Heavy Ion Collisions," Phys. Rev. C **98** (2018), 055201
167. U. Gursoy, D. Kharzeev and K. Rajagopal, "Magnetohydrodynamics, charged currents and directed flow in heavy ion collisions," Phys. Rev. C **89** (2014), 054905
168. E. Shuryak, "Strongly coupled quark-gluon plasma in heavy ion collisions," Rev. Mod. Phys. **89** (2017), 035001
169. L. Adamczyk *et al.* [STAR], "Directed Flow of Identified Particles in Au + Au Collisions at $\sqrt{s_N N} = 200$ GeV at RHIC," Phys. Rev. Lett. **108** (2012), 202301
170. V. Voronyuk, V. D. Toneev, W. Cassing, E. L. Bratkovskaya, V. P. Konchakovski and S. A. Voloshin, "(Electro-)Magnetic field evolution in relativistic heavy-ion collisions," Phys. Rev. C **83** (2011), 054911
171. P. Bozek and I. Wyskiel, "Directed flow in ultrarelativistic heavy-ion collisions," Phys. Rev. C **81** (2010), 054902
172. Y. Guo, F. Liu and A. Tang, "Directed flow of transported and non-transported protons in Au+Au collisions from UrQMD model," Phys. Rev. C **86** (2012), 044901
173. J. Adams *et al.* [STAR], "Azimuthal anisotropy at RHIC: The First and fourth harmonics," Phys. Rev. Lett. **92** (2004), 062301
174. C. Adler, A. Denisov, E. Garcia, M. J. Murray, H. Strobele and S. N. White, "The RHIC zero degree calorimeter," Nucl. Instrum. Meth. A **470** (2001), 488-499
175. M. Anderson, J. Berkovitz, W. Betts, R. Bossingham, F. Bieser, R. Brown, M. Burks, M. Calderon de la Barca Sanchez, D. A. Cebra and M. G. Cherney, *et al.* "The Star time projection chamber: A Unique tool for studying high multiplicity events at RHIC," Nucl. Instrum. Meth. A **499** (2003), 659-678
176. W. J. Llope, F. Geurts, J. W. Mitchell, Z. Liu, N. Adams, G. Eppley, D. Keane, J. Li, F. Liu and L. Liu, *et al.* Nucl. Instrum. Meth. A **522** (2004), 252-273
177. J. Adam et. al [ALICE Collaboration], Nature Phys. **13**, 535 (2017).
178. C. R. Singh, S. Deb, Raghunath Sahoo, Jan-e Alam, Eur. Phys. J. C **82**, 542 (2022).
179. T. Matsui and H. Satz, Phys. Lett. B **178**, 416 (1986).
180. B. Abelev et. al [ALICE Collaboration], Phys. Lett. B **712**, 165 (2012).
181. S. Acharya et. al [ALICE Collaboration], Phys. Lett. B **810**, 135758 (2022).
182. A. Morunga, Phys. Rev. C **69**, 034903 (2004).
183. S. Acharya et. al [ALICE Collaboration], Eur. Phys. J. C **81**, 256 (2021).
184. E. V. Shuryak, Nucl. Phys. A **750**, 64-83 (2005) [arXiv:hep-ph/0405066 [hep-ph]].
185. V. Skokov, A. Y. Illarionov and V. Toneev, Int. J. Mod. Phys. A **24**, 5925-5932 (2009) [arXiv:0907.1396 [nucl-th]].
186. A. Bzdak and V. Skokov, Phys. Lett. B **710**, 171-174 (2012) [arXiv:1111.1949 [hep-ph]].
187. D. Banerjee, S. Paul, P. Das, A. Modak, A. Budhraja, S. Ghosh and S. K. Prasad, [arXiv:2103.14440 [hep-ph]].
188. S. K. Das, S. Plumari, S. Chatterjee, J. Alam, F. Scardina and V. Greco, Phys. Lett. B **768**, 260-264 (2017) [arXiv:1608.02231 [nucl-th]].
189. D. E. Kharzeev, L. D. McLerran and H. J. Warringa, Nucl. Phys. A **803**, 227-253 (2008) [arXiv:0711.0950 [hep-ph]].
190. K. Fukushima, K. Hattori, H. U. Yee and Y. Yin, Phys. Rev. D **93**, no.7, 074028

(2016) [arXiv:1512.03689 [hep-ph]].
191. S. I. Finazzo, R. Critelli, R. Rougemont and J. Noronha, Phys. Rev. D **94**, no.5, 054020 (2016) [erratum: Phys. Rev. D **96**, no.1, 019903 (2017)] [arXiv:1605.06061 [hep-ph]].
192. G. S. Denicol, J. Noronha , 2020, Phys. Rev. Lett., **124**, 152301, 2020.
193. G. S.Denicol , H. Niemi, E. Molnar, D. H. Rischke, 2012, Phys. Rev. D. **85**, 114047, 2012.
194. Finzi, A. and Wolf, R. A. APJ **100** 835, 1968.
195. I. Easson. and C. J. Pethick, APJ **227**, 1979.
196. J. Madsen, *Phys. Rev. D* **46** 3290 (1992).
197. M. G. Alford and S. Mahmoodifar and K. Schwenzer, J. Phys. G **37**, 125202 (2010)
198. A. Schmitt and P. Shternin, Astrophys. Space Sci. Libr., **457**, 455 (2018).
199. E. R. Most, S. P. Harris, C. Plumberg, M. G. Alford, J. Noronha, J. Noronha-Hostler, F. Pretorius, H. Witek and N. Yunes, Mon. Not. Roy. Astron. Soc., **509**, 1096, 2021.
200. M. G. Alford, L. Bovard, M. Hanauske, L. Rezzolla and K. Schwenzer, Phys. Rev. Lett. **120** 041101 (2018).
201. M. Alford, A. Harutyunyan and A. Sedrakian, Phys. Rev. D. **100**, 103021 (2019).
202. S. L. Shapiro and S. A. Teukolsky, Black holes, white dwarfs, and neutron stars : the physics of compact objects, 1983.
203. D. G. Yakovlev, A. D. Kaminker, O. Y. Gnedin and P. Haensel, Phys. Rept. **354** 1, (2004).
204. R. R. Silbar and S. Reddy, American Journal of Physics **72**, 892 (2004).
205. A. Majumder et al., Prog. Part. Nucl. Phys. 66 (2011) 41–92.
206. A. Majumder, Nucl.andPart.Phys.P276-278(2016)1.
207. P. Caucal, et al., Phys. Rev. Lett. 120 (2018) 232001.
208. J. Putschke et al., *The JETSCAPE framework*, arXiv:1903.07706 [nucl-th].
209. *JETSCAPE collaboration.* https://github.com/JETSCAPE/JETSCAPE.
210. ATLAS Collaboration,Phys. Rev. C 98, 024908 (2018).
211. STAR Collaboration, arXiv:2002.06217 [nucl-ex].
212. T. Sjostrand et al., arXiv: 0710.3820 [hep-ph].
213. A. Majumder, arXiv:1301.5323 [nucl-th].
214. B. Schenke et al., Phys. Rev. C80 (2009) 054913 [0909.2037].
215. J. Casalderrey-Solana et al., arXiv:1405.3864 [hep-ph].
216. W. A. Hiscock and L. Lindblom, Annals Phys. **151** (1983), 466-496.
217. W. A. Hiscock and L. Lindblom, Phys. Rev. D **35** (1987), 3723-3732.
218. I. Muller, Z. Phys. **198** (1967), 329-344
219. W. Israel and J. M. Stewart, Annals Phys. **118** (1979), 341-372
220. J. Anderson and H. Witting, Physica **74**, 466 (1974).
221. D. Dash, S. Bhadury, S. Jaiswal and A. Jaiswal, Phys. Lett. B **831** (2022), 137202
222. G. S. Rocha, G. S. Denicol and J. Noronha, [arXiv:2205.00078 [nucl-th]].
223. M. P. Heller and M. Spalinski, Phys. Rev. Lett. **115**, no.7, 072501 (2015).
224. S. Jaiswal, C. Chattopadhyay, A. Jaiswal, S. Pal and U. Heinz, Phys. Rev. C **100**, no.3, 034901 (2019).
225. L. J. Naik, S. Jaiswal, K. Sreelakshmi, A. Jaiswal and V. Sreekanth, [arXiv:2107.08791 [hep-ph]].
226. J. D. Bjorken, Phys. Rev. D **27**, 140-151 (1983).
227. A. Jaiswal, Phys. Rev. C **88**, 021903 (2013).
228. ALICE Collaboration, Phys. Rev. Lett. **107** (2011), 032301. (2012), 014907.
229. CBM Collaboration, Eur. Phys. J. A **53** (2017) no.3, 60
230. V. Kekelidze *et al.*, Nucl. Phys. A **956** (2016), 846-849

231. S. A. Bass *et al.*, Prog. Part. Nucl. Phys. **41** (1998), 255-369
232. M. Bleicher *et al.*, J. Phys. G **25** (1999), 1859-1896
233. H. Petersen *et al.*, Phys. Rev. C **78** (2008), 044901
234. P. Huovinen *et al.*, Eur. Phys. J. A **48** (2012), 171
235. H. Liu *et al.* [E895], Phys. Rev. Lett. **84** (2000), 5488-5492
236. L. Adamczyk *et al.* [STAR], Phys. Rev. Lett. **112** (2014) no.16, 162301
237. C. Alt *et al.* [NA49], Phys. Rev. C **68** (2003), 034903
238. L. Adamczyk *et al.* [STAR], Phys. Rev. C **96** (2017) no.4, 044904
239. S. K. Kundu *et al.*, Phys. Rev. C **104** (2021) no.2, 024907
240. S. K. Kundu *et al.*, [arXiv:2204.09762 [nucl-th]].
241. J. Dey, S. Satapathy, P. Murmu, S. Ghosh, *Pramana* **95** (2021) 3, 125.
242. M. Greif, I. Bouras, C. Greiner, and Z. Xu, *Phys. Rev. D* **90**, (2014) 094014
243. W. Cassing, O. Linnyk, T. Steinert, and V. Ozvenchuk, *Phys.Rev. Lett* **110**, (2013) 182301.
244. D. Fernández-Fraile, and A. Gómez Nicola, *Eur. Phys. J. C* **62** (2009) 37–54.
245. P. Arnold, G. D. Moore and L. G. Yaffe, *JHEP* **05**, 051 (2003).
246. A. Amato, G. Aarts, C. Allton, P. Giudice, S. Hands, and J. I. Skullerud, *Phys. Rev. Lett*, **111**, (2013) 172001.
247. V. Skokov, A. Y. Illarionov and V. Toneev, *Int. J. Mod. Phys. A* **24**, 5925 (2009).
248. K. Tuchin, arXiv:1305.5806v1[hep-ph], "Time and space dependence of electromagnetic field in relativistic heavy-ion collisions", 24 May, 2013.
249. B. B. Brandt, A. Francis, H. B. Meyer, and H. Wittig, *J. High Energy Phys*, **03** (2013) 100.
250. R. Marty *et al.*,arXiv:1305.7180v1[hep-ph], "Transport coefficients from the Nambu-Jona-Lasinio model for SU(3)f", 30 May, 2013.
251. D.F.Fraile and A.G. Nicola, Eur.Phys.J.C (2009) 62: 37-54, "Transport Coefficients and resonances for a meson gas in chiral perturbation theory", 2013.
252. L. P. Csernai, J. I. Kapusta, L. D. McLerran, *Phys. Rev. Lett.* **97** (2006) 152303.
253. S. Bhadury, M. Kurian, V. Chandra and A. Jaiswal, J. Phys. G **48**, no.10, 10 (2021).
254. V. Chandra and V. Ravishankar, Eur. Phys. J. C **64**, 63-72 (2009).
255. S. Mitra and V. Chandra, Phys. Rev. D **97**, no.3, 034032 (2018).
256. L. J. Naik and V. Sreekanth, *manuscript under preparation.*
257. Denicol, Gabriel S. et.al. Phys.Rev.D 98 (2018) 7, 076009
258. Gabriel S. et.al. Phys.Rev.D 99 (2019) 5, 056017
259. Ankit Kumar et.al. JHEP 03 (2021) 216
260. Panda, Ankit Kumar et.al. Phys.Rev.D 104 (2021) 5, 054004
261. J. E. Bernhard et al., *Phys. Rev. C* **91** (2015) 054910.
262. J. E. Bernhard et al., *Phys. Rev. C* **94**, (2016) 024907
263. A. Jaiswal and V. Koch, [arXiv:1508.05878 [nucl-th]].
264. C. E. Rasmussen and C. K. I. Williams, Gaussian Pro- cesses for Machine Learning (MIT Press, Cambridge, MA, 2006).
265. M. D. Morris and T. J. Mitchell, *J.Stat.Plan.Inf.* **381** (1995) 43.
266. M. E. Tipping and C. M. Bishop, "Mixtures of Probabilistic Principal Component Analyzers",*Neural Computation* **43** (1999) 11, 443–482.
267. B. Abelev *et al.* [ALICE], *Phys. Rev. c* **044910** (2013) 88
268. J. Goodman and J. Wearel, *Comm.App.Math.Comp.Sc.* **5** (2010) 65.
269. S. Rath and B. K. Patra, *Phys. Rev. D* **100** (2019) 016009.
270. E. M. Lifshitz and L. P. Pitaevskii, "Physical Kinetics", Pergamon Press, 1981.
271. S. Rath and B. K. Patra, *Phys. Rev. D* **102** (2020) 036011.
272. B. Feng, *Phys. Rev. D* **96** (2017) 036009.

273. A. Hosoya and K. Kajantie, *Nucl. Phys. B* **250** (1985) 666.
274. S. Rath and S. Dash, arXiv:2112.11802 [hep-ph].
275. A. Peshier, B. Kämpfer and G. Soff, *Phys. Rev. D* **66** (2002) 094003.
276. Badalà Angela, EPJ Conf. Proc. 96, 01003 (2015).
277. K. Aamodt et al. (ALICE Collaboration), J. Instrum. 3, S08002 (2008).
278. B. Abelev et al. (ALICE Collaboration), Int. J. Mod. Phys. A 29, 1430044 (2014).
279. S. Acharya et al. (ALICE Collaboration), Phys.Rev.C 99 (2019) 024905.
280. S. Acharya et al. (ALICE Collaboration), E. Phys. J. C 80, 160 (2020)
281. A. Kisiel, Phys. Rev. C, **81**, 064906 (2010)
282. A. Kisiel, Acta Phys. Polon. B **48**, 717 (2017)
283. S. Acharya *et al.* [ALICE], Phys. Lett. B **813**, 136030 (2021)
284. D. Sahu, S. Tripathy, G. S. Pradhan and R. Sahoo, Phys. Rev. C **101**, 014902 (2020).
285. S. Singha, B. Mohanty and Z. W. Lin, Int. J. Mod. Phys. E **24**, 1550041 (2015).
286. K. Adcox *et al.* [PHENIX], Phys. Rev. C **69**, 024904 (2004).
287. U. Heinz and R. Snellings, Ann. Rev. Nucl. Part. Sci. **63**, 123 (2013).
288. S. Voloshin and Y. Zhang, Z. Phys. C **70**, 665 (1996).
289. J. Adams *et al.* (STAR Collaboration), Phys. Rev. Lett. **92**, 052302 (2004).
290. K. Aamodt *et al.* (ALICE Collaboration), Phys. Rev. Lett. **105**, 252302 (2010).
291. N. Mallick, S. Prasad, A. N. Mishra, R. Sahoo and G. G. Barnaföldi, Phys. Rev. D **105**, 114022 (2022).
292. G. Bíró, B. Tankó-Bartalis and G. G. Barnaföldi, [arXiv:2111.15655 [hep-ph]].
293. L. G. Pang, K. Zhou, N. Su, H. Petersen, H. Stöcker and X. N. Wang, Nature Commun. **9**, 210 (2018).
294. P. Xiang, Y. S. Zhao and X. G. Huang, [arXiv:2112.03824 [hep-ph]].
295. Z. W. Lin, C. M. Ko, B. A. Li, B. Zhang and S. Pal, Phys. Rev. C **72**, 064901 (2005).
296. J. Adam *et al.* (ALICE Collaboration), Phys. Rev. Lett. **116**, 132302 (2016).
297. A. Adare *et al.* (PHENIX Collaboration), Phys. Rev. C **99**, 024903 (2019).
298. V. V. Sokov, A. Y. Illarionov, and V. D. Toneev, *International Journal of Modern Physics A* **24** (2009) 5925.
299. K. Tuchin, *Phys. Rev. C* **82**, 3 (2010).
300. K. Fukushima and Y. Hidaka, *Phys. Rev. Lett.* **120**, 162301 (2018).
301. B. Schenke, P. Tribedy, and R. Venugopalan, *Phys. Rev. Lett.* **108**, 252301 (2012).
302. B. Karmakar, A. Bandyopadhyay, N. Haque, M. G. Mustafa, *The European Physical Journal C* **79**, 658 (2019).
303. A. Das, A. Bandyopadhyay, P. K. Roy, and M. G. Mustafa, *Phys. Rev. D* **97**, 034024 (2018).
304. P. Panday and B. K. Patra, *Phys. Rev. D* **105**, 116009 (2022).
305. H. B. Callen, *Thermodynamics and an Introduction to Thermostatistics*, 2nd ed. (Wiley, New York, 1991).
306. K. Tuchin, Phys. Rev. C **88**, 024911 (2013).
307. L. McLerran and V. Skokov, Nucl. Phys. A **929**, (2014) 184-190.
308. E. Stewart and K. Tuchin, Phys. Rev. C **97**, 044906 (2018).
309. V. M. Bannur, J. High Energy Phys. **09** (2007) 046.
310. L. D. Landau, E. M. Lifshitz, *Course of Theoretical Physics, Volume 10, Physical Kinetics* (Pergamon International Library, 1981).
311. D. J. Gross, R. D. Pisarski and L. G. Yaffe, Rev. Mod. Phys. **53**, 43 (1981)
312. R. Kobes and G. Kunstatter, Phys. Rev. Lett. **61**, 392 (1988)
313. R. D. Pisarski, Phys. Rev. Lett. **63**, 1129 (1989)
314. E. Braaten and R. D. Pisarski, Phys. Rev. Lett. **64**, 1338 (1990)
315. E. Braaten and R. D. Pisarski, Phys. Rev. D **42**, 2156-2160 (1990)

316. N. Haque, A. Bandyopadhyay, J. O. Andersen, M. G. Mustafa, M. Strickland and N. Su, JHEP **05**, 027 (2014)
317. H. A. Weldon, Phys. Rev. D **26**, 2789 (1982)
318. A. Abada, K. Benchallal and K. Bouakaz, JHEP **03**, 058 (2015)
319. Sumit, N. Haque and B. K. Patra [arxiv:2201.07173]
320. S. Acharya *et al.* [ALICE], JHEP **01**, 174 (2022) doi:10.1007/JHEP01(2022)174 [arXiv:2110.09420 [nucl-ex]].
321. [CMS], CMS-PAS-HIN-19-002.
322. [ALICE preliminary] Prottoy Das and Debjani Banerjee's talk.
323. L. Adamczyk *et al.* [STAR], Phys. Rev. Lett. **110**, no.14, 142301 (2013) doi:10.1103/PhysRevLett.110.142301 [arXiv:1301.2347 [nucl-ex]].
324. [STAR Preliminary], Chitrasen Jena's talk
325. ALICE preliminary Sonali Padhan's talk
326. ALICE preliminary Abhik Modak's talk
327. L. Adamczyk *et al.* [STAR], Phys. Rev. Lett. **114**, no.2, 022301 (2015) doi:10.1103/PhysRevLett.114.022301 [arXiv:1408.4360 [nucl-ex]].
328. CMS Preliminary Raghunath Pradhan's talk
329. STAR experiment Lokesh Kumar's talk